

# **Tribology of the Head-Disk Interface**

Guest Editors: Bruno Marchon, Norio Tagawa, Bo Liu, Tom Karis,  
and Jia-Yang Juang





## **Tribology of the Head-Disk Interface**

Advances in Tribology

---

## **Tribology of the Head-Disk Interface**

Guest Editors: Bruno Marchon, Norio Tagawa, Bo Liu,  
Tom Karis, and Jia-Yang Juang



---

Copyright © 2013 Hindawi Publishing Corporation. All rights reserved.

This is a special issue published in "Advances in Tribology." All articles are open access articles distributed under the Creative Commons Attribution License, which permits unrestricted use, distribution, and reproduction in any medium, provided the original work is properly cited.

## **Editorial Board**

George G. Adams, USA

Arvind Agarwal, USA

Mihai Arghir, France

Pranesh B. Aswath, USA

Shyam Bahadur, USA

B. Bhushan, USA

Navin Chand, India

Huseyin Çimentoğlu, Turkey

Enrico Ciulli, Italy

J. Paulo Davim, Portugal

Patrick De Baets, Belgium

Abdallah Elsharkawy, Kuwait

Liang Fang, China

Kambiz Farhang, USA

Michel Fillon, France

K. Friedrich, Germany

Hiromu Hashimoto, Japan

Meng Hua, Hong Kong

Said Jahanmir, USA

Gun Hee Jang, Korea

Yuansheng Jin, China

Mitjan Kalin, Slovenia

Motohiro Kaneta, Japan

Yuan Kang, Taiwan

Ajay Kapoor, Australia

Koji Kato, Japan

T. G. Keith, USA

M. M. Khonsari, USA

Dae Eun Kim, Korea

Bankim C. Majumdar, India

Braham Prakash, Sweden

Richard Salant, USA

Jerzy T. Sawicki, USA

Ian Sherrington, UK

Sujeet Kumar Sinha, Singapore

G. W. Stachowiak, Australia

Andras Z. Szeri, USA

J. Vižintin, Poland

Anna Walicka, Poland

Qian Wang, USA

Si-Wei Zhang, China

## Contents

**Tribology of the Head-Disk Interface**, Bruno Marchon, Norio Tagawa, Bo Liu, Tom Karis, and Jia-Yang Juang  
Volume 2013, Article ID 574158, 2 pages

**A Description of Multiscale Modeling for the Head-Disk Interface Focusing on Bottom-Level Lubricant and Carbon Overcoat Models**, Myung S. Jhon, Pil Seung Chung, Robert L. Smith, and Lorenz T. Biegler  
Volume 2013, Article ID 794151, 27 pages

**The Head-Disk Interface Roadmap to an Areal Density of 4 Tbit/in<sup>2</sup>**, Bruno Marchon, Thomas Pitchford, Yiao-Tee Hsia, and Sunita Gangopadhyay  
Volume 2013, Article ID 521086, 8 pages

**A Correlative Defect Analyzer Combining Glide Test with Atomic Force Microscope**, Jizhong He  
Volume 2013, Article ID 657363, 8 pages

**Atomistic Frictional Properties of the C(100)2x1-H Surface**, Paul M. Jones, Huan Tang, Yiao-Tee Hsia, Xiaoping Yan, James D. Kiely, Junwei Huang, Christopher Platt, Xiaoding Ma, Michael Stirniman, and Lang Dinh  
Volume 2013, Article ID 850473, 11 pages

**Nanorheometry of Molecularly Thin Liquid Lubricant Films Coated on Magnetic Disks**, Shintaro Itoh, Yuya Hamamoto, Koki Ishii, Kenji Fukuzawa, and Hedong Zhang  
Volume 2012, Article ID 209630, 12 pages

**Dependence of Pin Surface Roughness for Friction Forces of Ultrathin Perfluoropolyether Lubricant Film on Magnetic Disks by Pin-on-Disk Test**, H. Tani, Y. Mitsuya, T. Kitagawa, and N. Tagawa  
Volume 2012, Article ID 923818, 7 pages

**Flying Instability due to Organic Compounds in Hard Disk Drive**, Koji Sonoda  
Volume 2012, Article ID 170189, 6 pages

**Parametric Investigations at the Head-Disk Interface of Thermal Fly-Height Control Sliders in Contact**, Sripathi V. Canchi, David B. Bogy, Run-Han Wang, and Aravind N. Murthy  
Volume 2012, Article ID 303071, 11 pages

**Low Molecular Weight Z-Tetraol Boundary Lubricant Films in Hard Disk Drives**, R. J. Waltman and H. Deng  
Volume 2012, Article ID 964089, 7 pages

**Slider Posture Effects on Air Bearing in a Heat-Assisted Magnetic Recording System**, Kyaw Sett Myo, Weidong Zhou, Xiaoyang Huang, Shengkai Yu, and Wei Hua  
Volume 2012, Article ID 169207, 6 pages

## Editorial

# Tribology of the Head-Disk Interface

**Bruno Marchon,<sup>1</sup> Norio Tagawa,<sup>2</sup> Bo Liu,<sup>3</sup> Tom Karis,<sup>1</sup> and Jia-Yang Juang<sup>4</sup>**

<sup>1</sup> HGST, San Jose Research Center, 3403 Yerba Buena Road, San Jose, CA 95135, USA

<sup>2</sup> Department of Mechanical Engineering, Faculty of Engineering Science, Kansai University, 3-3-35 Yamate-cho, Suita, Osaka 564-8680, Japan

<sup>3</sup> Data Storage Institute, Agency for Science, Engineering and Research, DSI Building, 5 Engineering Drive, Singapore 117 608

<sup>4</sup> Department of Mechanical Engineering, National Taiwan University, 713 Engineering Building, No. 1, Section 4, Roosevelt Road, Taipei 10617, Taiwan

Correspondence should be addressed to Bruno Marchon; [bruno.marchon@hgst.com](mailto:bruno.marchon@hgst.com)

Received 3 March 2013; Accepted 3 March 2013

Copyright © 2013 Bruno Marchon et al. This is an open access article distributed under the Creative Commons Attribution License, which permits unrestricted use, distribution, and reproduction in any medium, provided the original work is properly cited.

Hard Disk Drives (HDD) are perhaps the unsung heroes of today's information technology. The rise and growth of the Internet search engines, social media, and cloud computing have been enabled, in part, by the inexpensive and massive storage capabilities that HDD technology provides. Less than 60 years after its invention by IBM in San Jose in 1956, the hard disk drive has seen an unrelentless, Moore's Law-like growth in storage density, as well as a concomitant decrease in price and form factor. The first HDD ever commercialized, IBM's RAMAC, had a mere 5 megabytes of storage, cost over a million dollar in today's currency, and weighted over a ton. Today's largest capacity disk drives hold 4 terabytes of data in a small 3.5 inch form factor and at a price similar to that of small household appliances such as a coffee maker, a hair dryer, or a toaster.

Unlike other components of modern computers, the disk drive has moving parts, with a read/write head flying over a rotating disk. The thickness of the air gap between the flying head and the disk is now of the order of a nanometer or so, for velocities greater than 10 m/s, thus making the head-disk interface (HDI) one of the most advanced tribological systems available to the consumer in today's marketplace. As a result, great advances have been made over the last few decades in the field of nanotribology (the tribology of nanoscale systems), both in a fundamental, and an applied point of view.

This special issue contains 10 papers of great interest to the field, touching on an array of relevant topics, and research papers as well as review papers. A useful backdrop

to this issue is a review of the HDI roadmap to an areal density of 4 terabit-per-square inch, discussed by researchers from the two largest HDD companies. Three papers attempt to describe and model the frictional behavior of head-disk contacts when they occur. H. Tani et al. present experimental friction data from a pin rubbing against a disk and discuss how it is affected by the roughness of the contact as well as the chemical nature of the lubricant end-group functionalities. S. Itoh et al. use a "fiber wobbling" method to understand the viscoelastic properties of the lubricant film under confinement. They provide evidence of a transition from a viscous to a viscoelastic behavior when the film becomes molecularly thin. Finally, P. Jones et al. present some molecular dynamics simulations of two hydrogen-terminated diamond surfaces in sliding contact and demonstrate a JKR/DMT-like behavior at the molecular scale.

As far as the dynamics of the flying head is concerned, S. Canchi et al. discuss the behavior of the thermally actuated head when it contacts the disk, a topic of great importance as such a scheme is used in all disk drives today in order to calibrate the head-to-disk clearance. K. S. Myo et al., on the other hand, elaborate on how the use of Heat-Assisted Magnetic Recording (HAMR) will affect the head air-bearing characteristics.

On the topic of disk lubricant, R. Waltman and H. Deng offer new evidence that using a low molecular weight disk lubricant enhances head-disk clearance, owing to energetic considerations, but perhaps at the expense of small evaporation losses. Furthermore, M. S. Jhon et al. present a review of

multiscale molecular dynamics, allowing the modeling and prediction of the lubricant behavior and spanning orders of magnitude in time and length from nano- to meso- and to macroscales. Finally, the issue of HDD reliability is also addressed with a paper by J. He that describes a novel instrumentation for nanoscale disk defect detection and characterization, as well as a paper by K. Sonoda discussing how organic contamination affects the dynamics of the flying head.

We would like to thank the authors of all these papers for publishing such a valuable set of papers that provide an important scientific backdrop to the state of the head-disk interface technology in today's disk drives. We hope that this issue will stimulate further fundamental insight in this topic, to enable the HDD industry to keep delivering high-performance storage solutions to our digital world.

*Bruno Marchon  
Norio Tagawa  
Bo Liu  
Tom Karis  
Jia-Yang Juang*

## Review Article

# A Description of Multiscale Modeling for the Head-Disk Interface Focusing on Bottom-Level Lubricant and Carbon Overcoat Models

Myung S. Jhon,<sup>1,2</sup> Pil Seung Chung,<sup>1</sup> Robert L. Smith,<sup>1</sup> and Lorenz T. Biegler<sup>1</sup>

<sup>1</sup> Department of Chemical Engineering and Data Storage Systems Center, Carnegie Mellon University, Pittsburgh, PA 15213, USA

<sup>2</sup> School of Advanced Materials Science and Engineering, Sungkyunkwan University, Suwon 440-330, Republic of Korea

Correspondence should be addressed to Myung S. Jhon; [mj3a@andrew.cmu.edu](mailto:mj3a@andrew.cmu.edu)

Received 1 October 2012; Accepted 19 December 2012

Academic Editor: Bruno Marchon

Copyright © 2013 Myung S. Jhon et al. This is an open access article distributed under the Creative Commons Attribution License, which permits unrestricted use, distribution, and reproduction in any medium, provided the original work is properly cited.

The challenges in designing future head disk interface (HDI) demand efficient theoretical modeling tools with flexibility in investigating various combinations of perfluoropolyether (PFPE) and carbon overcoat (COC) materials. For broad range of time and length scales, we developed multiscale/multiphysical modeling approach, which can bring paradigm-shifting improvements in advanced HDI design. In this paper, we introduce our multiscale modeling methodology with an effective strategic framework for the HDI system. Our multiscale methodology in this paper adopts a bottom to top approach beginning with the high-resolution modeling, which describes the intramolecular/intermolecular PFPE-COC degrees of freedom governing the functional oligomeric molecular conformations on the carbon surfaces. By introducing methodology for integrating atomistic/molecular/mesoscale levels via coarse-graining procedures, we investigated static and dynamic properties of PFPE-COC combinations with various molecular architectures. By bridging the atomistic and molecular scales, we are able to systematically incorporate first-principle physics into molecular models, thereby demonstrating a pathway for designing materials based on molecular architecture. We also discussed future materials (e.g., graphene for COC, star-like PFPEs) and systems (e.g., heat-assisted magnetic recording (HAMR)) with higher scale modeling methodology, which enables the incorporation of molecular/mesoscale information into the continuum scale models.

## 1. Introduction

The continuous increase in the areal recording density specification beyond 1 Tb/in<sup>2</sup> has led to ever decreasing head media spacing (HMS) requirements at the head disk interface (HDI). The key material components of the HDI are the carbon overcoat (COC) and lubricant layers, which protect the magnetic media from corrosion and tribological damage. Perfluoropolymers (PFPE) with both functional and nonfunctional groups are standard HDI lubricants due to their low vapor pressure and low surface tension as well as good chemical and thermal stability. To make a more reliable product, improved lubricant and COC materials must have self-healing capability and lubricant-COC adhesion in addition to molecularly thin spreading layer thickness.

The challenges involved in designing improved HDI materials require efficient theoretical modeling tools which

allow flexibility in investigating various pairs of PFPE-COC materials. Due to the broad range of time and length scales of interest in the HDI components, a multiscale/multi-physical modeling approach can be utilized to produce paradigm-shifting improvements in advanced HDI design [1–13]. We believe that the multiscale modeling methodology as described in this paper is an effective strategy for this system, although it is far from being complete. The essence of multiscale modeling involves integrating low- and high-resolution models of a system so that information is passed seamlessly between adjacent scales. This can be accomplished via either a top to bottom, bottom to top, or middle-out approach supplemented by optimization as illustrated in Figure 1. In the top to bottom approach, low-resolution descriptions are established, and inputs from lower-scale descriptions are incorporated to pass information to the upper-scale model. An advantage of this approach is

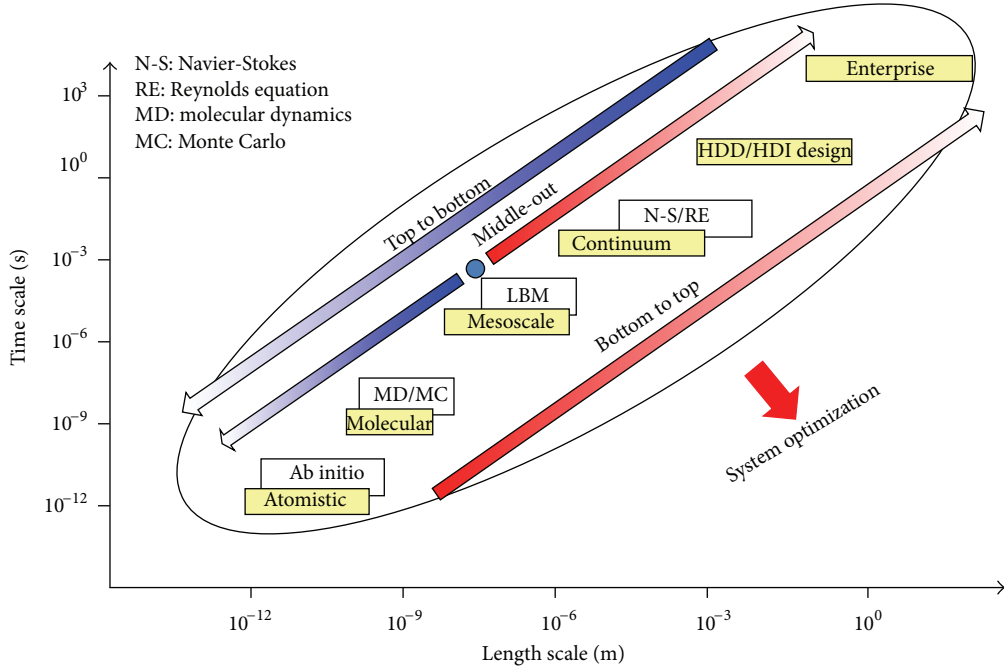


FIGURE 1: An illustration of the several multiscale modeling methodologies.

that it is often more practical to construct a model closer to the device/macroscale scale first so that the device performance determines the lower scale information that is needed. However, it may be more difficult to make fundamentally significant changes in material design in the top to bottom procedure with the present modeling paradigm. In the inverse approach (bottom to top), the detailed, high-resolution descriptions are constructed first, and via coarse-graining procedures, the outputs from the model are inputs for the development of lower resolution descriptions. This multiscale integration style is particularly useful in impacting device performance via nanoscale materials science and engineering, since the molecular architecture is at the root of material properties. A unique middle-out approach employs an intermediate scale model and outputs information to models at adjacent scales above and below the primary model allowing for a flexible integration strategy.

For the HDI system, constructing a multiscale description involves establishing an integrated model for both lubricant and overcoat materials. In this paper, we adopt a bottom to top approach to outline our methodology, although top to bottom or middle-out approaches with optimization are also suitable for HDI design. Due to the polymeric structure of the PFPE system, we begin at the high-resolution, fully atomistic scale with the construction of models which describe the intramolecular PFPE degrees of freedom governing the chain conformations. We transition to intermolecular interactions between PFPEs as well as between PFPE-COC combinations to predict lubricant self-healing (mobility) and adhesive behavior. We then discuss methods for integrating the atomistic models with molecular/mesoscale models via coarse-graining procedures. The coarse-grained descriptions allow us to approach the time and length scales most relevant

for HDI operation. By bridging the two scales, we are able to systematically incorporate first-principle physics into molecular models, thereby demonstrating a pathway for designing materials based on molecular architecture. This approach allows us to describe the conformations, dynamics, morphology, rheology, and thermal performance of HDI materials.

We begin the paper with an overview of intramolecular and intermolecular studies of PFPE and COC materials at the fully atomistic scale where ab initio methods have been utilized. The atomistic review is followed by a survey of works investigating the HDI at the molecular/mesoscale via molecular dynamics simulations. This is followed by an overview of novel integration methods and a discussion of the perceived impact of multiscale modeling on the challenges facing advanced HDI design.

## 2. Atomistic Scale Models

The atomistic scale models include the most physically detailed description necessary for linking material performance with molecular architecture. Investigations at the atomistic scale have included the intramolecular and intermolecular PFPE interactions as well as PFPE-COC interactions. The intramolecular study is motivated by the need to describe the conformational behavior of PFPEs. In the study reviewed here, Z-dol and Z-tetraol serve as examples of this method, although similar treatment can be applied to other lubricants. This is followed by a PFPE-PFPE interaction energy study, since the strength of the intermolecular interactions influences the dynamic behavior of the molecules and thereby, the mobility and self-healing capability of the PFPE in the event of head-disk contact or lubricant

pick-up by the head. To determine the PFPE-COC combinations which promote strong adhesion, an interaction energy study for various PFPEs on COCs is given.

**2.1. Intramolecular PFPE Potential Energy.** The intramolecular study [14] provided bond stretching, angle bending, and torsional potential energy parameters for PFPE molecules for use in atomistic MD simulations. In this paper, we start with a detailed ab initio treatment of the functional PFPE (Z-dol and Z-tetraol as benchmark examples) intramolecular force field as the foundation for larger scale models so that the fundamental physics of the microscopic scale is linked with the macroscopic. Here Z-dol and Z-tetraol are chosen for this analysis due to their prevalence in PFPE research; however, this method will be extended to other lubricants with various functionalities and molecular architecture. In order to investigate the oligomers with computationally intensive ab initio methods, model Z-dol ( $\text{HOCH}_2\text{CF}_2\text{OCF}_2\text{CF}_3$ ) and Z-tetraol ( $\text{HOCH}_2\text{HOCHCH}_2\text{OCH}_2\text{CF}_2\text{OCF}_2\text{CF}_3$ ) molecules are utilized which preserve the end-group structure.

The relaxed structures are calculated via geometry optimizations, followed by the intramolecular force field parameters using the method of Seminario [15]. We developed a code which uses LAPACK [16] routines for eigenvalue analysis of the ab initio second-derivative tensor (Hessian) and calculates stretching and bending parameters for harmonic potentials:

$$\begin{aligned} U_r &= \frac{1}{2}K_r(r - r_0)^2, \\ U_\theta &= \frac{1}{2}K_\theta(\theta - \theta_0)^2, \end{aligned} \quad (1)$$

where  $U_r$  and  $U_\theta$  are the stretching and bending potentials, respectively,  $K_r$  is the stretching force constant,  $K_\theta$  is the bending force constant,  $r_0$  is the equilibrium bond length, and  $\theta_0$  is the equilibrium angle. The stretching interactions take place between two bonded atoms, while the bending accounts for the bending of the angle formed by two adjacent bonds. The torsional potential parameters, describing four bonded atoms, were calculated by generating the torsional energy profiles via a series of constrained geometry optimizations. The form of the torsional potential is

$$U_\phi = \sum_{n=0}^{N-1} A_n \cos^n \phi, \quad (2)$$

where  $U_\phi$  is the torsional potential,  $A_n$  are the torsional potential coefficients,  $N$  is the truncation order, and  $\phi$  is the torsional angle. These potential energy forms were selected due to their widespread use in popular MD codes.

Selected equilibrium bond lengths and angles and the corresponding Hessian-derived force constants are displayed in Table 1 for Z-dol. The study reveals the stiffness of short polar bonds such as H–O as well as the higher frequency of bond stretching modes in comparison to angle bending modes. In general, the bond and angle force constants we calculate are lower than those given in a force field such as the General AMBER Force Field [17]. These differences are due

TABLE 1: Selected parameters for the intramolecular Zdol atomistic model.

Bonds	$K_r$ (kJ/mol Å <sup>2</sup> )	$r_0$ (Å)	Angles	$K_\theta$ (kJ/mol rad <sup>2</sup> )	$\theta_0$ (rad)
O–H	4850.4	0.9677	H–O–C	619.6	1.857
C–O	2656.1	1.404	O–C–H	720.5	1.883
C–H	3081.5	1.101	O–C–C	886.8	1.939
C–F	2689.2	1.354	H–C–H	454.7	1.895
C–C	2289.8	1.527	C–O–C	1329.3	2.077

TABLE 2: The torsional parameters calculated from the ab initio energy profiles for the five-term ( $N = 5$ ) truncation of the potential energy function of (2). The coefficients  $A_n$  have units of kJ/mol.

Atoms	$A_0$	$A_1$	$A_2$	$A_3$	$A_4$
F–C–C–F	9.986	-29.852	0.996	39.724	-0.791
F–C–C–H	10.798	-32.389	0.000	43.187	0.000
H–O–C–C	6.971	-20.913	0.000	27.884	0.000
H–C–C–O	9.303	-24.761	-5.309	33.390	4.338

to the different methods used in the calculation. As shown in Table 2, torsional parameters for Z-dol were calculated for four torsional angles that would describe twisting along the chain: F–C–C–F, F–C–C–H, H–O–C–C, and H–C–C–O. The potential was parameterized to predict the energy barrier as well as the behavior of the profile near equilibrium. The F–C–C–F and F–C–C–H angles had the highest energetic barrier to rotation at ~20 kJ/mol indicating less twisting relative to the H–O–C–C and H–C–C–O (~15 and ~17 kJ/mol, resp.). Similar energy torsional behavior can be expected for Z-tetraol.

The type of intramolecular analysis described here is necessary for accurately simulating an atomistic system with the numerous degrees of freedom of PFPEs. It provides the basis for atomistic molecular dynamics useful in validating higher scale models as will be described in a later section on integration.

**2.2. Intermolecular PFPE Interactions.** Although the functional PFPE end-groups are designed to have strong COC surface adhesion during disk rotation, the dynamic property of lubricant replenishment, or self-healing, capability must be addressed to ensure consistent surface coverage during intermittent head-disk contact and lubricant pick-up by the head. Superior lubricant replenishment requires rapid molecular mobility which is influenced by the strength of intermolecular interactions. In essence, lubricants with the strongest molecular interaction may have more sluggish self-healing performance. In determining the best lubricant to meet HDI performance criteria, we introduce the concept of PFPE nanobLENds to obtain optimal material performance. This allows flexibility in designing lubricants which can adhere to the COC while simultaneously having superior self-healing properties. Thus, we evaluated interactions between lubricants of the same type (pure) and between lubricants of different forms (blend). The blended PFPEs with different

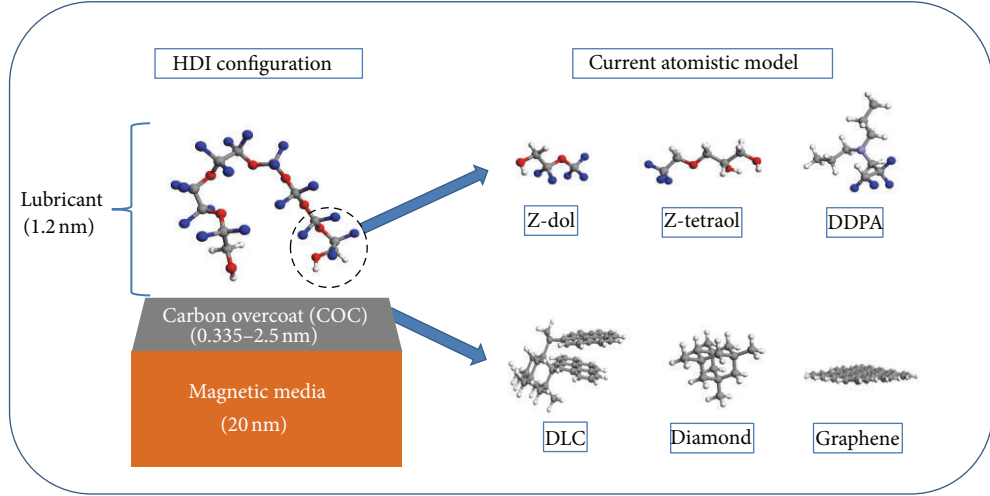


FIGURE 2: Model PFPE and COC materials for atomistic scale study.

forms could be a novel concept in designing the optimal lubricant. Our work on atomistic intermolecular interactions can be found in [18]. Several previous studies used molecular and mesoscale simulation techniques to model lubricant films at the HDI [19–23]. However, in this work we evaluated the intermolecular interaction as a function of end-group structure using ab initio theory to make inferences regarding the lubricant replenishment performance. End groups were truncated into model structures, as in the previous section, retaining the characteristic functionality. The summary of model structures used for the analysis is shown in Figure 2. Here, Z-dol, Z-tetraol, and dipropylamine (DDPA) are used as benchmark PFPE structures for the calculations allowing us to compare hydroxylated and nonhydroxylated functional forms. Dimers composed of two PFPE structures are relaxed, and a frequency analysis is performed to classify the stationary point as a minimum on the potential energy surface. The uncorrected interaction energy represented by the potential energy of the configuration is calculated as

$$U_{\text{int}} = U_{(A-B)} - U_A - U_B, \quad (3)$$

where  $U_{\text{int}}$  is the energy of the dimer and  $U_A$  and  $U_B$  are the energies of isolated monomers  $A$  and  $B$ , respectively. In simulating each case, a fixed position of the lubricant is used as a starting point, and a geometry relaxation was performed to obtain the energy at the equilibrium structure along with a frequency analysis to ensure that the result is neither a saddle point nor a transition state but rather a minimum on the potential energy surface.

The finite basis sets used in the calculations cause each monomer to share basis functions with other monomers in the dimer calculation, which is known as basis set superposition error (BSSE). As a consequence, the interaction energy is overestimated by (3). Thus, to reduce the BSSE associated

with our computational techniques, a counterpoise correction (CP) [24] is utilized for (3):

$$\begin{aligned} U_{\text{int}}^{\text{CP}} &= U_{\text{int}} + \text{BSSE}, \\ \text{BSSE} &= U_{(A-0)} - U_{(A-X)} + U_{(B-0)} - U_{(B-X)}, \end{aligned} \quad (4)$$

where  $U_{(A-0)}$  is the energy of monomer  $A$  at the dimer geometry and  $U_{(A-X)}$  is the energy of monomer  $A$  at the dimer geometry with the added basis functions of monomer  $B$ , with an analogous treatment for monomer  $B$ .

Figures 3 and 4 give the relaxed configurations for the PFPE dimers. The shortest intermolecular bond among the hydroxylated end groups is between the hydrogen and oxygen of the OH groups. This indicates that interaction between the monomers is influenced by hydrogen bonding where the positively charged hydrogen is attracted to the electronegative oxygen. For DDPA, the shortest intermolecular bond occurs between the propyl group's hydrogen and the fluorinated group pointing toward an attraction between hydrogen and the electronegative fluorine.

Table 3 shows the counterpoise corrected energies of interaction for the dimers. For the pure complexes corresponding to Figure 3, the Z-dol and Z-tetraol have the strongest interactions of  $-34.4 \text{ kJ/mol}$  and  $-59.0 \text{ kJ/mol}$ , respectively, where the negative value denotes a stable interaction. A much weaker interaction is observed for the DDPA dimer with a value of  $3.97 \text{ kJ/mol}$ . The shortest intermolecular bonds are among the hydroxylated end-groups for Z-dol and Z-tetraol occurring between the hydrogen and oxygen of the OH groups. For DDPA, the shortest intermolecular bond occurs between the hydrogens of the propyl groups. Compared to DDPA, the hydrogen bonding among the hydroxylated end groups gives them a greater capacity to form strongly bound dimer complexes. This indicates that the hydroxylated PFPEs would have sluggish mobility compared to the DDPA forms due to the strong intermolecular interactions. However, condensed phase molecular simulation must be performed to establish a more concrete linkage

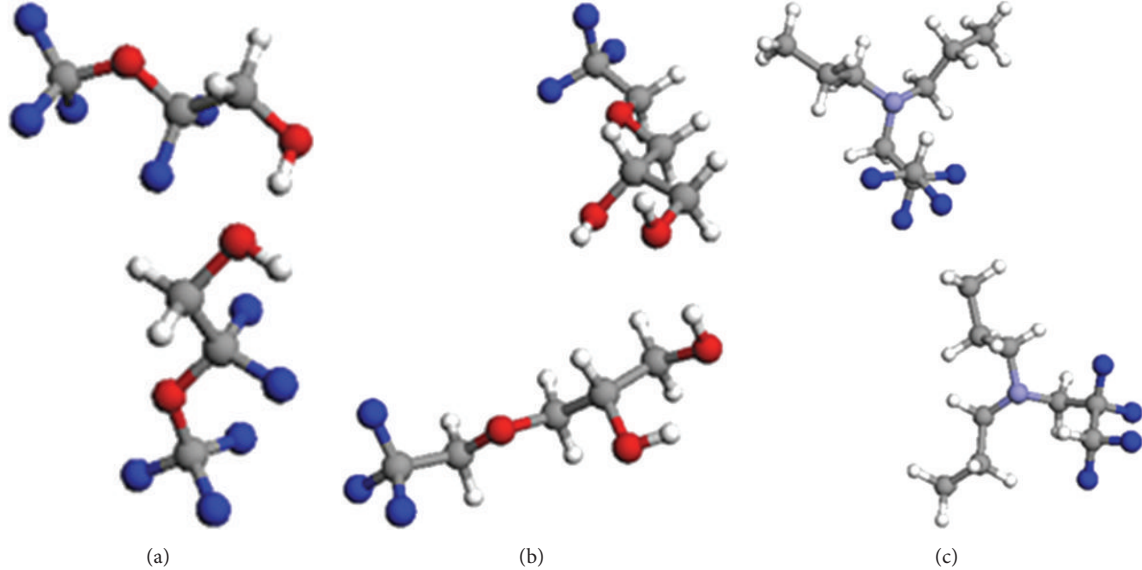


FIGURE 3: Pure relaxed lubricant dimers for (a) Z-dol, (b) Z-tetraol, and (c) DDPA. Red: oxygen, purple: nitrogen, blue: fluorine, grey: carbon, and white: hydrogen.

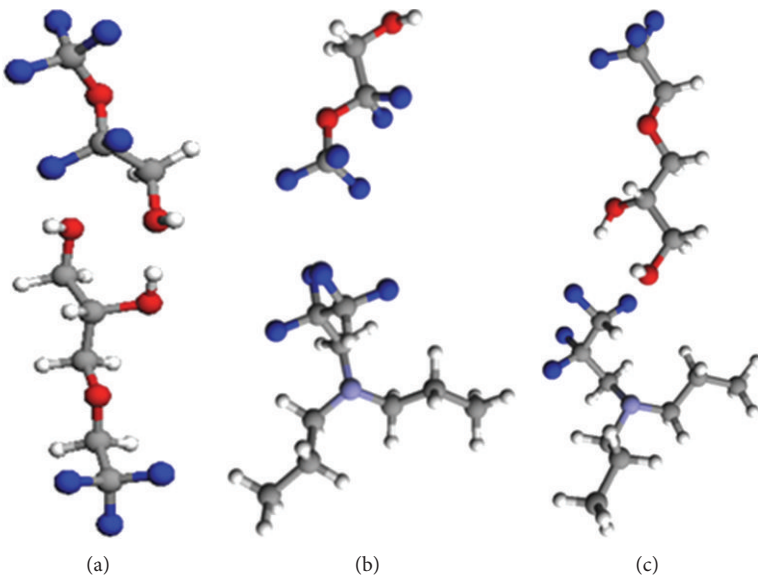


FIGURE 4: Blended relaxed lubricant dimers for (a) Z-dol-Z-tetraol, (b) Z-dol-DDPA, and (c) Z-tetraol-DDPA. Red: oxygen, purple: nitrogen, blue: fluorine, grey: carbon, and white: hydrogen.

TABLE 3: The interaction energies for pure and blended PFPE end groups. All units are in kJ/mol.

Pure	$U_{\text{int}}$	Blended	$U_{\text{int}}$
Z-dol	-34.4	Z-dol-Ztetraol	-35.6
Z-tetraol	-59.0	Z-dol-DDPA	5.23
DDPA	3.97	Z-tetraol-DDPA	-6.53

between the strength of end-group interaction and molecular diffusion, particularly in the presence of finite temperature.

For the blended structures in Figure 4, the closest intermolecular bond for the Z-dol-Z-tetraol dimer is between

the hydrogen and oxygen of the hydroxyl group similar to the pure Z-dol and Z-tetraol cases. This similarity in orientation between the pure and blended cases indicates that the mechanism of interaction is still driven by hydrogen bonding when the hydroxylated lubricants are blended. The Z-dol-DDPA complex in Figure 4(b) shows that the closest interaction takes place between fluorines on each monomer. The orientation of the dimer represents the case where the portion of the end group closest to the backbone interacts. Alternatively, as shown in Figure 4(c), the Z-tetraol-DDPA dimer has a close contact between the hydrogen of the first OH group and the DDPA fluorines. This type of orientation is expected to

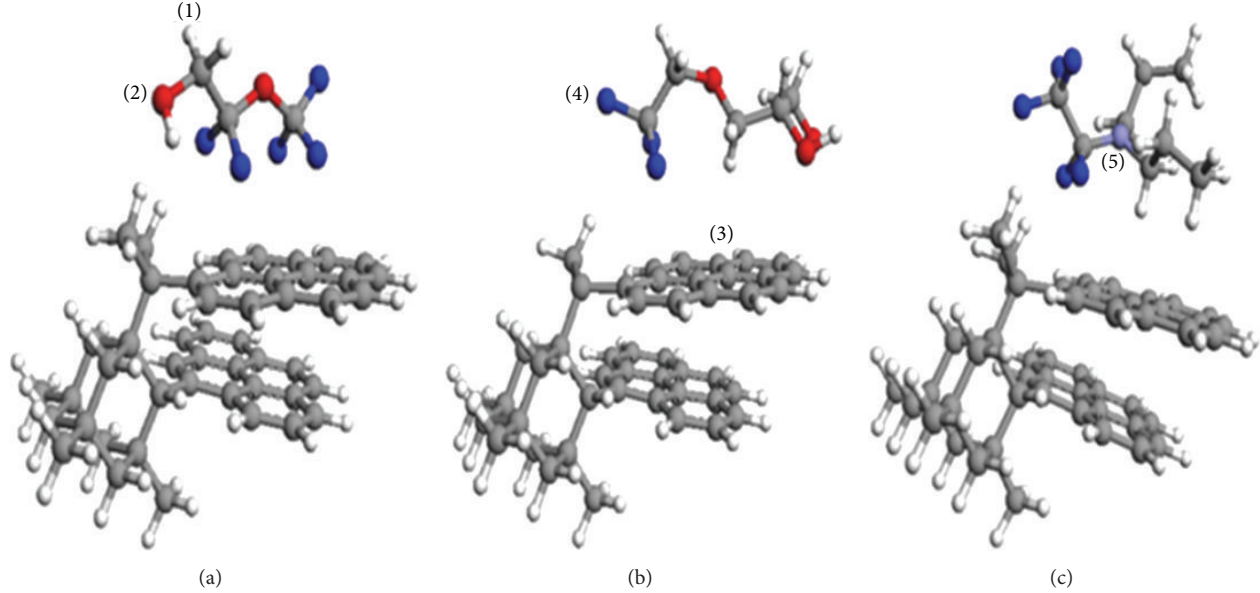


FIGURE 5: The relaxed PFPE-DLC dimers for (a) Z-dol, (b) Z-tetraol, and (c) DDPA. White = hydrogen, red = oxygen, grey = carbon, blue = fluorine, and violet = nitrogen.

produce a more stable interaction than the Z-dol-DDPA orientation.

As given in Table 3, consistent with the configuration of Figure 4(a), the Z-dol-Z-tetraol dimer has the strongest interaction of  $-35.6 \text{ kJ/mol}$ . This is also similar to the strength of the interaction for the Z-dol and Z-tetraol pure dimers providing further support for the point that hydrogen bonding is the key binding mechanism in both the pure and blended cases. Thus, there are no significant changes in the interaction when going from the pure case to the blended case for the hydroxylated end groups. As the orientation in Figure 4(b) indicates, the interaction for the Z-dol and DDPA is unstable with a value of  $5.23 \text{ kJ/mol}$ . In contrast, the dimer of Figure 4(c) has a stable interaction of  $-6.53 \text{ kJ/mol}$  most likely due to the interaction between the fluorines and hydrogens. Thus, we have obtained both weakly repulsive and more strongly attractive dimer configurations for hydroxylated end groups with DDPA. In order to translate the strength of the end group functionality to lubricant self-healing performance, we are developing intermolecular force field parameters for molecular dynamics simulation where temperature effects can be evaluated.

We have examined intermolecular interactions among various model PFPE lubricants which augment our earlier studies of intramolecular interactions. For the pure lubricant complexes, we found superior intermolecular interaction between lubricant end groups with hydrogen bonding capabilities. However, the pure DDPA complex displays longer intermolecular bond lengths as well as a slightly repulsive interaction. The binary lubricant blends demonstrated strong interaction between blended hydroxylated lubricants and diminished strength of interaction when adding DDPA to hydroxylated lubricants. Therefore, we have identified the ability to tune lubricant interaction by introducing blends of various functional end-group types. This result indicates that

TABLE 4: Counterpoise corrected interaction energies for relaxed PFPE-COC dimers. All units are in  $\text{kJ/mol}$ .

PFPE	DLC	COC	Graphene
		Diamond	
Z-dol	$-104.2$	$-38.0$	$-80.2$
Z-tetraol	$-126.4$	$-63.8$	$-86.9$
DDPA	$-76.0$	$-39.9$	$-73.5$

self-healing properties may be tailored by selecting optimal blend ratios which can be investigated using optimization formulations. Our capabilities in determining force constants that govern both intermolecular and intramolecular degrees of freedom allow us to make a linkage between ab initio atomistic descriptions and molecular/mesoscale many-molecule models via coarse-graining procedures.

**2.3. PFPE-COC Interactions.** Although the interaction strength between PFPE functional groups is one component which governs lubricant behavior, the PFPE-COC interactions are also key, since lubricants need strong COC adhesion to prevent spin-off and resist head pick-up. The details of the PFPE-COC interaction analysis can be found in [25]. To simulate PFPE adhesion on conventional COC material, we construct a model DLC structure which includes both  $\text{sp}^3$ - (diamond-like) and  $\text{sp}^2$ - (graphitic) type carbon as in Figure 5. Figure 5 gives the relaxed geometries for Z-dol-, Z-tetraol-, and DDPA-DLC dimers. The configurations indicate a stronger attraction for the  $\text{sp}^2$  bonded carbon compared to the  $\text{sp}^3$  form. The interaction energies are summarized in Table 4. All three PFPEs have large attractive interactions with the DLC where the highest value of  $-126.02 \text{ kJ/mol}$  is observed for the DLC-Z-tetraol dimer. The closest contacts for Z-dol and Z-tetraol are between

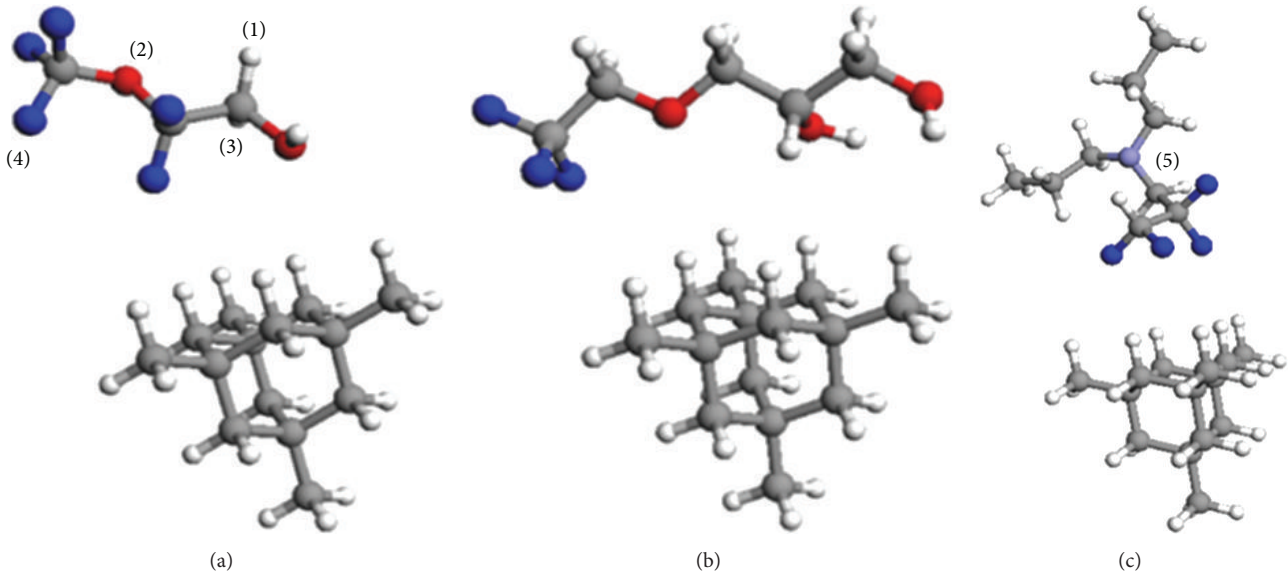


FIGURE 6: The relaxed PFP-diamond dimers for (a) Z-dol, (b) Z-tetraol, and (c) DDPA. White = hydrogen, red = oxygen, grey = carbon, blue = fluorine, and violet = nitrogen.

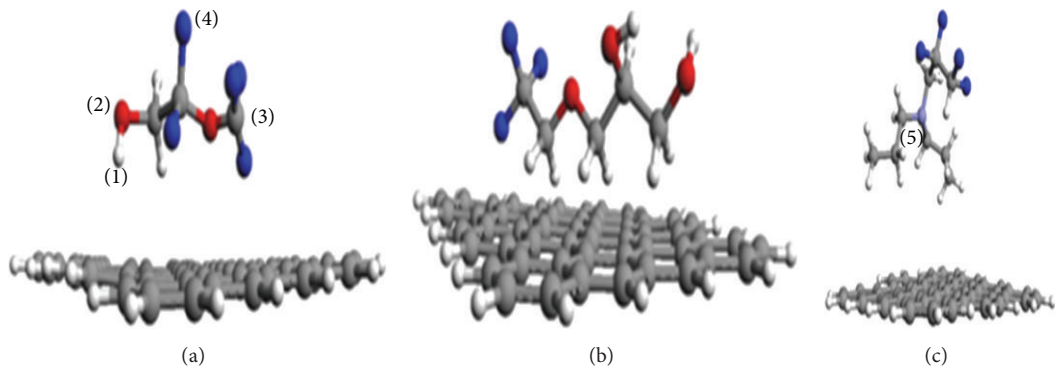


FIGURE 7: The relaxed PFP-graphene dimers for (a) Z-dol, (b) Z-tetraol, and (c) DDPA. White = hydrogen, red = oxygen, grey = carbon, blue = fluorine, and violet = nitrogen.

the PFPE and graphitic carbons, while for DDPA, the fluorines and DLC hydrogens. Based upon the interaction energies, it is predicted that Z-tetraol would adhere more strongly to DLC with potentially less spin-off. In addition to the chemical composition of the DLC, the dimensional characteristics could also contribute to enhanced adhesion since the structure the PFPE encounters is not smooth. One may expect a less smooth structure in the DLC case than in the case of pure graphene or diamond due to the processes used in manufacturing the  $sp^2/sp^3$  hybrid.

Although the PFPE-DLC relaxations indicate that the PFPE is more strongly attracted to the graphitic form of carbon, we systematically examine the effect of carbon structure on PFPE adhesion by independently calculating interactions with diamond and graphitic carbon. To simulate PFPE interaction with pure diamond without periodic boundaries, we choose a simplified structure of  $sp^3$  bonded carbons with hydrogens terminating all dangling bonds. Figure 6 gives the relaxed PFPE geometries with pure diamond. Table 4 shows

that the interactions for all three PFPE-diamond dimers are attractive. As with the PFPE-DLC dimers, Z-tetraol has the highest interaction energy of  $-63.8 \text{ kJ/mol}$  with similar values of  $-38.0 \text{ kJ/mol}$  for Z-dol and  $-39.9 \text{ kJ/mol}$  for DDPA. For the diamond case, the Z-dol and Z-tetraol hydroxyl groups have the closest contact with the diamond hydrogens. For DDPA, the fluorines have the closest contact with the diamond hydrogens. All three PFPEs exhibit weaker interactions with the pure diamond than they did with the DLC structure. This supports the observation in the DLC relaxed structures that the PFPEs were interacting more strongly with the graphitic structures as evidenced by their positions.

We utilize a single graphene flake in order to represent the purely graphitic carbon. Figure 7 shows the relaxed geometries for the PFPEs with a graphene flake, and the interaction energies for the PFPEs with graphene are given in Table 4 where the Z-tetraol has a slightly stronger interaction. For all three cases, the interaction energies are larger than those for the PFPE-diamond cases. This again indicates that

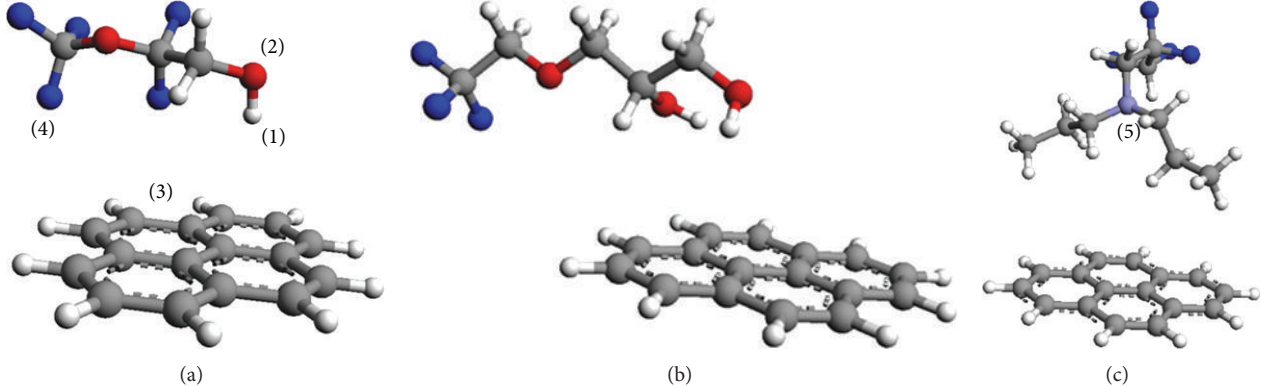


FIGURE 8: (a) Z-dol-graphene equilibrium geometry, (b) Z-tetraol-graphene equilibrium geometry, and (c) DDPA-graphene equilibrium geometry. Red = oxygen, violet = nitrogen, blue = fluorine, grey = carbon, and white = hydrogen.

the PFPE end-group structures are more strongly attracted to the graphitic carbon. The hydroxyl group interacting with the graphene carbons gives the closest contact in the case of Z-dol, and the Z-tetraol hydrogens have the closest contact with graphene. DDPA's propyl hydrogens have the closest graphene contact for the complex. For the graphitic carbon, the high electron density in the  $sp^2$  bonds allows for transfer of charge to the PFPE, which most likely leads stronger bond than what is possible in the PFPE-diamond complex. The closest interatomic contacts are between the PFPE hydrogens and graphene carbons in Figure 7 supporting the existence of charge transfer between the hydrogens and  $sp^2$ -bonded carbons. These results provide evidence that a higher  $sp^2$  carbon fraction in COCs could produce stronger PFPE adhesion. Thus, this analysis demonstrates the power of molecular architecture to provide guidelines for achieving the desired material properties such as adhesion. The exact  $sp^2/sp^3$  ratio which maximizes adhesion could be determined more precisely via optimization procedures.

Since graphene has the potential to be a paradigm-shifting overcoat due to the savings in thickness, we investigated in more detail the PFPE-graphene interaction. In the case of a graphene overcoat (GOC), a few layers may be necessary to adequately protect the media. The effect of the number of graphene layers on its properties is a topic that has been previously investigated in the literature [26, 27]. The interesting phenomenon in these studies is the dimensional crossover from a two-dimensional structure to a three-dimensional one. In our context, the dimensional crossover can be evaluated in terms of the effect of GOC thickness on PFPE interaction. Thus, we evaluated the effect of single-versus double-layer graphene on interactions with our model PFPEs: Z-dol, Z-tetraol, and DDPA. The interaction energies of each PFPE-GOC dimer in these test cases are examined.

Since the atomically thin graphene structure has never been utilized as a disk overcoat adjacent to PFPE lubricant, we studied, for the first time, the interaction between PFPE and a model graphene. The interaction energy results of Table 5 indicate that all of the end groups have stable interactions with the model graphene. However, DDPA's interaction energy with the GOC is still much lower compared to Z-dol and Z-tetraol which is consistent with the intermolecular

TABLE 5: The counterpoise corrected interaction energies for lubricant-GOC clusters for single-layer (denoted as *(s)*) and double-layer (denoted as *(d)*) graphene. All values are in kJ/mol.

PFPE	$U_{int}^{CP}$ ( <i>s</i> )	$U_{int}^{CP}$ ( <i>d</i> )
Z-dol	-7.75	-10.17
Z-tetraol	-6.11	-25.04
DDPA	-1.70	-16.37

separations between the structures in Figure 8. To evaluate the effect of having a two-layer graphene surface on lubricant adhesion, an additional layer was added to the lubricant-GOC dimers as shown in Figure 9. The additional layer was added at the experimental graphene-layer separation of 3.35 Å, and the interaction energy of the lubricant at this geometry was calculated. Table 5 shows that the lubricant adhesion improves with the introduction of the second layer, particularly for the Z-tetraol and DDPA forms. For the single-layer GOC, the Z-dol and Z-tetraol hydroxyl groups have the closest contacts, while the DDPA hydrogens are the closest for the DDPA-single GOC layer dimer. Similar close contacts are observed for the double-layer GOC cases. Thus, in addition to the extra protection to the magnetic media offered by an additional layer of graphene, our calculations indicate that more desirable lubricant adhesion can be achieved as well.

By our atomistic scale investigation, we have demonstrated a qualitative trend in end-group structure's influence on adsorption on graphene. Our feasibility study indicates that graphene could replace existing COC when using conventional lubricants like Z-dol and Z-tetraol due to significant adhesive properties, and they may be superior to alternative lubricant materials like DDPA. However, Z-tetraol and DDPA exhibit the much stronger adhesion with the addition of a second layer. We further introduced the novel concept of a solid-state buffer layer between PFPE and graphene to add extra lubrication and protection of the GOC. Our study will eventually lead to rigorous investigation of the PFPE-PFPE and PFPE-COC interactions that can be tuned to develop atomistic design criteria in lubricant technology. Large size graphene sheets with significant defects including

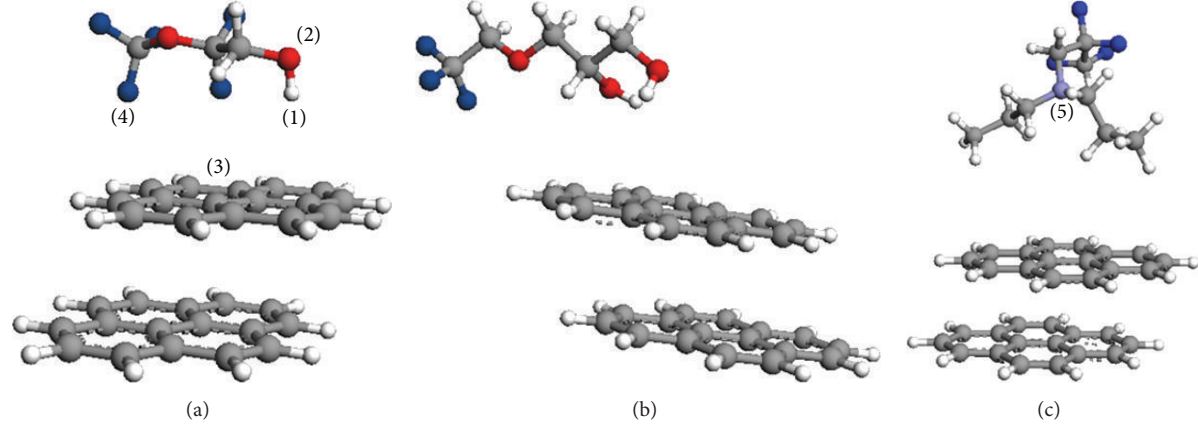


FIGURE 9: Two-layer graphene with (a) Z-dol, (b) Z-tetraol, and (c) DDPA. Red = oxygen, violet = nitrogen, blue = fluorine, grey = carbon, and white = hydrogen.

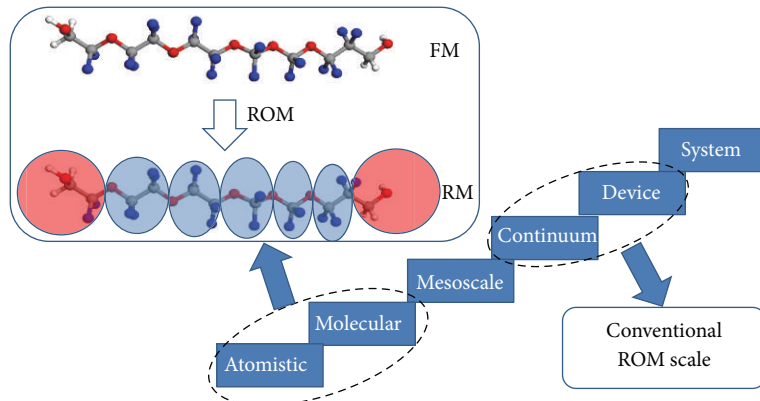


FIGURE 10: The full Z-dol model (above) is mapped onto the reduced Z-dol model (below). Red atoms = oxygen, blue atoms = fluorine, white atoms = hydrogen, and grey atoms = carbon.

grain boundaries and its interaction with PFPEs are currently being investigated.

### 3. Integration of Atomistic and Molecular Scales

Although our atomistic scale study provides valuable information regarding the fundamental role of molecular architecture on material performance, the oligomeric structure of PFPE presents a challenge for efficient molecular/mesoscale computation of the extremely large number of atomic degrees of freedom in molecular simulations. Therefore, a method to reduce the number of degrees of freedom in the atomistic models of oligomeric PFPE is essential from the computational view point. Extensions beyond the atomistic scale are necessary to evaluate the lubricant/COC behavior in a manner more closely linked with realistic HDI materials. The power of the multiscale approach is the ability to base the higher scale descriptions upon the information gleaned from the lowest-scale descriptions.

Historically, reduced order modeling (ROM) [28] has been used to describe continuum/device scale models using

fewer degrees of freedom as shown in Figure 10. In this paper, we describe how the ROM methodology techniques can be applied in bridging atomistic/molecular scale models of PFPE. In ROM, the full model (FM) is solved for various inputs to generate snapshots of the model output spanning a predefined domain. The dimension of the snapshot set is then reduced by projecting onto a fewer basis functions and expanding the output in terms of the reduced basis resulting in a reduced model (RM).

The atomistic FM introduced here is defined via the following intramolecular Hamiltonian,  $h_a$ :

$$h_a = \sum_i 0.5k_i^a(r_i - r_0)^2 + \sum_j 0.5k_j^a(\theta_j - \theta_0)^2 + \sum_{m,l} A_{m,l} P_{m,l}. \quad (5)$$

Here,  $k_i^a$ ,  $k_j^a$ , and  $A_{m,l}$  are the coefficients of the bond, bending, and torsional potentials, respectively. The parameters  $r_i$ ,  $\theta_j$ ,  $r_0$ , and  $\theta_0$  are the instantaneous and equilibrium bond lengths and angles, respectively.  $P_{m,l}$  represents a Legendre polynomial. These parameters for the FM simulation are generated via the method of Hessian eigenvalue analysis

as previously described in Section 2.2. The snapshots are generated via FM molecular dynamics (MD) simulation which yields atom trajectories,  $\mathbf{x} = \{x^1, \dots, x^{na}\}$ ,  $\mathbf{x} \in \mathbf{R}^{t \times na}$  corresponding to the coordinates of an atom, na, over time, t. To reduce the dimension of the model, based on the snapshot data, we incorporate a mapping operator which maps clusters of atoms onto single RM sites. Our RM sites have a physical linkage to the FM. Noid et al. [29] showed that a center of mass mapping operator

$$X = \frac{\sum m_i x^i}{\sum m_i} \quad (6)$$

is sufficient for consistency between an atomistic and coarse-grained (molecular) model in phase space. Here, we map  $\mathbf{x} \in \mathbf{R}^{t \times na}$  onto  $\mathbf{X} \in \mathbf{R}^{t \times nm}$ , with the new dimension nm < na. Thus, with this reduction, we have the trajectories of only nm RM sites over time. From this analysis, for simplicity, we generate a new RM intramolecular stretching Hamiltonian,  $h_m$ :

$$h_m = \sum_i k_i^m (R_i - R_0)^2. \quad (7)$$

In our earlier analysis, MD of coarse oligomer models has been accomplished using a bead-spring model with only bond stretching constraints which can adequately capture chain conformational behavior at this larger molecular scale. The coefficients of  $h_m$  are calculated by fitting the Boltzmann distribution

$$C \exp\left(-\frac{h_m}{k_B T}\right), \quad (8)$$

which describes statistics in the canonical ensemble, into the probability distribution of the  $\mathbf{X}$  data set obtained from mapping  $\mathbf{x}$  onto reduced space. Here,  $k_B$  is the Boltzmann constant,  $T$  is the absolute temperature, and  $C$  is a normalization constant. We apply our ROM methodology to the lubricant PFPE Z-dol, where we reduce 42 atoms to 7 RM sites. Table 6 shows selected bond and angle parameters for the FM intramolecular Hamiltonian. After the ROM procedure, as illustrated in Figure 10, we obtain the 6 RM force constants corresponding to (7) where selected values are given in Table 6. Compared to the stretching parameters of the FM, the RM parameters have significantly smaller values indicating more flexible bonds between the RM sites. Since the angle bending parameters in the FM are consistently less than the stretching parameters, it is justified to describe the RM using the bead-spring approach since RM bending would be a relatively insignificant constraint. In summary, we have applied a traditionally continuum/device level ROM methodology to link atomistic/molecular scale models which can span the entire scale integration, as shown in Figure 10, yielding a full scale HDI design.

In the next section, we move our focus to coarse-grained descriptions of PFPEs established on RM Hamiltonians such as those described in this section. Based upon this lower resolution molecular scale model (bead-spring chains), we investigate the static and dynamic properties of PFPEs via

TABLE 6: Parameters for reduced model intramolecular Hamiltonian.

RM Bond	$k_i^m$ (kJ/mol Å <sup>2</sup> )	$R_0$ (Å)
End-backbone	244.09	2.52
Backbone-backbone	179.20	2.45

both equilibrium and nonequilibrium MD. In this higher scale approach, the functionality is dependent upon bead type instead of the detailed atomistic architecture. In addition, the nanorheology and nanomechanics are explored to determine the effect of lubricant blend composition and chain structure on the molecular/mesoscale behavior that is critical in the HDI application. We also extend our atomistic calculation of various PFPE/COC combination properties, as was done in Section 2.3, to the molecular scale by utilizing the atomistic scale interaction results.

#### 4. Molecular Simulation

*4.1. Coarse-Grained Model.* PFPE molecules were characterized via a coarse-grained MD (CGMD), which simplifies the detailed atomistic structures by categorizing groups of atoms with uniform bead size for backbone and end group based on the dimension of the oligomer. This approach, nevertheless, retains the essence of molecular structure and chain flexibility. To implement the atomistic level theory in MD models, we applied a coarse-graining procedure linking atomistic potentials and molecular/mesoscale simulations combining the parameters obtained from quantum mechanical calculation, as illustrated in Figure 11.

A flat and smooth surface was assumed to model the COC. Coarse-grained bead-spring PFPE is composed of a finite number of beads with different physical or chemical properties. For simplicity, we assume that all the beads, including the end beads, have the same radius. Force field in this model is constructed by Lennard-Jones (LJ1) and van der Waals (LJ2) potentials for dispersive bead-bead and bead-wall interactions, respectively (Figure 12). For polar interactions, exponential potential functions (EXP1 and 2) were added to both bead-bead and bead-wall cases. For the bonding potential between adjacent beads in the chain, a finitely extensible nonlinear elastic (FENE) model was used. For example, PFPE Z-dol can be characterized differently from PFPE Z by assigning the end bead a polarity originating from the hydroxyl group in the chain end.

Neighboring beads are connected via a FENE spring as shown in the following equation:

$$U_{\text{FENE}}(l) = \begin{cases} -\frac{1}{2} k R_0^2 \ln\left[1 - \left(\frac{l - l_0}{R_0}\right)^2\right] & l_0 - R_0 \leq l \leq l_0 + R_0 \\ \infty & \text{otherwise,} \end{cases} \quad (9)$$

where  $l$  is the bond length,  $l_0$  is the equilibrium bond length,  $R_0$  is the maximum extensible range of the spring, and  $k$  is the spring constant which quantifies the rigidity of the bond.

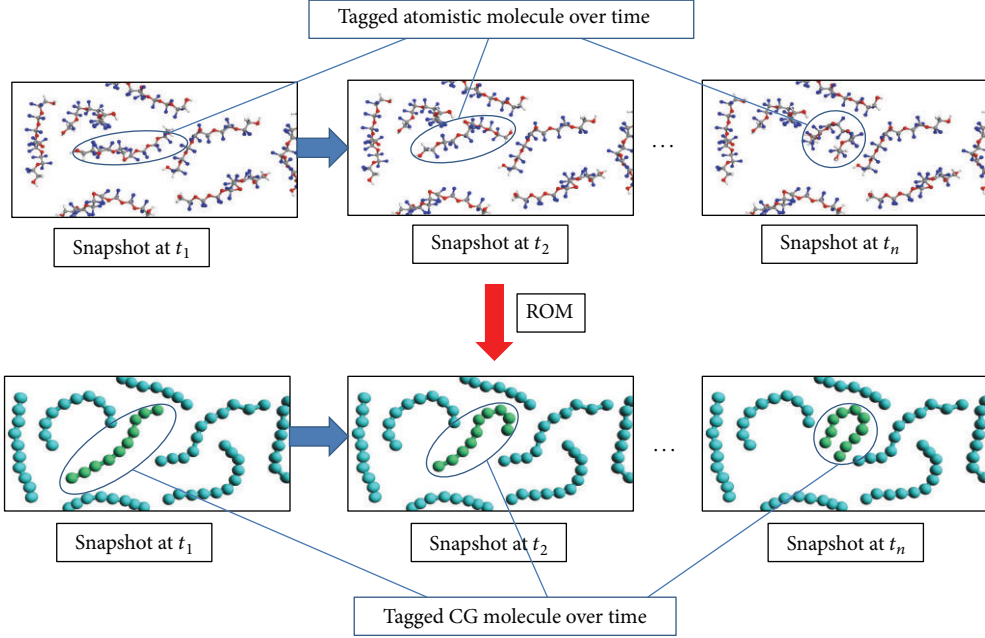


FIGURE 11: Illustration of coarse-graining procedure by using ROM for PFPE molecular systems.

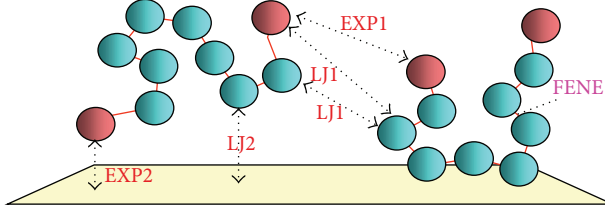


FIGURE 12: Potential energies for the bead-spring model. LJ1: Lennard-Jones potential, LJ2: van der Waals potential, EXP1 and EXP2: short-range polar potential, FENE: finitely extensible nonlinear elastic potential.

All beads, including the end beads in PFPE Z-dol, interact with each other by a pairwise, dispersive, truncated Lennard-Jones (LJ) potential as shown in the following equation:

$$U_{\text{LJ}}(r) = \begin{cases} 4\epsilon \left[ \left(\frac{\sigma}{r}\right)^{12} - \left(\frac{\sigma}{r}\right)^6 \right] & r < 2.5\sigma \\ 0 & r \leq 2.5\sigma, \end{cases} \quad (10)$$

where  $r$  is the distance between beads,  $\epsilon$  represents the well depth of LJ interaction, and  $\sigma$  is the bead diameter.

For the dispersive bead- (db-)wall interaction, we used the attractive potential,  $U_{\text{db-wall}}(z)$ :

$$U_{\text{db-wall}}(z) = \begin{cases} -\frac{\epsilon_w \sigma^3}{(z + \sigma)^3} & z \geq 0 \\ \infty & z \leq 0. \end{cases} \quad (11)$$

Here,  $z$  is the distance from the wall and  $\epsilon_w = 4\epsilon$  is the potential depth.

Previous studies have indicated that the coupling between end groups and their binding to the solid surface is more like a hydrogen bonding interaction [30] from an ab initio

TABLE 7: Endbead-endbead interaction ( $\epsilon^P$ ) between PFPEs, that is, Z-dol, Z-tetraol, and DDPA (kJ/mol).

	PFPE		
	Z-dol	Z-tetraol	DDPA
Z-dol	-34.46	-35.63	5.23
Z-tetraol	—	-59.03	-6.53
DDPA	—	—	-3.98

calculation [31]. While other studies considered the possibilities of hydrogen transfer [32] and esterification as a result of annealing [33]. In the functional PFPE model, the polarity interaction is assumed to happen within a short range and is modeled as an exponential decay function. Equation (12) describes the potential function among end beads:

$$U_{\text{eb-eb}}(r) = -\epsilon^P \exp\left(-\frac{r - r_c}{d}\right), \quad (12)$$

where  $\epsilon^P$  represents the interaction strength between end beads (Table 7),  $r_c$  is the critical distance between a pair of end beads, which is defined by the diameter of an endbead, and  $d$  is the decay length in the exponential function, which must be small to meet the criteria of the short-range interaction.

Further, end beads interact with the solid wall as

$$U_{\text{eb-wall}}(z) = -\epsilon_w^P \exp\left(-\frac{z - z_c}{d}\right), \quad (13)$$

where  $z_c$  is the critical distance of the interaction. Note that the larger the  $\epsilon_w^P$  (Table 4), the stronger the interaction.

By varying molecular structures and inputting ab initio-based  $\epsilon^P$ , atomistically architected PFPEs are modeled in this simulation. Monolayer and multilayer films were investigated within the simulation box dimensions in the  $x$

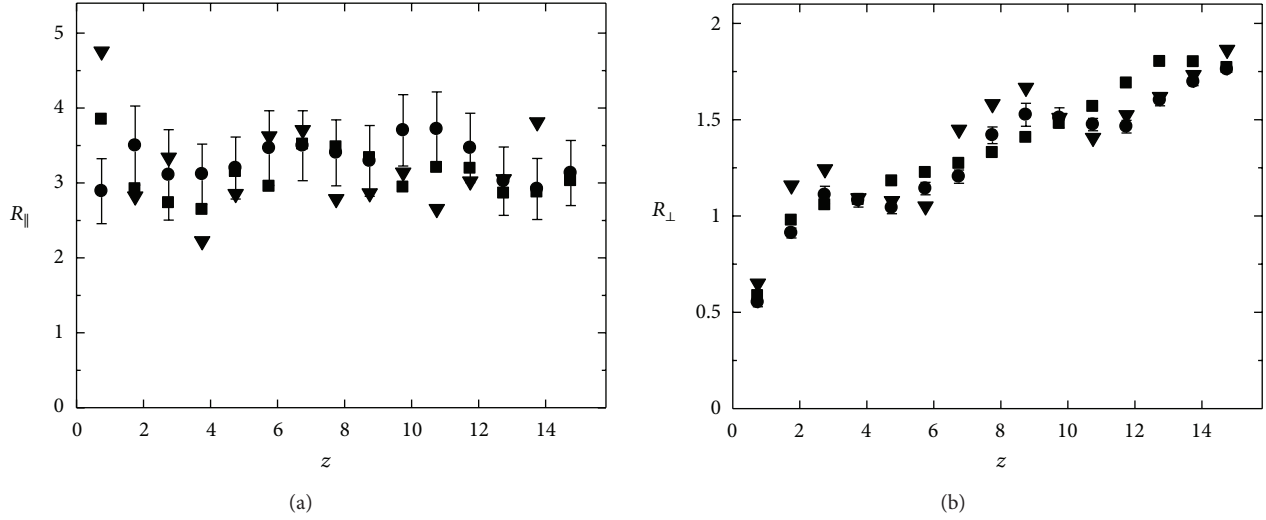


FIGURE 13: Radius of gyration as a function of the distance from the wall,  $z[\sigma]$ , for  $N_p = 10$ : (a) parallel component  $R_{\parallel}[\sigma]$  and (b) perpendicular component  $R_{\perp}[\sigma]$  for (■)  $\epsilon_b^P = \epsilon_w^P = 0$ , (●)  $\epsilon_b^P = \epsilon_w^P = \epsilon$ , and (▼)  $\epsilon_b^P = \epsilon_w^P = 2\epsilon$ . Error bars indicate one-half of the standard deviation and are shown only for  $\epsilon_b^P = \epsilon_w^P = \epsilon$ .

and  $y$  directions of  $40\sigma \times 40\sigma$  with NVT ensemble, where  $\sigma$  is the diameter of the bead. After the system equilibration, the simulations were performed for  $40\,000\tau$  with the time step of  $0.005\tau$ , where  $\tau$  is  $\sigma(m/e)^{0.5}$ , and  $m$  is the mass of the bead. Periodic boundary conditions were applied in the  $x$  and  $y$  directions.

**4.2. Molecular Dynamics.** The equation of motion can be expressed in the following Langevin equation form [34–36]:

$$m \frac{d^2 r_{\alpha i}}{dt^2} = -\frac{\partial U}{\partial r_{\alpha i}} - \zeta \cdot \frac{dr_{\alpha i}}{dt} + f_{\alpha i}(t). \quad (14)$$

Here,  $i$  spans  $1, 2, \dots, N$  and  $\alpha$  spans  $1, 2, \dots, N_p$ , where  $N$  and  $N_p$  imply the number of PFPE molecules and monomers, respectively,  $m$  is the mass of the beads, and  $U$  is the potential energy of the system expressed as some of all potential energy given in (9)–(13).

$\zeta$  is the frictional tensor. We assume it to be isotropic; that is,  $\zeta = \Gamma\mathbf{I}$  ( $\mathbf{I}$  is unit tensor).  $f_{\alpha i}$  is assumed to be Gaussian white noise, which is generated according to the fluctuation-dissipation theorem [35, 37]

$$\langle \mathbf{f}_{\alpha i}(t) \mathbf{f}_{\beta j}(t') \rangle = 2k_B T \Gamma \delta_{\alpha\beta} \delta_{ij} \delta(t - t') \mathbf{I}. \quad (15)$$

Here, the angular brackets denote an ensemble average, which is the same as time average from the ergodic hypothesis.  $\delta_{\alpha\beta}$  and  $\delta_{ij}$  are Kronecker delta and  $\delta(t - t')$  is Dirac's delta function.

**4.3. Static and Dynamic Properties.** We examined the molecular conformations of the confined film via the anisotropic

radius of gyration ( $R_g^2 = R_{\perp}^2 + 2R_{\parallel}^2$ ) in parallel (||) and perpendicular (⊥) components:

$$R_{\parallel}^2 = \frac{1}{2N_p} \sum_{i=1}^{N_p} \left[ (x_i - x_g)^2 + (y_i - y_g)^2 \right], \quad (16)$$

$$R_{\perp}^2 = \frac{1}{N_p} \sum_{i=1}^{N_p} (z_i - z_g)^2,$$

where  $x_g$ ,  $y_g$ , and  $z_g$  are the locations of the chain's center of mass. The anisotropic radius of gyration as a function of distance from the wall  $z$  (Figure 13) demonstrates that the chain conformation becomes more oblate as the wall distance decreases.

The chains in the film extend more in a perpendicular direction than in a parallel direction, resulting in a layered structure. However, the endbead interaction does not significantly affect the conformation of both  $\epsilon_b^P = \epsilon_w^P \equiv \epsilon$  and  $\epsilon_b^P = \epsilon_w^P \equiv 2\epsilon$ , where  $R_{\perp}$  oscillates around that of chains with  $\epsilon_b^P = \epsilon_w^P = 0$ .

The difference  $\Delta R_{\perp} \equiv R_{\perp} - R_{\perp}^0$  plotted in Figure 14 shows that  $\Delta R_{\perp}$  maximizes near  $z = 3$  and  $z = 8$  and minimizes near  $z = 5$  and  $z = 12$  ( $R_{\perp}^0$  represents the mean perpendicular radius of gyration.). This conformational fluctuation is due to the coupling and orientation of the functional end beads.

Figure 15 shows the density profile as a function of the distance from the wall. The polymer chains ( $N_p = 10$ ) with functional end beads ( $\epsilon_b^P = \epsilon_w^P = \epsilon$  and  $\epsilon_b^P = \epsilon_w^P = 2\epsilon$ ) exhibit pronounced peaks, while the nonfunctional end beads ( $\epsilon_b^P = \epsilon_w^P = 0$ ) are monotonic. The end beads are believed to couple near the peak. Because the end beads in the first layer attach to the wall due to the attractive functional interaction, the orientation of end beads is induced in the second layer, and likewise, the orientation propagates to

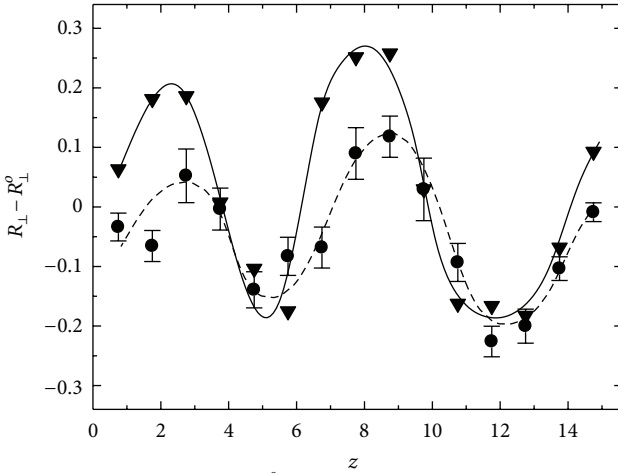


FIGURE 14:  $\Delta R_{\perp} \equiv R_{\perp} - R_{\perp}^0 [\sigma]$  for the chains ( $N_p = 10$ ) with functional end beads for (•)  $\epsilon_b^P = \epsilon_w^P = \epsilon$  and (▼)  $\epsilon_b^P = \epsilon_w^P = 2\epsilon$ . ( $z[\sigma]$  is the distance from the wall.) Error bars indicate one-half of the standard deviation and are shown only for  $\epsilon_b^P = \epsilon_w^P = \epsilon$ .

subsequent layers. In the case of the chains located within the end beads' density peak, the functional end beads also stay within the peak to couple with other end beads resulting in a flatter conformation. The chains located out of the peak unfold themselves so that their end beads can reach other end beads. The characteristic oscillation in the molecular conformation (Figure 14) and the density profile (Figure 15) is induced by functional end beads.

To establish a qualitative relationship between orientation and the layer structure, we examined the number of layers at  $z$ , and the endbead density is plotted in Figure 16 for  $\epsilon_b^P = \epsilon_w^P = 2\epsilon$ . The bead density profile has three peaks: at the wall, between the second and third layers, and between the fourth and fifth layers. The adsorption of functional end beads results in an alternate ordering in the subsequent layers, that is, up in the second layer, down in the third, and so forth. Our result provides a direct interpretation of experimental surface energy data for PFPE films with functional end groups [30]. The nondispersive component of surface energy exhibited an oscillatory pattern with increasing film thickness and was shown to be approximately proportional to end-group density, as demonstrated in our previous study [30, 38]. Our simulation results also suggest that the density variation of the end groups is related to the characteristic behavior of the surface energy of PFPE films.

Furthermore, functional end-group density variation could qualitatively explain the spreading profiles of PFPE films. The surface diffusion coefficient obtained from the experimental spreading profile depends strongly on the layer positions via end-group orientation [39]. That is, the diffusion coefficient between the second and third layers is smaller than that between the first and second layers because of the endbead coupling, which is consistent with the observation made by Ma et al. [40], who also provided a qualitative explanation for the anomalous peaks in thickness-dependent diffusion coefficients.

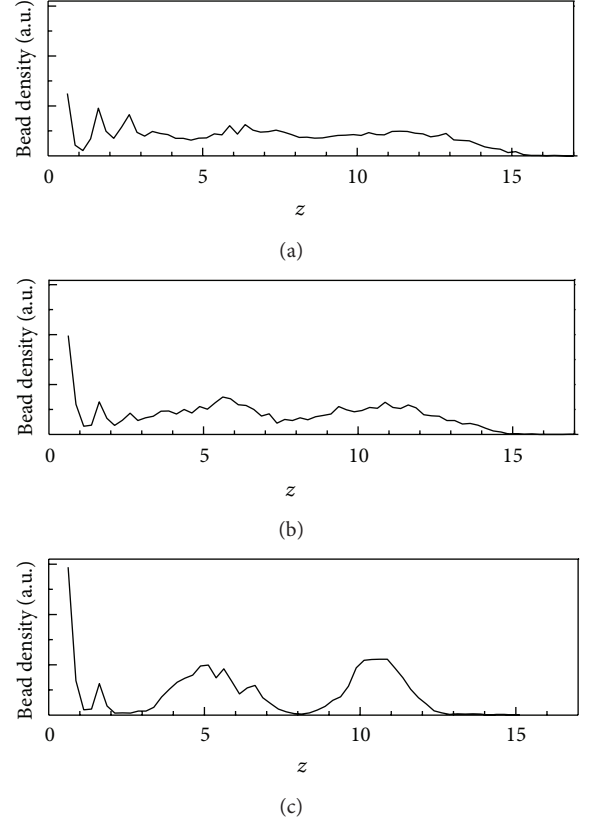


FIGURE 15: Density profiles of the end beads as a function of the distance from the wall,  $z[\sigma]$ : (a)  $\epsilon_b^P = \epsilon_w^P = 0$  and (b)  $\epsilon_b^P = \epsilon_w^P = \epsilon$ , and (c)  $\epsilon_b^P = \epsilon_w^P = 2\epsilon$ .

As temperature increases, the layer expands and the orientation of end beads smears. This is shown in Figure 17. The observed expansion of layer thickness is attributed mainly to the temperature dependence of the intermolecular interaction and excluded volume effect not due to bond stretching. Temperature dependence, which is pertinent to the annealing process of thin polymeric lubricant films, has been carefully examined by Hsia et al. [41].

The steady-state nanoscopic properties were examined, and the result agrees qualitatively with the simulation results obtained via the simple reactive sphere (SRS) model discussed. Our results provide a direct interpretation of experimental surface energy data for PFPE films with functional end groups [30, 38, 42, 43]. Stable films did not experience dewetting or film rupture. However, a rougher surface morphology was observed for smaller molecular weights (Figure 18(b)) and strong endbead functionality (Figure 18(c)). Visualizations of surface morphology could provide powerful tool for describing air bearing stability.

Another noteworthy observation is the segregation, or localization, of chain-ends at the film surface, which was found both in the nonfunctional and functional chain-ends. The endbead density obtained from the MD simulations is normalized with respect to the total number of beads and plotted in Figure 19 as a function of endbead functionality. The segregation of the nonfunctional chain-ends at the

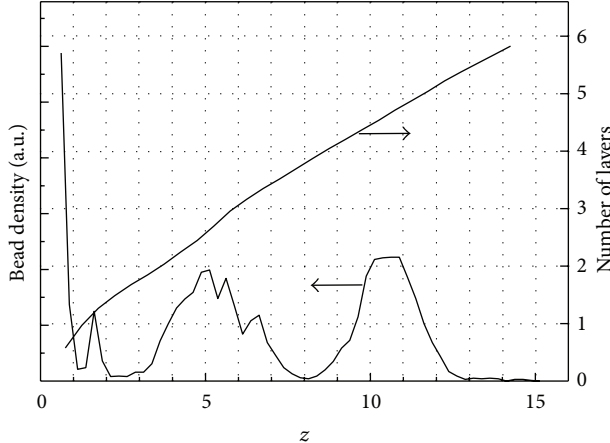


FIGURE 16: Density profiles of end beads and number of layers ( $N_p = 10$ , and  $\varepsilon_b^P = \varepsilon_w^P = 2\varepsilon$ ) as a function of the distance from the wall ( $z[\sigma]$ ).

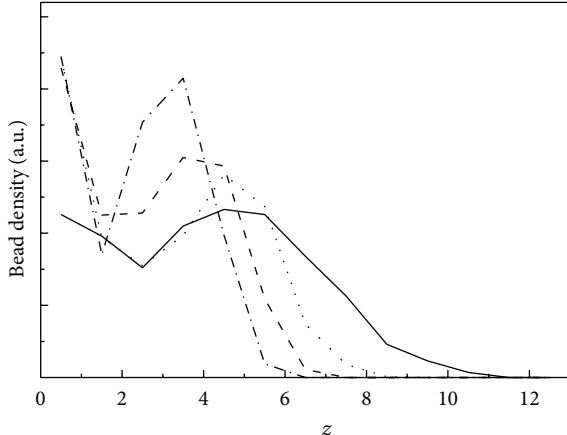


FIGURE 17: Temperature effect on the density profiles of end beads ( $\varepsilon_w^P = 2\varepsilon_b^P = 2\varepsilon$ ) as a function of the distance from the wall ( $z[\sigma]$ ).  $T = 0.5\varepsilon/k_B$  (dot-dashed line),  $T = 0.8\varepsilon/k_B$  (dashed line),  $T = 1.0\varepsilon/k_B$  (dotted line), and  $T = 1.5\varepsilon/k_B$  (solid line).

surface ( $\varepsilon^P = \varepsilon_w^P = 0$ ) assures that the driving force is entirely entropic. The chains can avoid the decrease in entropy by having the nonfunctional ends localized at the film surface where the number of configurations is reduced due to chain folding. The mildly functional end beads ( $\varepsilon^P = \varepsilon_w^P = \varepsilon$ ) still localize at the film surface, which suggests that the entropic contribution is more dominant, and, as a result, the free energy of the system is minimized by having the end beads localized. The strongest functional end beads, on the other hand, are totally depleted from the surface ( $\varepsilon^P = \varepsilon_w^P = 3\varepsilon$ ). The contribution of surface enthalpy to the free energy is too large to be compensated by the entropic component. In this case, therefore, all of the functional end beads minimize the energy of their functional interaction by coupling with other end beads inside the film. In the same manner, the segregation of small molecular weight fraction at interfaces was observed from our binary MD simulations.

For the dynamic property, we will examine the self-diffusion process of a tagged PFPE molecular center of mass from the simulation to achieve insight into the excitation of translational motion, that is, spreading and replenishment. The squared displacement of the center mass of a molecule or a bead is used as a measure of translational movement. The self-diffusion coefficient,  $D$ , can be represented as a velocity autocorrelation function:

$$\begin{aligned} D &= \lim_{t \rightarrow \infty} \frac{1}{6t} \langle |\mathbf{r}(t) - \mathbf{r}(0)|^2 \rangle \\ &= \int_0^\infty \langle \dot{\mathbf{r}}(t) \cdot \dot{\mathbf{r}}(0) \rangle dt = \int_0^\infty \langle \dot{\mathbf{x}}(t) \dot{\mathbf{x}}(0) \rangle dt \\ &\quad + \int_0^\infty \langle \dot{\mathbf{y}}(t) \dot{\mathbf{y}}(0) \rangle dt + \int_0^\infty \langle \dot{\mathbf{z}}(t) \dot{\mathbf{z}}(0) \rangle dt \\ &\equiv D_x + D_y + D_z = 2D_{\parallel} + D_{\perp}, \end{aligned} \quad (17)$$

where  $\dot{\mathbf{r}}(t) \equiv \dot{\mathbf{x}}(t)i + \dot{\mathbf{y}}(t)j + \dot{\mathbf{z}}(t)k$  denotes the velocity vector of the center of mass for a PFPE molecule. Figure 20 illustrates the results for the  $D_{\parallel}$  and  $D_{\perp}$  (the components of the diffusion coefficients in the directions parallel and perpendicular to the solid surface) obtained from our preliminary MD simulations.

We may also study the molecular relaxation process, which has been investigated by the autocorrelation function of normal modes for a linear polymer chain [44]. The relaxation spectrum can be analyzed by the Kohlrausch-Williams-Watts function [45]:

$$C(t) \equiv C(0) \exp \left[ -\left( \frac{t}{\tau^*} \right)^\beta \right]. \quad (18)$$

Here,  $\tau^*$  represents the elementary relaxation time and the stretching parameter  $\beta$  is descriptive for the nonexponential decay process (or distribution of relaxation times), or it physically quantifies the confinement effect; that is, the larger the  $\beta$  is, the stronger the confinement becomes. Figure 21 demonstrates the contribution of the solid surface to the relaxation process for end-functional PFPEs ( $\varepsilon^P = \varepsilon_w^P = 2\varepsilon$ ) by comparing the bulk ( $\varepsilon_w = 0$ ) with nanofilm ( $\varepsilon_w = 4\varepsilon$ ). A longer  $\tau^*$  is observed for the nanofilm than for the PFPE bulk, but the MW dependence, that is,  $\tau^* \propto (N_p)^\theta$ , is weakened. For instance,  $\theta = 2.01 \pm 0.05$  for the bulk as the Rouse model predicts [46], but it decreases to  $1.84 \pm 0.07$  for the nanofilm. In addition,  $\beta$  for the nanofilm increased slightly (about 0.15) with MW as seen from the solid line in Figure 22. Note that the end-group ratio,  $2/N_p$ , decreases for higher MW and that the functional end groups interact strongly with the solid surface. Consequently, the higher the end-group ratio in a PFPE chain is, the stronger the PFPE-solid surface interaction results. Compared with lower-MW PFPEs, the effective interaction with the surface reduces for higher MW PFPEs.

**4.4. Various PFPEs and COCs.** For the future HDI design, which increases the stability while reducing the

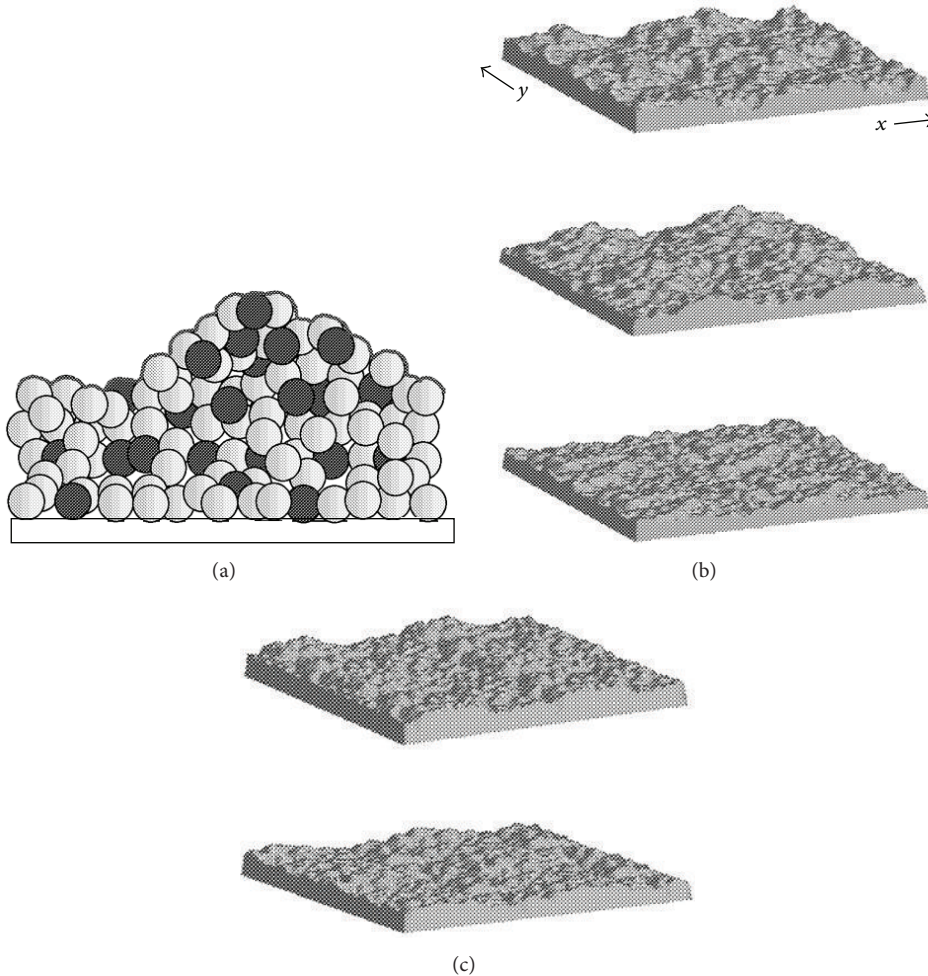


FIGURE 18: Morphology of PFPE films from MD simulations: (a) schematic of simulated surface roughness for (b) molecular weight dependence ( $N_p = 10$  (upper), 15 (middle), and 20 (bottom)) and (c) endbead functionality dependence ( $\epsilon_w^P = \epsilon^P = 1$  (upper) and  $\epsilon_w^P = \epsilon^P = 4$  (bottom)).

configuration scale to obtain the higher sensitivity of the head and magnetic layer interactions, we introduced various COC materials including graphene. Due to the advantages of graphene including the single atomic thickness of graphene and superior mechanical and thermal characteristics, HDI with graphene will provide significant reduction in HMS along with high reliability if we optimize the lubricant structures (Figure 23). Various PFPEs properties on the selected COCs were also investigated and compared. As shown in Figure 24, all PFPEs (Z-dol, Z-tetraol, and DDPA) show a flat conformation ( $R_{\perp}/R_{||} < 1$ ) on three different carbon surfaces. By comparing the end-group functionalities listed in Tables 4 and 7, Figure 25 illustrates that the strength of interactions among end groups and the surface barely affects the perpendicular molecular conformation as long as the total number of beads (i.e., molecular weight) remains constant. Particularly, similar  $R_{\perp}$  values for all cases, which mainly determine the film thickness in a monolayer lubricant system, indicate that intramolecular factors such as chain flexibility, molecular weight, or molecular structural complexity may affect film thickness and conformation more

than intermolecular factors such as end-group functionality or COC material.

Although the molecular conformations were identical, we observed that the end-group clusters on the surface vary for different PFPEs. Figure 26 shows the bottom view of Z-dol, Z-tetraol, and DDPA, where the end groups are located on the surface. Both Z-dol and Z-tetraol (Figures 26(a) and 26(b)) exhibit clusters and network structures, and the end groups of Z-dol form smaller clusters, while DDPA lubricant film, which has the lowest end-group interaction energy (-3.98 kJ/mol) between end groups (Table 7), does not display any clustering. In addition to the PFPEs on the diamond surface in Figure 26, we also found that PFPEs on the other surfaces including novel graphene surface (i.e., DLC and graphene) form similar end-group distributions as those on the diamond surface.

From this result, we observed that the clusters formed in PFPE films depend on the interactions between end groups (Z-tetraol > Z-dol > DDPA) while the interaction between carbon surfaces and the end groups merely affects the size of clusters.

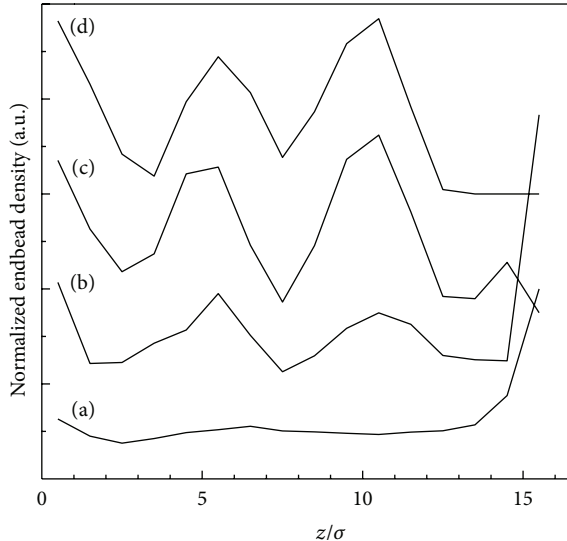


FIGURE 19: Normalized endbead densities as a function of distance from the surface ( $N = 10$ ) for (a)  $\epsilon^P = \epsilon_w^P = 0$ , (b)  $\epsilon^P = \epsilon_w^P = \varepsilon$ , (c)  $\epsilon^P = \epsilon_w^P = 2\varepsilon$ , and (d)  $\epsilon^P = \epsilon_w^P = 3\varepsilon$ .

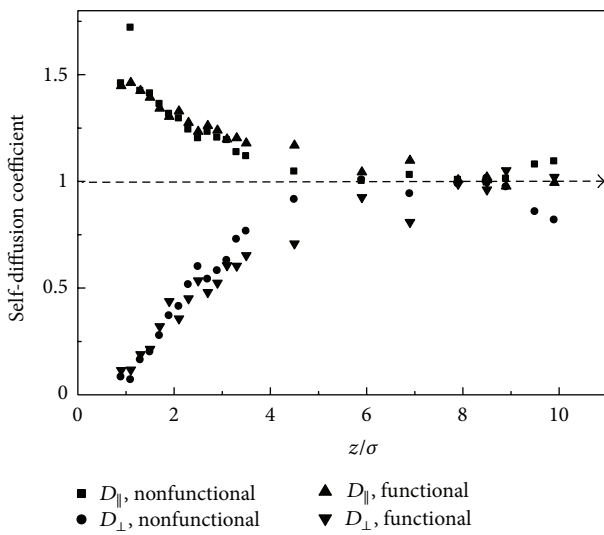


FIGURE 20: Self-diffusion coefficients ( $D[\sigma^2/\tau]$ ) ( $N_p = 6$ ,  $T = 0.5$ ) as a function of distance from the surface for nonfunctional ( $\epsilon_w^P = 0$ ,  $\epsilon_w = 5$ ) and functional chain-ends ( $\epsilon_w^P = \epsilon^P = 2$ ,  $\epsilon_w = 5$ ).

Figures 27 and 28 compare self-diffusion coefficients of each component for Z-dol, Z-tetraol, and DDPA on the diamond, DLC, and graphene. The comparison between  $D_{\parallel}$  and  $D_{\perp}$  values indicates that  $D_{\parallel}$  is the dominant diffusion process since perpendicular diffusion is confined by the monolayer thickness of PFPE films. The  $D_{\parallel}$  of PFPEs is ranked in reverse order compared to the interaction strength between end groups (Z-tetraol < Z-dol < DDPA). Also, the self-diffusion is affected by the carbon surface structure. Z-dol exhibits similar mobility on all carbon surfaces, while Z-tetraol shows minimal mobility which is sensitive to the carbon surface. DDPA, consisting of a different type of end

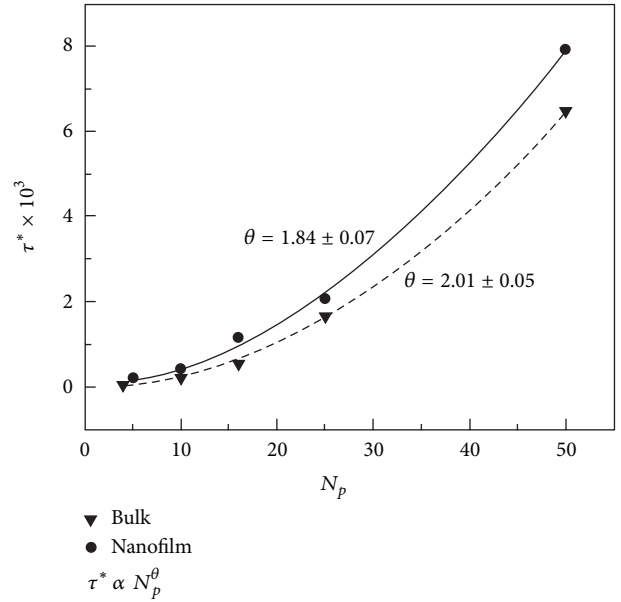


FIGURE 21:  $\tau^* [\tau]$  as a function of  $N_p$  ( $N_p$ : the number of beads per molecule) for the PFPE ( $\epsilon^P = \epsilon_w^P = 2\varepsilon$ ) in the bulk state ( $\epsilon_w = 0$ ) and in the nanofilm ( $\epsilon_w = 4\varepsilon$ ) with  $T = 1.0\varepsilon/k_B$ .

group from Z-dol and Z-tetraol (hydroxyl end groups), shows significantly higher self-diffusion coefficients on the diamond and graphene structure COC. When the molecular conformation of PFPEs is considered, this result indicates that Z-tetraol may not be the best choice for the COC beyond the conventional materials, since a significant disadvantage in the self-healing ability exists. However, we see that the mobility of DDPA, which is similar to Z-dol on the conventional DLC overcoat, significantly increases on the graphene as well as diamond.

Here, we found that the changes in the monolayer film conformation affected by the perpendicular profile of PFPE molecular structures on the surface are insensitive to the kind of end groups or carbon surfaces. However, we observed that the end-group distributions on the surface depend on the end-group-end-group interactions. Also, different chemical types of end groups on PFPEs vary the mobility of PFPEs with respect to the carbon surface characteristics. In addition to the various linear functional PFPEs examined thus far, we investigated different types of PFPEs, which are atomistically/molecularly architected functional lubricant molecules on the existing and novel COC layers (Figure 29). Since the multiscale methodology provides the advantage of scale integration, complicated combinatorial problems of PFPFs and COCs and numerous parameters can be estimated, and the optimal lubricant design criteria for the future HDI will be selected by considering the performance parameters from the bottom scale.

Star-like molecules (TA-30 and QA-40), which prevent lubricant decomposition at high temperature by eliminating the acid labile unit ( $-\text{OCF}_2\text{O}-$ ), were also investigated via coarse-grained model (Figure 30). It has been reported that an additional functional group in ZTMD affects the film

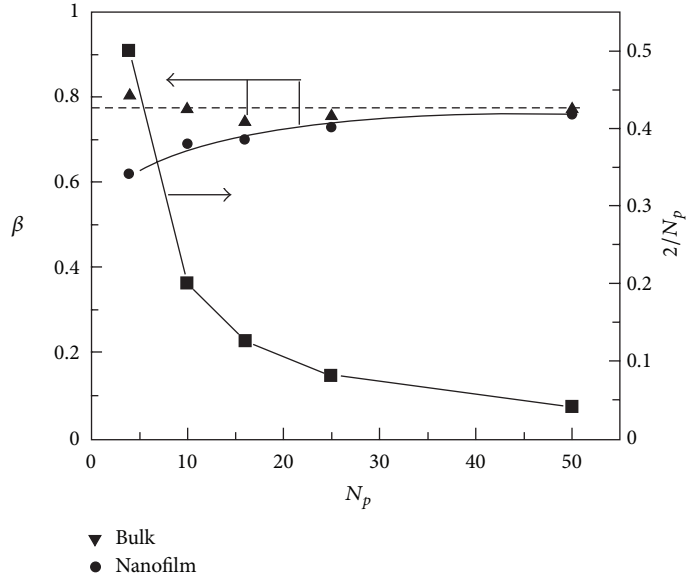


FIGURE 22: The stretching parameter  $\beta$  and end-group ratio  $2/N_p$  as a function of  $N_p$  for the PFPE ( $\varepsilon^P = \varepsilon_w^P = 2\varepsilon$ ) in the bulk state ( $\varepsilon_w = 0$ ) and in the nanofilm ( $\varepsilon_w = 4\varepsilon$ ) with  $T = 1.0\varepsilon/k_B$ .

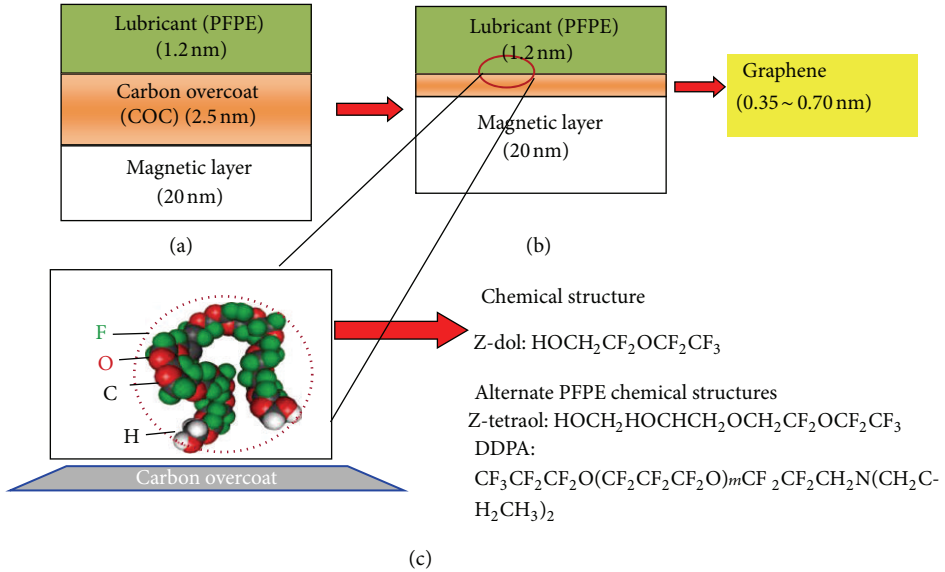


FIGURE 23: HDI configuration and graphene for the COC layer.

conformation by anchoring the backbone [47, 48], which is adsorbed on the surface so that the structure results in a smaller film thickness compared to the linear PFPEs. Tani et al. compared branched PFPEs (e.g., TA-30 and D-4OH) with Z-tetraol by using the atomic force microscopy (AFM) and the molecular dynamics, and they found that TA-30 shows the highest surface coverage and lowest molecular height among the examined PFPEs [49]. Branches with functional end groups in star-like PFPEs also form backbones, anchored on the surface; however, TA-30 and QA-40 may exhibit different film conformations from the ZTMD due to the

flexible branch backbone. To understand this, we specifically examined structural effects of anchoring arms on TA-30 and QA-40 on the film thickness. As shown in Figure 31, star-like PFPEs form similar end-group anchored structures while QA-40 exhibits more severe network structure due to the additional functional arm, which may provide the film stability as well as diminishing mobility (bottom view). Since QA-40 forms larger clusters inside and at the bottom of the film, less functional end groups on the surface of the film represent the reduction of film surface energy, improving the stability in the near-contact HMS system. The

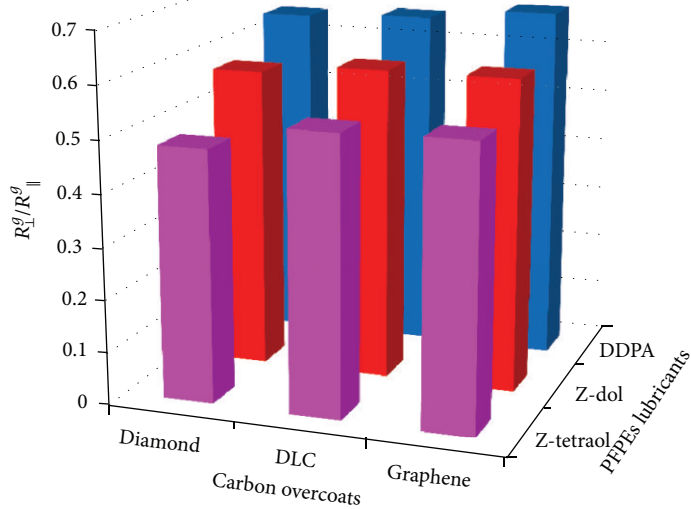


FIGURE 24: The ratio of  $R_{\parallel}$  to  $R_{\perp}$  for each component of the material matrix.

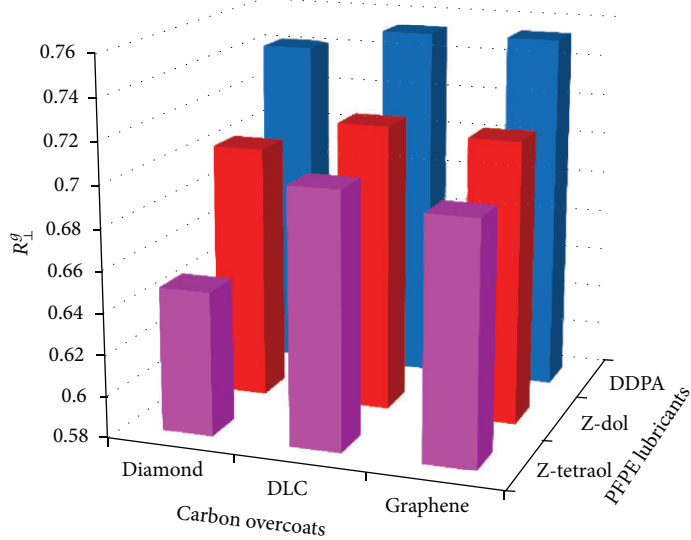


FIGURE 25: The perpendicular component of radii of gyration ( $R_{\perp}^g$ ) for each component of the material matrix.

flexibility of arms and end-group interactions results in less flat molecular conformation as well as thicker film as shown in Figure 32.

**4.5. Nanorheology and Mechanics.** In addition to the inherent PFPE/COC properties, we further explored the nonequilibrium dynamics of HDI operation and PFPE/COC responses. By adopting the coarse-grained model described in previous sections to the nonequilibrium MD, we have examined the nanorheological and nanomechanical responses for the nonfunctional PFPEs as a function of wall separation/film thickness and the molecule-solid surface interaction. We also examined the effect of end-group functionality and further

compared the relaxation time of nanometer thick confined PFPE films with PFPE bulk.

**4.5.1. Nanorheology.** There has been great interest in resolving the rheological and tribological issues of PFPE lubricants during the intermittent contact between the head and the disk. We first examined the confinement effect. Figure 33 plots the shear-rate-dependent viscosity of nonfunctional PFPE ( $\varepsilon_b^P = \varepsilon_w^P = 0$ ) nanofilms with three different wall separation lengths ( $h$ ), where  $\varepsilon_b^P$  and  $\varepsilon_w^P$  are endbead functionalities. As  $h = 10\sigma$ , the shear viscosity is slightly larger than the bulk value. However, as the wall separation gets smaller, for example, 5 $\sigma$  or even 3 $\sigma$ , which contains only 1-2 layers

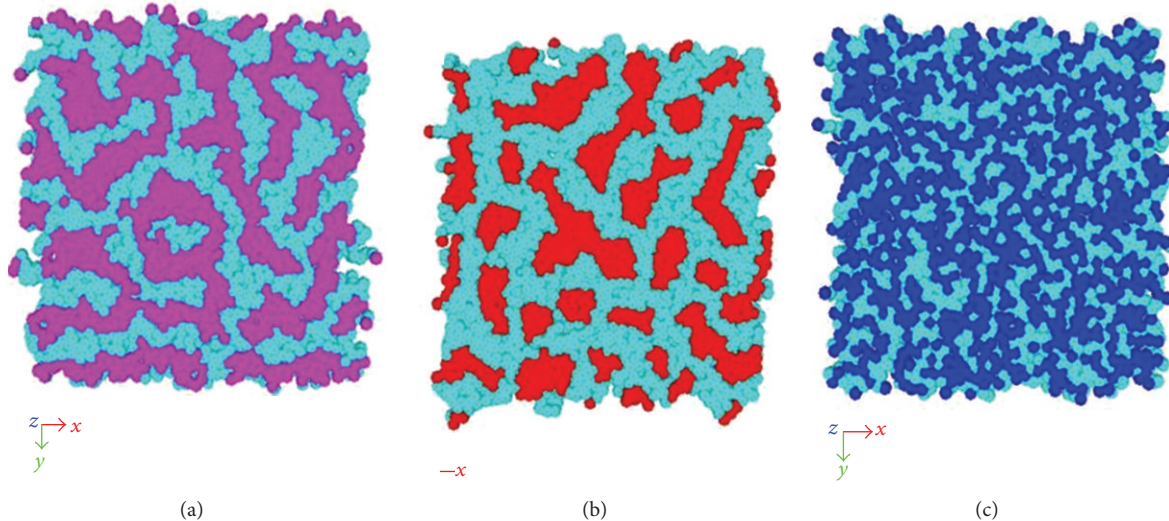


FIGURE 26: Bottom view snapshots of (a) Z-dol (pink: end-group), (b) Z-tetraol (red: end-group), and (c) DDPA (blue: end-group) on diamond overcoat surface (light blue: backbone).

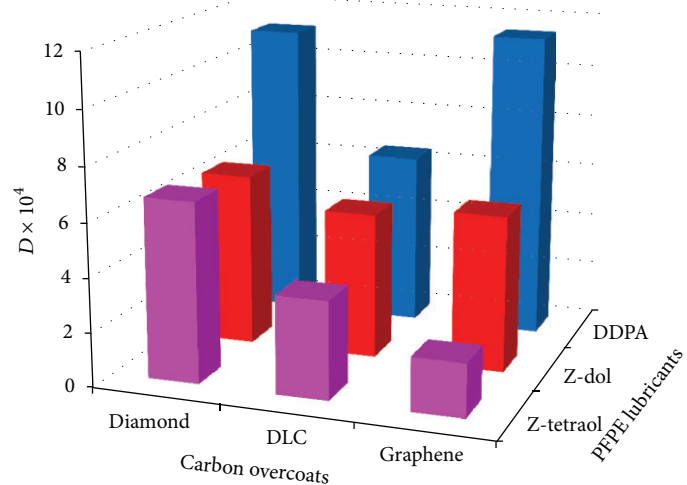


FIGURE 27: Parallel component of self-diffusion coefficients ( $D_{\parallel}[\sigma^2/\tau]$ ) for each component of the material matrix.

of PFPEs, the film shear viscosity increases significantly, indicating a much stronger external confinement to the examined films. Thus, the confinement depends nonlinearly on the wall separation.

We found that the surface confinement plays a vital role in determining the shear viscosity of PFPE nanofilms. Nonfunctional PFPE nanofilms confined between two solid surfaces with a separation of  $3\sigma$  under different surface interaction strengths were simulated. The calculated shear viscosity at the shear rate of  $0.1\tau^{-1}$  as a function of end-group functionalities is shown in Figure 34, where a second degree of polynomial dependence is found. Note that this dependence may vary with the wall separation and shear rate.

Using the conventional rheometer, Kono et al. [50] experimentally examined the rheological properties of PFPE bulk systems for the shear rate range of  $10^{-6} \sim 10^3$  sec $^{-1}$ . The bulk

rheology examines the dynamic response of PFPE system under deformation (e.g., shear or elongation) while the nanorheology for PFPE, for the first time, provides additional information about PFPE relaxation (or shear viscosity) due to the nanoscale confinement as well as interaction between surface and confined molecules. Due to the ease in assigning external conditions, that is, shear/normal stress into the simulations, molecular dynamics (MD) turns out to be an alternative approach to understand the above-mentioned issues. Here, by modifying our previous simulation model [22] and incorporating two confined walls, we studied the rheological responses of PFPE nanofilm as a complementary tool to estimate the nanoscale lubricant tribological performance.

We have examined the viscosity dependence on the end-group functionality. Figure 35 plots the shear-rate-dependent

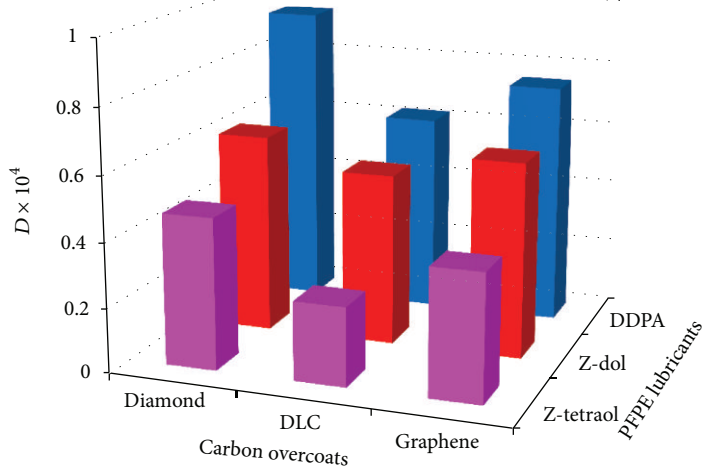


FIGURE 28: Perpendicular component of self-diffusion coefficients ( $D_{\perp} [\sigma^2/\tau]$ ) for each component of the material matrix.

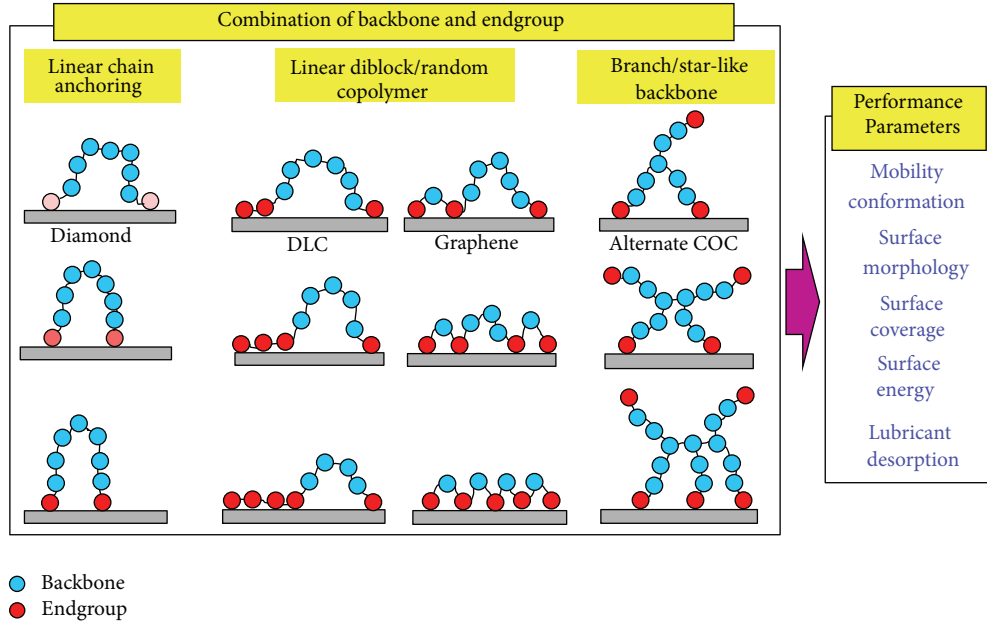


FIGURE 29: Different types of PFPEs with atomistically/molecularly architected functional molecular structures on the various COC layers and output parameters.

viscosity of both nonfunctional ( $\varepsilon_b^P = \varepsilon_w^P = 0$ ) and functional ( $\varepsilon_b^P = \varepsilon_w^P = 3\varepsilon$ ) PFPE films confined between two solid surfaces with a separation of  $5\sigma$ . Here, the “shear thinning” behavior is observed as the shear rate increases. In addition, when compared to the shear viscosity for the bulk PFPE system ( $O(\sim 10^1)$ ) [51], the solid surfaces have significantly confined dynamic behavior of nonfunctional PFPE films (square symbols), which leads to a huge increase ( $O(\sim 10^4)$ ) in the shear viscosity at the low shear rate region. On the other hand, the confined functional PFPE shows less increase in the steady shear viscosity than the bulk state ( $O(\sim 10^3)$ ) [51]. A similar increase ( $O(\sim 10^2)$ ) in the steady shear viscosity for

the functional PFPE films is also observed (circled symbols). Therefore, we found that although functional end-group coupling can slow down the PFPE dynamics, the surface confinement plays a more dominant role in the rheological properties of PFPE nanofilms.

**4.5.2. Nano-Mechanics.** During the HDD operation, the intermittent contact between the slider and lubricant surface inevitably results in lubricant pick-up, where the lubricant molecules could be partially transferred to the air bearing surface due to the horizontal air shear stress as well as the vertical head-disk interaction and eventually affect

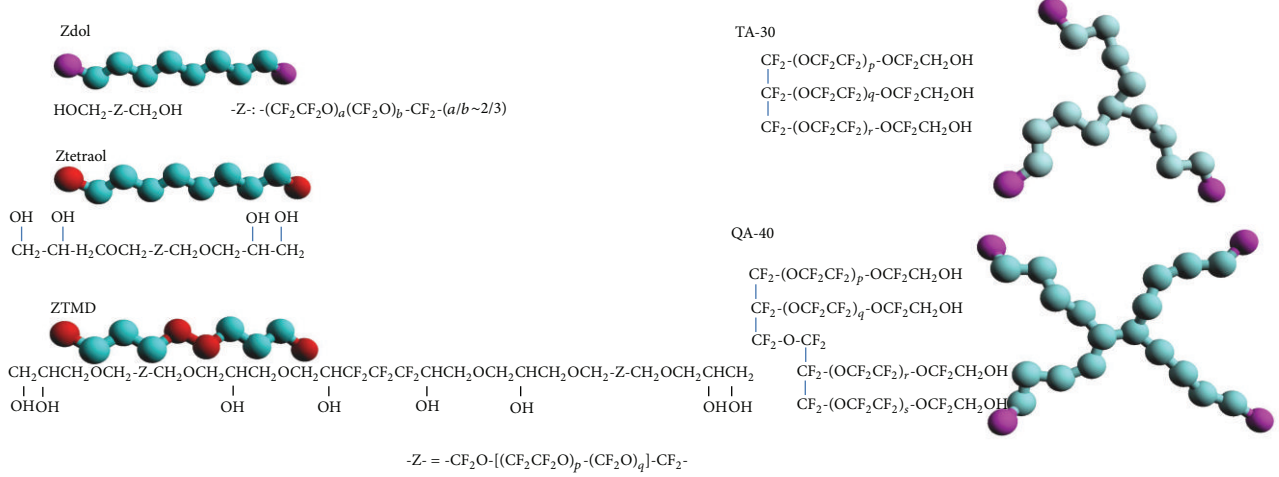


FIGURE 30: Coarse-grained bead-spring models of linear PFPEs (Z-dol, Z-tetraol, and ZTMD) and star-like PFPEs with three and four arms (TA-30 and QA-40), where magenta and red beads represent hydrogenated functional groups.

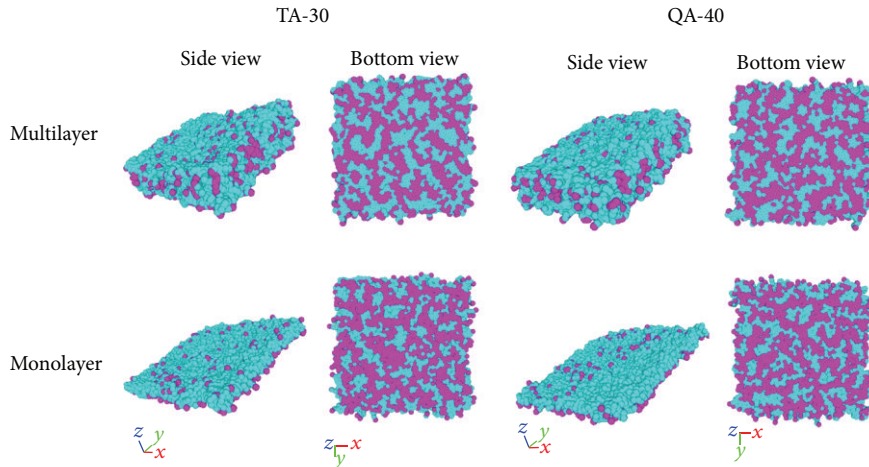


FIGURE 31: Snapshots of multilayer and monolayer TA-30 and QA-30: side and bottom views.

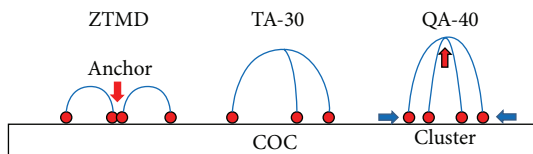


FIGURE 32: Schematic description of molecular conformations of ZTMD, TA-30, and QA-40 on COC.

the tribological performance of the HDI integration, that is, lubricant depletion and head vertical displacement. Therefore, nanomechanics of the PFPE films, such as “compression” and “tension” along the normal coordinate, are of technical significance in the HDI integration. In addition, nanomechanics of PFPE films allows us to explore several interesting nano-lubrication fundamentals, that is, film surface tension,

disjoining pressure, and work of adhesion and separation, which have been attempted via both experimental [52] and theoretical [53] tools. Here, using molecular dynamics (MD) simulation [54], we examined the nanomechanics of PFPE films, including “compression” and “tension,” where the lubricant end-group functionality is found to be a key determining factor in the event of HDI contact. Based upon the calculated normal stress profile, we further investigated the rheological property of PFPE nanofilms via the  $N$ -modes Maxwell model.

In our “thought nanomechanics experiment,” 150 functional PFPE molecules ( $\epsilon_b^P = \epsilon_w^P = 3\epsilon$ ) with the chain length of 20 beads per molecule were randomly “coated” onto two solid surfaces facing each other with the horizontal dimension of  $15\sigma \times 15\sigma$  and a vertical separation of  $25\sigma$ . The simulated nanomechanics snapshots are captured in Figure 36. The MD simulation was first executed to relax

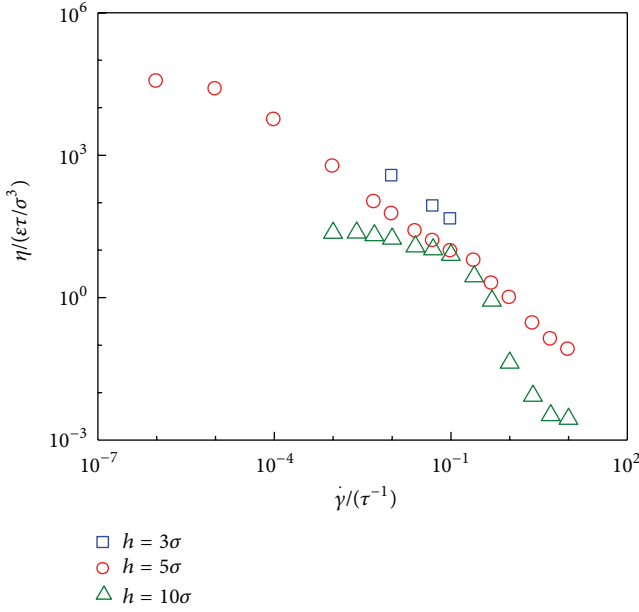


FIGURE 33: The shear viscosity of nonfunctional PFPE ( $\epsilon_b^P = \epsilon_w^P = 0$ ) nanofilms with three different wall separations ( $h = 3\sigma, 5\sigma$ , and  $10\sigma$ ) as a function of shear rate.

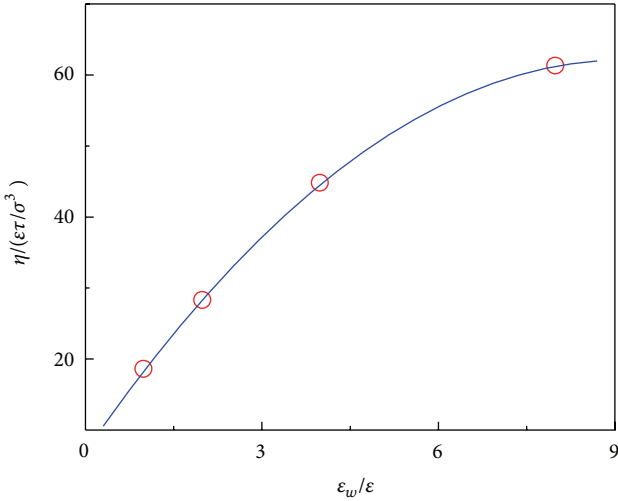


FIGURE 34: The shear viscosity of nonfunctional PFPE ( $\epsilon_b^P = \epsilon_w^P = 0$ ) films with the thickness of  $3\sigma$  as a function of surface interactions ( $\epsilon_w$ ) at the shear rate of  $0.1\tau^{-1}$ . Note that 230 functional PFPEs with  $N_p = 10$  are confined in the unit cell of  $30\sigma \times 30\sigma \times 3\sigma$ .

PFPE films to the equilibrium state (Figure 36(a)), where functional end beads in red are either localized near the solid surface or clustered. The “compression” mode was then carried out by moving down the top surface at a constant speed of  $0.002\sigma/\tau$ . As the separation became less than the LJ interaction range, interfacial molecules began to interact with each other (Figure 36(b)) and eventually merged into single nanoconfined film (Figure 36(c)). During the “tension” process, while the top surface was retracted with the same constant speed, a fluid bridge was found in between

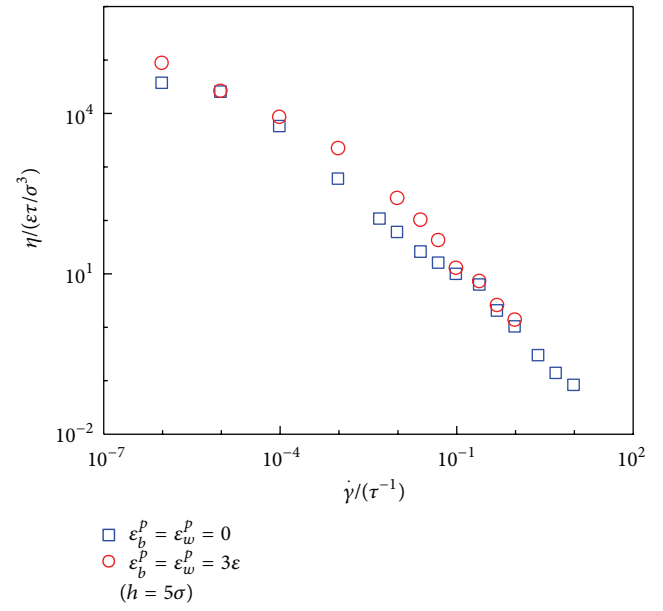


FIGURE 35: The shear viscosity of both nonfunctional ( $\epsilon_b^P = \epsilon_w^P = 0$ ) and functional ( $\epsilon_b^P = \epsilon_w^P = 3\epsilon$ ) PFPE films confined between two solid surfaces with a separation of  $5\sigma$  and with  $\epsilon_w = 4\epsilon$  under  $T = 1.0\epsilon/k_B$ .

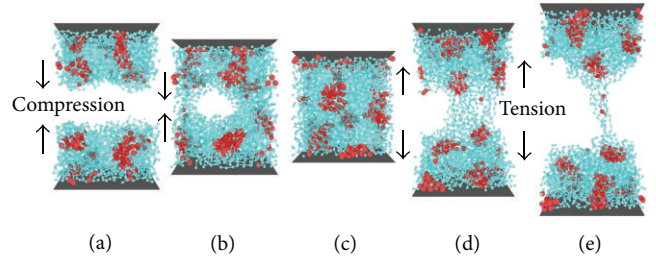


FIGURE 36: The simulated nanomechanics for functional PFPE ( $\epsilon_b^P = \epsilon_w^P = 3\epsilon$ ) films: (a) two well-equilibrated films approach each other, so-called “compression”; (b) two films are in contact; (c) two films completely contact and merge into one confined film; (d) the top surface is retracted, so-called “tension”; and (e) the confined film is being separated into two parts in the nearly end of the “tension.” Note that light blue indicates the backbone beads and red represents the functional end beads.

(Figure 36(d)), became thinner and thinner as the wall separation increased (Figure 36(e)), and eventually separated into two individual films. A similar nanomechanics simulation was also performed for nonfunctional PFPE nanofilm as shown in Figure 37, which showed significant difference compared to the functional PFPE nanofilm during the “tension” process. With the same time interval for data output, no apparent fluid bridge was observed for nonfunctional film. Also, the wall separation at the fluid bridge “break” point for nonfunctional PFPE film ( $\sim 24\sigma$ ) is much smaller than that of functional PFPE film ( $\sim 33\sigma$ ).

The corresponding normal stresses,  $\tau_{zz}$  ( $z$  is the coordinate perpendicular to disk surface), during “compression”

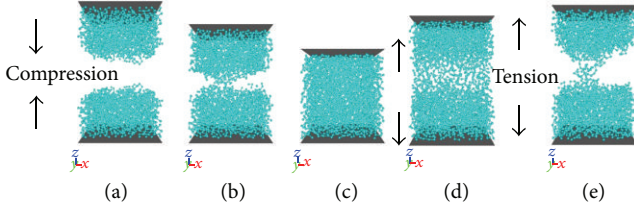


FIGURE 37: The simulated nanomechanics for nonfunctional PFPE ( $\varepsilon_b^P = \varepsilon_w^P = 0$ ) films: (a) two well-equilibrated films approach each other, so-called “compression”; (b) two films are in contact; (c) two films completely contact and merge into one confined film; (d) the top surface is retracted, so-called “tension”; and (e) the confined film is being separated into two parts in the nearly end of the “tension.”

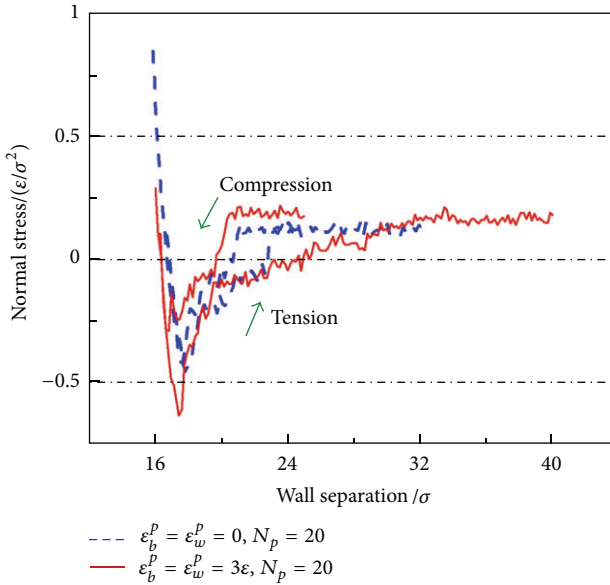


FIGURE 38: The normal stress of both nonfunctional (dashed lines) and functional (solid) PFPE films with  $N_p = 20$  during the simulated nanomechanics, that is, “compression” and “tension.”

and “tension” processes were further calculated for both nonfunctional and functional PFPE films. It is shown in Figure 38 that the film normal stress remains constant as the top surface moves downwards, but sharply drops when interfacial molecular attraction occurs and eventually reaches the minimum. The normal stress may be significantly increased afterwards with even a minor compressive strain due to the strong intermolecular repulsion force, that is, the LJ potential. In fact, our “compression” mechanics study suggests  $\sim 1\sigma$  clearance gain for functional film than nonfunctional film before the HDI interaction takes place, indicating less lubricant pick-up event for functional PFPEs. During the “tension” mechanics, an irreversible normal stress profile (hysteresis) was observed, especially for the functional PFPE film, which could be relevant to the viscoelasticity and stiction of PFPE nanofilm and also depends on the retraction rate of the top surface.

As one of the most classical viscoelastic models for a polymer system, the Maxwell model with multiple relaxation

TABLE 8: The elastic moduli and relaxation times for the  $N$ -modes ( $N = 2$ ) Maxwell model for both nonfunctional and functional PFPE films.

PFPE mode	Nonfunctional		Functional	
	1	2	1	2
$g_i(\varepsilon/\sigma^4)$	0.29	0.09	0.44	0.12
$v_{w,z}\lambda(\sigma)$	1.13	$1.1 \times 10^{19}$	1.68	18.36
$\lambda_i(\tau)$	565	Unphysical	840	9180

modes is employed here to understand the viscoelastic properties of PFPE nanofilms. The Maxwell model can be represented by a purely viscous dash pot with a viscosity of  $\eta$  and a purely elastic spring with the spring constant of  $k$  connected in series, as shown in Figure 39(a).

The relaxation process of polymeric/oligomeric systems usually cannot be described by single relaxation time; therefore,  $N$ -modes Maxwell model is typically preferred (Figure 39(b):  $N = 2$ ), where the relaxation moduli are given by

$$G_N(t) = \sum_{i=1}^N g_i \exp\left(-\frac{t}{\lambda_i}\right). \quad (19)$$

Here,  $g_i$  and  $\lambda_i$  ( $1 \leq i \leq N$ ) are the discrete spring constant and the associated relaxation times of the material, respectively. This idea can be translated from the time domain to the space domain in that the retraction rate ( $v_{w,z}$ ) of the top wall remains constant. Therefore, (19) is employed to fit the simulated film normal stress  $\tau_{zz}(z)$  with  $v_{w,z} = 0.002\sigma/\tau$ . This fit is only limited to the tension process as indicated by the blue symbols in Figures 40 and 41:

$$[\tau_{zz}(z) - \tau_0] = \sum_{i=1}^N g_i \exp\left(-\frac{z - z_0}{v_{w,z}\lambda_i}\right)(z - z_0). \quad (20)$$

Here, “0” stands for the reference point, where two films are completely merged into one confined film before the retraction occurs inside the film.

From the “tension” normal stress profiles, we observed that the PFPE molecules might experience two steps of relaxation, especially for the functional PFPEs, showing a sharp slope in the beginning of the “tension” process while the slope gets compromised once the wall separation is larger than  $20\sigma$  in Figure 41. Therefore,  $N$  is set to be 2 in (19). The fitted elastic moduli  $g_i$  and  $\lambda_i$  via the  $N$ -modes Maxwell model for both nonfunctional and functional PFPE films are listed in Table 8, where only one physical mode is observed for the nonfunctional PFPE film, related to the relaxation of the backbone beads, while a second mode with weaker elastic modulus but longer relaxation time is captured for the functional PFPE film, related to the relaxation of the functional end beads. Therefore, we believe that in the initial state of the “tension” process, the relaxation of backbone beads is dominant. However, the second stage of “tension,” which shows the apparent long-tail behavior, is mainly ascribed to functional end beads.

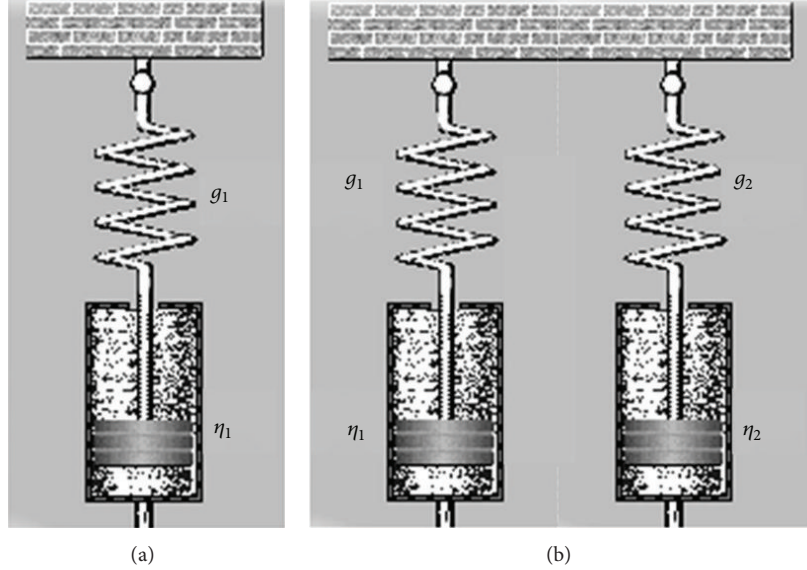


FIGURE 39: The schematics of the (a) single mode Maxwell and (b)  $N$ -modes ( $N = 2$ ) Maxwell model. Note that  $g_i$  is the spring constant and  $\eta_i$  is the viscosity of the dash pot.

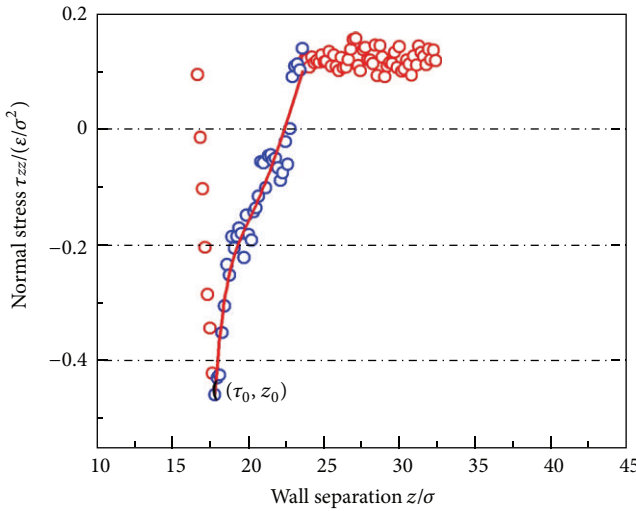


FIGURE 40: The nonlinear square fit of normal stress data using (19) for nonfunctional PFPE ( $\varepsilon_b^P = \varepsilon_w^P = 0$ ) films.

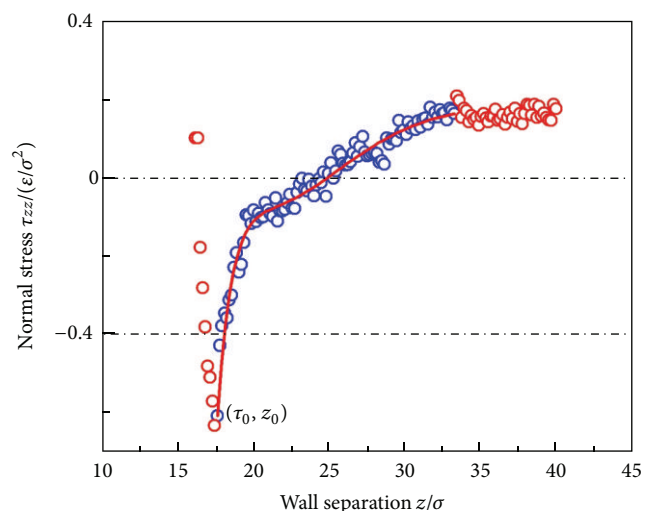


FIGURE 41: The nonlinear square fit of normal stress data using (19) for functional PFPE ( $\varepsilon_b^P = \varepsilon_w^P = 3\varepsilon$ ) films.

## 5. Summary and Discussion

In this paper, we have described a multiscale framework for modeling HDI materials. Beginning with the atomistic scale, we investigated the effect of detailed atomistic architecture on intramolecular and intermolecular PFPE degrees of freedom. The bottom-scale models allow us to investigate the strength of atomistic interactions between various PFPE/COC material pairs motivated by the need to engineer mobile lubricants with strong COC adhesion. Via a bottom to top approach, the atomistic information is passed to the molecular scale via coarse-graining procedures. This coarse-graining involves developing Hamiltonians with reduced degrees of freedom

based on atomistic conformations and interaction strengths. At the molecular scale, molecular dynamics allows for the investigation of bulk and surface PFPE properties for a range of functional group compositions. These properties include diffusion, radii of gyration, film morphology, and nanorheological performance. Thus, we have demonstrated a systematic methodology for probing the HDI; however, this approach can be applied to other physical systems with phenomena occurring over a range of time and length scales. Following this same methodology, extensions will be made to other critical issues in the performance of the HDI system. As discussed earlier, advanced COC materials such as graphene have the potential to provide significant savings in

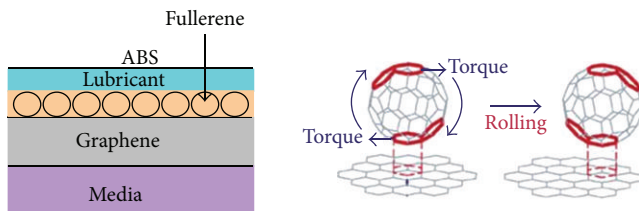


FIGURE 42: A schematic of the HDI with fullerene buffer layer between the PFPE lubricant and graphene. The motion of the fullerene on graphene can provide additional lubrication.

the COC layer thickness. However, factors such as the thermo-mechanical properties in the harsh HDI environment must be well understood. Thus, we apply our multiscale approach to investigating the mechanical performance of graphene under stress with various defects and grain boundaries via ab initio and molecular dynamics calculations [55]. Other COC configurations are also being considered with graphene reinforced by fullerenes in a novel solid-state buffer layer as shown in Figure 42.

Due to significant interest in heat-assisted magnetic recording (HAMR), we also study heat transfer in graphene and other nanoscale films via MD and the mesoscale lattice Boltzmann method (LBM) [56–58]. Consistent with our multiscale approach, the issue of HAMR's effect on HDI materials is also investigated at the atomistic scale using density functional theory-based ab initio molecular dynamics (AIMD). The AIMD simulation is in the context of HAMR conditions and is a natural complement to the higher scale classical MD/LBM studies where the best performing materials at the bottom, high resolution scale are further evaluated at higher scales.

In our integration model, we obtained the mesoscale properties from the coarse-grained model, which enables the bottom-up approach. This implies that the mesoscale model can be systematically derived from ab initio simulations via sequential coarse graining. LBM is the mesoscale/continuum theory, which can be incorporated to the highest coarse-grained model (e.g., SRS model [59]) since the LBM is on particle-based assumption [60–65]. Therefore, LBM can be used as a fundamental building block for constructing mesoscale/continuum models descriptive for lubricant as well as air bearing system (ABS). Since the LBM has the nature of transient physics and simple algorithm for the parallel calculation, thermal/mechanical models will be incorporated with the integrated model also covering adsorption/desorption kinetics, evaporation, and thermal oxidative degradation of PFPE lubricant at elevated temperature.

## Acknowledgments

This work is supported by Seagate Technology, and the publication fee was paid by HGST, a Western Digital Company.

## References

- [1] D. Kim, P. S. Chung, P. Jain, S. H. Vemuri, and M. S. Jhon, "Multiscale modeling of head disk interface," *IEEE Transactions on Magnetics*, vol. 46, no. 6, pp. 2401–2404, 2010.
- [2] L. J. Chen, H. J. Qian, Z. Y. Lu, Z. S. Li, and C. C. Sun, "An automatic coarse-graining and fine-graining simulation method: application on polyethylene," *The Journal of Physical Chemistry B*, vol. 110, no. 47, pp. 24093–24100, 2006.
- [3] J. Fish, "Bridging the scales in nano engineering and science," *Journal of Nanoparticle Research*, vol. 8, no. 5, pp. 577–594, 2006.
- [4] O. Al-Khayat and H. P. Langtangen, "Computational aspects of multiscale simulation with the lumped particle framework," *Communications in Computational Physics*, vol. 12, pp. 1257–1274, 2012.
- [5] A. Lyubartsev, Y. Tu, and A. Laaksonen, "Hierarchical multiscale modelling scheme from first principles to mesoscale," *Journal of Computational and Theoretical Nanoscience*, vol. 6, no. 5, pp. 951–959, 2009.
- [6] F. Müller-Plathe, "Coarse-graining in polymer simulation: from the atomistic to the mesoscopic scale and back," *ChemPhysChem*, vol. 3, no. 9, pp. 754–769, 2002.
- [7] A. B. Mhadeshwar and D. G. Vlachos, "Hierarchical multiscale mechanism development for methane partial oxidation and reforming and for thermal decomposition of oxygenates on Rh," *Journal of Physical Chemistry B*, vol. 109, no. 35, pp. 16819–16835, 2005.
- [8] T. Murtola, A. Bunker, I. Vattulainen, M. Deserno, and M. Karthunen, "Multiscale modeling of emergent materials: biological and soft matter," *Physical Chemistry Chemical Physics*, vol. 11, pp. 1689–1892, 2009.
- [9] N. Sheng, M. C. Boyce, D. M. Parks, G. C. Rutledge, J. I. Abes, and R. E. Cohen, "Multiscale micromechanical modeling of polymer/clay nanocomposites and the effective clay particle," *Polymer*, vol. 45, no. 2, pp. 487–506, 2004.
- [10] S. P. Xiao and T. Belytschko, "A bridging domain method for coupling continua with molecular dynamics," *Computer Methods in Applied Mechanics and Engineering*, vol. 193, no. 17–20, pp. 1645–1669, 2004.
- [11] Q. Shi, S. Izvekov, and G. A. Voth, "Mixed atomistic and coarse-grained molecular dynamics: simulation of a membrane-bound ion channel," *Journal of Physical Chemistry B*, vol. 110, no. 31, pp. 15045–15048, 2006.
- [12] K. Kremer and F. Müller-Plathe, "Multiscale simulation in polymer science," *Molecular Simulation*, vol. 28, no. 8–9, pp. 729–750, 2002.
- [13] H. Wang, C. Junghans, and K. Kremer, "Comparative atomistic and coarse-grained study of water: what do we lose by coarse-graining?" *The European Physical Journal E*, vol. 28, no. 2, pp. 221–229, 2009.
- [14] R. Smith, P. Seung Chung, J. A. Steckel, M. S. Jhon, and L. T. Biegler, "Force field parameter estimation of functional perfluoropolyether lubricants," *Journal of Applied Physics*, vol. 109, no. 7, Article ID 07B728, 2011.
- [15] J. M. Seminario, "Calculation of intramolecular force fields from second-derivative tensors," *International Journal of Quantum Chemistry*, vol. 60, no. 7, pp. 1271–1277, 1996.
- [16] E. Anderson, Z. Bai, C. Bischof et al., *LAPACK Users' Guide*, SIAM, Philadelphia, Pa, USA, 1999.
- [17] J. Wang, R. M. Wolf, J. W. Caldwell, P. A. Kollman, and D. A. Case, "Development and testing of a general Amber force field," *Journal of Computational Chemistry*, vol. 25, no. 9, pp. 1157–1174, 2004.
- [18] R. L. Smith, P. S. Chung, S. H. Vemuri, G. Y. Yeom, L. T. Biegler, and M. S. Jhon, "Atomistic simulation method in head-disk interface of magnetic data storage systems," *Journal of Applied Physics*, vol. 111, no. 7, Article ID 07B717, 3 pages, 2012.

- [19] P. S. Chung, H. Park, and M. S. Jhon, "The static and dynamic responses of binary mixture perfluoropolyether lubricant films-molecular structural effects," *IEEE Transactions on Magnetics*, vol. 45, no. 10, pp. 3644–3647, 2009.
- [20] Q. Guo, P. S. Chung, M. S. Jhon, and H. J. Choi, "Nanorheology of single unentangled polymeric lubricant films," *Macromolecular Theory and Simulations*, vol. 17, no. 9, pp. 454–459, 2008.
- [21] H. Chen and M. S. Jhon, "Relationship between surface coverage and end group functionality of molecularly thin perfluoropolyether films," *Journal of Applied Physics*, vol. 103, no. 7, Article ID 07F536, 3 pages, 2008.
- [22] P. S. Chung, H. Chen, and M. S. Jhon, "Molecular dynamics simulation of binary mixture lubricant films," *Journal of Applied Physics*, vol. 103, no. 7, Article ID 07F526, 3 pages, 2008.
- [23] Q. Guo, P. S. Chung, H. Chen, and M. S. Jhon, "Molecular rheology of perfluoropolyether lubricant via nonequilibrium molecular dynamics simulation," *Journal of Applied Physics*, vol. 99, no. 8, Article ID 08N105, 3 pages, 2006.
- [24] R. M. Balabin, "Communications: intramolecular basis set superposition error as a measure of basis set incompleteness: can one reach the basis set limit without extrapolation?" *Journal of Chemical Physics*, vol. 132, no. 21, Article ID 211103, 4 pages, 2010.
- [25] R. Smith, P. S. Chung, S. H. Vemuri, L. T. Biegler, and M. S. Jhon, "Atomistically tuning lubricant adhesion on carbon overcoat surface," *IEEE Transactions on Magnetics*, vol. 48, no. 11, pp. 4273–4276, 2012.
- [26] S. Ghosh, W. Bao, D. L. Nika et al., "Dimensional crossover of thermal transport in few-layer graphene," *Nature Materials*, vol. 9, no. 7, pp. 555–558, 2010.
- [27] W. R. Zhong, M. P. Zhang, B. Q. Ai, and D. Q. Zheng, "Chirality and thickness-dependent thermal conductivity of few-layer graphene: a molecular dynamics study," *Applied Physics Letters*, vol. 98, no. 11, Article ID 113107, 3 pages, 2011.
- [28] A. Agarwal, L. T. Biegler, and S. E. Zitney, "Simulation and optimization of pressure swing adsorption systems using reduced-order modeling," *Industrial and Engineering Chemistry Research*, vol. 48, no. 5, pp. 2327–2343, 2009.
- [29] W. G. Noid, J. W. Chu, G. S. Ayton et al., "The multiscale coarse-graining method. I. A rigorous bridge between atomistic and coarse-grained models," *Journal of Chemical Physics*, vol. 128, no. 24, Article ID 244114, 11 pages, 2008.
- [30] S. Izumisawa and M. S. Jhon, "Stability analysis of ultra-thin lubricant films with chain-end functional groups," *Tribology Letters*, vol. 12, no. 1, pp. 75–81, 2002.
- [31] R. J. Waltman, G. W. Tyndall, and J. Pacansky, "Computer-modeling study of the interactions of Zdol with amorphous carbon surfaces," *Langmuir*, vol. 15, no. 19, pp. 6470–6483, 1999.
- [32] P. H. Kasai and A. M. Spool, "Z-DOL and carbon overcoat: bonding mechanism," *IEEE Transactions on Magnetics*, vol. 37, no. 2, pp. 929–933, 2001.
- [33] R. J. Waltman, D. J. Pocker, and G. W. Tyndall, "Studies on the interactions between ZDOL perfluoropolyether lubricant and the carbon overcoat of rigid magnetic media," *Tribology Letters*, vol. 4, no. 3-4, pp. 267–275, 1998.
- [34] T. Aoyagi, J. Takimoto, and M. Doi, "Molecular dynamics study of polymer melt confined between walls," *Journal of Chemical Physics*, vol. 115, no. 1, pp. 552–559, 2001.
- [35] M. S. Jhon, G. Sekhon, and R. Armstrong, "The response of polymer molecules in a flow," in *Advances in Chemical Physics*, I. Prigogine and S. A. Rice, Eds., vol. 66, pp. 153–211, John Wiley, New York, NY, USA, 1987.
- [36] Q. Guo, S. Izumisawa, D. M. Phillips, and M. S. Jhon, "Surface morphology and molecular conformation for ultrathin lubricant films with functional end groups," *Journal of Applied Physics*, vol. 93, no. 10, pp. 8707–8709, 2003.
- [37] K. Kremer and G. S. Grest, "Dynamics of entangled linear polymer melts: a molecular-dynamics simulation," *Journal of Chemical Physics*, vol. 92, no. 8, pp. 5057–5086, 1990.
- [38] S. Izumisawa and M. S. Jhon, "Stability analysis and molecular simulation of nanoscale lubricant films with chain-end functional groups," *Journal of Applied Physics*, vol. 91, no. 10, p. 7583, 2002.
- [39] S. J. Vinay, D. M. Phillips, Y. S. Lee et al., "Simulation of ultrathin lubricant films spreading over various carbon surfaces," *Journal of Applied Physics*, vol. 87, no. 9, pp. 6164–6166, 2000.
- [40] X. Ma, J. Gui, L. Smoliar et al., "Spreading of perfluoropolyalkylether films on amorphous carbon surfaces," *Journal of Chemical Physics*, vol. 110, no. 6, pp. 3129–3137, 1999.
- [41] Y. T. Hsia, Q. Guo, S. Izumisawa, and M. S. Jhon, "The dynamic behavior of ultrathin lubricant films," *Microsystem Technologies*, vol. 11, no. 8-10, pp. 881–886, 2005.
- [42] G. W. Tyndall, R. J. Waltman, and D. J. Pocker, "Concerning the interactions between Zdol perfluoropolyether lubricant and an amorphous-nitrogenated carbon surface," *Langmuir*, vol. 14, no. 26, pp. 7527–7536, 1998.
- [43] G. W. Tyndall, T. E. Karis, and M. S. Jhon, "Spreading profiles of molecularly thin perfluoropolyether films," *Tribology Transactions*, vol. 42, no. 3, pp. 463–470, 1999.
- [44] K. Binder, *Monte Carlo and Molecular Dynamics Simulations in Polymer Science*, Oxford University Press, Oxford, UK, 1995.
- [45] Q. Guo, S. Izumisawa, M. S. Jhon, and Y. T. Hsia, "Transport properties of nanoscale lubricant films," *IEEE Transactions on Magnetics*, vol. 40, no. 4, pp. 3177–3179, 2004.
- [46] P. G. de Gennes, *Scaling Concepts in Polymer Physics*, Cornell University Press, Ithaca, NY, USA, 1979.
- [47] X.-C. Guo, B. Knigge, B. Marchon, R. J. Waltman, M. Carter, and J. Burns, "Multidentate functionalized lubricant for ultralow head/disk spacing in a disk drive," *Journal of Applied Physics*, vol. 100, no. 4, Article ID 044306, 2006.
- [48] X.-C. Guo, T. Karis, H. Deng, Q. Dai, J. Burns, and R. J. Waltman, "Fomblin multidentate lubricants for ultra-low magnetic spacing," *IEEE Transactions on Magnetics*, vol. 42, no. 10, pp. 2504–2506, 2006.
- [49] H. Tani, K. Sakamoto, and N. Tagawa, "Conformation of ultrathin pfpe lubricants with different structure on magnetic disksdirect observation and MD simulation," *IEEE Transactions on Magnetics*, vol. 45, no. 11, pp. 5050–5054, 2009.
- [50] R. N. Kono, S. Izumisawa, M. S. Jhon, C. A. Kim, and H. J. Choi, "Rheology of perfluoropolyether lubricants," *IEEE Transactions on Magnetics*, vol. 37, no. 4 I, pp. 1827–1829, 2001.
- [51] H. J. Choi, Q. Guo, P. S. Chung, and M. S. Jhon, "Molecular rheology of perfluoropolyether lubricant via nonequilibrium molecular dynamics simulation," *IEEE Transactions on Magnetics*, vol. 43, no. 2, pp. 903–905, 2007.
- [52] C. M. Mate and V. J. Novotny, "Molecular conformation and disjoining pressure of polymeric liquid films," *The Journal of Chemical Physics*, vol. 94, no. 12, pp. 8420–8427, 1991.
- [53] S. Izumisawa and M. S. Jhon, "Calculation of disjoining pressure for lubricant films via molecular simulation," *IEEE Transactions on Magnetics*, vol. 42, no. 10, pp. 2543–2545, 2006.

- [54] Q. Guo, *The static and dynamic properties of nano-structured thin oligomeric films [Ph.D. thesis]*, Carnegie Mellon University, Pittsburgh, Pa, USA, 2006.
- [55] Y. I. Jhon, S. E. Zhu, J. H. Ahn, and M. S. Jhon, "The mechanical responses of tilted and non-tilted grain boundaries in graphene," *Carbon*, vol. 50, no. 10, pp. 3708–3716, 2012.
- [56] W. T. Kim, D. Kim, S. H. Vemuri, S. C. Khang, P. S. Chung, and M. S. Jhon, "Multicomponent gas mixture air bearing modeling via lattice Boltzmann method," *Journal of Applied Physics*, vol. 109, no. 7, Article ID 07B759, 3 pages, 2011.
- [57] H. M. Kim, J. H. Kang, and M. S. Jhon, "Hydro-kinetic approach in non-Newtonian lattice Boltzmann flow simulation," *Journal of the Korean Physical Society*, vol. 58, article 444, 2011.
- [58] D. Kim, H. M. Kim, M. S. Jhon, S. J. Vinay, and J. Buchanan, "A characteristic non-reflecting boundary treatment in lattice Boltzmann method," *Chinese Physics Letters*, vol. 25, no. 6, article 1964, 2008.
- [59] X. Ma, C. L. Bauer, M. S. Jhon, J. Gui, and B. Marchon, "Monte Carlo simulations of liquid spreading on a solid surface: effect of end-group functionality," *Physical Review E*, vol. 60, no. 5, pp. 5795–5801, 1999.
- [60] D. M. Phillips, A. S. Khair, and M. S. Jhon, "Mathematical simulation of ultra-thin polymeric film spreading dynamics," *IEEE Transactions on Magnetics*, vol. 37, no. 4 I, pp. 1866–1868, 2001.
- [61] D. M. Phillips and M. S. Jhon, "Dynamic simulation of nano-scale lubricant films," *Journal of Applied Physics*, vol. 91, no. 10, p. 7577, 2002.
- [62] W. T. Kim, M. S. Jhon, Y. Zhou, I. Staroselsky, and H. Chen, "Nanoscale air bearing modeling via lattice Boltzmann method," *Journal of Applied Physics*, vol. 97, no. 10, Article ID 10P304, 3 pages, 2005.
- [63] Q. Guo, L. Li, Y.-T. Hsia, and M. S. Jhon, "A spreading study of lubricant films via optical surface analyzer and molecular dynamics," *IEEE Transactions on Magnetics*, vol. 42, no. 10, pp. 2528–2530, 2006.
- [64] Q. Guo, L. Li, Y.-T. Hsia, and M. S. Jhon, "Stability analysis of ultrathin lubricant films via surface energy measurements and molecular dynamics simulations," *Journal of Applied Physics*, vol. 97, no. 10, Article ID 10P302, 3 pages, 2005.
- [65] H. M. Kim, D. Kim, W. T. Kim, P. S. Chung, and M. S. Jhon, "Langmuir slip model for air bearing simulation using the Lattice Boltzmann method," *IEEE Transactions on Magnetics*, vol. 43, no. 6, pp. 2244–2246, 2007.

## Review Article

# The Head-Disk Interface Roadmap to an Areal Density of 4 Tbit/in<sup>2</sup>

Bruno Marchon,<sup>1</sup> Thomas Pitchford,<sup>2</sup> Yiao-Tee Hsia,<sup>3</sup> and Sunita Gangopadhyay<sup>2</sup>

<sup>1</sup> HGST, San Jose, CA 95135, USA

<sup>2</sup> Seagate Technology, Minneapolis, MN 55435, USA

<sup>3</sup> Western Digital, San Jose, CA 95138, USA

Correspondence should be addressed to Bruno Marchon; bruno.marchon@hgst.com

Received 10 December 2012; Accepted 12 February 2013

Academic Editor: Tom Karis

Copyright © 2013 Bruno Marchon et al. This is an open access article distributed under the Creative Commons Attribution License, which permits unrestricted use, distribution, and reproduction in any medium, provided the original work is properly cited.

This paper reviews the state of the head-disk interface (HDI) technology, and more particularly the head-medium spacing (HMS), for today's and future hard-disk drives. Current storage areal density on a disk surface is fast approaching the one terabit per square inch mark, although the compound annual growth rate has reduced considerably from ~100%/annum in the late 1990s to 20–30% today. This rate is now lower than the historical, Moore's law equivalent of ~40%/annum. A necessary enabler to a high areal density is the HMS, or the distance from the bottom of the read sensor on the flying head to the top of the magnetic medium on the rotating disk. This paper describes the various components of the HMS and various scenarios and challenges on how to achieve a goal of 4.0–4.5 nm for the 4 Tbit/in<sup>2</sup> density point. Special considerations will also be given to the implication of disruptive technologies such as sealing the drive in an inert atmosphere and novel recording schemes such as bit patterned media and heat assisted magnetic recording.

## 1. Introduction

As the areal density of commercial hard disk drives is quickly approaching the terabit per square inch milestone [1–5] (Figure 1), the need to improve the reliability of the head-disk interface (HDI) and to further decrease the head-medium spacing (HMS) is becoming evermore critical [3, 6, 7]. Low HMS is a necessary enabler to good writability as well as strong read-back signal integrity [8, 9]. It is estimated that the HMS will soon need to cross the 7 nm mark in order to reach this terabit per square inch density point [2, 6]. It is remarkable to realize that the error rate of the stored digital signal that is being read back improves approximately by about 2x for every 0.3–0.5 nanometer of decreased HMS. In addition to relentless demand for novel, ultrathin protecting films of overcoat and lubricant, and subnanometer air gap between the disk and the head, alternative recording technologies presently being contemplated involve heating the disk to over 500°C (heat-assisted magnetic recording or HAMR) [10–12] and/or physically isolating magnetic bits on small islands of sub-30 nm in physical dimensions (bit-patterned recording or BPR) [13–16].

In this paper, the roadmap to an areal density of 4 terabits per square inches will be discussed. Particular emphasis will be given to the various spacing components that comprise the HMS budget and their physical limits. The various implications of recording technologies incorporating HAMR and/or BPR will also be addressed.

## 2. Historical Perspective

Hard drive technology has constantly evolved to achieve consistent areal density growth. As one technology such as longitudinal recording has reached its limit, another such as perpendicular recording has taken over [18]. Along with advances in heads, media, signal processing, and servo technology, areal density growth is sustained through improvements in the head-disk interface (HDI). Head-media spacing (HMS) is the most important HDI parameter related to areal density growth [6]. Continued developments in the tribological design of disk drives have maintained the reliability of the head/disk interface despite decreased spacing.

Analysis of long-term trends shows that HMS has steadily declined over time (Figure 2). The historical trends indicate

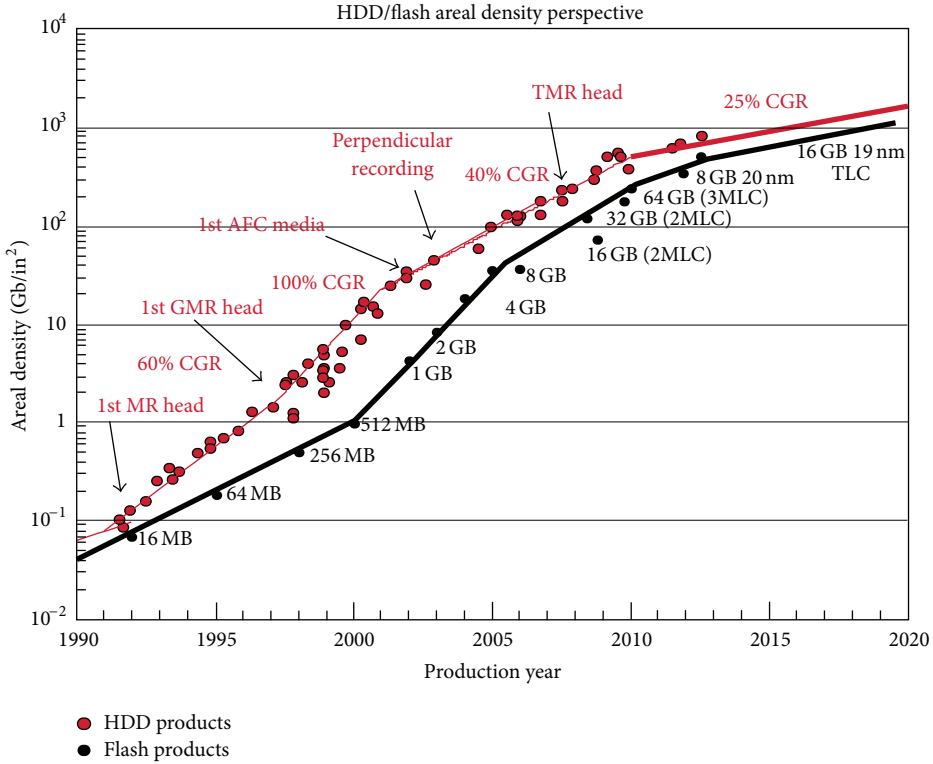


FIGURE 1: Areal density evolution of HDD and flash memory. After Grochowski [17], with permission.

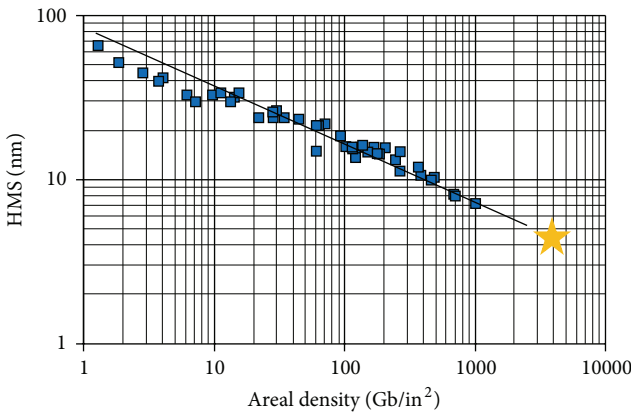


FIGURE 2: Historical variations of HMS versus areal density from [6]. The yellow star is an extrapolation to 4 Tb/in<sup>2</sup>.

that the HMS of recent products is  $\sim 60\%$  of bit length (Figure 3) [6]. The HMS for recording demonstrations has been typically more aggressive, at  $\sim 50\%$  of bit length.

Research consortia such as the Information Storage Industry Consortium (INSIC—<https://www.insic.com/>), Storage Research Consortium (SRC—<http://www.srcep.jp.gr.jp/>), and the Advanced Storage Technology Consortium (ASTC—[http://www.idema.org/?page\\_id=3193](http://www.idema.org/?page_id=3193)) have included collaborations on HDI technology development. For each areal density, the HMS target has typically been set by the Recording Subsystem (RSS) groups. The past and current HMS

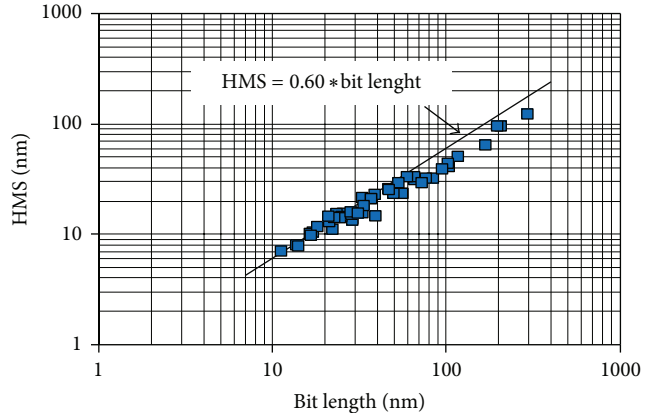


FIGURE 3: Historical variations of HMS versus bit length from [6].

trends for the different consortia are shown in Figure 4. The HMS trends have typically followed the overall trends of Figures 2 and 3 fairly well. For the HMS roadmaps released in 2003–2010, the INSIC trend tended to be lower than for SRC. For the current update (2012), the ASTC trend is higher than SRC.

For ASTC the main areal density targets are 2 Tb/in<sup>2</sup> and 4 Tb/in<sup>2</sup>, with scheduled product introductions of 2016 and 2020, respectively. The current HMS targets for these two density points is  $\sim 5\text{--}6$  and  $4\text{--}5$  nm, respectively, that is, less aggressive than those for INSIC. The 4 Tb/in<sup>2</sup> HMS goal will be discussed in more details in Section 4.

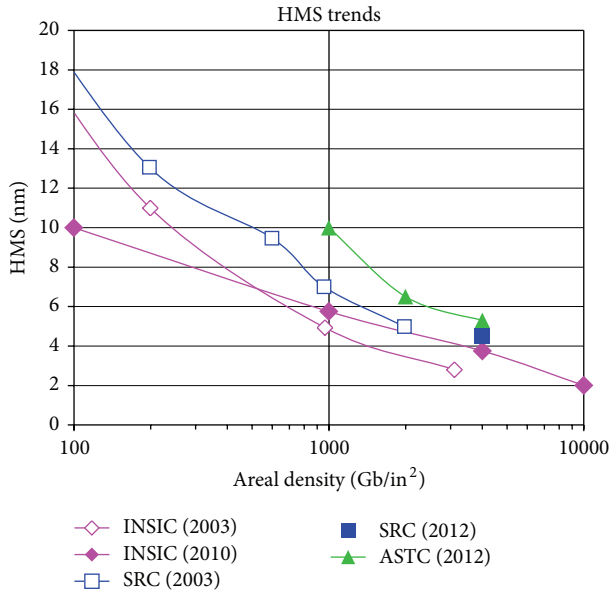


FIGURE 4: HMS trends of industry research consortia.

### 3. Definition of the Head-Media Spacing Components

As the capacity and performance of disk drives has improved, the mechanical interface has evolved. The spacing between the head and the media has steadily decreased to achieve the rapid improvements in areal density. Figure 5 is a diagram of head-media spacing (HMS). The HMS is comprised of the fly height and coatings (head and disk overcoats, disk lubricant).

In the diagram of Figure 5(b), the surfaces are assumed to be perfectly smooth—they do not include factors such as surface topography and variability of the fly height. The fly height denotes the spacing between the centerline surfaces of the head and disk. The clearance denotes the spacing between the close points of the surfaces. The distinction between fly height and clearance is depicted in Figure 6.

Below are some definitions of terms commonly used by the HDI/tribology community.

- (1) Head-media spacing (HMS): the spacing between the top of the magnetic layer and the surface of the transducer.
- (2) Flying clearance: difference or margin in fly height between nominal operation and contact between the head and disk.
- (3) Glide avalanche/touchdown height (TDH): the lowest slider flying height above the mean roughness level without significant slider-disk contact
- (4) Flying height = flying clearance + touchdown height
- (5) Media lubricant thickness: the average thickness of the lubricant, assumed to be on top of the media overcoat

(6) Media overcoat thickness: the average thickness of the media overcoat, assumed to follow the topography of the underlying surface

(7) Head overcoat: head adhesion layer (e.g., silicon) + diamond-like carbon (DLC)

$$\text{HMS} = \text{head overcoat} + \text{TDH} + \text{clearance} \\ + \text{media lubricant} + \text{media overcoat} \quad (1)$$

For current hard drives, HMS reductions have been achieved mostly through reductions in the clearance and disk and head overcoats. While this trend will continue for the immediate future, additional HMS reductions will soon require nontraditional HDI designs in order to meet the demanding recording requirements for areal densities beyond 1 Tb/in<sup>2</sup>.

In older drive designs, the air bearing design and passive topography of the slider determined the fly height and clearance of the transducer. In newer drive designs, the fly height is actively controlled by a signal that changes the shape of the slider. The most common method used for this control is to embed an electrical resistive heater in the slider that will cause the transducer area to protrude closer to the disk, as is shown in Figure 6 [19–21]. At some point the interface may need to be designed to withstand intermittent or continuous contact [22–27].

Current products have HMS on the order of 10 nm or slightly below [6]. For the 1 Tb/in<sup>2</sup> products under development, a Hi-Lo range bracket can be defined, since this areal density point is no longer precompetitive. For beyond 1 Tb/in<sup>2</sup>, achievable and stretch values were estimated. The technological development required to achieve the targets will be discussed in Section 4. The assessment indicated that there is promise for achieving 4–6 nm HMS in the long term. While advancements in HDI design could enable significant reduction in HMS, new recording schemes could add to the challenge due to new sources of HMS loss: heat assisted magnetic recording (HAMR) will experience effects of high temperature at the interface [28–30], and bit-patterned magnetic recording (BPR) could have issues with added disk topography that would add to the touchdown height [31–34].

### 4. ASTC HDI Roadmap to 4 Tb/in<sup>2</sup> and Major Research Challenges

As shown in Figure 2, a good estimation of the HMS is ~60% of the length of the bit, and some rationale for this was recently proposed [6]. This offers a convenient way to project future HMS values, as the following simple equations can be derived. If one defines areal density (AD) in bits per square inch as the product of the linear density in bit per inch (BPI) and track density (TPI),  $AD = BPI \cdot TPI$ . Furthermore, the bit aspect ratio BAR is usually defined as  $BAR = BPI/TPI$ ; hence, the bit length (BL), in inches, can be expressed as

$$BL = (AD \cdot BAR)^{-1/2}. \quad (2)$$

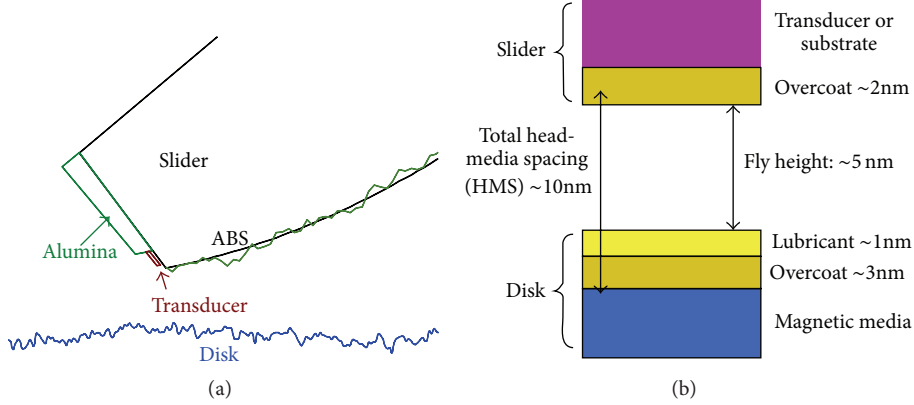


FIGURE 5: Components of head-disk spacing: (a) schematic of trailing end of head as it flies over disk. (b) Idealized HMS stacks up.

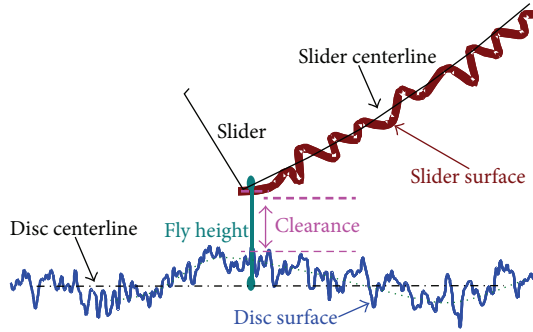


FIGURE 6: Parameters related to head-disk clearance and fly height.

TABLE 1: Estimated HMS (nm) values as a function of AD and BAR.

AD (Tb/in <sup>2</sup> )	BAR			
	3.0	3.5	4.0	4.5
2	6.2	5.8	5.4	5.1
4	4.4	4.1	3.8	3.6

With the HMS approximation of 60% of BL, we now have a very convenient expression linking HMS (in nanometer) to AD (in Tb/in<sup>2</sup>), for a given BAR:

$$\text{HMS (nm)} \approx 15 \cdot (\text{AD} \cdot \text{BAR})^{-1/2}. \quad (3)$$

Numerical HMS values based on (3) are reproduced in Table 1 below.

As shown in Table 1, achieving a 4 Tb/in<sup>2</sup> areal density will require an HMS in the vicinity of ~4.4 nm, assuming a bit aspect ratio (BAR) of 3. Table 2 offers two scenarios for the HMS breakdown into its various components. In the table, the 2010 projection from INSIC is also presented, as well as a realistic range for the 1 Tb/in<sup>2</sup> density point that sponsor companies are working towards. For the 4 Tb/in<sup>2</sup> point, both “Achievable” and “Stretch” values are offered, corresponding to roughly 60–100% and <60% chance of success, respectively. It is clear from the table that achieving the ~4.4 nm goal is a high risk, and it will require evolutionary as well as revolutionary changes in materials, processes, and clearance

control schemes. HDD architecture (e.g., sealing in inert atmosphere) might also be needed [35]. This is discussed in the following sections.

**4.1. Materials: Disk and Head Overcoat.** It is clear from Table 2 that the biggest contributor to today’s HMS is the carbon overcoat, both on the disk and on the head. Combined, they amount to about half of today’s (aka 1 Tb/in<sup>2</sup>) HMS budget. Historically, overcoat thickness reduction on both components has been enabled by denser carbon, as well as smoother underlying surfaces for the magnetic medium (disk) and RW elements (head). Head carbon has evolved from sputtered to plasma-enhanced chemical vapor deposition (PE-CVD) to filtered cathodic arc (f-CAC) carbon [36–39], which increased the density, sp<sup>3</sup>/sp<sup>2</sup> ratio, and hardness [40]. On the disk side, f-CAC technology has not yet been made manufacturable [41, 42], mostly because of particle and deposition rate challenges, and most if not all disks shipped today are coated with some sort of PE-CVD deposited amorphous carbon overcoat. It is believed that disk deposition tools will soon need to offer new carbon technologies, able to closely emulate a high sp<sup>3</sup> bonded, f-CAC-type carbon film. On the head side, evolutionary optimization of the overcoat technology might allow to reach the 4 Tb/in<sup>2</sup> goal of ~1 nm, believed to be the ultimate coverage limit of f-CAC. Finally, although many attempts have been made by disk manufacturers to develop and ship noncarbon overcoated disks, it remains an open question whether any thin film materials other than carbon can be made as hard, dense, and chemically inert as carbon films [43–47]. The latter issue could be alleviated if HDD’s can be sealed in an inert environment [35]. It is also believed that such a drastic change in the drive mechanical platform could help reduce overcoat thickness on both heads and disks, as magnetic medium and read/write alloy corrosion could then be suppressed, or at least drastically reduced. Our estimate of such benefit is in the range of 0.2–0.3 nm or greater, for an overall reduction of ~0.5 nm, that is, a substantial amount of about 10% of the total HMS. Another potential alternative is to develop a disk surface modification process such that the highly corrosion-susceptible media material surface is

TABLE 2: HMS breakdown scenarios for 4 Tb/in<sup>2</sup>.

HMS Budget	1 Tb/in <sup>2</sup>		4 Tb/in <sup>2</sup>			HMS adder	
Components	INSIC 2010	Target HMS by ~2014	INSIC 2010	Target HMS by ~2020-21	(effect of HAMR, BPM)	BPM	HAMR
Component	Hi	Lo		Medium risk	High risk		
TDH	1.8	2.0	1.0	1.4	1.1	0.6	0.3
Disc overcoat	0.9	2.5	2.0	0.6	1.8	1.5	0.3
Disk lubricant	0.9	1.2	1.0	0.8	1.0	0.8	0.6
Clearance	1.3	1.2	1.0	0.6	0.6	0.5	0.2
Head overcoat	1.0	2.0	1.5	0.7	1.1	0.9	0.3
Total	5.8	8.9	6.5	4.0	5.6	4.3	0.8
							1.4

The HMS adder columns corresponding to HAMR and BPM will be discussed in Section 4.

treated or modified without contributing to spacing loss with a creation of a nonfunctional or weakened layer of magnetic material on the media surface [48, 49].

**4.2. Materials: Disk Lubricant.** Table 2 shows that a 0.2 nm reduction of lubricant thickness from 1.0–1.2 to 0.8–1.0 is needed. This does not seem like much, but with today's extremely tight reliability/HMS margins, this change is actually significant, and it is believed that inventions will be needed to reach those goals [50, 51]. The lubricant industry is now more diversified than before, and new lubricant structures are now routinely offered by at least three different companies. It remains to be seen whether conventional lubricant chemistries (functionalized perfluoropolyether) will be able to achieve this thickness goal. Perhaps unconventional approaches, such as direct surface treatment/functionalization of the disk overcoat will be needed [48].

**4.3. TDH: Topography.** Touchdown height (TDH) globally defines all residual disk and head topographies that prevent the head from coming into close proximity to the magnetic medium (Figure 6). It is affected by waviness ( $\sim 1\text{--}1000\text{ }\mu\text{m}$  wavelength range) and roughness ( $<1\text{ }\mu\text{m}$ ) of the substrate [52–54], as well as the nanoroughness of the magnetic film-overcoat structure of the disk [55]. Unlike materials thicknesses (lubricant, overcoat), TDH is not a requirement for proper HDD reliability and could, in theory, be brought to zero. It assumed that engineering evolutionary optimization of polishing (disk substrate, slider) and deposition (media/overcoat) processes will be possible to achieve the HMS goal. Finally, it has been proposed that disk lubricant “roughness”, both at the nanoscale (conformation) [56] and the microscale (thickness modulation or “moguls” [57] and “ripples” [58, 59]), also contributes to TDH, and lubricant optimization, as discussed previously, will be needed to also lower its contribution.

**4.4. Head-Disk Clearance.** Of all the HMS contributors, clearance has probably exhibited the largest decrease in the last 10 years or so, thanks to the advent of thermal flying height control (TFC—Figure 7) [19, 21]. This revolutionary approach has allowed the HDD industry to achieve a 10-fold reduction in clearance from ca. 10 nm ten years ago to  $\sim 1.5$  nm

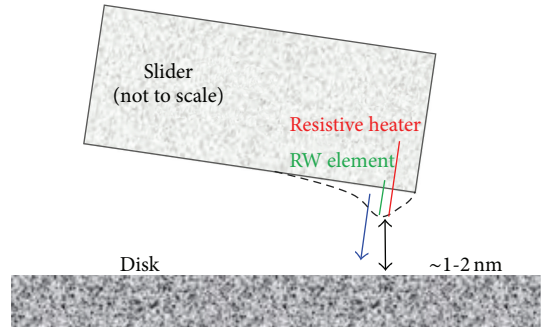


FIGURE 7: Schematics of the active fly height control scheme using an embedded resistive heater.

today (Table 2). To achieve the 0.6 nm ASTC clearance goal and to easily compensate for clearance changes induced by temperature, altitude, or humidity, further enhancement of clearance control will be needed such as closed-loop TFC control. “Surfing” of light contact recording has also been suggested [26], but it remains to be seen whether this approach can be made reliable.

## 5. Tribology and HDI Challenges for Alternate Technologies

As discussed earlier, to advance HDD magnetic recording beyond the  $\sim 1\text{ Tb/in}^2$  believed achievable with PMR/SMR, HAMR and BPM technologies are being developed. It is believed that HAMR will first be introduced. To go beyond  $\sim 6\text{ Tb/in}^2$ , the ASTC roadmap shows that HAMR will be augmented with BPM recording technology [11]. While these will enable significant gains in areal density, they will present challenges for the HDI.

In terms of HMS, the effect of these technologies is shown in the “HMS Adder” columns of Table 2. The touchdown height is increased due to added media roughness for HAMR or residual topography for BPM [32, 60]. The increased roughness also drives the need for added media overcoat thickness to maintain adequate coverage. With regards to clearance, HAMR would require added margin as a guardband for possible thermal protrusion of the near-field transducer (NFT) [10], whereas BPM will require clearance

margin as a guardband against residual topography that could induce head wear. It is believed that BPM will not require head overcoat thickness adder.

As the HDD industry moves towards the introduction of HAMR recording technologies, there is a high demand for the HDI to demonstrate robustness at higher temperatures [30, 61–63]. If the current disk overcoat and lubricant films are not capable of withstanding the high recording temperature ( $>500^{\circ}\text{C}$ ), new materials will be needed. On the head side, it is currently believed that the temperature should be limited to  $\sim 150^{\circ}\text{C}$  in order to provide long-term interface reliability to the current overcoat material. In any event, further development in tribological materials for both heads and media seem likely needed in order to insure proper reliability of the HAMR interface.

The later introduction of BPM recording technology will present further challenges for HDI design. Residual topography left behind by the BPM manufacturing process challenges air bearing designers to design a slider that can better follow residual topography [34, 64, 65] as well as media manufacturers to have a uniform overcoat and lubricant coverage of the media surface. Moreover, the residual media topography could lead to excessive induced lubricant roughness on the microscale (lubricant moguls and ripples) unless a new lubricant can be designed.

## 6. Conclusion

In summary, head-media spacing continues to be an enabler for continued march to increase the areal density to fend off the assault and encroachment by nonvolatile solid-state memory technologies. To maintain HDD leadership and competitive edge in the data storage arena, the industry must continue to develop new component technologies to support this areal density advance. However, to be successful, the design of the head-disk interface must be an integrated effort where the component technologies are developed in concert to solve the system problem. The success of the areal density growth will depend on how successful we, as an industry, are in integrating this development.

## References

- [1] R. W. Wood, J. Miles, and T. Olson, “Recording technologies for terabit per square inch systems,” *IEEE Transactions on Magnetics*, vol. 38, no. 4, pp. 1711–1718, 2002.
- [2] R. Wood, “The feasibility of magnetic recording at 1 Terabit per square inch,” *IEEE Transactions on Magnetics*, vol. 36, no. 1, pp. 36–42, 2000.
- [3] C. M. Mate, Q. Dai, R. N. Payne, B. E. Knigge, and P. Baumgart, “Will the numbers add up for sub-7-nm magnetic spacings? Future metrology issues for disk drive lubricants, overcoats, and topographies,” *IEEE Transactions on Magnetics*, vol. 41, no. 2, pp. 626–631, 2005.
- [4] M. E. Schabes, “Micromagnetic simulations for terabit/in<sup>2</sup> head/media systems,” *Journal of Magnetism and Magnetic Materials*, vol. 320, no. 22, pp. 2880–2884, 2008.
- [5] M. Mallary, A. Torabi, and M. Benakli, “One terabit per square inch perpendicular recording conceptual design,” *IEEE Transactions on Magnetics*, vol. 38, no. 4, pp. 1719–1724, 2002.
- [6] B. Marchon and T. Olson, “Magnetic spacing trends: from LMR to PMR and beyond,” *IEEE Transactions on Magnetics*, vol. 45, no. 10, pp. 3608–3611, 2009.
- [7] J. Gui, “Tribology challenges for head-disk interface toward 1 Tb/in<sup>2</sup>,” *IEEE Transactions on Magnetics*, vol. 39, no. 2, pp. 716–721, 2003.
- [8] R. L. Wallace, “The reproduction of magnetically recorded signals,” *Bell System Technical Journal*, vol. 30, pp. 1145–1173, 1951.
- [9] B. Marchon, K. Saito, B. Wilson, and R. Wood, “The limits of the Wallace approximation for PMR recording at high areal density,” *IEEE Transactions on Magnetics*, vol. 47, pp. 3422–3425, 2012.
- [10] M. H. Kryder, E. C. Gage, T. W. McDaniel et al., “Heat assisted magnetic recording,” *Proceedings of the IEEE*, vol. 96, no. 11, pp. 1810–1835, 2008.
- [11] B. C. Stipe, T. C. Strand, C. C. Poon et al., “Magnetic recording at 1.5 Pb/m<sup>2</sup> using an integrated plasmonic antenna,” *Nature Photonics*, vol. 4, no. 7, pp. 484–488, 2010.
- [12] W. A. Challener, C. Peng, A. V. Itagi et al., “Heat-assisted magnetic recording by a near-field transducer with efficient optical energy transfer,” *Nature Photonics*, vol. 3, pp. 220–224, 2009.
- [13] E. A. Dobisz, Z. Z. Bandić, T. W. Wu, and T. Albrecht, “Patterned media: nanofabrication challenges of future disk drives,” *Proceedings of the IEEE*, vol. 96, no. 11, pp. 1836–1846, 2008.
- [14] B. D. Terris, T. Thomson, and G. Hu, “Patterned media for future magnetic data storage,” *Microsystem Technologies*, vol. 13, no. 2, pp. 189–196, 2007.
- [15] X. Yang, S. Xiao, W. Wu et al., “Challenges in 1 Teradotin. 2 dot patterning using electron beam lithography for bit-patterned media,” *Journal of Vacuum Science & Technology B*, vol. 25, no. 6, pp. 2202–2209, 2007.
- [16] A. Kikitsu, “Prospects for bit patterned media for high-density magnetic recording,” *Journal of Magnetism and Magnetic Materials*, vol. 321, no. 6, pp. 526–530, 2009.
- [17] E. Grochowski, Future Technology Challenges for NAND Flash and HDD Products, Flash Memory Summit, 2012.
- [18] S. I. Iwasaki, “Principal complementarity between perpendicular and longitudinal magnetic recording,” *Journal of Magnetism and Magnetic Materials*, vol. 287, pp. 9–15, 2005.
- [19] M. Suk, K. Miyake, M. Kurita, H. Tanaka, S. Saegusa, and N. Robertson, “Verification of thermally induced nanometer actuation of magnetic recording transducer to overcome mechanical and magnetic spacing challenges,” *IEEE Transactions on Magnetics*, vol. 41, no. 11, pp. 4350–4352, 2005.
- [20] K. Miyake, T. Shiramatsu, M. Kurita, H. Tanaka, M. Suk, and S. Saegusa, “Optimized design of heaters for flying height adjustment to preserve performance and reliability,” *IEEE Transactions on Magnetics*, vol. 43, no. 6, pp. 2235–2237, 2007.
- [21] T. Shiramatsu, M. Kurita, K. Miyake et al., “Drive-integration of active flying-height control slider with micro thermal actuator,” *IEEE Transactions on Magnetics*, vol. 42, no. 10, pp. 2513–2515, 2006.
- [22] J. Itoh, Y. Sasaki, K. Higashi, H. Takami, and T. Shikanai, “An experimental investigation for continuous contact recording technology,” *IEEE Transactions on Magnetics*, vol. 37, no. 4, pp. 1806–1808, 2001.
- [23] C. M. Mate, P. C. Arnett, P. Baumgart et al., “Dynamics of contacting head-disk interfaces,” *IEEE Transactions on Magnetics*, vol. 40, no. 4, pp. 3156–3158, 2004.

- [24] S. C. Lee and A. A. Polycarpou, "Microtribodynamics of pseudo-contacting head-disk interfaces intended for 1 Tbit/in<sup>2</sup>," *IEEE Transactions on Magnetics*, vol. 41, no. 2, pp. 812–818, 2005.
- [25] B. Liu, M. S. Zhang, S. K. Yu et al., "Towards fly- and lubricant-contact recording," *Journal of Magnetism and Magnetic Materials*, vol. 320, no. 22, pp. 3183–3188, 2008.
- [26] B. Liu, M. S. Zhang, S. K. Yu et al., "Lube-surfing recording and its feasibility exploration," *IEEE Transactions on Magnetics*, vol. 45, no. 2, pp. 899–904, 2009.
- [27] W. Hua, B. Liu, S. K. Yu, and W. D. Zhou, "Contact recording review," *Microsystem Technologies-Micro-and Nanosystems-Information Storage and Processing Systems*, vol. 16, pp. 493–503, 2010.
- [28] L. Wu and F. E. Talke, "Modeling laser induced lubricant depletion in heat-assisted-magnetic recording systems using a multiple-layered disk structure," *Microsystem Technologies*, vol. 17, no. 5-7, pp. 1109–1114, 2011.
- [29] Y. S. Ma, L. Gonzaga, C. W. An, and B. Liu, "Effect of laser heating duration on lubricant depletion in heat assisted magnetic recording," *IEEE Transactions on Magnetics*, vol. 47, no. 10, pp. 3445–3448, 2011.
- [30] W. D. Zhou, Y. Zeng, B. Liu, S. K. Yu, W. Hua, and X. Y. Huang, "Evaporation of polydisperse perfluoropolyether lubricants in heat-assisted magnetic recording," *Applied Physics Express*, vol. 4, no. 9, Article ID 095201, 3 pages, 2011.
- [31] L. Wu, "Lubricant distribution and its effect on slider air bearing performance over bit patterned media disk of disk drives," *Journal of Applied Physics*, vol. 109, no. 7, Article ID 074511, 2011.
- [32] B. E. Knigge, Z. Z. Bandic, and D. Kercher, "Flying characteristics on discrete track and bit-patterned media with a thermal protrusion slider," *IEEE Transactions on Magnetics*, vol. 44, no. 11, pp. 3656–3662, 2008.
- [33] S. Shen, B. Liu, S. Yu, and H. Du, "Mechanical performance study of pattern media-based head-disk systems," *IEEE Transactions on Magnetics*, vol. 45, no. 11, pp. 5002–5005, 2009.
- [34] L. Li and D. B. Bogy, "Dynamics of air bearing sliders flying on partially planarized bit patterned media in hard disk drives," *Microsystem Technologies*, vol. 17, no. 5–7, pp. 805–812, 2011.
- [35] W. D. Zhou, B. Liu, S. K. Yu, and W. Hua, "Inert gas filled head-disk interface for future extremely high density magnetic recording," *Tribology Letters*, vol. 33, no. 3, pp. 179–186, 2009.
- [36] J. Robertson, "Requirements of ultrathin carbon coatings for magnetic storage technology," *Tribology International*, vol. 36, no. 4–6, pp. 405–415, 2003.
- [37] X. Shi, Y. H. Hu, and L. Hu, "Tetrahedral amorphous carbon (ta-C) ultra thin films for slider overcoat application," *International Journal of Modern Physics B*, vol. 16, no. 6–7, pp. 963–967, 2002.
- [38] G. G. Wang, X. P. Kuang, H. Y. Zhang et al., "Silicon nitride gradient film as the underlayer of ultra-thin tetrahedral amorphous carbon overcoat for magnetic recording slider," *Materials Chemistry and Physics*, vol. 131, pp. 127–131, 2011.
- [39] N. Yasui, H. Inaba, K. Furusawa, M. Saito, and N. Ohtake, "Characterization of head overcoat for 1 Tb/in<sup>2</sup> magnetic recording," *IEEE Transactions on Magnetics*, vol. 45, no. 2, pp. 805–809, 2009.
- [40] J. Robertson, "Ultrathin carbon coatings for magnetic storage technology," *Thin Solid Films*, vol. 383, no. 1–2, pp. 81–88, 2001.
- [41] T. Yamamoto and H. Hyodo, "Amorphous carbon overcoat for thin-film disk," *Tribology International*, vol. 36, no. 4–6, pp. 483–487, 2003.
- [42] C. Y. Chan, K. H. Lai, M. K. Fung et al., "Deposition and properties of tetrahedral amorphous carbon films prepared on magnetic hard disks," *Journal of Vacuum Science & Technology A*, vol. 19, pp. 1606–1610, 2001.
- [43] B. K. Yen, R. L. White, R. J. Waltman, C. Mathew Mate, Y. Sonobe, and B. Marchon, "Coverage and properties of a-SiNx hard disk overcoat," *Journal of Applied Physics*, vol. 93, no. 10, pp. 8704–8706, 2003.
- [44] Y. Hijazi, E. B. Svedberg, T. Heinrich, and S. Khizroev, "Comparative corrosion study of binary oxide and nitride overcoats using in-situ fluid-cell AFM," *Materials Characterization*, vol. 62, no. 1, pp. 76–80, 2011.
- [45] E. B. Svedberg and N. Shukla, "Adsorption of water on lubricated and non lubricated TiC surfaces for data storage applications," *Tribology Letters*, vol. 17, no. 4, pp. 947–951, 2004.
- [46] F. Rose, B. Marchon, V. Rawat, D. Pocker, Q. F. Xiao, and T. Iwasaki, "Ultrathin TiSiN overcoat protection layer for magnetic media," *Journal of Vacuum Science & Technology A*, vol. 29, Article ID 051502, 11 pages, 2011.
- [47] M. L. Wu, J. D. Kiely, T. Klemmer, Y. T. Hsia, and K. Howard, "Process-property relationship of boron carbide thin films by magnetron sputtering," *Thin Solid Films*, vol. 449, no. 1–2, pp. 120–124, 2004.
- [48] M. A. Samad, E. Rismani, H. Yang, S. K. Sinha, and C. S. Bhatia, "Overcoat free magnetic media for lower magnetic spacing and improved tribological properties for higher areal densities," *Tribology Letters*, vol. 43, pp. 247–256, 2011.
- [49] E. Rismani, S. K. Sinha, H. Yang, and C. S. Bhatia, "Effect of pretreatment of Si interlayer by energetic C+ ions on the improved nanotribological properties of magnetic head overcoat," *Journal of Applied Physics*, vol. 111, Article ID 084902, 10 pages, 2012.
- [50] X. C. Guo, B. Knigge, B. Marchon, R. J. Waltman, M. Carter, and J. Burns, "Multidentate functionalized lubricant for ultralow head/disk spacing in a disk drive," *Journal of Applied Physics*, vol. 100, no. 4, Article ID 044306, 2006.
- [51] X. C. Guo, B. Marchon, R. H. Wang et al., "A multidentate lubricant for use in hard disk drives at sub-nanometer thickness," *Journal of Applied Physics*, vol. 111, Article ID 024503, 7 pages, 2012.
- [52] D. Gonzalez, V. Nayak, B. Marchon, R. Payne, D. Crump, and P. Dennig, "The dynamic coupling of the slider to the disk surface and its relevance to take-off height," *IEEE Transactions on Magnetics*, vol. 37, no. 4, pp. 1839–1841, 2001.
- [53] Z. Jiang, M. M. Yang, M. Sullivan, J. L. Chao, and M. Russak, "Effect of micro-waviness and design of landing zones with a glide avalanche below 0.5μ" for conventional pico sliders," *IEEE Transactions on Magnetics*, vol. 35, no. 5, pp. 2370–2372, 1999.
- [54] B. Marchon, D. Kuo, S. Lee, J. Gui, and G. C. Rauch, "Glide avalanche prediction from surface topography," *Transactions of the ASME Journal of Tribology*, vol. 118, no. 3, pp. 644–650, 1996.
- [55] Q. Dai, U. Nayak, D. Margulies et al., "Tribological issues in perpendicular recording media," *Tribology Letters*, vol. 26, no. 1, pp. 1–9, 2007.
- [56] M. F. Toney, C. M. Mate, and K. A. Leach, "Roughness of molecularly thin perfluoropolyether polymer films," *Applied Physics Letters*, vol. 77, no. 20, pp. 3296–3298, 2000.
- [57] R. Pit, B. Marchon, S. Meeks, and V. Velidandla, "Formation of lubricant "moguls" at the head/disk interface," *Tribology Letters*, vol. 10, no. 3, pp. 133–142, 2001.

- [58] X. Ma, H. Tang, M. Stirniman, and J. Gui, "Lubricant thickness modulation induced by head-disk dynamic interactions," *IEEE Transactions on Magnetics*, vol. 38, no. 1, pp. 112–117, 2002.
- [59] Q. Dai, F. Hendriks, and B. Marchon, "Modeling the washboard effect at the head/disk interface," *Journal of Applied Physics*, vol. 96, no. 1, pp. 696–703, 2004.
- [60] I. Takekuma, H. Nemoto, H. Matsumoto et al., "Capped L1(0)-ordered FePt granular media with reduced surface roughness," *Journal of Applied Physics*, vol. 111, Article ID 07B708, 3 pages, 2012.
- [61] N. Wang and K. Komvopoulos, "Thermal stability of ultrathin amorphous carbon films for energy-assisted magnetic recording," *IEEE Transactions on Magnetics*, vol. 47, pp. 2277–2282, 2011.
- [62] N. Tagawa, H. Tani, and K. Ueda, "Experimental investigation of local temperature increase in disk surfaces of hard disk drives due to laser heating during thermally assisted magnetic recording," *Tribology Letters*, vol. 44, pp. 81–87, 2011.
- [63] N. Tagawa, H. Andoh, and H. Tani, "Study on lubricant depletion induced by laser heating in thermally assisted magnetic recording systems: effect of lubricant thickness and bonding ratio," *Tribology Letters*, vol. 37, no. 2, pp. 411–418, 2010.
- [64] C. Choi, Y. Yoon, D. Hong, Y. Oh, F. E. Talke, and S. Jin, "Planarization of patterned magnetic recording media to enable head flyability," *Microsystem Technologies*, vol. 17, pp. 395–402, 2011.
- [65] H. Li and F. E. Talke, "Numerical simulation of the head/disk interface for bit patterned media," *IEEE Transactions on Magnetics*, vol. 45, no. 11, pp. 4984–4989, 2009.

## Research Article

# A Correlative Defect Analyzer Combining Glide Test with Atomic Force Microscope

Jizhong He<sup>1,2</sup>

<sup>1</sup> Institute of Engineering, College of Engineering, Peking University, Nanjing, Jiangsu 210012, China

<sup>2</sup> MicroFocus Technologies, Inc., Wuxi, Jiangsu 214125, China

Correspondence should be addressed to Jizhong He; [jz.he@ufocustech.com](mailto:jz.he@ufocustech.com)

Received 2 January 2013; Accepted 11 February 2013

Academic Editor: Tom Karis

Copyright © 2013 Jizhong He. This is an open access article distributed under the Creative Commons Attribution License, which permits unrestricted use, distribution, and reproduction in any medium, provided the original work is properly cited.

We have developed a novel instrument combining a glide tester with an Atomic Force Microscope (AFM) for hard disk drive (HDD) media defect test and analysis. The sample stays on the same test spindle during both glide test and AFM imaging without losing the relevant coordinates. This enables an *in situ* evaluation with the high-resolution AFM of the defects detected by the glide test. The ability for the immediate follow-on AFM analysis solves the problem of relocating the defects quickly and accurately in the current workflow. The tool is furnished with other functions such as scribing, optical imaging, and head burnishing. Typical data generated from the tool are shown at the end of the paper. It is further demonstrated that novel experiments can be carried out on the platform by taking advantage of the correlative capabilities of the tool.

## 1. Introduction

Media defect control has always been a critical part of the HDD manufacturing process. It has a direct effect on the manufacturing product yield which drives the bottom line of business. In the hard disk drive, high media defect level can also cause reliability problems resulting in unforeseen economic losses. Furthermore, defect-free media is an enabler for implementing new HDD technologies. On the other hand, in order to allow high areal density recording necessary for sustained market growth, the head disk spacing in HDD has been pushed down to an extremely small margin [1–3]. As a result, even defects with very small sizes are now becoming serious performance and reliability challenges.

Defect failure analysis (DFA) which analyzes media defects on rejected disks from the production lines plays a central role in the defect process control as it finds the root causes and provides clues for corrective actions. The DFA is done separately from the line test, for example, the glide test. The normal procedure is to send a small portion of the line rejects to the DFA lab where the technicians try to relocate the defects manually, for example, with an optical microscope, before sending them off for examination with an analytical

tool such as an AFM. As the criteria for the defects of interest become smaller, manual defect relocation becomes a bigger problem. There are often cases of missed defects when doing DFA or not finding the right ones within the contaminations generated during the handling after the line test, leading to long frustrating days with negative impacts on manufacturing progress.

We have developed a tool which combines glide with AFM. We choose the glide test for its unique sensitivity to only asperities with height, as these are more likely to be in the “killer” defect category in the drive [4, 5]. On the other hand, AFM has been widely used in the medial DFA labs [6, 7]. It provides critical topographic data with the nanometer resolution, perfect for analyzing media defects of the high-density HDD media. AFM has a typical maximum scan range of  $100 \mu\text{m}$  or less. As a result, the defect has to be located right in the middle of the AFM scan range which is oftentimes proven to be difficult to do it manually. This severely restricts the access of the defect analysis with AFM.

The combination of glide with AFM solves a number of problems. It enables an immediate *in situ* analysis with the AFM after the glide test because the disk sample stays on the same chuck without losing the coordinates. It enables

finding the smaller defects more accurately. The combination also makes the automation possible resulting in orders of magnitude faster throughput for media DFA. We call the tool the Correlative Defect Analyzer (CDA) because multiple tests or analyses are integrated in a single tool to perform on the same correlated defects.

## 2. Design and Construction

The concept of combining AFM with glide is not new. There was at least one attempt by one of the HDD companies where an AFM module was added to an existing glide tester. No specific technical details are known to the author, but there were reported problems of vibration and weak algorithm, resulting in low AFM image quality and missed defects. (Private communication with relevant engineers familiar with the tool; no commercial product was ever released to the general market.)

The CDA tool described in the paper is designed from the ground up. It consists of four major functional blocks; see Figure 1. A spindle is mounted on a plate secured to a granite base by a pair of high rigid precision linear guides. A high precision ball screw drives the stage in the X direction as the X-stage; see part A of Figure 1. The ball screw provides a stiffness of  $15 \text{ N}/\mu\text{m}$ , while the guides secure the lateral movement with a stiffness better than  $100 \text{ N}/\mu\text{m}$ . The high stiffness is necessary to control the spindle vibration at high RPM. The granite is chosen for its unique vibration damping characteristics. The AFM is mounted on a miniature ball screw stage bolted on a vertical granite arch; see part B of Figure 1. A Z-stage is also mounted vertically on the arch. The Z-stage is comprised of a pair of linear guides, a ball screw driving mechanism, and a housing for the optics. The housing also provides an attachment plane for an automatic turret; see part C of Figure 1. The glide head mount is installed on the automatic turret along with optical objectives, a burnish head mount, and a scribe; see part D of Figure 1.

The air bearing spindle has a dual mode capable of both high speed spinning for glide test, the G mode, and high precision positioning for AFM imaging, the A mode (Chinese patent pending, 201110142434.1). In the G mode, the spindle operates with the controller set to run the RPM to a very low jitter level. In the A mode, the controller is switched to turn the spindle as a rotatory stage capable of a resolution of about 3 arc sec. After the desired location is reached, the lower part of the air support is removed so that the spindle body is pushed down by the upper air support and sits securely to the spindle housing; see Figure 2. The solid contact between the spindle shaft and the spindle housing is necessary for achieving low-noise high-resolution AFM imaging.

Care has been taken during the design phase to select the right components with matching material and functional properties in order to achieve the stringent requirements for long-term stability and high positioning repeatability. To verify the performance of the tool, we have designed experiments to measure the positioning repeatability of the stages. Here in this paper, we only show one example measurement on the X-stage. The measurement method on the other stages is similar.

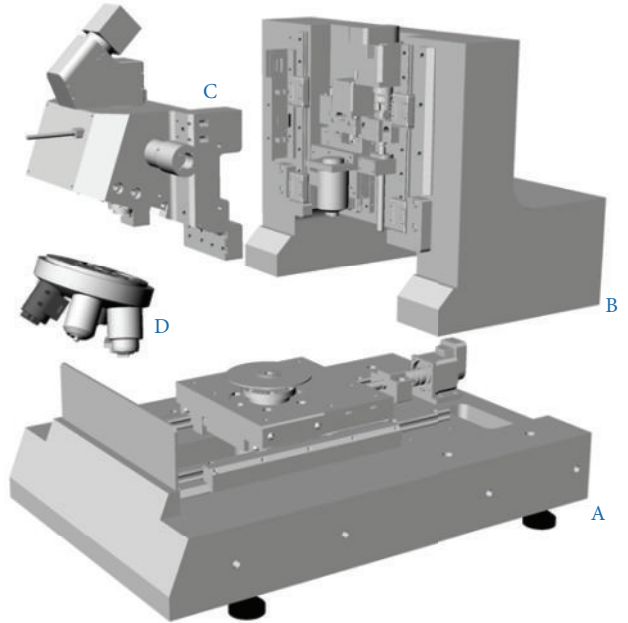


FIGURE 1: The exploded view of the CDA-101A. Part A, the granite base with the spindle mounted on the X-stage. Part B, the vertical granite arch with the AFM stage and the Z-stage. Part C, the optical housing with CCD camera and automatic turret mount. Part D, the automatic turret with glide, burnish, scribe, and optical objectives. Read the text for further detailed description.

A disk with a micrometer sized defect is clamped on a chuck driven by the X-stage. It serves as the target for measuring the repeatability with the stage repeatedly moved to a predetermined command location. A 50x objective is focused on the disk sample surface and takes the images whenever the disk is moved into the predetermined command position. Images are analyzed automatically by designated software to determine the offset of the target defect to the center. From the offset, the equivalent X-stage position is determined, where the image of the defect will be centered under the microscope.

Statistical data is shown in Figure 3 where the frequency occurrence is plotted against the position of the X-stage with a bin size of  $1 \mu\text{m}$ . At these X-stage positions, the target defect is at the exact center in the microscope view. The scatter of the defect location is attributed primarily to the minute shift in the mechanical stage every time it is moved. The two peaks in the plot indicate the two populations of the stage position. For each population, the stage is found to have very high short term repeatability with a standard deviation of about 50 nm. The reason for the two position population is because that the experiment is carried out at an elevated room temperature first and repeated after overnight cooling at another temperature, resulting in two stable positions at the two temperatures. The overnight temperature swing is about 10 deg Celsius, resulting in a drift of  $6 \mu\text{m}$ . With a characteristic length of 30 cm, this corresponds to 2 ppm/C, a very respectable figure and sufficiently low enough for current applications.

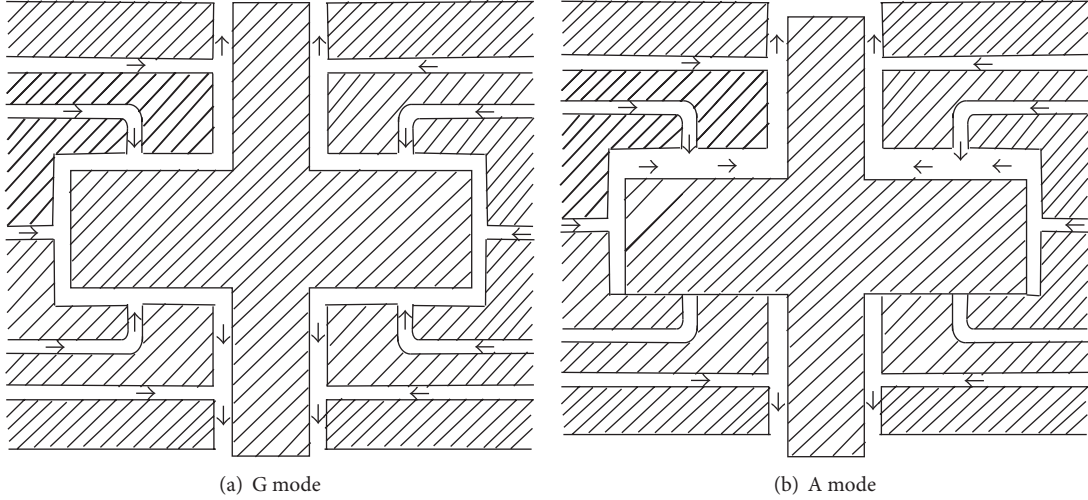


FIGURE 2: The dual mode spindle. (a) The G mode. The arrows indicate the flow direction of the air support. In the G mode, the spindle is supported both radially and axially like a conventional air bearing spindle. The spindle is under speed control circuitry to achieve high speed spinning with minimal jitter. (b) The A mode. In the A mode, the spindle is under the positioning control circuitry. It functions as a slow turning rotary table and can be clamped down for imaging when in position. To clamp down the spindle, the bottom axial air support is removed. As the result, the spindle body is pressed against the housing. The working pressure for the air spindle is 5 bars. Note the spindle shown in (b) is already in the clamped position.

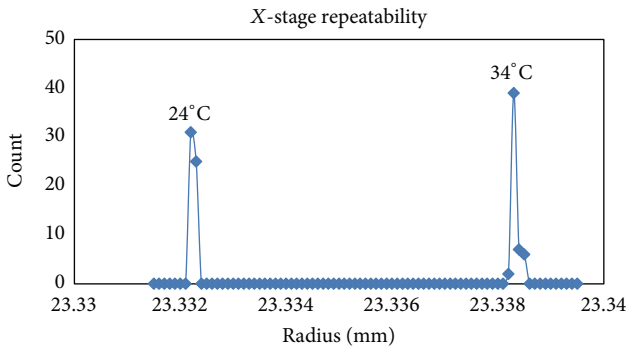


FIGURE 3: The frequency count plot of the X-stage position, with a bin size of 0.001 mm, that the X-stage must be moved to in order for the target defect to be in the middle of the microscope view. The two peaks correspond to the two highly repeatable positions of 23.332 mm and 23.338 mm due to the two stabilized room temperatures. See text for more detailed description.

The AFM scanner is an OEM component. It has a very compact body with a size of a typical microscope objective. The optical interferometry detection scheme has a published noise level of 10 pm. To realize the full potential, we mount the scanner with the approach stage on the massive granite arch to maintain high rigidity. The key is to design the system with the shortest mechanical loop possible; see Figure 4. The short mechanical loop reduces the susceptibility of the scanner to external disturbances. We carry out an effectively still scan (scan range is 1 nm) to measure the mechanical noise floor. Since the tip essentially stays at one spot on the sample, the resulting scan is a measure of the vibration the tip experiences. The data taken with the tool on a homebuilt isolation table without an acoustic enclosure and on the

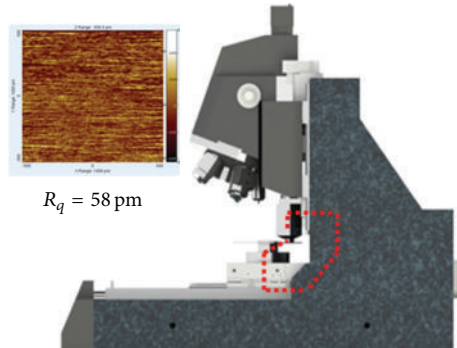


FIGURE 4: The illustration of the mechanical loop in the AFM. The mechanical loop in sequence consists of the sample, the sample chuck, the stage, the linear guides, the granite base, the granite arch, the approach stage, the scanner body, and the cantilever tip. Test image for noise floor measurement is shown in the insert. The  $z$ -scale is  $\pm 250$  pm. The RMS noise is estimated to be 58 pm.

fourth floor of a building shows the RMS noise floor to be about 60 pm. The figure of the noise floor is determined with the commercial application SPIP by using the roughness calculator (SPIP SPM Image Processor application by Image Metrology, Horsholm, Denmark; the roughness,  $S_q$ , calculation at zero scan range by definition is the direct measure of the system mechanical RMS noise floor); see the insert in Figure 4. The image shows overall random signal fluctuation. The streaking in the image is the result of the low frequency noise showing up as an artifact from the raster scan and has no significance towards the calculation of the roughness.

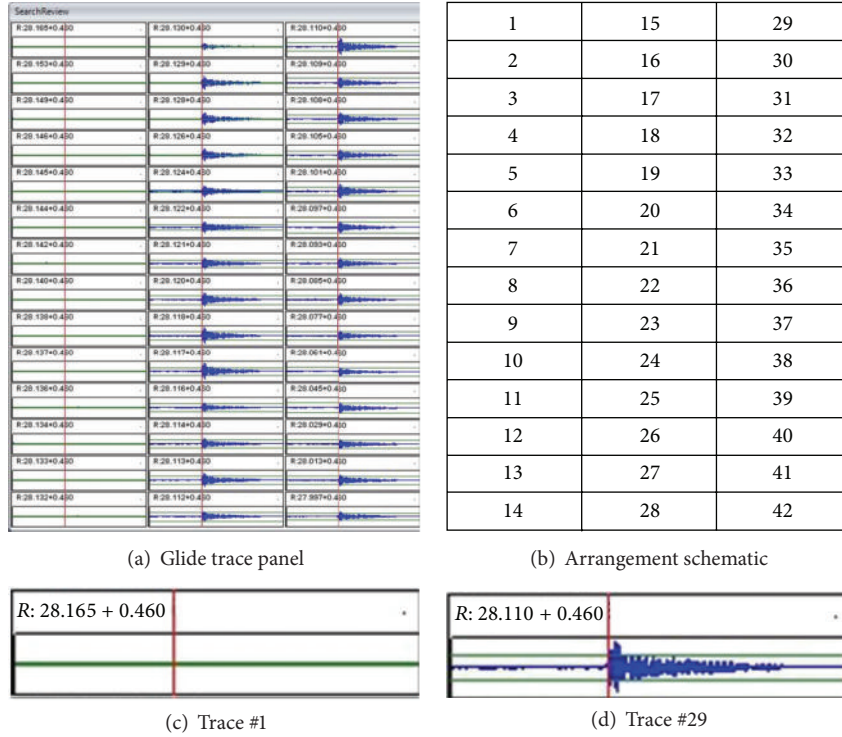


FIGURE 5: Signal analysis panel illustrating the “Glide Edge Finder” algorithm with signal at 42 tracks. The first track with the glide signal is track no. 15 with a radius of 28.130 mm. (a) Glide signal panel showing the signal at each track arranged in descending order of the radius. (b) Schematic of the track arrangement. (c) Signal trace at track no. 1 with the radius equal to 28.165 mm. No signal due to defect is present. (d) Signal trace at track no. 29 with the radius equal to 28.110 mm. Peak signal from defect is present. The starting radius with defect signal defines the edge, 28.130 mm. The value 0.460 mm is the glide head edge offset. The angle is obtained from the averaging of the peak angular position of the data, shown as the red line in (a).

### 3. Defect Indexing and Unified Coordinate System (UCS)

The width of a typical glide head is about one millimeter. Glide heads with wider sensor area can complete a full surface scan in fewer tracks. This is necessary in order to meet the throughput requirement on the production lines because every disk goes through the glide before shipping. Due to the large sensor width, the uncertainty from the glide test is about a few hundred micrometers in the radial direction and a few millimeters in the track direction. We have developed a “Glide Edge Finder” algorithm that narrows down the location of the defects to within  $5\text{ }\mu\text{m}$ . The algorithm moves the glide head track by track in very fine steps in the vicinity of the defect based on results from the prior glide test. It finds the edge of the glide head where the defect first makes contact with the glide head. This method is independent of the shape of the glide air bearing slider. However, the exact shape of a glide head does affect the glide head edge offset. As a result, every new glide head will need to be calibrated for the edge offset when first installed on the tool.

To help explain the process, we show a screen capture of a signal review panel of the CDA software for an actual defect indexing; see Figure 5. The glide signal traces are displayed for each individual tracks. The transition from the tracks with no signal to the ones with signal determines the edge. The

angular position is determined by the peak of the signal in relationship to the encoder position of the spindle. For the tracks with the glide signal, the angular positions of the peaks are collected and averaged for statistics. The algorithm has certain logic built-in to handle small defects with marginal signals.

The tool also automatically monitors the glide head position variation, for example, from the time when the glide head is replaced. We have designed an integrated glide head holder which has a set of objective lens group to image the back of the glide head for its exact position. Since it has the optical function of a 5x objective, it is called a glide objective; see Figure 6. The image of the glide head is automatically taken and analyzed by the software for correcting glide head position shift, as much as  $100\text{ }\mu\text{m}$ . from head to head. The dimple in the suspension HGA is chosen as the target for position calibration with an estimated uncertainty of about  $10\text{ }\mu\text{m}$ . We also integrate the glide channel preamplifier inside the glide objective in order to make the glide head electric connection to the preamp as short as possible in order to achieve maximum SNR.

Since there are multiple tests and sensors correlated in the same tool, there will be multiple position offsets among them to be corrected, for example, between glide and AFM, AFM and optical, AFM and scribe, and so forth. It is one of the goals for the tool to make the offset calibration as transparent

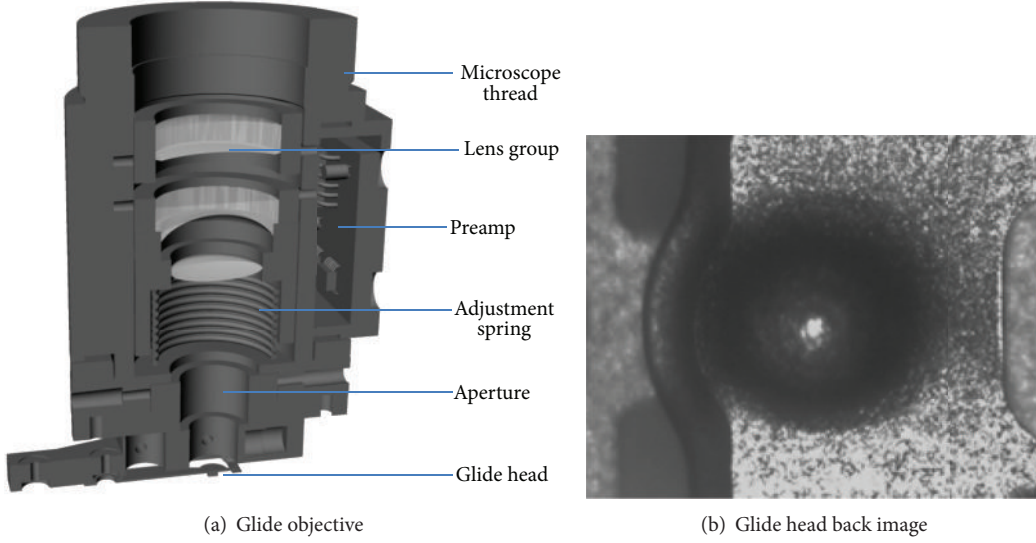


FIGURE 6: Glide objective illustration. (a) shows the internal construction of the glide objective with a 5x lens group enables the imaging on the back of the glide head. An adjustable spring enables the fine focus on the glide head. The preamplifier is integrated to the glide objective to achieve short wire length to the glide sensor. (b) The image of the back of the glide head. In the field of the view, only the center part of the glide head is visible, showing the dimple of the suspension HGA. Glide head position is calibrated against the dimple position.

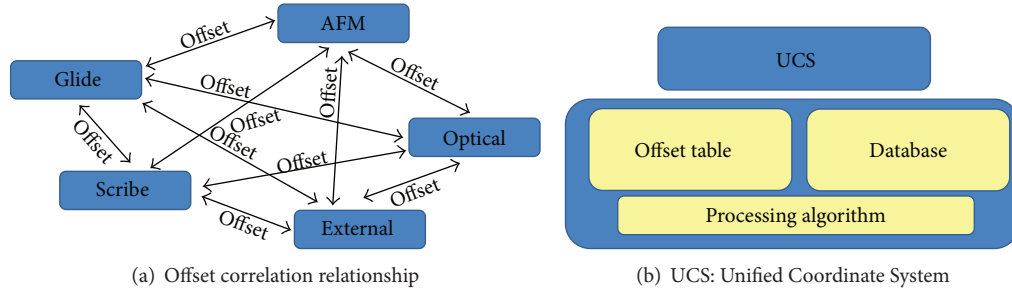


FIGURE 7: Schematic drawing showing the relationship and conversion among various coordinate systems. (a) Offset transformations that need to be handled if done individually. (b) Unified Coordinate System created to handle the transformation among the various coordinates with background algorithm and offset table. The parameters are stored in the database and undergo constant update when necessary.

as possible to the users. We have developed a Unified Coordinate System (UCS) to handle the transformation. The UCS processes the offset parameters from an offset table. The initial and current parameters are stored in the database processed by the UCS algorithm.

Within the CDA tool, there are multiple sets of coordinates: the stage or machine, the AFM, the glide, the burnish, the scribe, the optical, as well as the external and the UCS. The stage or machine coordinate system is the special one. The tool relies on the stage coordinate system to position the sample. Because of the existing offsets, there will be different stage coordinates for the same physical spot under different sensors. This creates problems for the user practically and sometimes conceptually. The UCS coordinate system is a defined one. It has a specific defined offset relationship with the various sensor coordinate systems, determined by measuring the actual offsets. Under the UCS system, there is only one set of coordinates to deal with by the user. The UCS can also interface with external coordinator systems of customized

formats. The function of the UCS is illustrated in the schematics in Figure 7.

#### 4. Example Test

We use a disk from a defunct vintage HDD teardown to test run the CDA tool. Since we have designed a very easy-to-operate user interface, the procedure to run the tool is very straightforward. The sample is loaded and automatically clamped down by a vacuum disk chuck of the conventional design but with increased suction area to meet the specific requirement of the tool. The vacuum chuck is necessary not only for the easiness of mounting samples, but also for the absence of the center obstruction. This allows a full radius range of the sample for test and analysis and also prevents the possible collision between the chuck and a sensor close to the ID radius.

Following the procedure outlined in Figure 8, the sample goes through the glide test scan first with the CDA in the

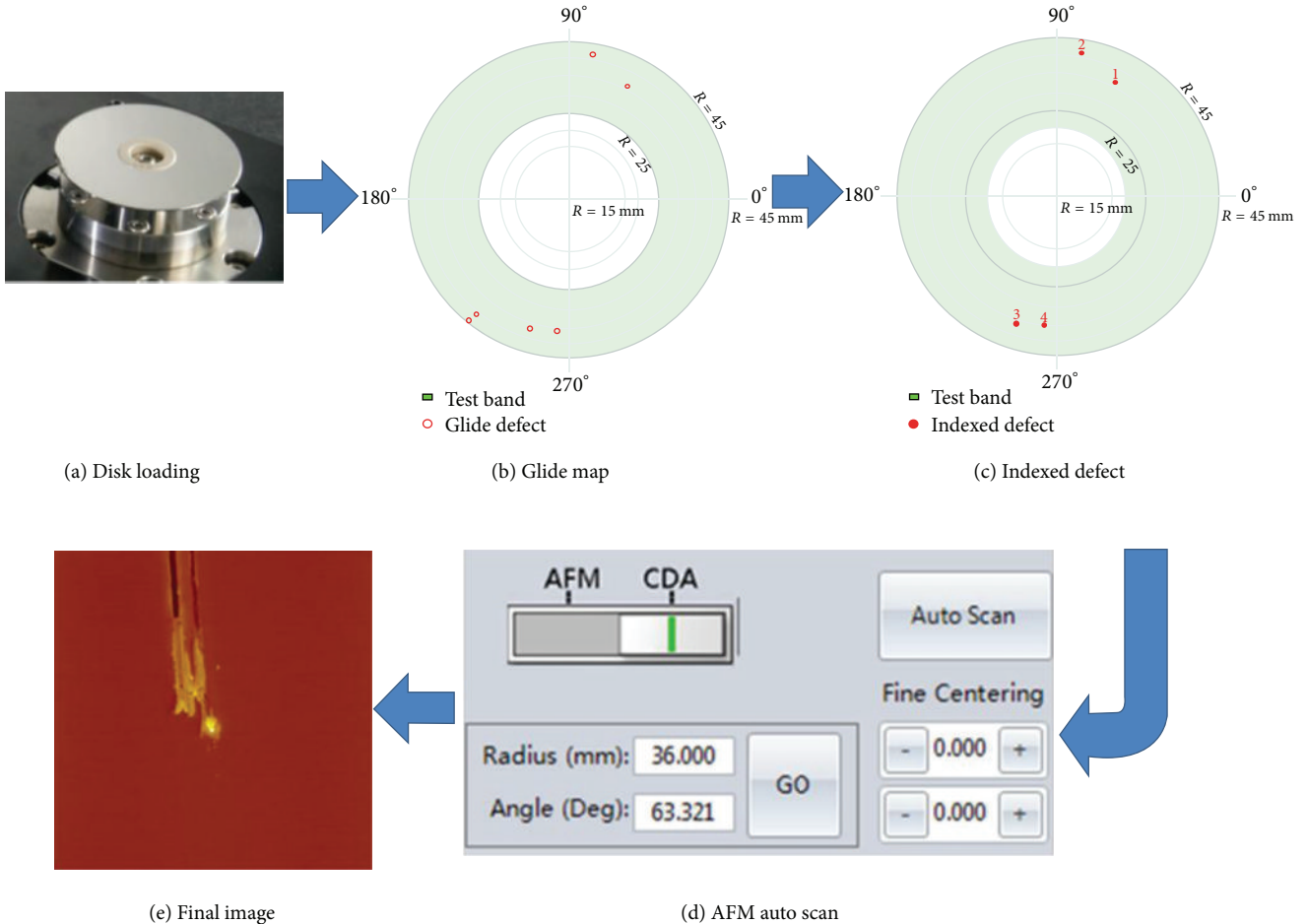


FIGURE 8: Test flow illustration, from sample load to AFM image. (a) Load the disk sample to the chuck. (b) Glide defect mapping from glide test. (c) Map of indexed defect from glide defect search. (d) CDA to AFM switch panel. A simple press of the “Auto Scan” button will start the automatic AFM scan routine. (e) Final AFM image of one of the scanned defects.

G mode. The operator then selects which one, or all, of the defects for AFM imaging. An indexing run follows on the selected defects before the tool is switched to the AFM mode or the A mode. After the indexing run, the selected defects can be relocated with an uncertainty of  $\pm 5 \mu\text{m}$ . The AFM scan can be carried out either manually or fully automatically. The automated AFM scan procedure includes sample positioning, tip approaching, scanning, tip retracting, and data saving.

The time it takes to complete the whole process depends on a number of factors such as disk form factor, glide head velocity, AFM scanning speed, and the number of scan lines. In general, the time for the initial glide test portion is about 100 sec and about 30 sec additional per defect for the indexing. AFM imaging takes about 130 sec with, for example, 256 lines and 2 Hz scan speed, which produces images with reasonable qualities. So the overall time needed from start to end could be under 10 minutes for one defect, a vast improvement over the traditional DFA involving AFM imaging.

With the precisely known positions, defects can be further analyzed with other available means in the tool such as an optical microscope. For the same defect on the sample disk,

the images of the bright field and the dark field optics and the AFM scan are shown together in Figure 9. The defect is visible in the bright field, but the dark field image shows higher contrast and also reveals a long scratch mark originating from the defect. AFM image has much high resolution, showing the defect with a lateral size of about  $3 \mu\text{m}$  and a height of about 30 nm.

Not only the same defect can be analyzed with various sensors, media process specific technology can also be applied to work on the defect correlatively. In our example test, after the initial AFM imaging, a burnish head is used to sweep the defect multiple times. To study the effect of burnishing, the defect is again imaged with the AFM for the second time. The after burnish AFM image is shown in Figure 9(d). The defect retains the same general shape compared with that before the burnish. But the defect height is reduced from 30 nm to 28 nm. We also estimate the apparent volume of the defect before and after with the SPIP software. It turns out the volume number from the software actually increases slightly from  $0.080 \mu\text{m}^3$  to  $0.082 \mu\text{m}^3$ . We conclude within the experiment error, there is no change in defect volume due to the burnish head sweep. Rather, the contamination on the

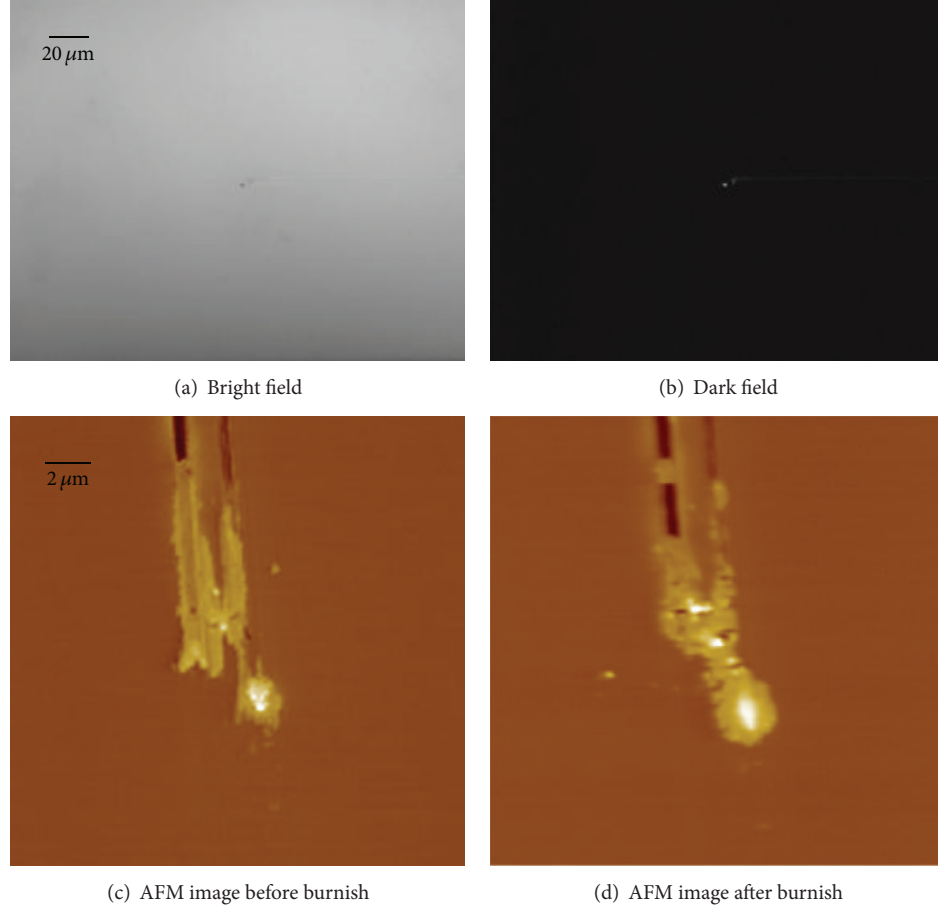


FIGURE 9: Correlated images of a media defect from a teardown disk sample. (a) Bright field image. The defect is very small but can be seen as speck of dark spot in the center of the image. (b) Dark field image. The defect is more visible and a scratch is also revealed against the dark background. (c) AFM images before the burnish sweeps. (d) AFM images after the burnish sweeps.

defect is redistributed. Further more elaborate experiment can be designed and carried out in order to obtain more concrete result on the burnish effect on defects.

## 5. Conclusion

We have demonstrated a unique tool, combining the glide with the AFM, which can be used to drastically speed up the defect failure analysis process. By performing the AFM analysis in situ, the accuracy of defect relocation and identification is guaranteed. The precision defect indexing algorithm is shown to be robust. High mechanical precision is achieved with the careful selection of components during the design phase. Coupled with the sophisticated software algorithm, a successful correlated defect analysis and a high-resolution low-noise AFM imaging have been demonstrated. With the transparent UCS coordinate system, the users are free from the burden of performing tedious coordinate transformations among the various tests available in the tool. A simple experiment of using the AFM to study the effect of the burnish on the defect shows the advantage of correlative test and analysis. Because of the open frame design and the general layout of the CDA tool, additional processes can be

considered for integration into the tool. This will open up new ways of conducting test and analysis by combining various tools in one single unit correlative.

## References

- [1] B. Marchon and T. Olson, "Magnetic spacing trends: from LMR to PMR and beyond," *IEEE Transactions on Magnetics*, vol. 45, no. 10, pp. 3608–3611, 2009.
- [2] W. Song, A. Ovcharenko, M. Yang, H. Zheng, and F. E. Talke, "Contact between a thermal flying height control slider and a disk asperity," *Microsystem Technologies*, vol. 18, pp. 1549–1557, 2012.
- [3] V. Sharma, S. H. Kim, and S. H. Choa, "Head and media design considerations for reducing thermal asperity," *Tribology International*, vol. 34, no. 5, pp. 307–314, 2001.
- [4] J. He, G. Sheng, J. Hopkins, and S. Duan, "Head and media instantaneous contact friction measurement and glide test," *IEEE Transactions on Magnetics*, vol. 46, no. 10, pp. 3767–3771, 2010.
- [5] H.-L. Leo and G. B. Sinclair, "So how hard does a head hit a disk?" *IEEE Transactions on Magnetics*, vol. 27, pp. 5154–5156, 1991.

- [6] Z. W. Zhong and S. H. Gee, "Failure analysis of ultrasonic pitting and carbon voids on magnetic recording disks," *Ceramics International Journal*, vol. 30, pp. 1619–1622, 2004.
- [7] J. Windeln, C. Bram, H. L. Eckes et al., "Applied surface analysis in magnetic storage technology," *Applied Surface Science*, vol. 179, no. 1–4, pp. 167–180, 2001.

## Research Article

# Atomistic Frictional Properties of the C(100)2x1-H Surface

**Paul M. Jones,<sup>1</sup> Huan Tang,<sup>1</sup> Yiao-Tee Hsia,<sup>2</sup> Xiaoping Yan,<sup>1</sup> James D. Kiely,<sup>3</sup> Junwei Huang,<sup>1</sup> Christopher Platt,<sup>1</sup> Xiaoding Ma,<sup>1</sup> Michael Stirnimann,<sup>1</sup> and Lang Dinh<sup>1</sup>**

<sup>1</sup> Seagate Technology LLC, 40710 Kato Road, Fremont, CA 94538, USA

<sup>2</sup> Western Digital Corporation, 5863 Rue Ferrari, San Jose, CA 95138, USA

<sup>3</sup> Seagate Technology LLC, Recording Heads Operations, 7801 Computer Avenue South, Bloomington, MN 55435, USA

Correspondence should be addressed to Paul M. Jones; paul.m.jones@seagate.com

Received 3 August 2012; Accepted 5 November 2012

Academic Editor: Bruno Marchon

Copyright © 2013 Paul M. Jones et al. This is an open access article distributed under the Creative Commons Attribution License, which permits unrestricted use, distribution, and reproduction in any medium, provided the original work is properly cited.

Density functional theory- (DFT-) based ab initio calculations were used to investigate the surface-to-surface interaction and frictional behavior of two hydrogenated C(100) dimer surfaces. A monolayer of hydrogen atoms was applied to the fully relaxed C(100)2x1 surface having rows of C=C dimers with a bond length of 1.39 Å. The obtained C(100)2x1-H surfaces (C–H bond length 1.15 Å) were placed in a large vacuum space and translated toward each other. A cohesive state at a surface separation of 4.32 Å that is stabilized by approximately 0.42 eV was observed. An increase in the charge separation in the surface dimer was calculated at this separation having a 0.04 e transfer from the hydrogen atom to the carbon atom. The Mayer bond orders were calculated for the C–C and C–H bonds and were found to be 0.962 and 0.947, respectively. σ C–H bonds did not change substantially from the fully separated state. A significant decrease in the electron density difference between the hydrogen atoms on opposite surfaces was seen and assigned to the effects of Pauli repulsion. The surfaces were translated relative to each other in the (100) plane, and the friction force was obtained as a function of slab spacing, which yielded a 0.157 coefficient of friction.

## 1. Introduction

Carbon-based surface films are now ubiquitous as frictional barriers that lower the wear rates of interacting bodies. They have found extensive use within the information storage industry as films for protecting both the hard disk surface and the sensitive read-write transducers from damage due to friction during incremental and in some instances purposeful head-to-disk contact [1, 2]. Because of this industrial importance, a rich and extensive literature exists of both theoretical and experimental studies probing the fundamental properties of these complicated and diverse surface films [3, 4]. Within the range of these studies single crystal diamond surfaces have been extensively employed as models of the more important larger-scale industrial surfaces. Insight gained from these studies has helped the community understand surface energetic processes, including the recent manifestation of super lubricity of hydrogen-covered surfaces [5, 6].

Carbon films deposited under energetic conditions assume complicated amorphous structures, which depend on

the exact conditions of deposition. Specifically, the extent of surface wear protection has been attributed to film properties that can be tailored through the manipulation of deposition parameters, precursor materials, and postdeposition processing, the combination of which can result in films ranging from “diamond-like” to softer films. In most instances a highly dense, diamond-like film is sought [3]. One of the principal metrics used to predict this attribute is the amount of tetrahedrally bound carbon-to-carbon atoms contained within the film. This important metric is found to correlate to many important mechanical and electronic properties, including film hardness, density, and optical gap [7, 8].

Recently high quality hydrogenated diamond surfaces have been proposed for use as cathode materials where their negative electron (NEA) affinity makes them a highly effective and robust material [9–11]. Previous ab initio theoretical studies have elucidated the NEA mechanism as due to the strong bonding of hydrogen to the surface π C=C bonds on the reconstructed diamond surface [12, 13]. It is believed that these surface electronic states are also observed in the super

lubricious state between two hydrogen-covered diamond surfaces [6, 14]. The mechanism for the marked decrease in interfacial friction on hydrogenated carbon surfaces has been further elucidated with surface spectroscopy and tight-binding quantum mechanical methods [15] showing that the bonded hydrogen atom passivates the carbon dangling bonds at the surface, thereby decreasing the adhesive interaction between surfaces [16]. Fluorination of these surfaces has also been explored in an effort to further reduce the coefficient of friction (COF); in particular it was noted that the significant accumulated negative charge on the surface fluorine atom and its tight surface structure, due to strong lateral interactions, lead to a strong repulsive force between interacting surfaces (larger than when hydrogen terminated) [17]. This decrease in friction between interacting surfaces can have far ranging industrial and environmental importance [5, 18, 19].

The frictional properties of diamond and other crystalline surfaces have been probed with both classical methods and ab initio-based calculations [6, 14, 20–22]. Typically, a slab model of the interacting surface is created that incorporates not only the crystalline features of the surface facet under investigation but also enough material bulk to accurately model the desired properties while remaining computationally tractable. Classical methods usually entail solving Newton's equations of motion under time-dependent conditions and allowing the use of very large material models that has been extensively and profitably applied to the hydrogenated diamond surfaces by Harrison and coworkers [20, 23]. The subject of this report is the application of density functional theory- (DFT-) based ab initio calculations to the interaction of hydrogenated C(100)2x1 surfaces by probing the electronic and bonding structure changes during the frictional interaction of these surfaces. The main thrust of this work will then be the movement of electronic charge during the surface-to-surface interaction and the nature of the commensurate repulsive state between the surfaces.

## 2. C(100)2x1-H Model and Computational Method

We start our discussion of the slab model used in this calculation by first considering the relaxed (100) surface of diamond, which contains unsaturated dimers with significant carbon-carbon double bond character that has been successfully functionalized with a Diels-Adler reaction [24]. The C(100) surface is one of the high surface energy facets and is one of the growth faces of DLC surface films. Its cleavage energy is highest amongst the principal diamond surface planes, and its surface chemistry and interesting electronic structure are principal reasons for using it as the focus of our study [25, 26].

As preparation for the study of surface-to-surface interactions we assembled a C(100)2x1 slab model of the diamond surface (before hydrogenation) and calculated its relaxed geometry and electronic states (model and results are not shown as this study is focused on the hydrogenated surface). This model contained eight layers of carbon atoms (not including the dimer) in a large vacuum space that was set at forty times the layer spacing to ensure minimal effects of slab-to-slab interactions. DFT ab initio theory, as implemented in

the DMOL code [27, 28], was used to probe the electronic and geometric effects important in the interaction of surfaces. This implementation of density functional theory is a total electron calculation and does not use pseudopotentials or frozen electron cores. The three-dimensional cell structure was sampled using a  $4 \times 2 \times 1$  grid in the Monkhorst-Pack scheme (larger sampling was explored and found not to yield any important advantage). The local density approximation (LDA) of Perdew and Wang was used for the exchange-correlation interaction to make the calculation tractable [29]. We should note that density functional theory does not treat van der Waals (vdW) interactions properly. In particular, the use of the LDA approximation for the exchange-correlation interaction (which assumes the exchange and correlation are a function of the electron density at the point of evaluation only) can lead to an overestimation of binding energies. Conversely, the generalized gradient approximation or GGA (which takes into account the gradient of the electron density at the point of evaluation) frequently underestimates the binding energy and leads to a shallow or flat adsorption profile [30, 31]. Recent efforts have been made to include dispersion forces within DFT [32, 33]. The results from these efforts generally yield an increase in the cohesive energy when compared to DFT with no correction. Since, the explicit inclusion of vdW forces increases the binding energy over the GGA result, the LDA will be used in this study because we are interested in relative changes with slab spacing and offset. A numerically derived basis was used and included polarization functions. The self-consistent field (SCF) calculations were considered converged when the largest deviation between cycles was less than  $10^{-6}$  Hartree. To improve SCF convergence, charge smearing was allowed for orbitals within 0.01 Ha of the Fermi level. The geometry was considered converged based on the iterative change in bond length, energy, and force gradient ( $5.0 \times 10^{-3}$  Å,  $2 \times 10^{-5}$  Ha, and  $1 \times 10^{-2}$  Ha/Bohr, resp.). The carbon atoms in the bottom layer of this model were held fixed for all calculations while all other carbon atoms were allowed to relax. The results of this optimization clearly show the presence of the surface dimer structure with a calculated bond length of 1.39 Å, which is approximately the length of the carbon-carbon bond in  $C_2H_4$ , and are in good agreement with previous ab initio calculations that explored this surface [13].

The electronic structure of the hydrogen-covered C(100)2x1 surface has been previously explored by various authors who found that the monolayer covered surface is the most stable [13, 30]. To begin the exploration of the hydrogen interaction with the C(100)2x1 surface, the previously optimized dimer surface was saturated with hydrogen atoms and optimized as described previously. The obtained optimized (relaxed) surface is shown in Figure 1(a), which highlights the interaction of the hydrogen atoms with the surface carbon atoms. The C-H and C-C bond lengths of 1.15 Å and 1.61 Å are obtained after optimization; these lengths are similar to the bond lengths in ethane and previous calculations [13]. The electronic structure of this surface changes significantly from that observed on the clean surface. Whereas, the C(100) dimer surface density of states

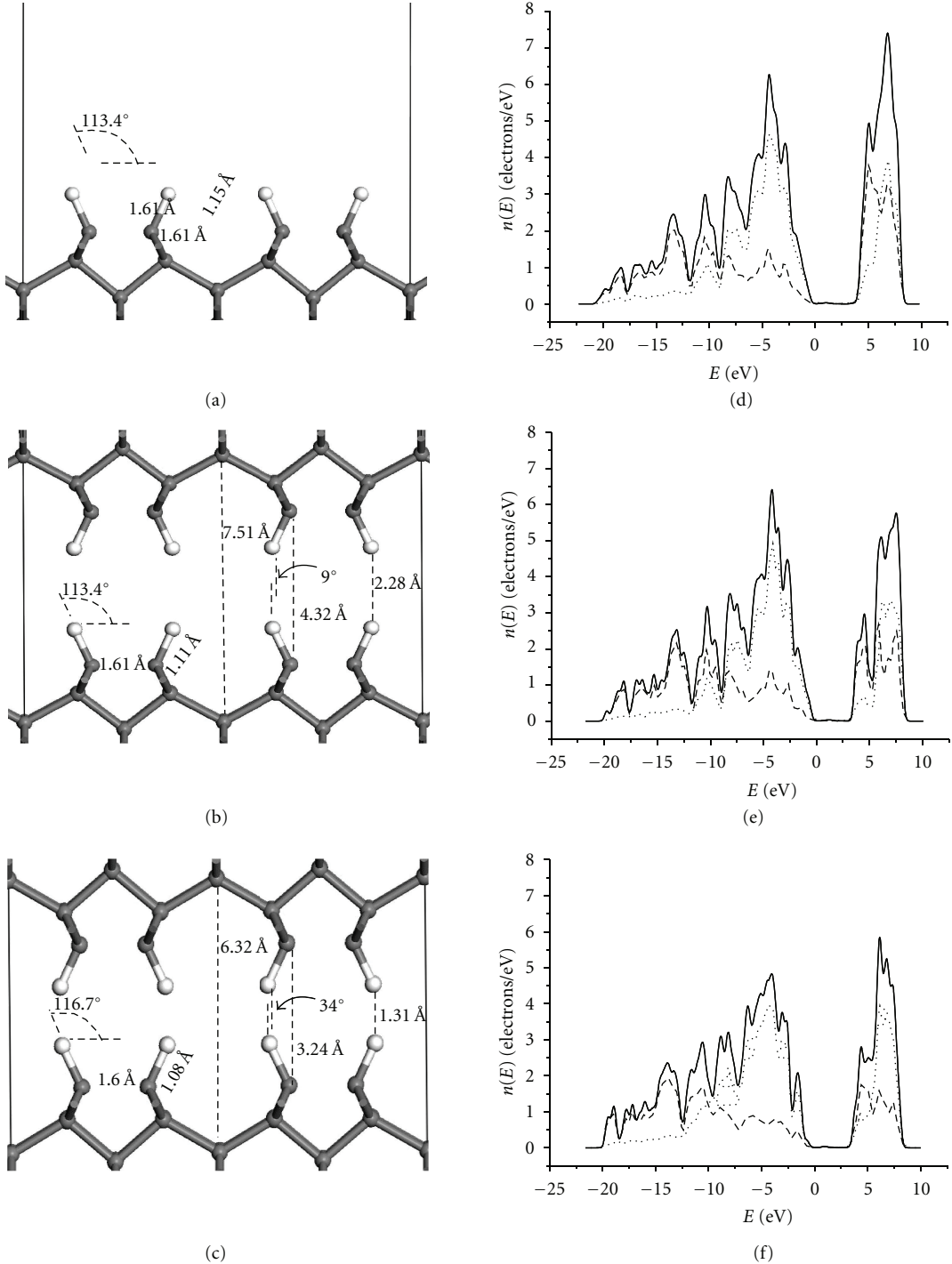


FIGURE 1: (a) Surface dimer geometry of the fully relaxed C(100)2x1-H; (b) spacing and geometry of the cohesive state between C(100)2x1-H surfaces at 4.32 Å dimer carbon-to-opposite surface dimer carbon spacing; (c) geometry of slab-to-slab repulsive state at a 3.24 Å dimer-to-dimer spacing; (d) DOS of the dimer and first carbon atom layer shown in part (a), solid line is total DOS, dashed line the s-states partial DOS and the dotted line the p-states partial DOS, VBM = 0 eV; (e) similar DOS of the cohesive state shown in part (b); (f) similar DOS of (c) the repulsive interaction between surfaces. Gray spheres represent carbon atoms and white are hydrogen atoms, in all figures.

(DOS) contains recognizable  $\pi$ ,  $\pi^*$ ,  $\sigma$ , and  $\sigma^*$  states, the monohydride surface DOS (see Figure 1(d), DOS obtained from the outer hydrogen and first two carbon atom layers) is well separated with a clear band gap of  $\sim 3.3$  eV (DFT is

known to underestimate band gaps). The  $\sigma$  C–H bonding states can be readily identified in the DOS peaking in the  $-4$  eV range measured from the valence band maximum (VBM) (see Figure 1(d)) and are due to the interaction of

the hydrogen 1s and the carbon 2p states. The conduction band is largely composed of states localized on the hydrogen layer. Maps of the difference in electron density (total density minus the density due to the separate atoms) enable the visualization of the concentration or removal of electron density and are presented in Figure 2(a) as a slice through the surface carbon-hydrogen bonds parallel to the *c* direction. An accumulation of electron density between the dimer carbon and hydrogen atoms defines the C-C and C-H bonds. The calculated Mayer bond orders, which are 0.962 and 0.942 for the two bonds, respectively, (see Table 1), further support this visualization and indicate the reduction in the  $\pi$  bond character of the dimers [34]. The calculated Mulliken charge distribution places a 0.085 e positive charge on the surface hydrogen atoms and a -0.102 e charge on the carbon atoms in the dimer (see Table 1) [35]. This charge separation at the surface yields the well-known dipolar layer observed in other similar calculations and is the mechanism behind the NEA observed on this surface. The formation of the surface dipole moment is also thought to be an important contributor to the surface reactivity, conductivity, and wetting characteristics of this surface [36]. The lowest energy electronic orbital dominantly centered on the dimer is due to the  $\sigma$  C-C bond (see Figure 2(d)). The highest occupied orbital dominantly centered on the C-H bond (shown in Figure 2(e)) is obviously composed of hydrogen 1s and C 2p components and shows that this orbital overlaps neighboring hydrogen atoms.

Thus the hydrogen-saturated C(100)2x1 surface contains a surface dipole layer whose aliphatic nature is revealed in its electronic structure. The outlined changes in this surface electronic structure from one dominated by olefinic character, and its resultant facile chemistry, to a dominantly aliphatic surface, makes further surface chemistry difficult and contributes to the known stability of this surface.

### 3. Results and Discussion

**3.1. Approach of the C(100)2x1-H Slabs.** To begin our study of the friction between two C(100)2x1-H surfaces, we have placed two of the previously described hydrogenated surfaces facing one another in a large vacuum space to minimize unwanted interactions. We have frozen the outer carbon layers in each slab and allowed all other layers, including the surface hydrogen atoms, to relax as the slabs are brought incrementally and commensurately closer together. Figure 1(b) illustrates the arrangement of the slabs and defines the distance between them as the distance between opposing dimer carbon atoms. The surface charge distribution of the widely spaced (noninteracting) slabs does not change from the single slab result (data not shown), supporting the lack of slab-to-slab interaction at these separation distances. The DOS of the slab was checked to further assure the robustness of our scheme (the utilization of large vacuum spaces). The change in total energy as the surfaces are brought incrementally together is shown in Figure 3(a). No interaction of the surfaces is calculated until they are approximately 6.5 Å apart where a net stabilization begins and increases in strength until approximately 4 Å when

the interaction becomes rapidly repulsive. The depth of the calculated stabilization at 4.32 Å is 0.42 eV (total energy of the slabs at incrementally smaller separation minus total energy of separated slabs) and is significantly larger than previous calculations of this interaction [6, 14]. However, the work of adhesion, defined as the energy to separate the two surfaces divided by the cell area (in this instance ~0.133 J/m<sup>2</sup>), compares favorably with a previous AFM study using a hydrogen-covered diamond single crystal surface and a diamond-coated tip having approximately single atom at its apex (~0.159 J/m<sup>2</sup>) and a more recent study on C(111) and C(001) surfaces [37, 38]. Interestingly, studies of interacting hydrogenated diamond surfaces using widely divergent ab initio theories, most using super cell methods along with pseudopotentials, have found a similar weakly bound state [6]. In contrast, calculations using small molecules as models of the surface interaction along with Hartree-Fock methods yield only a strong repulsive barrier [39]. The divergence in these calculated results shows the need for an adequate slab size to correctly model this weak interaction.

Thus, the compression of the C(100)2x1-H surfaces (see Figure 1(b)) results in a stabilized state at approximately 2.28 Å (hydrogen atom-to-opposing hydrogen atom) separation (or 4.32 Å carbon atom-to-opposing carbon atom in the dimers, see Figure 1(b)) and thereafter a strong interlayer repulsion.

The surface geometry of the cohesive configuration (see Figure 1(b)) changes little from the C(100)2x1-H surface. The C-H bond at 1.11 Å has contracted by approximately 0.04 Å from the free surface and correlates with the larger charge separation in the dimer in this configuration (vide infra) while the C-C bond length remains at its free slab value of 1.61 Å as does the H-C-C angle 113.4°. Interestingly, the angle between C-H bond pairs on opposite slab surfaces is approximately 9° and signals the incipient effects of slab-to-slab repulsion, especially on the C-H bond. Significant changes in the distribution of charge near the surface take place as the slabs have been incrementally brought into near contact. In this geometry, which is weakly cohesive, approximately 0.04 e (net +0.125 e) is transferred from the hydrogen atoms to the carbon atoms in the dimer (net -0.144 e), thereby increasing the charge separation and hence the surface dipole moment (see Table 1). The increased surface dipole has little effect on the peak due to the  $\sigma$  C-H states at approximately 4.5 eV below the VBM. The rest of the valence band (see Figure 1(e)) also changes little from the VB of the separated state. In contrast, the shape of the conduction band changes to a distinct two-peak structure with the lower edge of the band at approximately 3.0 eV. It is dominantly composed of empty hydrogen 1s states (see Figure 1(e)). The electron density difference maps shown in Figure 2(b) portray an increase of density between the carbon atoms in the surface dimer and an increase centered on the hydrogen atoms, which is similar to the density map of the separated slab (see Figure 2(a)). Increasing the range of the displayed density difference (see Figure 2(b) inset), however, reveals a somewhat larger increase in density centered between the dimer carbons for the stabilized configuration and a slightly

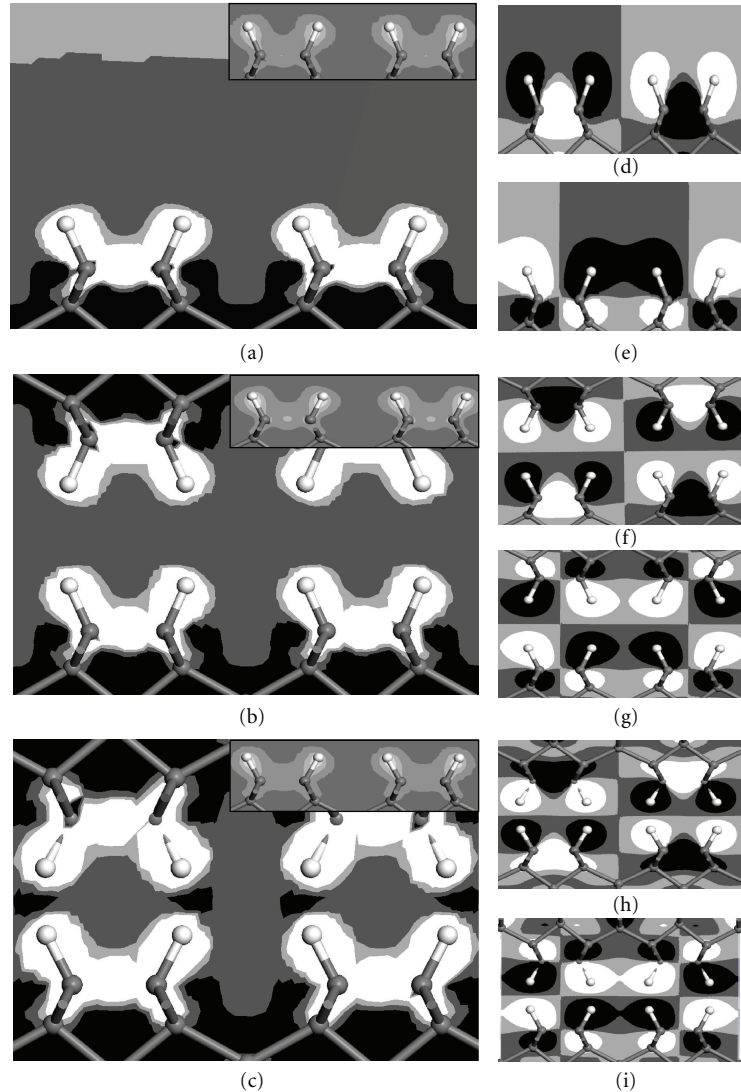


FIGURE 2: (a) Electron density difference map through the C-H bonds in the dimer parallel to the  $c$ -axis of the C(100)2x1 slab, black = (-10%) to (-5%), dark gray = (-5%) to (0%) density loss, light gray = (0%) to (5%) density gain, and white = (5%) to (10%) density gain, inset is the same map with -100% to +100% in four equal steps from density loss to gain as in part (a) and shows little density build up; however, some  $+25\% \pm 25\%$  density difference light gray areas are slightly visible between the carbon atoms in the dimer. (b) Electron density map through the C-H bonds on the upper and lower slabs dimers when at a separation with a net cohesive stabilization, electron density difference color scheme is the same as part (a); inset is map through the lower slab dimer C-H with color scheme as in inset to part (a), showing more electron density build up between the C-C atoms in the dimer than (a). (c) Electron density map through the C-H bonds on the upper and lower slab dimers at a separation having a net repulsive interaction, electron density difference color scheme is the same as part (a) black patches between opposing dimer hydrogen atoms, has negative electron density difference, and is assigned to Pauli repulsion at this separation; inset is map through the lower slab dimer C-H with color scheme as in inset to part (a), showing no electron density build up between the C-C atoms in the dimer. (d) Map of the highest occupied orbital centered on the dimer on the C(100)2x1-H surface through the C-H bonds and parallel to the  $c$ -axis, darker colors are negative phase and lighter colors the positive; steps plotted are from -0.02 to -0.01, -0.01 to 0, 0 to 0.01, and 0.01 to 0.02 electron/ $\text{\AA}^3$ ; orbital is dominantly due to the  $\sigma$  C-C bond with highest values between the carbon atoms. (e) Map of the highest occupied orbital centered on the C-H on the C(100)2x1-H surface through the C-H bonds, color scheme is the same as in part (d); orbital is dominantly due to the  $\sigma$  C-H bond with some overlap between neighboring hydrogen atoms on different dimers. (f) Similar map of the highest occupied orbital centered on the dimers on the C(100)2x1-H surface-to-surface interaction at a separation having a net cohesive stabilization, orbital is dominantly due to the  $\sigma$  C-C bond that has changed little from part (d). (g) Similar map of the highest occupied orbital centered on the C-H when slabs have net cohesive stabilization; orbital is dominantly due to the  $\sigma$  C-H bond with no overlap between neighboring hydrogen atoms on different dimers. (h) Similar map of the highest occupied orbital centered on the dimer when the slabs are experiencing a repulsive interaction; orbital is dominantly due to the  $\sigma$  C-C bond now having high orbital values moved from between the carbon atoms to beneath and outside of the C-C bond. (i) Similar map of the highest occupied orbital centered on the C-H when the interacting slabs experience a net repulsion; orbital is dominantly due to the  $\sigma$  C-H bond now with some overlap between neighboring hydrogen atoms on different dimers.

TABLE 1: The geometry, charges, and the Mayer bond order of the dimer, for the C(100)2x1-H surface, the C(100)2x1-H//C(100)2x1-H slabs interacting at a separation that is cohesive (net stabilized), and these slabs at a smaller repulsive separation.

Dimer	C(100)2x1-H slab			C(100)2x1-H//C(100)2x1-H (cohesive)			C(100)2x1-H//C(100)2x1-H (repulsive)					
	Bond length (Å)	Angle	Bond order	Charge (e)	Bond length (Å)	Angle	Bond order	Charge (e)	Bond length (Å)	Angle	Bond order	Charge (e)
C-C	1.61	na	0.963	na	1.61	na	0.962	na	1.60	na	0.933	na
C-H	1.15	na	0.942	na	1.11	na	0.947	na	1.08	na	0.933	na
H-C-C	na	113.4°	na	na	na	113.4°	na	na	na	116.7°	na	na
H-C <sub>up</sub> /H-C <sub>down</sub>	na	na	na	na	na	9°	na	na	na	34°	na	na
C	na	na	na	-0.102	-0.144	na	na	-0.144	na	na	na	-0.147
H	na	na	+0.085	+0.125	na	na	+0.125	na	na	na	na	+0.129

more density centered on the hydrogen atoms for this configuration (compare inset in Figures 2(a) and 2(b)). The orbitals centered on the dimer allow a fuller description of a potential interaction between the slabs. Figures 2(f) and 2(g) present the highest occupied level centered on the  $\sigma$  C-C and the C-H bonds, respectively. Little change can be seen in the  $\sigma$  C-C when compared to the same orbital on the separated slab in Figure 2(d). The spatial extent of the  $\sigma$  C-H orbital, shown in Figure 2(g), appears to be at least qualitatively contracted so that it no longer overlaps at neighboring hydrogen atoms on different dimers. This may be due to the previously noted increase in net positive charge on the hydrogen atom in this geometry. The Mayer bond order of the dimer C-C bond is 0.962, which is the same as for the separated slab. The C-H bond order is 0.947, a slight increase from the separate slab.

Thus, as the slabs incrementally approach one another, a shallow energy minimum is observed at 4.32 Å, which has a surface geometry similar to that calculated on the separated slab but with a slightly contracted C-H bond and an approximately 9° angle between C-H bonds on opposite surfaces. An additional transfer of charge from the hydrogen atoms to the carbon atoms takes place in the dimer. An increase in electron density between the carbon atoms in the dimer is observed along with a more subtle increase at the hydrogen atoms (compared to C(100)2x1-H). The highest occupied electronic state centered on the C-H reveals a decrease in the interdimer overlap at neighboring hydrogen atoms on the same surface, which we assign to the increased positive charge at the hydrogen atom center contracting the spatial extent of the orbital at that site.

Further compression of the layers rapidly decreases the difference in total energy and becomes highly repulsive (see Figure 3(a)). Figure 1(c) presents the geometry of a configuration along this repulsive end of the curve at an interslab distance of 3.24 Å (between opposite dimer carbons) as an illustrative example. The dimer C-C bond length at 1.60 Å has changed little; in contrast the C-H bond has further contracted to approximately 1.08 Å. Perhaps more important than these bond length changes are the changes in the overall dimer geometry on the surface. Of these, the most dramatic is the large increase in the angle between the opposing C-H bonds (see Figure 1(c) and Table 1) to approximately 34° and shows the effect on the C-H bond due to the compression of the surfaces. This dramatic effect has been previously discussed based on molecular dynamics (MD) calculations, where it was noted that at higher compression the opposing hydrogen atoms in the C-H bonds “revolve” around each other to minimize their contact [40]. A significant bending of the C-H bond in the dimer toward the slab surface (H-C-C angle increases to 116.7°, see Figure 1(c) and Table 1) takes place at this slab-to-slab separation. The Mulliken charges have changed little (see Table 1). In contrast, the Mayer bond orders for the dimer C-C and C-H bonds have significantly decreased to 0.945 and 0.933, respectively, and indicate the weakening of these surface bonds due to the repulsion under the compression of the surfaces. A change in the electron density difference is also observed at this geometry. The inset in Figure 2(c) presents the difference map for this slab-to-slab spacing; it reveals no increase in density along the

C-C bond thus supporting its lower bond order. Figure 2(c) shows the density difference, in a more sensitive range, where a large decrease in the electron density (black region) in the vacuum space approximately between the hydrogen atoms on opposite slab surfaces is observed. We assign this large decrease, which is not observed in either of the other geometries (compare Figures 2(a) and 2(b)), to the effects of repulsion from the Pauli principle and must be centered on or near the hydrogen atoms of the dimer. The highest occupied surface state centered on the C-C dimer is shown in Figure 2(h) where the effects of the bending of the C-H bond are especially evident. The displacement of high orbital values from the center of the C-C bond of the dimer to between the dimer carbon and the first carbon layer (compare Figures 2(d) and 2(f)), decreases the electron density between these carbon atoms. This decrease in electronic density between the carbon atom centers weakens the dimer bond and thereby decreases its bond order. We note that due to the noted “bending” of the C-H bond toward the surface the overlap of similarly phased orbitals at neighboring hydrogen atoms in the highest occupied state centered on the C-H bond in this slab-to-slab geometry is increased when compared to the stabilized configuration (see Figure 2(i)).

Thus, for slab-to-slab spacing smaller than ~4.3 Å a strong repulsion between the slabs is expected. The effect of the small spacing is to deform the geometry of the dimer by increasing the angle between pairs of upper and lower H-C bonds, indicating that the hydrogen atom pairs on opposite surfaces “revolve” around one another, while the C-H bond angle is bent toward the slab surface. These geometric changes are due to the effects of Pauli repulsion, which is clearly observed as a depleted electron density zone in the vacuum space between opposing hydrogen atom pairs, weakening the bonding within the dimer by removing electron density from the  $\sigma$  C-C and C-H bonds strength.

**3.2. Slab-to-Slab Atomistic Friction.** To investigate the changes of friction with sliding we have adopted the theory and procedure of Zhong and Tománek and have translated the slabs relative to each other in the (100) plane at different interslab spacing, while relaxing the entire structure (subject to the constraints previously discussed) at each step [41]. We assume the entire two-slab structure is at equilibrium at each step in its translation across the surface by noting that the range of relative motion is small. Figure 3(b) assembles the resulting family of interaction curves obtained by this procedure. Each curve in this figure was obtained at a fixed spacing and interfacial load. As a prelude to the analysis of these curves we explored many of them over a longer sliding distance to convince ourselves that they are indeed periodic (with period ~2.5 Å) and have no more structure than is shown in Figure 3(b). Thus all curves were obtained over approximately the same relative range, which encompassed the maximum and minimum of the interaction curve and therefore represents the full range of the surface potential corrugation. In general, the curves pass through a maximum as the hydrogen atoms on opposing surfaces are aligned. The depth (energy maximum to minimum) of the curves increases with load and is reflective of the increasing

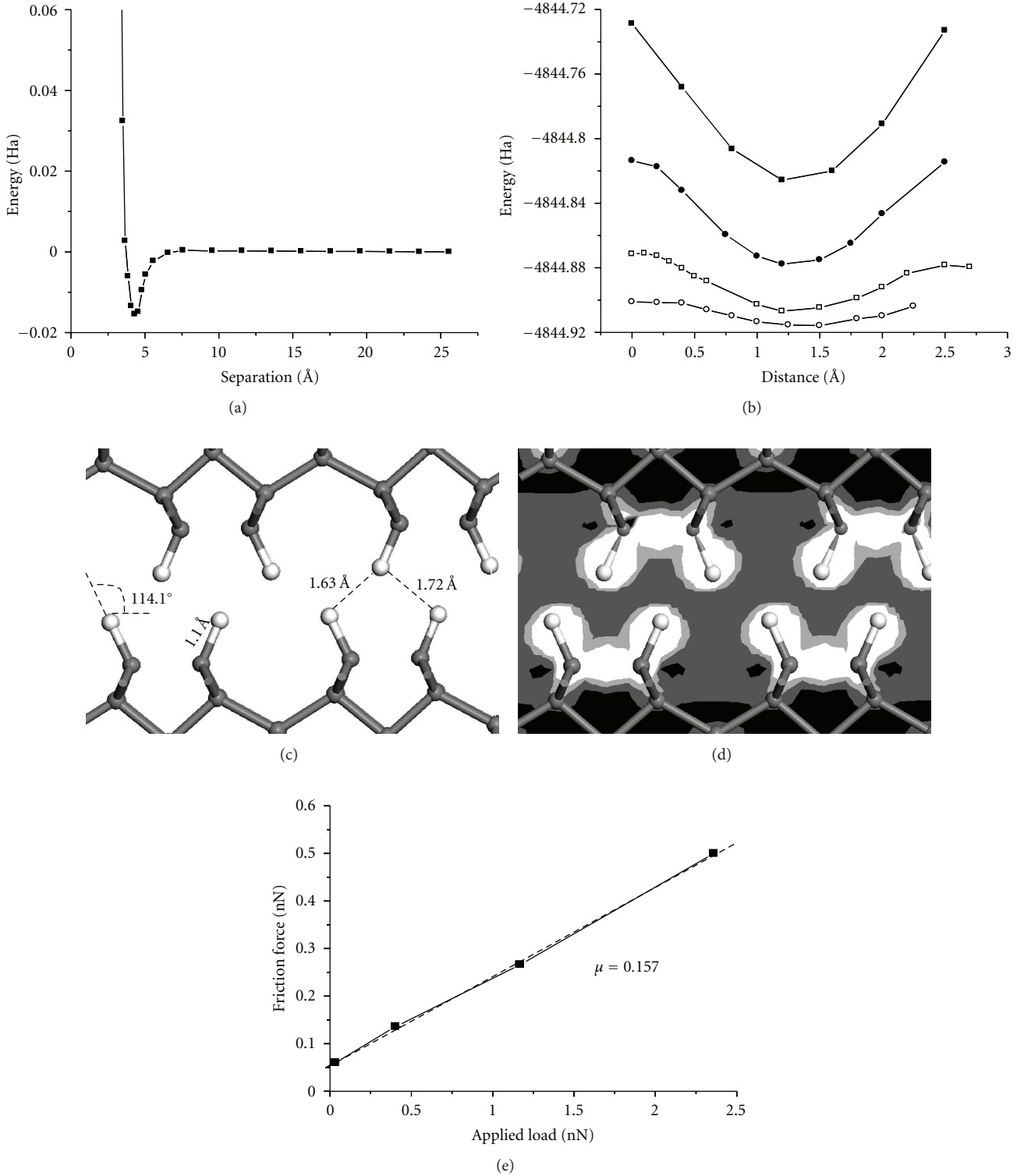


FIGURE 3: (a) The total energy difference (with separated configuration at 25 Å) of two C(100)2x1-H surfaces with incrementally decreasing separation, a cohesive interaction at approximately 4.5 Å separation is observed with increasingly repulsive interactions at smaller spacing (distance as measured between the carbon atoms of the dimer between upper and lower surfaces). (b) Total energy of interaction of C(100)2x1-H surfaces at fixed distance and load while surfaces are slid in the (100) plane: open circle load is 0.0326 nN, open square load is 0.4034 nN, solid circle load is 1.1694 nN, and solid square load is 2.3590 nN. (c) Geometry of interacting surfaces at 3.24 Å (Figure 1(c)) spacing when translated ~1.2 nm into relative minima, showing relative positions of opposing hydrogen atoms. (d) Electron density difference map of part (c) coloration as described in Figure 2(c). (e) Friction force derived from part (b) as a function of applied load, coefficient of friction is  $\mu = 0.157$ .

Pauli repulsion as the slabs are brought closer together. Similarly, the decreasing value of the total energy, observed as an incremental offset in the energy as more load is applied, reflects this same repulsion mechanism. We will use the previously discussed high-energy state at 2.36 nN loading (Figure 3(b)) to illustrate the effect of sliding on the geometry of the layers in the slab. Note that a significant relative stabilization is encountered as the slabs are slid from this position, at a fixed spacing, by approximately 1.2 Å. Figure 3(c) gives the geometry of this configuration. In contrast to the fully aligned and highly destabilized geometry, the geometry of this state brings the surface hydrogen atoms on each slab into positions approximately half way between those on the opposite face. In this geometry the C-H bond lengthens to 1.10 Å, and the H-C-C angle decreases to 114.1°. The net increase in stabilization is therefore highly correlated to the significant changes in this angle and must reflect the change in repulsion between the surfaces. It is well known that the net overlap of the hydrogen 1s orbital and the carbon sp<sup>3</sup> hybrid orbital rapidly decreases as this angle increases, thus significant changes in the angle directly contribute to the calculated changes in total energy [42]. The electron density deformation maps of this geometry, shown in Figure 3(d), support this view. In contrast to the repulsive electron density difference observed between hydrogen atoms in the aligned geometry, the offset of the C-H bonds and the hydrogen atoms on opposite faces decreases this effect and allows the small relaxation of the H-C-C angle toward the equilibrium geometry on the free C(100)2x1-H surface (113.4°). In general, as the slabs are translated at fixed spacing, the noted and discussed interactions abate and then build with an approximate 2.5 Å period due to the hydrogen-to-hydrogen spacing on the surface.

The frictional force acting on the sliding surface is obtained from Figure 3(b) using Zhong's method [41]. Plotting this force versus the normal load we obtain a coefficient of friction of approximately 0.157 (see Figure 3(e)). This value is in surprising agreement with an MD calculation using a bond order potential method [43] and with AFM measurements on similar surfaces [2, 39], but is smaller than that obtained using large-scale MD simulations of Scanning Force Microscope (SFM) experiments that included an MD model of a spherical tip [44]. This range of agreement is understandable as friction at the level modeled here is velocity dependent; in contrast the present study is assumed at equilibrium at each incremental step of the opposing surfaces. Nonetheless, we note that the present results show that the friction force is linear over the load range studied, in contrast to force-field based results that are nonlinear albeit over a wider load range [20]. A residual friction force is obtained if the friction force versus load curve is extrapolated to zero in Figure 3(e) [20, 39]. However, we cannot discount a nonlinear behavior in the friction force below the range of loads probed in this report.

Regarding the size of the present coefficient of friction and its relationship to previous results, it is clear that they are on the lower end. Perry and Harrison found  $\mu \sim 0.2$ ; though they probed a larger load range [40], and the results of an effort using DFT with pseudopotentials, plane waves, and

GGA did not reveal the presence of an energy minimum at any slab-to-slab spacing. Additionally, their calculated value of  $\mu \sim 0.05$  was noted as "too low" [6]. Another study that used small discrete models for the hydrogenated surface along with a Hartree-Fock method and the split valence basis sets found no energy minimum as the two-slab models approached, and the authors obtained a friction coefficient of  $\mu \sim 0.22$  with apparently no residual friction force at zero load [39].

Regarding the residual friction force at zero load, popular models of adhesive microscopic friction, the JKR and DMT for example, that are routinely applied to AFM-based friction measurements each exhibit a nonzero contact area at zero load and a minimum normal load which exhibits nonzero contact [45]. Each of these nanoscale contact formulations include attractive forces (JKR short-range adhesion and DMT longer-range surface force) that are missing in the hard-wall repulsion used to derive Hertz's model. It is believed that similar adhesive forces are the source of the nonzero friction at zero load.

#### 4. Conclusions

DFT calculations using the LDA formalism reveal a cohesive state between two C(100)2x1 surfaces passivated with a monolayer of hydrogen (at a spacing of 4.32 Å). This state is characterized by strong charge transfer from the surface hydrogen atoms to the first layer of carbon atoms in the slab and a relative strengthening of the surface C-C of the dimer. No change in the H-C-C bond angle is observed due to the lack of repulsion at this slab-to-slab spacing. No significant change in the highest occupied orbital centered on the C-H bond is observed. In fact, this state appears as the superposition of the same states on the single C(100)2x1-H surface and indicates that no direct surface-to-surface chemical bonding interaction takes place. In contrast, the repulsive interaction of the two slabs at spacing smaller than the cohesive state is characterized by significant changes in the dimer geometry that can be assigned to the influence of repulsion at this close proximity. Visualization of the effect of repulsion on the electron density is facilitated using electron density difference maps that specifically show a large decrease in density between the hydrogen atoms on opposite surfaces. Slabs set at increasingly close proximity were translated in the (100) plane with the total energy going through maxima and minima when surface hydrogen atoms are directed toward each other and between the opposing C-H bonds, respectively. No bond breaking was observed as a consequence of these movements. The coefficient of friction ( $\mu \sim 0.157$ ) was obtained from the relationship of the calculated friction force to applied load and was found to be linear with a residual force at zero load. This residual force is assigned to the discussed cohesive state between C(100)2x1-H slabs and is consistent with pertinent theories (JKR and DMT) of nanoscale contact and friction.

Magnetic recording technology uses a rapidly evolving set of materials to obtain greater information density on the surface of the storage disk. Amongst the most important of these materials is the carbon overcoat on the storage

medium. This nanothick film protects the recorded information from environmental and mechanical degradation. Significant effort is now focused on the further densification of this surface film especially in light of the near term adoption of heat-assisted magnetic recording needed to further extend this recording technology [46]. The current study has been made as a tractable approximation to these advanced films. The C(100) surface is one of the principal growth surfaces of these COC films allowing the transferability of the principal learning from this study. The deposition of the COC takes place within a vacuum space that is likely to have a significant partial pressure of hydrogen, therefore, as these films grow under energetic conditions hydrogen is likely to saturate the surface of the finished film. Further, the C(100) is expected to be enriched at the surface and thus becomes hydrogenated. Due to the inverted dipole moment at the surface (positive end out) caused by the passivation of the dangling bonds by hydrogen and their concomitant rearrangement on the surface, a large decrease in the wetting of the surface by the widely used disk surface perfluorolubricant is anticipated [47]. This change will make it more difficult to stabilize the lubricant on the surface and keep it at the thickness required. Friction at the interface between the media COC and the read-write transducer is due to an adhesion component (modeled here) and the applied load (and obviously contains a shear component not considered in this study) [2]. There has been a large reduction in the surface roughness of each of these interacting bodies as this recording technology has progressed (now approaching near atomic smoothness  $\sim 1\text{--}3 \text{ \AA}$  average roughness). Thus, a model of asperity contact may no longer be a fully accurate model of this frictional interaction. The interaction of these surfaces at the loads used in this study do not cause damage to the surface and reinforces the fundamental role that hydrogenation plays in this result: keeping the surfaces apart at high applied loads and passivating the  $\pi$  dimer bonds on the reconstructed diamond surface with a reasonably inert layer.

## References

- [1] A. Anders, W. Fong, A. V. Kulkarni, F. W. Ryan, and C. S. Bhatia, "Ultrathin diamond-like carbon films deposited by filtered carbon vacuum arcs," *IEEE Transactions on Plasma Science*, vol. 29, no. 5 I, pp. 768–775, 2001.
- [2] C. M. Mate, "Nanotribology studies of carbon surfaces by force microscopy," *Wear*, vol. 168, no. 1-2, pp. 17–20, 1993.
- [3] J. Robertson, "Diamond-like amorphous carbon," *Materials Science and Engineering (R)*, vol. 37, no. 4–6, pp. 129–281, 2002.
- [4] D. R. McKenzie, "Tetrahedral bonding in amorphous carbon," *Reports on Progress in Physics*, vol. 59, no. 12, pp. 1611–1664, 1996.
- [5] A. Erdemir, "Superlubricity and wearless sliding in diamondlike carbon films," in *Surface Engineering 2001—Fundamentals and Applications*, vol. 697 of *MRS Proceedings*, pp. 391–403, November 2001.
- [6] S. Dag and S. Ciraci, "Atomic scale study of superlow friction between hydrogenated diamond surfaces," *Physical Review B*, vol. 70, no. 24, Article ID 241401(R), 4 pages, 2004.
- [7] F. Demichelis, C. F. Pirri, A. Tagliaferro et al., "Mechanical and thermophysical properties of diamond-like carbon (DLC) films with different  $\text{sp}^3/\text{sp}^2$  ratios," *Diamond and Related Materials*, vol. 2, no. 5–7, pp. 890–892, 1993.
- [8] J. T. Titantah, D. Lamoen, E. Neyts, and A. Bogaerts, "The effect of hydrogen on the electronic and bonding properties of amorphous carbon," *Journal of Physics Condensed Matter*, vol. 18, no. 48, pp. 10803–10815, 2006.
- [9] L. Diederich, P. Aebi, O. M. Küttel, and L. Schlapbach, "NEA peak of the differently terminated and oriented diamond surfaces," *Surface Science*, vol. 424, no. 2, pp. L314–L320, 1999.
- [10] J. van der Weide, Z. Zhang, P. K. Baumann, M. G. Wensell, J. Bernholc, and R. J. Nemanich, "Negative-electron-affinity effects on the diamond (100) surface," *Physical Review B*, vol. 50, no. 8, pp. 5803–5806, 1994.
- [11] H. Kawarada, "Hydrogen-terminated diamond surfaces and interfaces," *Surface Science Reports*, vol. 26, no. 7, pp. 205–259, 1996.
- [12] S. J. Sque, R. Jones, and P. R. Briddon, "Structure, electronics, and interaction of hydrogen and oxygen on diamond surfaces," *Physical Review B*, vol. 73, no. 8, Article ID 085313, 15 pages, 2006.
- [13] J. Furthmüller, J. Hafner, and G. Kresse, "Dimer reconstruction and electronic surface states on clean and hydrogenated diamond (100) surfaces," *Physical Review B*, vol. 53, no. 11, pp. 7334–7351, 1996.
- [14] G. Zillobotti, M. Ferrario, C. M. Bertoni, and M. C. Righi, "Ab initio calculation of adhesion and potential corrugation of diamond (001) interfaces," *Computer Physics Communications*, vol. 182, no. 9, pp. 1796–1799, 2011.
- [15] K. Hayashi, K. Tezuka, N. Ozawa, T. Shimazaki, K. Adachi, and M. Kubo, "Tribochemical reaction dynamics simulation of hydrogen on a diamond-like carbon surface based on tight-binding quantum chemical molecular dynamics," *Journal of Physical Chemistry C*, vol. 115, no. 46, pp. 22981–22986, 2011.
- [16] O. L. Eryilmaz and A. Erdemir, "On the hydrogen lubrication mechanism(s) of DLC films: an imaging TOF-SIMS study," *Surface and Coatings Technology*, vol. 203, no. 5–7, pp. 750–755, 2008.
- [17] F. G. Sen, Y. Qi, and A. T. Alpas, "Surface stability and electronic structure of hydrogen-and fluorine-terminated diamond surfaces: a first principles investigation," *Journal of Materials Research*, vol. 24, no. 8, pp. 2461–2470, 2009.
- [18] J. A. Johnson, J. B. Woodford, X. Chen, J. Andersson, A. Erdemir, and G. R. Fenske, "Insights into near-frictionless carbon films," *Journal of Applied Physics*, vol. 95, no. 12, pp. 7765–7771, 2004.
- [19] A. Erdemir, "Developing a near-frictionless carbon coating," *Tribology and Lubrication Technology*, vol. 61, no. 10, pp. 12–14, 2005.
- [20] J. A. Harrison, C. T. White, R. J. Colton, and D. W. Brenner, "Molecular-dynamics simulations of atomic-scale friction of diamond surfaces," *Physical Review B*, vol. 46, no. 15, pp. 9700–9708, 1992.
- [21] M. Garvey, M. Weinert, and W. T. Tysoe, "On the pressure dependence of shear strengths in sliding, boundary-layer friction," *Tribology Letters*, vol. 44, no. 1, pp. 67–73, 2011.
- [22] G. Zillobotti and M. C. Righi, "Ab initio calculation of the adhesion and ideal shear strength of planar diamond interfaces with different atomic structure and hydrogen coverage," *Langmuir*, vol. 27, no. 11, pp. 6862–6867, 2011.
- [23] G. Gao, R. J. Cannara, R. W. Carpick, and J. A. Harrison, "Atomic-scale friction on diamond: a comparison of different

- sliding directions on (001) and (111) surfaces using MD and AFM,” *Langmuir*, vol. 23, no. 10, pp. 5394–5405, 2007.
- [24] G. T. Wang, S. F. Bent, J. N. Russell Jr., J. E. Butler, and M. P. D'Evelyn, “Functionalization of diamond (100) by diels-alder chemistry,” *Journal of the American Chemical Society*, vol. 122, no. 4, pp. 744–745, 2000.
- [25] T. Halicioglu, “Calculation of surface energies for low index planes of diamond,” *Surface Science*, vol. 259, no. 1-2, pp. L714–L718, 1991.
- [26] R. H. Telling, C. J. Pickard, M. C. Payne, and J. E. Field, “Theoretical strength and cleavage of diamond,” *Physical Review Letters*, vol. 84, no. 22, pp. 5160–5163, 2000.
- [27] B. Delley, “An all-electron numerical method for solving the local density functional for polyatomic molecules,” *The Journal of Chemical Physics*, vol. 92, no. 1, pp. 508–517, 1990.
- [28] B. Delley, “A standard tool for density functional calculations: review and advances,” in *Modern Density Functional Theory: A Tool for Chemistry*, J. M. Seminario and P. Politzer, Eds., vol. 2 of *Theoretical and Computational Chemistry*, Elsevier Science B, Amsterdam, The Netherlands, 1995.
- [29] J. P. Perdew and Y. Wang, “Accurate and simple analytic representation of the electron-gas correlation energy,” *Physical Review B*, vol. 45, no. 23, pp. 13244–13249, 1992.
- [30] D. Henwood and J. D. Carey, “Ab initio investigation of molecular hydrogen physisorption on graphene and carbon nanotubes,” *Physical Review B*, vol. 75, no. 24, Article ID 245413, 10 pages, 2007.
- [31] S. K. Nayak, B. K. Rao, and P. Jena, “Equilibrium geometries, electronic structure and magnetic properties of small manganese clusters,” *Journal of Physics Condensed Matter*, vol. 10, no. 48, pp. 10863–10877, 1998.
- [32] T. Bučko, J. Hafner, S. Lebègue, and J. G. Ángyán, “Improved description of the structure of molecular and layered crystals: Ab initio DFT calculations with van der Waals corrections,” *Journal of Physical Chemistry A*, vol. 114, no. 43, pp. 11814–11824, 2010.
- [33] Y. Liu and W. A. Goddard, “First-principles-based dispersion augmented density functional theory: from molecules to crystals,” *Journal of Physical Chemistry Letters*, vol. 1, no. 17, pp. 2550–2555, 2010.
- [34] I. Mayer, “Bond orders and valences from ab initio wave functions,” *International Journal of Quantum Chemistry*, vol. 29, no. 3, pp. 477–483, 1986.
- [35] R. S. Mulliken, “Electronic population analysis on LCAO-MO molecular wave functions. II. Overlap populations, bond orders, and covalent bond energies,” *The Journal of Chemical Physics*, vol. 23, no. 10, pp. 1841–1846, 1955.
- [36] L. Ostrovskaya, V. Perevertailo, V. Ralchenko, A. Dementjev, and O. Loginova, “Wettability and surface energy of oxidized and hydrogen plasma-treated diamond films,” *Diamond and Related Materials*, vol. 11, no. 3-6, pp. 845–850, 2002.
- [37] G. Tanasa, *Atomic scale friction: a scanning probe study on crystalline surfaces [Ph.D. thesis]*, Eindhoven University of Technology, 2005.
- [38] P. L. Piotrowski, R. J. Cannara, G. Gao, J. J. Urban, R. W. Carpick, and J. A. Harrison, “Atomistic factors governing adhesion between diamond, amorphous carbon and model diamond nanocomposite surfaces,” *Journal of Adhesion Science and Technology*, vol. 24, no. 15-16, pp. 2471–2498, 2010.
- [39] R. Neitola and T. A. Pakkanen, “Ab initio studies on the atomic-scale origin of friction between diamond (111) surfaces,” *Journal of Physical Chemistry B*, vol. 105, no. 7, pp. 1338–1343, 2001.
- [40] M. D. Perry and J. A. Harrison, “Universal aspects of the atomic-scale friction of diamond surfaces,” *Journal of Physical Chemistry*, vol. 99, no. 24, pp. 9960–9965, 1995.
- [41] W. Zhong and D. Tománek, “First-principles theory of atomic-scale friction,” *Physical Review Letters*, vol. 64, no. 25, pp. 3054–3057, 1990.
- [42] T. A. Albright, J. K. Burdett, and M. H. Whangbo, *Orbital Interactions in Chemistry*, John Wiley & Sons, New York, 1985.
- [43] T. Çağın, J. Che, M. N. Gardos, A. Fijany, and W. A. Goddard, “Simulation and experiments on friction and wear of diamond: a material for MEMS and NEMS application,” *Nanotechnology*, vol. 10, no. 3, pp. 278–284, 1999.
- [44] Y. Mo, K. T. Turner, and I. Szlufarska, “Friction laws at the nanoscale,” *Nature*, vol. 457, no. 7233, pp. 1116–1119, 2009.
- [45] D. S. Grierson, E. E. Flater, and R. W. Carpick, “Accounting for the JKR-DMT transition in adhesion and friction measurements with atomic force microscopy,” *Journal of Adhesion Science and Technology*, vol. 19, no. 3–5, pp. 291–311, 2005.
- [46] E. C. Gage, T. W. McDaniel, W. A. Challener et al., “Heat assisted magnetic recording,” *Proceedings of the IEEE*, vol. 96, no. 11, pp. 1810–1835, 2008.
- [47] R. Z. Lei, A. J. Gellman, and P. Jones, “Thermal stability of Fomblin Z and Fomblin Zdol thin films on amorphous hydrogenated carbon,” *Tribology Letters*, vol. 11, no. 1, pp. 1–5, 2001.

## Review Article

# Nanorheometry of Molecularly Thin Liquid Lubricant Films Coated on Magnetic Disks

Shintaro Itoh,<sup>1</sup> Yuya Hamamoto,<sup>1</sup> Koki Ishii,<sup>1</sup> Kenji Fukuzawa,<sup>1</sup> and Hedong Zhang<sup>2</sup>

<sup>1</sup>Department of Micro-Nano Systems Engineering, Nagoya University, Furo-cho, Chikusa-ku, Nagoya, Aichi 464-8603, Japan

<sup>2</sup>Department of Complex Systems Science, Nagoya University, Furo-cho, Chikusa-ku, Nagoya, Aichi 464-8601, Japan

Correspondence should be addressed to Shintaro Itoh, s.ito@nuem.nagoya-u.ac.jp

Received 3 August 2012; Revised 20 November 2012; Accepted 4 December 2012

Academic Editor: Tom Karis

Copyright © 2012 Shintaro Itoh et al. This is an open access article distributed under the Creative Commons Attribution License, which permits unrestricted use, distribution, and reproduction in any medium, provided the original work is properly cited.

Molecularly thin lubricant films are used for the lubrication of head disk interfaces in hard disk drives. The film thickness is reduced to 1–2 nm to minimize the magnetic spacing, and optimal, precise design is required to obtain sufficient lubrication. However, until now, there was no generally applicable method for investigating such thin films. Therefore, we developed a highly sensitive shear force measuring method and have applied it to the viscoelastic measurement of lubricant films coated on magnetic disk surfaces. In this paper, we review the method and summarize the useful findings we have demonstrated so far.

## 1. Introduction

High-recoding-density hard disk drives (HDDs) require the magnetic spacing to be as small as possible. Lubrication of the head disk interface (HDI) is achieved by a diamond-like carbon (DLC) overcoat on the magnetic layer and a liquid lubricant film on the DLC surface. Thus, the thicknesses of both these thin films must be minimized to reduce the magnetic spacing. Liquid lubricant films are typically 1–2 nm thick, which corresponds to a monolayer thickness. In addition, the magnetic head comes closer to the surface of liquid lubricant film and recently its gap was around 1 nm. A further increase in the recording density of HDDs will require the head to be in contact with the lubricant film surface. Although air bearing still plays an important role in maintaining the flying height, the lubrication regime between the head and disk changes from hydrodynamic to boundary lubrication. To guarantee HDD performance, effective design of the lubricant film becomes a crucial requirement. However, until recently there was no generally applicable method for characterizing the mechanical properties of such a thin film. A surface force apparatus (SFA) is a pioneering method that can measure the viscoelastic properties of a molecularly thin liquid film confined in two mica surfaces under shearing motion, and experiments using the SFA have revealed the thin films have

unique mechanical properties different from those in the bulk state, such as an enhanced viscosity and prolonged retardation time [1–3]. Understanding physical properties of molecularly thin liquid films is one of the important subjects not only in the HDI tribology but also in the field of soft condensed matter. Such a thin film is considered as one type of confinement. The confinement has various types such as liquids in porous media, and water in a cell, polymer blends, and so on [4]. The measurement methods typically used are dielectric spectroscopy, neutron scattering, NMR, differential scanning calorimetry, ellipsometry, and so on [4–7]. Jackson and McKenna observed large decrease of glass transition temperature  $T_g$  with liquids confined in nanometer size pores by using colorimetric measurements [8, 9]. This result means the mobility of confined liquids can increase. Similar results were obtained not only with liquids in pores but also with thin liquid films [10–13]. The thin films include free standing films and those coated on substrates. However, to the contrary, increase of  $T_g$  or no effect on  $T_g$  were also observed with similar confined systems [14–19]. These controversial and contradictory results are due to complexity of the phenomena and wide variety of the measurement methods and the universal explanation has not been made. He et al. described through solvation dynamics experiments that whether  $T_g$  increase or decrease depends

on the condition of confining surface, which is “soft” or “hard” [20]. In the case of soft surface,  $T_g$  decreased. The hard surface suppressed the molecular mobility and it led to the  $T_g$  increase. Based on the experimental results obtained by using the fluorescence probes, Torkelson’s group reported that thin films coated on substrates had  $T_g$  gradient from the free surface to the substrate [21]. The molecular mobility decreased as the substrate was approached, which led to the  $T_g$  increase. In the case of liquid lubricant films used in HDI, they are confined in two solid substrates during shearing. The same type of confinement was realized in the SFA and the experimental results indicated the decrease of molecular mobility, which corresponds to the  $T_g$  increase. However, the solid substrates that confine the liquid film are limited to mica in the SFA measurements. In addition, dynamic measurements are limited to frequencies below 100 Hz. Many of the experimental results in previous studies show that the lubrication characteristics of the magnetic disk surface depend largely on the interaction between the DLC surface and the lubricant molecules [22, 23]. Therefore, the liquid lubricant films used for the HDI lubrication must be characterized on the DLC surface. Additionally, since the relative speeds between the head and disk are quite high, highly dynamic measurements are preferred. To measure the dynamic viscoelastic properties of molecularly thin lubricant films on the magnetic disk surface, we developed a highly sensitive shear force measuring method. We call the method the fiber wobbling method (FWM) [24]. In this paper, we review our previous research concerning the FWM and introduce our major results including some new findings.

## 2. Fiber Wobbling Method

**2.1. Concept.** There are two major requirements for the viscoelastic measurements of molecularly thin liquid films under shearing motion. One is the sensitive detection of the shear force and the other is the precise control of the shearing gap width. The FWM concept meets both of these demands. We use an optical fiber with a spherical end as the shearing probe and set it to be perpendicular to the sample surface. During the shearing of the sample by the probe tip, the shear force acting on the tip can be measured by detecting the fiber deflection as shown schematically in Figure 1(a). Since the rigidity of the probe in the axial direction is much higher than that in the bending direction, we can attain both a high shear force sensitivity and precise gap control.

In the dynamic viscoelastic measurements using the FWM, the probe was oscillated sinusoidally at a constant frequency and amplitude. The amplitude change and phase shift of the probe tip oscillation was measured, and these values were used to obtain the viscoelastic properties of the lubricant films. Since the size of the probe is typically a few millimeters in length and 100  $\mu\text{m}$  in diameter (Figure 1(b)), the natural frequency of the probe is higher than a few kilohertz. This means that dynamic measurements with frequencies of up to a few kilohertz can be achieved with the FWM. The spherical end of probe was made by laser

melting and its root-mean-square roughness is typically around 0.2 nm.

**2.2. Shear Force Measurement.** The shear force  $F$  acting on the probe tip can be estimated using the following equation [2]:

$$F = \eta \Omega U, \quad (1)$$

where  $\eta$  is the viscosity of the lubricant and  $U$  is the sliding speed. The parameter  $\Omega$  is a geometrical parameter determined from the shape and gap of the two sliding surfaces. When a sphere of diameter  $d$ , which represents the probe tip, moves parallel to the plane surface with a gap  $h$ ,  $\Omega$  is written as:

$$\Omega = 3\pi d \left[ \frac{8}{15} \log\left(\frac{d}{h}\right) + \dots \right] \approx \frac{8}{5}\pi d \log\left(\frac{d}{h}\right). \quad (2)$$

The approximation holds when  $h \ll d$ . Substituting typical values of  $\eta = 0.1 \text{ Pa} \cdot \text{s}$ ,  $U = 10 \text{ mm/s}$ ,  $h = 1 \text{ nm}$ , and  $d = 200 \mu\text{m}$  into (1) and (2) gives an estimate of  $F$  to be on the order of 1 nN. Since the spring constant of the probe is around 10 N/m, we have to attain a sensitivity of 0.1 nm in the displacement measurement of the probe deflection. To meet this requirement, we developed an original method as shown in Figure 2. We use the fiber as a lens to focus the laser onto a position sensitive detector (PSD). The laser beam is incident in a direction perpendicular to the plane of probe deflection. When the fiber is deflected, the laser spot on the PSD moves, and therefore, the amount of deflection can be obtained from the displacement of the laser spot. The sensitivity of the measurement strongly depends on the numerical aperture of the objective lens and the distance between the lens and probe. The optimal conditions were determined by a numerical calculation using a ray tracing method and experimentally verified. The details of the optical system design are described in [25]. Figure 3 shows the experimentally obtained relationship between the probe amplitude and signal-to-noise ratio. In the experiment, the probe was oscillated sinusoidally with the amplitude synchronously detected by a lock-in amplifier. The data represented by the circles, triangles, and squares correspond to numerical apertures of 0.3, 0.25, and 0.1, respectively. A least-squares method is used to fit the experimental data, and the results are shown as the straight lines. From the fitted functions, we determine the detection limit of the measurement to be the probe amplitude for a signal-to-noise ratio of 1. Consequently, the detection limits are 0.006, 0.007, and 0.01 nm for  $N = 0.3, 0.25, \text{ and } 0.1$ , respectively. This corresponds to a shear force sensitivity on the order of 0.1 nN, and we can thus conclude that the sensitivity of the FWM is sufficient for the measurement of molecularly thin films.

**2.3. Precise Control and Determination of the Gap Width.** The width of the shearing gap, which is the width of the gap between the probe tip and substrate, is controlled by a piezo stage on which the sample is mounted. Since the longitudinal rigidity of the probe is sufficiently high, the

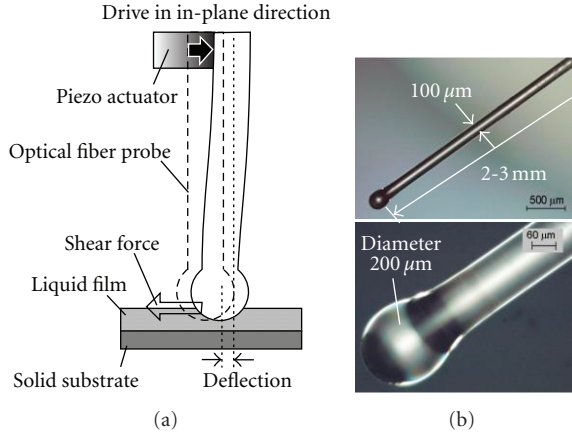


FIGURE 1: (a) Concept of shear force detection in the fiber wobbling method and (b) micrographs of the optical fiber probe.

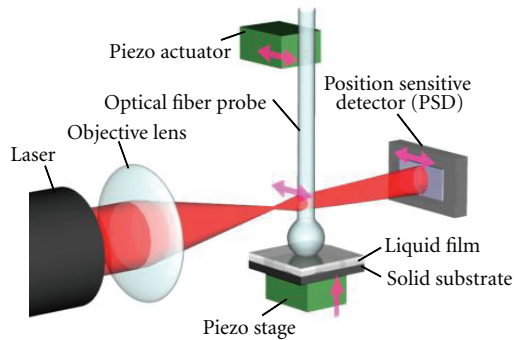


FIGURE 2: Schematic diagram of the fiber wobbling method (FWM).

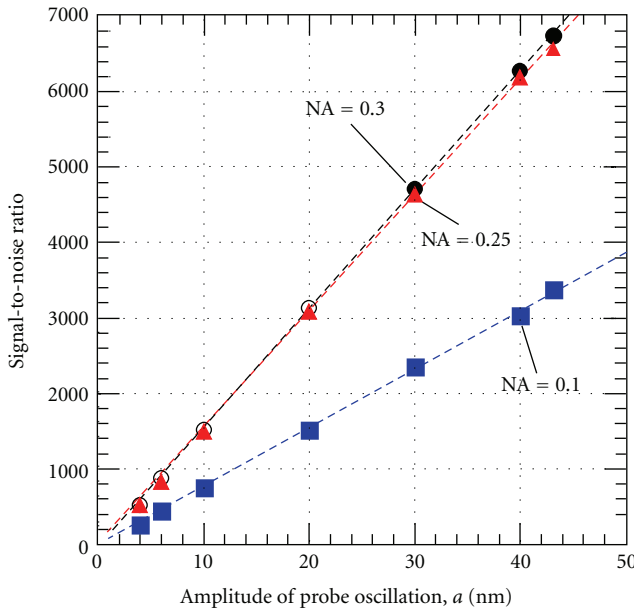


FIGURE 3: Experimental results of the measured relationship between the probe oscillation amplitude and the signal-to-noise ratio of the displacement measurement.

change in the gap width is equal to the displacement of the piezo stage. Therefore, we can control the gap width with the same resolution as that of the piezo stage, which is 0.1 nm. However, the absolute value of the gap width cannot be measured directly. Therefore, we determine the solid contact point experimentally, define it as the zero point of the gap width, and the shearing gap is determined by the displacement of the piezo stage from this point. Thus, the probe tip must make contact with the solid substrate at least once in the measurements. The basic experimental procedure in the FWM measurements is shown schematically in Figure 4. In the initial state, the gap was set to be much larger than a nanometer-size gap, such as 1 μm, and the sinusoidal oscillation of the probe at a constant frequency and amplitude was started. The gap was then gradually decreased at a constant rate, which is typically a few nanometers per second. As the gap width decreased, we synchronously measured the amplitude and phase of the probe tip oscillation, detected by the optical method described in Section 2.2, using the lock-in amplifier. The measurement was stopped when solid contact occurred.

According to the above procedure, the determination of the gap width depends on the sensitivity of the solid contact point detection. For this purpose, we developed an original technique that detects the excitation of the resonant oscillation of the shearing probe [26]. In the initial stage of solid contact, intermittent asperity contact occurs between two sliding surfaces owing to the surface roughness. The asperity contact causes an impulsive force to act on the probe tip and excites the resonant oscillation of the probe. We detect solid contact by monitoring the increase in the resonant oscillation amplitude. The frequency of the forced oscillation during lubricant shearing is much smaller than the natural frequency of the probe, and so two lock-in amplifiers can be used to measure the forced oscillation component and the resonant oscillation component separately in different frequency ranges. This technique enables us to define the solid contact point with an accuracy on the order of 0.1 nm.

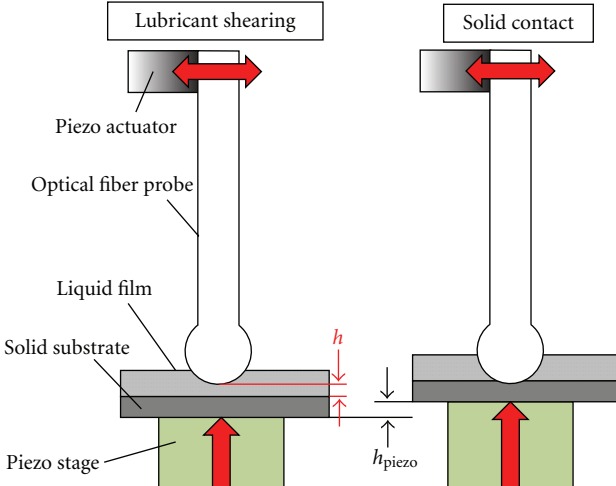


FIGURE 4: Gap determination procedure in the FWM measurements. Shearing gap  $h$  is equal to the displacement of the piezo stage until the solid contact occurs, which is represented by  $h_{\text{piezo}}$ .

TABLE 1: Lubricants used in the experiment.

	Z03	Zdol2000	Zdol4000
Main chain structure	X-CF <sub>2</sub> (OCF <sub>2</sub> CF <sub>2</sub> ) <sub>m</sub> (OCF <sub>2</sub> ) <sub>n</sub> OCF <sub>2</sub> -X		
End groups (-X)	-CF <sub>3</sub>	-CH <sub>2</sub> OH	-CH <sub>2</sub> OH
Molecular weight (amu)	4000	2000	4000
Bulk Viscosity at RT (Pas)	0.05	0.15	0.18

### 3. Viscoelastic Measurement with the Immersed System

The probe tip was immersed into a relatively thick lubricant film (e.g., 200  $\mu\text{m}$ ), and the gap was decreased to the nanometer scale [24, 27]. The lubricant film was confined in the nanometer-sized gap and its viscoelasticity was measured. In this immersed system, the gap between the two sliding surfaces is completely filled with the lubricant, and since the gap width varies with the radius of curvature of the probe tip, the obtained viscoelastic properties represent those of the average. However, since the shear force generated for the narrowest gap plays a dominant role in the measured mechanical response, we observe a strong dependency of the viscoelasticity on the gap variance when the lubricant is confined to the nanometer-sized gap. In immersed-system measurements, we can investigate the entire viscoelasticity transition process of confined lubricants as the gap changes from the micrometer to nanometer scale.

**3.1. Materials and Method.** We used a magnetic disk as the solid substrate, and the top layer of the disk is a DLC overcoat with a surface roughness of 0.59 nm. As the lubricant, we used three different types of perfluoropolyether (PFPE) lubricants as listed in Table 1. All have the same main chain structure but the end groups differ: Zdol2000 and Zdol4000 (with different molecular weights) have hydroxyl end groups on both sides of the main chain, making them

polar lubricants, and both ends of the Z03 main chain are terminated by fluorine, which means that Z03 is a nonpolar lubricant. The difference in polarity affects the affinity to the magnetic disk surface. The polar end groups are strongly adsorbed onto the DLC surface and chemical bonding can be formed. Lubricant molecules that are chemically adsorbed on the disk surface are known as immobile molecules or bonded molecules and those that are physically adsorbed are known as mobile molecules. The number of bonded molecules can be controlled by annealing or UV treatment.

We placed one drop of the lubricant on the disk surface and waited until the lubricant spread spontaneously over the surface and stabilized. The amount of liquid in the drop was controlled to produce a wet film with a thickness of around 200  $\mu\text{m}$ . As mentioned in the previous section, since the mechanical response obtained during the shearing of lubricant is dominated by the lubricant confined in the narrowest gap, any variation in the immersion depth of the probe will have a negligible effect on the measurements. The sample was not annealed or UV treated.

A schematic diagram of the experimental setup is shown in Figure 5. The piezo actuator was used to oscillate the probe, and the gap between the probe tip and sample was controlled by the piezo stage. The deflection signal from the PSD, a current signal, was converted to a voltage and amplified by the  $I$ - $V$  converter. The amplified signal was divided into two lines; one line was detected by the lock-in amplifier that used the piezo actuator oscillation signal as a reference signal and its amplitude and phase were measured. The other line was detected by another lock-in amplifier to measure the amplitude of the resonant oscillation component for the solid contact point detection. The reference signal was generated by the function generator with a frequency equal to the natural frequency of the probe. These three measured values were simultaneously recorded on the computer via an analog-to-digital converter.

After the probe tip was immersed in the lubricant film and the shearing gap was set to around 1  $\mu\text{m}$ , we started the probe oscillating at a frequency of 800 Hz and a peak-to-peak amplitude of 30 nm. The gap was decreased at a constant rate of 10 nm/s, and the amplitude and phase of the probe oscillation was measured until solid contact occurred.

**3.2. Calculation of Viscoelasticity.** The mechanical model used to obtain the viscoelastic properties is shown in Figure 6. The equation of motion is expressed as

$$m \frac{d^2x}{dt^2} + c \frac{dx}{dt} + kx = F_0 e^{i\omega t}, \quad (3)$$

where  $F_0$ ,  $\omega$ ,  $x$ ,  $m$ ,  $k$ , and  $c$  are the driving force, driving frequency, displacement, effective mass of the spherical tip, spring constant of the probe, and damping coefficient of the liquid lubricant, respectively. The solution for (3) is written as

$$x = a \cos(\omega t - \delta), \quad (4)$$

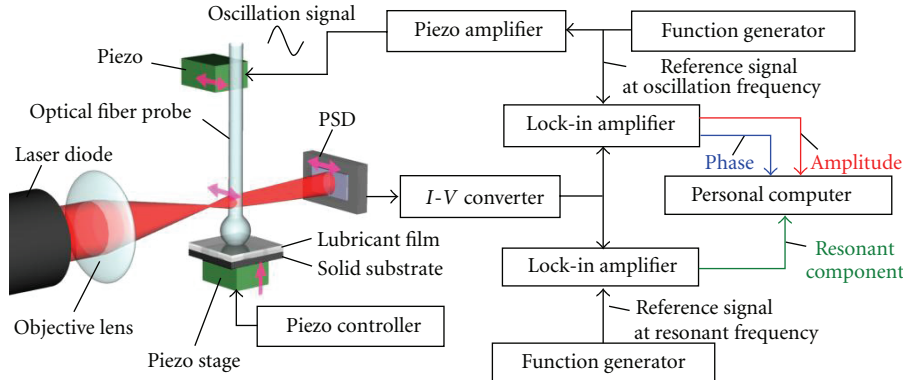


FIGURE 5: Experimental setup of the fiber wobbling method.

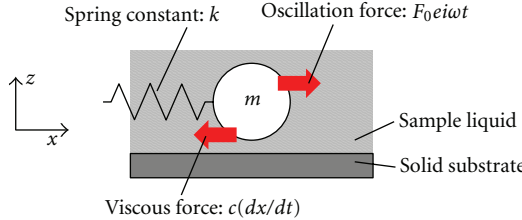


FIGURE 6: Mechanical model for the viscoelastic calculation.

where  $a$  and  $\delta$  are the amplitude and phase shift, respectively, defined as

$$a = \frac{F_0}{[(k - m\omega^2)^2 + \omega^2 c^2]^{1/2}}, \quad (5)$$

$$\delta = \tan^{-1} \left( \frac{\omega c}{k - m\omega^2} \right). \quad (6)$$

The driving force  $F_0$  is obtained by substituting  $c = 0$  and  $a = a_0$  into (5), where  $a_0$  represents the forced oscillation amplitude. The relationship between the damping coefficient and viscosity of the lubricant is expressed as follows:

$$c = \eta_{\text{eff}} \Omega. \quad (7)$$

Here,  $\eta_{\text{eff}}$  represents the effective viscosity since lubricant confined in a nanometer-sized gap is expected to be non-Newtonian. In the immersed system, the sliding surfaces were assumed to be a sphere and plane with the sphere moving parallel to the plane surface. In this case, the geometric parameter  $\Omega$  is given by (2). In our discussion on viscoelastic properties, the effective viscosity  $\eta_{\text{eff}}$  is represented by a complex function:

$$\eta_{\text{eff}} = \eta' - i\eta'', \quad (8)$$

where  $\eta'$  and  $\eta''$  represent the viscosity and elasticity, respectively. From (3) to (8), we obtain  $\eta'$  and  $\eta''$  as follows:

$$\begin{aligned} \eta' &= \frac{a_0(k - m\omega^2) \sin \delta}{a\omega\Omega}, \\ \eta'' &= \frac{(a_0 \cos \delta - a)(k - m\omega^2)}{a\omega\Omega}. \end{aligned} \quad (9)$$

In these equations, the amplitude  $a$  and phase shift  $\delta$  are the measured values of the probe tip oscillation. The other parameters are known values from the experimental conditions and probe specifications.

**3.3. Results and Discussion.** Using (9), we calculated  $\eta'$  and  $\eta''$  of each lubricant. The results are shown in Figures 7, 8, and 9. The closed circles are the viscosity values and the open circles are the elasticity values. In all the samples, the viscosity rapidly increased as the gap was decreased to the nanometer scale. The maximum value of the viscosity was approximately several dozen times larger than the bulk-state viscosity (listed in Table 1). This is caused by the lack of molecular mobility in the nanometer-sized gap width.

In the bulk state, the Z03, Zdol2000, and Zdol4000 lubricants have no elastic properties. However, elasticity appeared for gaps of less than a few nanometers. In other words, the transition from a viscous liquid to a viscoelastic liquid occurred. The elasticity also increased monotonically as the gap decreased. In a narrow gap, the physically and chemically adsorbed molecules on both sides of the confining surfaces can interact with each other, and it is considered that the mobility of these adsorbed molecules was extremely suppressed and thus the lubricants exhibited elasticity. The elasticity appeared at different gap widths for each tested lubricant: widths of 6.5, 13.2, and 13.4 nm for Z03, Zdol2000, and Zdol4000, respectively. These differences are considered to be due to the higher affinity of the polar lubricants to the magnetic disk surface; the polar lubricants may have formed a thicker adsorption layer that led to the appearance of elasticity at a wider gap width.

#### 4. Viscoelastic Measurement with the Thin-Film System

The FWM measurements were applied to thin lubricant films coated on magnetic disks as in the actual HDI [26, 28]. From the measured mechanical responses, we firstly discuss the deformation of the lubricant film caused by the approaching and separating probe tip, which imitates the touchdown and takeoff behavior in the HDI. Secondly, we discuss the effect

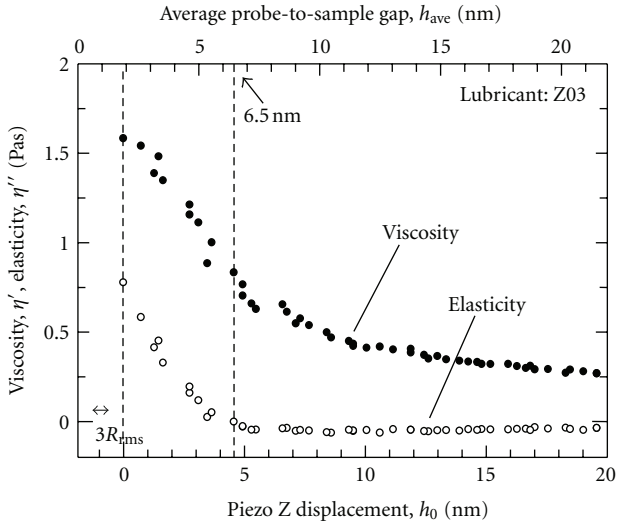


FIGURE 7: Effect of the shearing gap on the viscosity  $\eta'$  and elasticity  $\eta''$  measured with the Z03 lubricant [24].

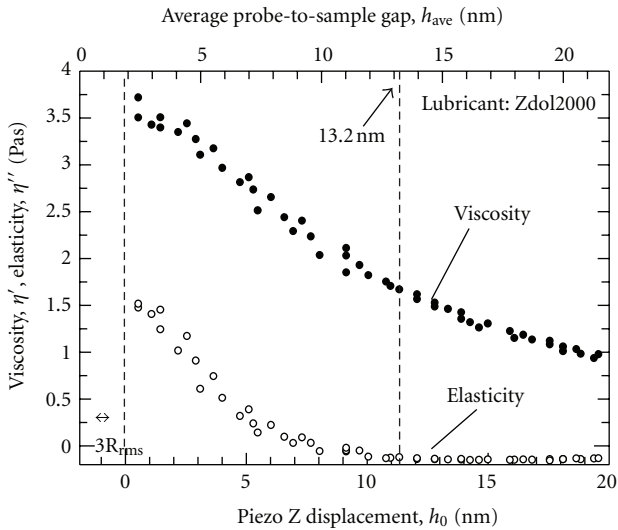


FIGURE 8: Effect of the shearing gap on the viscosity  $\eta'$  and elasticity  $\eta''$  measured with the Zdol2000 lubricant [24].

of the bonding ratio on the viscoelasticity. Finally, the shear rate dependence of the viscosity is shown.

**4.1. Materials and Method.** The Z03 and Zdol4000 lubricants, specified in Table 1, and Ztetraol were coated onto a magnetic disk to form the samples. Ztetraol has the same main chain structure as Z03 and Zdol4000, though it has different end groups that are  $X = -\text{CH}(-\text{OH})\text{CH}_2\text{OH}$ . Since Ztetraol has two hydroxyl groups on each end of the main chain, it has higher affinity to the magnetic disk surface than Zdol4000. The lubricant films were formed by the dip-coating method. The disk coated with Zdol4000 was annealed, and samples that had different numbers of bonded molecules were prepared. The proportion of bonded

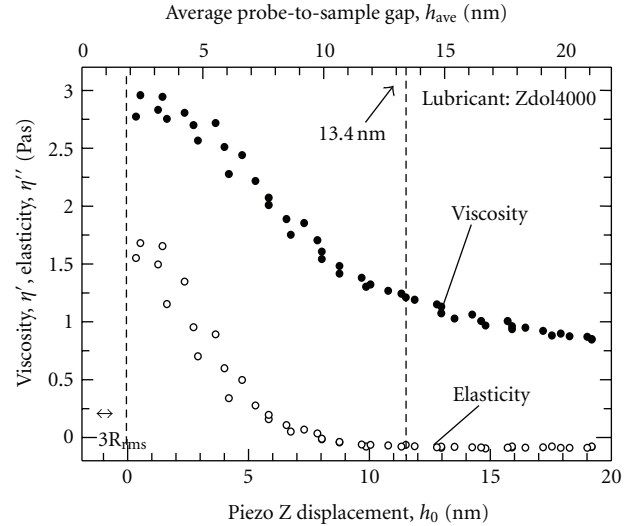


FIGURE 9: Effect of the shearing gap on the viscosity  $\eta'$  and elasticity  $\eta''$  measured with the Zdol4000 lubricant [24].

TABLE 2: Samples prepared for the FWM measurements with the thin-film system.

Type of lubricant	Film thickness, $h$ (nm)	Bonding ratio, $b$
Z03	2.2	0
Zdol4000	2.0	0.2
Zdol4000	2.0	0.5
Zdol4000	1.8	1.0
Ztetraol	1.9	0.3

molecules is represented by the bonding ratio  $b$ , which is defined by

$$b = \frac{h_b}{h}. \quad (10)$$

Here,  $h$  is the film thickness and  $h_b$  is the film thickness measured after the sample has been rinsed with solvent, which means  $h_b$  is the thickness composed only of the remaining bonded molecules. The bonding ratio was measured after all the viscoelastic measurements were finished, and an ellipsometer was used to measure the film thickness. The samples are listed in Table 2; since Z03 does not form chemically bonded molecules, its bonding ratio is 0.

The experimental procedure was similar to that of the immersed-system measurement; in this case, the amplitude change and phase shift of the probe tip oscillation were measured with decreasing gap rate of 3 nm/s. In the thin-film system, the probe does not make contact with the sample at the beginning of the measurement since the initial gap is set to be much larger than the film thickness. Therefore, the measured mechanical response is divided into three sequential stages: noncontact, lubricant shearing, and solid contact. We also measured the mechanical response as the gap was increased at a rate of 3 nm/s from the solid contact point. We call the former procedure the approaching process and the latter the separating process. The separating process

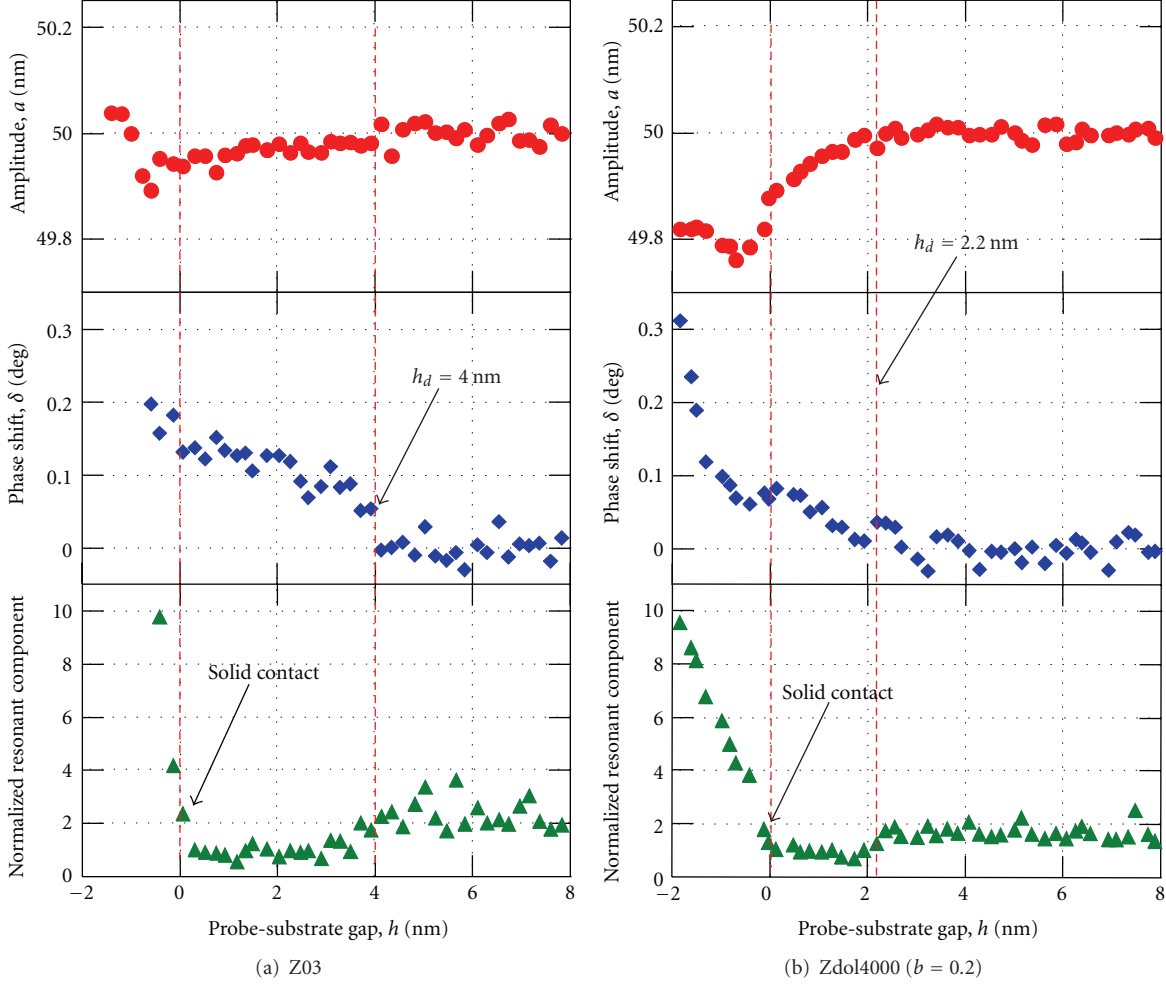


FIGURE 10: Probe amplitude, phase shift, and normalized resonant component measured for (a) Z03 and (b) Zdol4000 with a bonding ratio of 0.2 in the approaching process [26].

follows the approaching process. In the separating process, the three sequential stages occur in reverse order. These two processes imitate the touchdown and takeoff behavior in the HDI. Although the approaching and separating speeds differ greatly from the actual speeds, we can observe fundamental phenomena. In all measurements, we used an optical fiber probe with a tip radius of curvature of around  $8 \mu\text{m}$ .

**4.2. Calculation of the Viscoelasticity.** To calculate  $\eta'$  and  $\eta''$  using (9), we need to determine  $\Omega$  for this system. Since the gap width will be sufficiently smaller than the radius of curvature of the probe end, we can assume that the geometric configuration of the sliding surfaces is two flat plates moving parallel with a gap of  $h$ . In that case,  $\Omega$  is obtained as follows:

$$\Omega = \frac{S}{h}, \quad (11)$$

where  $S$  represents the contact area between the probe end and lubricant film. It is, however, difficult to determine an accurate value for  $S$  experimentally in our setup, which is a major obstacle in obtaining the absolute values of the viscosity and elasticity coefficients from the measured

experimental results in the thin-film system. Therefore, we used the relative viscosity  $\zeta'$  and elasticity  $\zeta''$  contributions, defined as follows, to discuss the viscoelastic properties [26]:

$$\begin{aligned} \zeta' &= \frac{\eta'}{(\eta'^2 + \eta''^2)} = \frac{a_0 \sin \delta}{(a_0^2 + a^2 - 2a_0 a \cos \delta)^{1/2}}, \\ \zeta'' &= \frac{\eta''}{(\eta'^2 + \eta''^2)^{1/2}} = \frac{a_0 \cos \delta - a}{(a_0^2 + a^2 - 2a_0 a \cos \delta)^{1/2}}. \end{aligned} \quad (12)$$

For a quantitative comparison, the damping coefficient  $c_f$  and elastic coefficient  $k_f$  of the samples can be obtained as follows [28]:

$$\begin{aligned} c_f &= \frac{a_0(k - m\omega^2) \sin \delta}{a\omega}, \\ k_f &= \frac{(a_0 \cos \delta - a)(k - m\omega^2)}{a\omega}. \end{aligned} \quad (13)$$

#### 4.3. Results and Discussion

**4.3.1. Touchdown and Takeoff Gap.** The touchdown gap width  $h_d$  was defined by the gap width for which the probe

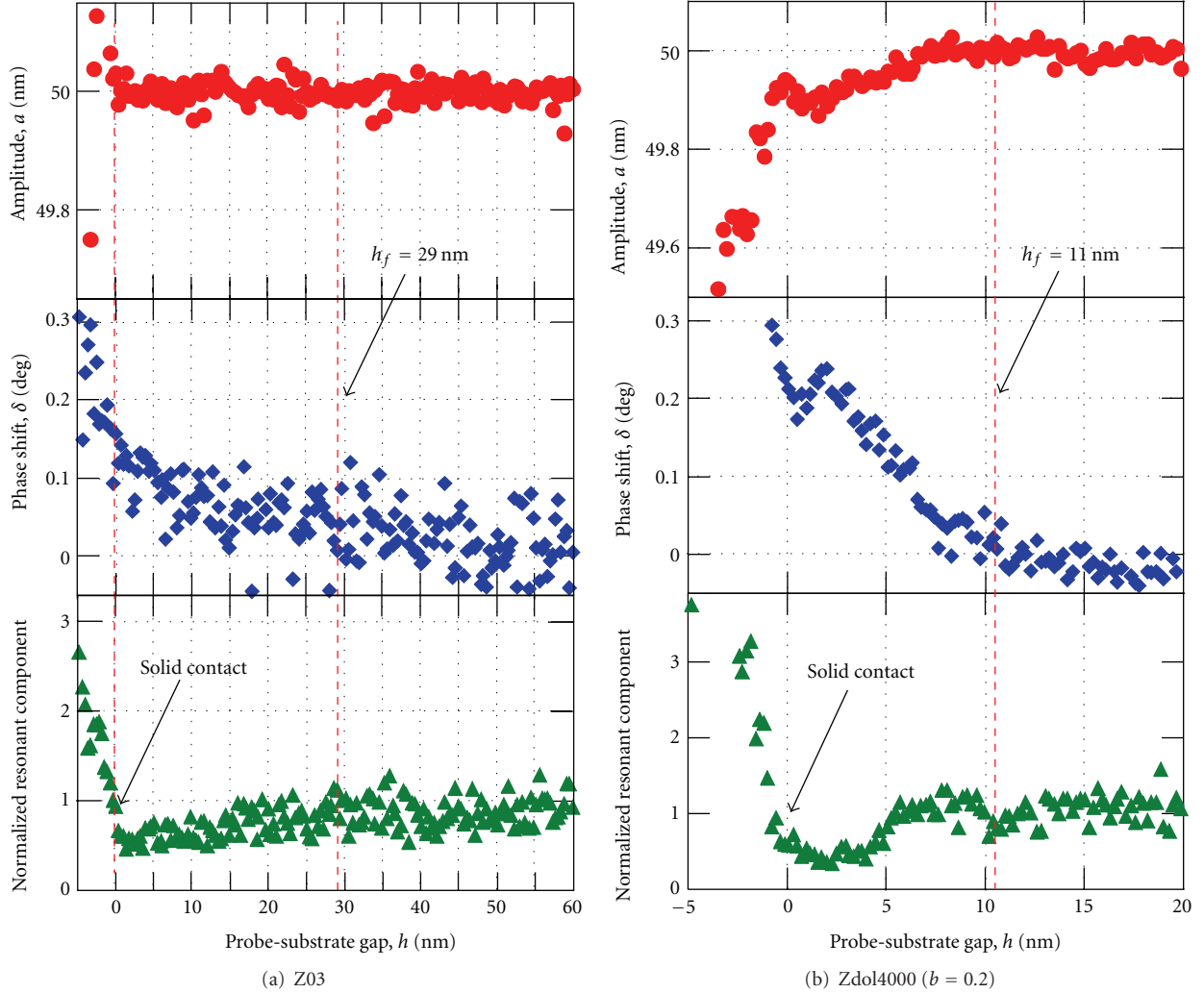


FIGURE 11: Probe amplitude, phase shift, and normalized resonant component measured for (a) Z03 and (b) Zdol4000 with a bonding ratio of 0.2 in the separating process [26].

tip first touches the lubricant film surface in the approaching process. The takeoff gap  $h_f$  was defined by the gap width for which the probe tip and lubricant film came apart in the separating process. These touchdown and takeoff gaps represent the gap range for which the probe end shears the lubricant film, and they are not necessarily equal to the film thickness since the lubricant film can be deformed. In the approaching process, we determined  $h_d$  by the gap width for which a decrease in the probe amplitude or an increase in the phase shift was first seen to exceed the noise levels of the measured signal. The  $h_f$  gap was determined by the gap width for which both an increasing probe amplitude and decreasing phase shift first agreed in the range of noise levels with their average values measured when the probe and the sample were completely apart. The noise levels were obtained by calculating the threefold variance in the measured data for a time when the probe was not in contact with the sample. Typical experimental results from the approaching process are shown in Figures 10(a) and 10(b) for Z03 ( $b = 0$ )

and Zdol4000 ( $b = 0.2$ ), respectively. The results measured in the subsequent separating process are shown in Figures 11(a) and 11(b). The touchdown and takeoff gaps are also indicated in Figures 10 and 11. During the approaching process, we observed that a decrease in the probe amplitude and an increase in the phase shift started below a certain gap width. In contrast, the probe amplitude increased and the phase shift decreased during the separating process and reached constant values, which means that the probe end and the sample came apart. The changes in the probe amplitude and phase shift were caused by the viscoelastic force acting on the probe end during the lubricant shearing. The touchdown and takeoff gaps determined for each sample are summarized in Figure 12. The oscillation amplitude was 50 nm (peak-to-peak) and frequency was 1 kHz in all measurements.

While the touchdown gaps of the Zdol4000 and Ztetraol samples had almost the same value as the film thicknesses, that of Z03 was almost twice the film thickness. In the case of Z03, we consider that the intermolecular attraction from the

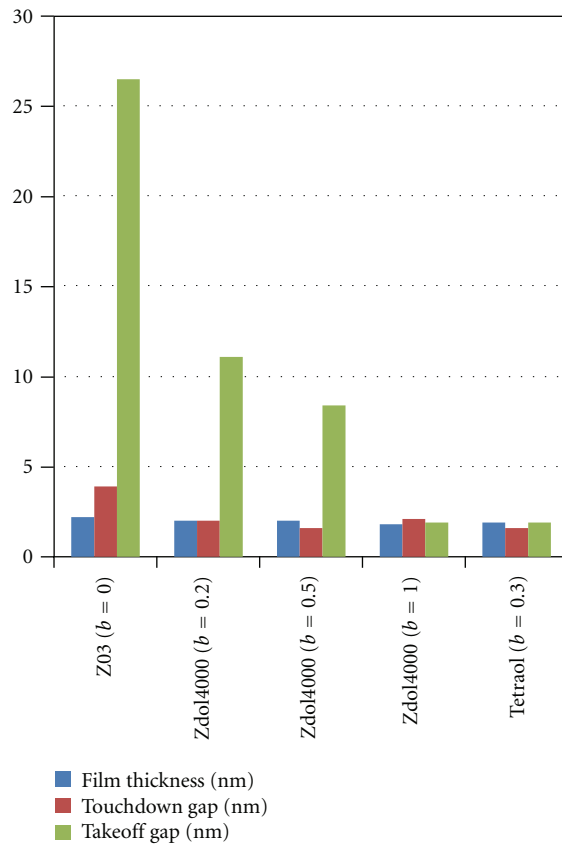


FIGURE 12: Experimental results of the touchdown gaps in the approaching process and takeoff gap in the separating process.

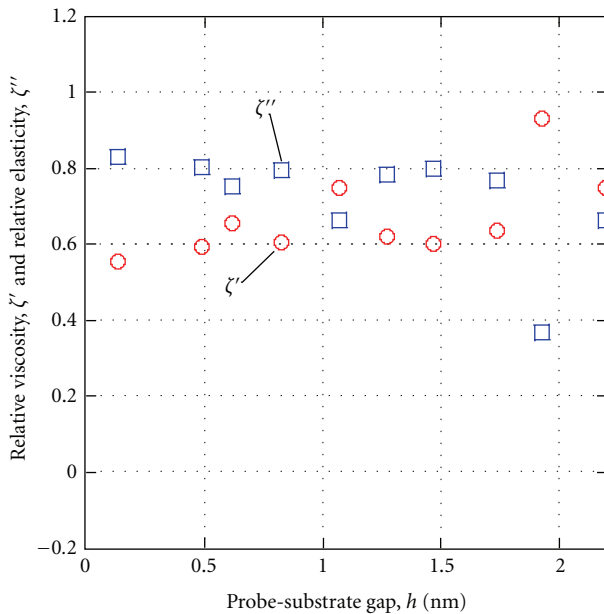


FIGURE 13: Relative viscosity and elasticity of Zdol4000 with a bonding ratio of 0.2 in the approaching process at  $h < 2.2$  nm [26].

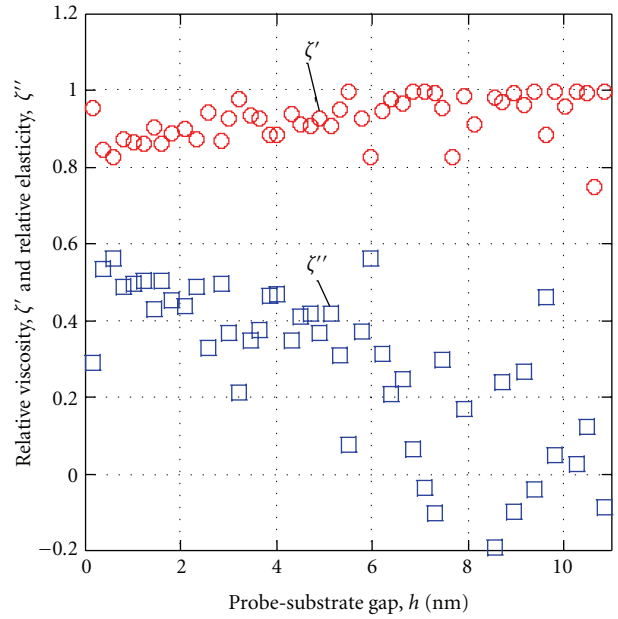


FIGURE 14: Relative viscosity and elasticity of Zdol4000 with a bonding ratio of 0.2 in the separating process at  $h < 11$  nm [26].

approaching probe tip caused the lubricant film to deform and a liquid bridge to form between the solid surfaces. This results in the contact between the probe tip and lubricant film starting at a gap width larger than the thickness of the lubricant film. A liquid bridge is unlikely to have formed for the Zdol4000 and Ztetraol samples since the touchdown gaps were almost equal to the film thicknesses. We consider these results to be reasonable because the Zdol4000 and Ztetraol molecules could form more energetically stable films than those of Z03 due to the strong interaction of the polar end groups with the disk surface. Since the polar interaction with the disk surface can be much larger than the intermolecular interaction with the probe surface, the Zdol4000 molecules could not form a liquid bridge.

The takeoff gaps were larger than the film thicknesses except in the case of Zdol4000 ( $b = 1.0$ ) and Ztetraol. In addition, samples with a smaller bonding ratio showed larger takeoff gaps. The small bonding ratio means there is a large number of mobile molecules and therefore suggests that the mobile molecules aggregate near the probe tip during contact with the lubricant film; the increasing gap elongated the cluster to form a liquid bridge that was maintained at gap widths, which were more than a few times larger than the film thickness.

Nonuniformity of the lubricant film thickness can be a significant disturbance to the stable movement of the magnetic head. Our results above indicate that the intermolecular interaction with the approaching probe surface does not cause any deformation in polar lubricant films even if they contain mobile molecules. In contrast, once the probe touches the lubricant film surface the mobile molecules aggregate near the contact region and form a cluster. In future HDDs, frequent contact between the head and disk

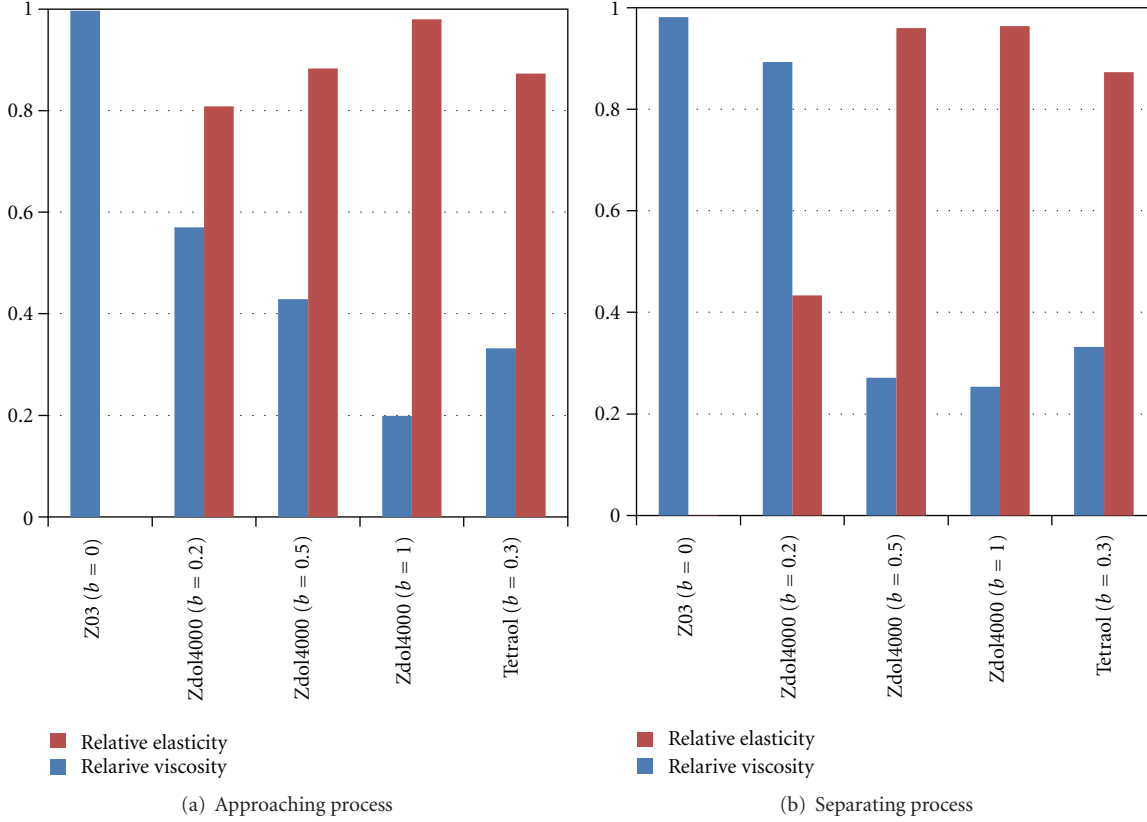


FIGURE 15: Relative viscosity and elasticity measured with different samples in (a) approaching and (b) separating processes.

is expected, and thus we suppose that lubricant films with mobile molecules may not be applied for realizing precise control of the magnetic spacing in future HDI. In this case, optimization of the lubricant film design is expected to attain sufficient lubrication without mobile molecules.

**4.3.2. Viscoelasticity.** We calculated the relative viscosity and elasticity for a gap width less than the touchdown gap in the approaching process and for a gap less than the takeoff gap in the separating process. Typical results for the Zdol4000 ( $b = 0.2$ ) sample are shown in Figures 13 and 14, with the circles indicating the relative viscosity and the squares indicating the relative elasticity. The average values in the gap range from 0 to 1.5 nm for all the samples are shown in Figure 15. As shown in Figure 15, the behavior of the Z03 ( $b = 0$ ) sample was dominated by the viscosity in both the approaching and separating processes because the Z03 lubricant film is only composed of mobile molecules. The Zdol4000 samples in the approaching process showed a decrease in viscosity and an increase in elasticity with an increase in the bonding ratio. This indicates solidification of the lubricant film caused by an increase in the number of bonded molecules. A significant change in the viscoelastic properties in the approaching and separating processes was observed for the Zdol4000 samples with bonding ratios of 0.2. While the viscosity was smaller to the elasticity in the approaching process, it became prominent in the

separation process. This is caused by the mobile molecules that aggregate around the probe tip. Ztetraol was elasticity dominant in both approaching and separating processes. Although its bonding ratio was 0.3, the viscoelasticity was qualitatively similar to that of Zdol4000 ( $b = 1.0$ ). Under the sliding condition in this study, the mobile molecules of Ztetraol may behave the same as the bonded ones of Zdol4000. If they are tested under the higher sliding speed, results may be different. This must be one of our future studies. From the results summarized in Figure 15, we can conclude that our method reveals the strong dependence of the viscoelasticity on the lubricant affinity to the disk surface. In addition, the viscoelastic response can be altered locally due to the behavior of mobile molecules.

**4.3.3. Shear Thinning Behavior.** To reveal the shear rate dependence of the viscoelasticity, we conducted measurements at different oscillating amplitudes of 50, 25, 17.5, 10, and 5 nm [28]. The oscillation frequency was fixed at 1 kHz in all of the experiments. The corresponding shear rate ranged from  $10^2$  to  $10^6$  s $^{-1}$ . We used a magnetic disk coated with a 2.0 nm thick Z03 film. We calculated the damping coefficient  $c_f$  and elastic coefficient  $k_f$  from the measured probe amplitude and phase shift by using (13). Since the sample was Z03, which is viscosity dominant, the elasticity  $k_f$  was quite small and comparable to the noise level. Therefore, at this point, we are not able to discuss the

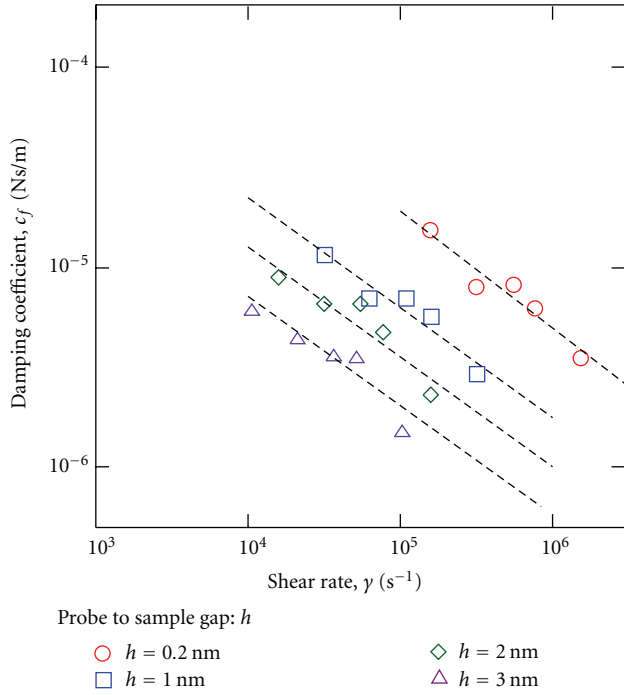


FIGURE 16: The relationship between the shear rate and viscous coefficient,  $c_f$  [28].

share rate dependence of  $k_f$ . The shear rate dependence of  $c_f$  is shown in Figure 16 on a log-log plot. Plots are shown for shearing gaps of 0.2, 1.0, 2.0, and 3.0 nm in the approaching process. The shear rates are calculated from the gap widths and maximum shearing speed, which were determined by the oscillation frequency and amplitude. As shown in Figure 16,  $c_f$  decreased exponentially with increasing shear rate. This phenomenon is generally known as shear thinning, and the behavior is well expressed by the empirical power law

$$\log c_f = -\alpha \log \gamma + \beta, \quad (14)$$

where  $\alpha$  and  $\beta$  are fitting parameters and  $\gamma$  represents the shear rate. This is shown by the dashed lines in Figure 16. The shear rate dependence of  $c_f$  is well represented by the empirical power law. Such a shear rate dependence has not been observed for thicker Z03 films [29], and we therefore consider the shear thinning to be unique to the nanometer-thick film.

## 5. Conclusion

We developed the fiber wobbling method (FWM) for dynamic viscoelastic measurements of molecularly thin lubricant films coated on magnetic disk surfaces. The FWM enables us to measure the shear force with a sensitivity of 0.1 nN and control the shearing gap with a resolution on the order of 0.1 nm, both of which are requirements for molecularly thin-film measurements.

We revealed in measurements using the immersed system that lubricants confined in a nanometer-sized gap width had

an enhanced viscosity that was several dozen times larger than the bulk viscosity. In addition, the elasticity, which is not observed in the bulk state, appeared at gaps of less than a few nanometers. The appearance of elasticity is considered to be due to the interaction between the adsorbed layers formed on both solid surfaces.

In the thin-film system, we succeeded in measuring the viscosity and elasticity of molecularly thin films and observed a strong dependence of the viscoelasticity on the bonding ratio. In addition, we found that shear thinning caused a decrease in the viscosity as the shear rate increased. Shear-thinning viscosity decrease is the opposite effect of the confinement-induced viscosity increase. Therefore, both the shearing gap and shear rate must be considered carefully to predict the friction force acting on the head during contact with the disk surface. The bonding ratio and type of lubricant will also affect the friction force. How these factors define the mechanical properties of the lubricant films must be clarified for the optimal design of future HDI. So far, the FWM has two major drawbacks. One is that the shearing speed is much slower than that in an actual HDI, and the other is that we cannot determine the contact area between the probe tip and lubricant films in the thin-film system, which is the biggest obstacle for a quantitative evaluation of the viscoelasticity. In our recent work, we succeeded in taking high-speed measurements using the resonant oscillation of the probe [30]. Additionally, observation of the contact area in the FWM measurements is one of our ongoing projects, and the first report will appear elsewhere. We believe that the FWM will be a promising and powerful method for improving our understanding of the basic phenomena concerning HDI lubrication.

## Acknowledgments

The present research was partially supported by a Grant-in-Aid for Scientific Research from the Japan Society for the Promotion of Science (no. 23686028), by the Storage Research Consortium, and by the Asahi Glass Foundation.

## References

- [1] H. W. Hu, G. A. Carson, and S. Granick, "Relaxation time of confined liquids under shear," *Physical Review Letters*, vol. 66, no. 21, pp. 2758–2761, 1991.
- [2] G. Luengo, F. J. Schmitt, R. Hill, and J. Israelachvili, "Thin film rheology and tribology of confined polymer melts: contrasts with bulk properties," *Macromolecules*, vol. 30, no. 8, pp. 2482–2494, 1997.
- [3] M. Ruths and S. Granick, "Tribology of confined fomblin-Z perfluoropolyalkylethers: molecular weight dependence and comparison between unfunctionalized and telechelic chains," *Tribology Letters*, vol. 7, no. 4, pp. 161–172, 1999.
- [4] G. B. McKenna, "Ten (or more) years of dynamics in confinement: perspectives for 2010," *European Physical Journal*, vol. 189, no. 1, pp. 285–302, 2010.
- [5] G. B. McKenna, "International workshop on dynamics in confinement : a personal summary," *Journal de Physique IV France*, vol. 10, pp. Pr7-343–PPr7346, 2000.

- [6] G. B. McKenna, "Status of our understanding of dynamics in confinement: perspectives from Confit 2003," *European Physical Journal E*, vol. 12, no. 1, pp. 191–194, 2003.
- [7] G. B. McKenna, "Confit III. Summary and perspectives on dynamics in confinement," *European Physical Journal: Special Topics*, vol. 141, no. 1, pp. 291–301, 2007.
- [8] C. L. Jackson and G. B. McKenna, "The glass transition of organic liquids confined to small pores," *Journal of Non-Crystalline Solids*, vol. 131–133, no. 1, pp. 221–224, 1991.
- [9] C. L. Jackson and G. B. McKenna, "Vitrification and crystallization of organic liquids confined to nanoscale pores," *Chemistry of Materials*, vol. 8, no. 8, pp. 2128–2137, 1996.
- [10] W. J. Orts, J. H. Van Zanten, W. L. Wu, and S. K. Satija, "Observation of temperature dependent thicknesses in ultra-thin polystyrene films on silicon," *Physical Review Letters*, vol. 71, no. 6, pp. 867–870, 1993.
- [11] J. A. Forrest, K. Dalnoki-Veress, J. R. Stevens, and J. R. Dutcher, "Effect of free surfaces on the glass transition temperature of thin polymer films," *Physical Review Letters*, vol. 77, no. 10, pp. 2002–2005, 1996.
- [12] J. A. Forrest, K. Dalnoki-Veress, and J. R. Dutcher, "Interface and chain confinement effects on the glass transition temperature of thin polymer films," *Physical Review E*, vol. 56, no. 5, pp. 5705–5716, 1997.
- [13] S. Kawana and R. A. L. Jones, "Character of the glass transition in thin supported polymer films," *Physical Review E*, vol. 63, no. 2, pp. 1–6, 2001.
- [14] J. L. Keddie, R. A. L. Jones, and R. A. Cory, "Interface and surface effects on the glass-transition temperature in thin polymer films," *Faraday Discussions*, vol. 98, pp. 219–230, 1994.
- [15] J. Dobbertin, A. Hensel, and C. Schick, "Dielectric spectroscopy and calorimetry in the glass transition region of semicrystalline poly(ethylene terephthalate)," *Journal of Thermal Analysis*, vol. 47, no. 4, pp. 1027–1040, 1996.
- [16] S. Wong, R. A. Vaia, E. P. Giannelis, and D. B. Zax, "Dynamics in a poly(ethylene oxide)-based nanocomposite polymer electrolyte probed by solid state NMR," *Solid State Ionics*, vol. 86–88, no. 1, pp. 547–557, 1996.
- [17] J. Y. Park and G. B. McKenna, "Size and confinement effects on the glass transition behavior of polystyrene/o-terphenyl polymer solutions," *Physical Review B*, vol. 61, no. 10, pp. 6667–6676, 2000.
- [18] F. Kremer, A. Huwe, M. Arndt, P. Behrens, and W. Schwieger, "How many molecules form a liquid?" *Journal of Physics Condensed Matter*, vol. 11, no. 10, pp. A175–A188, 1999.
- [19] K. Tanaka, Y. Tateishi, Y. Okada, T. Nagamura, M. Doi, and H. Morita, "Interfacial mobility of polymers on inorganic solids," *Journal of Physical Chemistry B*, vol. 113, no. 14, pp. 4571–4577, 2009.
- [20] F. He, L. M. Wang, and R. Richert, "Confined viscous liquids: interfacial versus finite size effects," *European Physical Journal: Special Topics*, vol. 141, no. 1, pp. 3–9, 2007.
- [21] R. D. Priestley, C. J. Ellison, L. J. Broadbelt, and J. M. Torkelson, "Materials Science: structural relaxation of polymer glasses at surfaces, interfaces, and in between," *Science*, vol. 309, no. 5733, pp. 456–459, 2005.
- [22] R. J. Waltman, "Experimental and theoretical investigation of the effect of lubricant structure on the bonding kinetics of perfluoroalkylpolyethers on CH(x) amorphous hydrogenated carbon," *Chemistry of Materials*, vol. 12, no. 7, pp. 2039–2049, 2000.
- [23] P. H. Kasai, "Carbon overcoat: structure and bonding of Z-DOL," *Tribology Letters*, vol. 13, no. 3, pp. 155–166, 2002.
- [24] S. Itoh, K. Fukuzawa, Y. Hamamoto, H. Zhang, and Y. Mitsuya, "Fiber wobbling method for dynamic viscoelastic measurement of liquid lubricant confined in molecularly narrow gaps," *Tribology Letters*, vol. 30, no. 3, pp. 177–189, 2008.
- [25] S. Itoh, K. Fukuzawa, K. Takahashi, T. Ando, H. Zhang, and Y. Mitsuya, "Optimization of dynamic shear force measurement for fiber wobbling method," *Microsystem Technologies*, vol. 11, no. 8–10, pp. 894–900, 2005.
- [26] Y. Hamamoto, S. Itoh, K. Fukuzawa, and H. Zhang, "Viscoelastic properties of monolayer lubricant films during touch-down and take-off behavior measured by fiber wobbling method," *Tribology Online*, vol. 6, no. 1, pp. 83–95, 2011.
- [27] S. Itoh, K. Fukuzawa, Y. Hamamoto, and H. Zhang, "Opposing effects of confinement and confinement-induced shear-thinning on viscoelastic properties of liquid lubricant in nanometer-scale gaps," *Tribology International*, vol. 44, no. 11, pp. 1333–1339, 2011.
- [28] Y. Hamamoto, S. Itoh, K. Fukuzawa, and H. Zhang, "Shear thinning behavior of monolayer liquid lubricant films measured by fiber wobbling method," *Journal of Physics*, vol. 258, no. 1, Article ID 012010, pp. 1–10, 2010.
- [29] C. D. Hahm and B. Bhushan, "High shear rate viscosity measurements of perfluoropolyether lubricants for magnetic thin-film rigid disks," *Journal of Applied Physics*, vol. 81, no. 8, pp. 5384–5386, 1997.
- [30] S. Itoh, K. Fukuzawa, K. Imai, and K. Ishii, "High-Speed Friction Measurements for a Molecularly Thin Lubricant Film Using a Fiber Wobbling Method," in *Proceedings of the IEEE International Magnetics Conference (INTERMAG '12)*, HH-06, Vancouver, Canada, 2012.

## Research Article

# Dependence of Pin Surface Roughness for Friction Forces of Ultrathin Perfluoropolyether Lubricant Film on Magnetic Disks by Pin-on-Disk Test

H. Tani,<sup>1</sup> Y. Mitsuya,<sup>2</sup> T. Kitagawa,<sup>3</sup> and N. Tagawa<sup>1</sup>

<sup>1</sup> Mechanical Engineering Department and High Technology Center, Kansai University, Osaka 564-8680, Japan

<sup>2</sup> Nagoya Industrial Science Research Institute, Nagoya 464-0819, Japan

<sup>3</sup> Department of Research and Development, Nomura Plating Co., Ltd., Osaka 555-0033, Japan

Correspondence should be addressed to H. Tani, hrstani@kansai-u.ac.jp

Received 14 August 2012; Accepted 4 December 2012

Academic Editor: Tom Karis

Copyright © 2012 H. Tani et al. This is an open access article distributed under the Creative Commons Attribution License, which permits unrestricted use, distribution, and reproduction in any medium, provided the original work is properly cited.

We fabricated supersmooth probes for use in pin-on-disk sliding tests by applying gas cluster ion beam irradiation to glass convex lenses. In the fabrication process, various changes were made to the irradiation conditions; these included one-step irradiation of Ar clusters or two-step irradiation of Ar and N<sub>2</sub> clusters, with or without Ar cluster-assisted tough carbon deposition prior to N<sub>2</sub> irradiation, and the application of various ion doses onto the surface. We successfully obtained probes with a centerline averaged surface roughness that ranged widely from 1.08 to 4.30 nm. Using these probes, we measured the friction forces exerted on magnetic disks coated with a molecularly thin lubricant film. Perfluoropolyether lubricant films with different numbers of hydroxyl end groups were compared, and our results indicated that the friction force increases as the surface roughness of the pin decreases and that increases as the number of hydroxyl end groups increases.

## 1. Introduction

In magnetic disk storage, the head-disk spacing must be minimized to maximize the bit density. Most recently, a spacing of 4–5 nm has been attained, which is the spacing between the bottom of the head pole tip and the rigid disk surface. To further reduce this spacing, the lubricant film coated over the disk was thinned and strengthened using lubricants with increased molecular polarity. Some of the commonly used lubricants are functionalized perfluoropolyethers (PFPE) with a linear backbone and hydroxyl end groups (−OH) called PFPE polar lubricants (Solvay-Solexis). The number of −OH groups has been increased in order to ensure that the lubricant film has a relatively strong retention function [1, 2].

Recently, the dynamic flying height (DFH) has been employed during read/write operations. After being heated, the bottom of the head pole tip protrudes, forming a hemisphere-shaped protrusion with a radius of curvature of several millimeters [3]. Therefore, the evaluation of the tribological features of the protruding head and that of the

disk lubricated with a molecularly thin polar lubricant film are of significant concern. Shimizu et al. studied the slider dynamics during the touchdown of sliders by using a laser Doppler vibrometer (LDV), acoustic emission (AE) measurement, and friction force measurement. They concluded that the friction force at the head disk interface (HDI) continues to increase during the touchdown sequence, even though the slider vibration and the AE signal decrease when the heater power is increased. The friction force at the HDI needs to be decreased to further reduce the HDI clearance [4]. Sonoda et al. studied the tribological properties of two types of PFPE lubricants on the basis of the component level and by performing drive level tests. Disks having a lower friction property and lower surface energy showed better HDI performances [5].

To date, many experimental studies have addressed the tribological behavior of monolayer lubricants, employing surface force apparatus (SFA), friction force microscopy (FFM), and the fiber wobbling method (FWM). Because each approach uses an elaborated probe, the direct application

of the probe to an actual head-disk interface is difficult. The radius of curvature of the probe for SFA is around 10 mm [6], which is comparable to that of an actual head-disk interface subject to DFH. For FFM, the radius is around 20 nm, and for FWM, it is around 4–100  $\mu\text{m}$ ; the values in both cases are considerably small [7, 8]. Large differences are observed between the friction forces measured using SFA and FFM on PFPE Z and polydimethylsiloxane (PDMS) monolayer films; these differences are attributed to whether or not the probe penetrated the film [9]. Recently, friction coefficients obtained using FFM have been confirmed to be almost the same when FFM experiments were performed under a very light load [10]. These methods are based on ideal conditions without roughness (SFA) or with a very sharp tip (FFM), which are considerably different from the conditions of an actual head-disk interface. The friction force basically consists of two components: one is load-controlled and the other is adhesion-controlled [11]. The former component represents the friction linearly varying with an external normal load, known as Amonton's law, and the latter represents the nonlinear friction-versus-load characteristic, which is typically in proportion to 2/3 of the power of the loading force. In the case of multiasperity contact, load-controlled friction becomes dominant, whereas in the case of single-asperity contact, adhesion-controlled friction becomes dominant. Switching from multiasperity to single-asperity contact is induced by confining the contaminant film that intervenes between the two surfaces [12].

These results suggest that even nanometer-scale roughness profoundly affects the tribological behavior of monolayer lubricant films, and thus, a supersmooth probe or probes with different roughnesses are required. In this study, to evaluate the tribological behavior of a thin lubricant film under similar geometric conditions of a practical head-disk interface, we fabricated supersmooth probes for use in pin-on-disk sliding tests by applying gas cluster ion beam (GCIB) irradiation [13, 14] to commercially available glass convex lenses. We successfully obtained probes with a centerline averaged surface roughness ( $R_a$ ) that ranged from 1.08 to 4.30 nm. Using these probes, we measured the friction forces exerted on magnetic disks coated with a PFPE lubricant film having different numbers of –OH groups. The results indicated that the newly developed probe is useful for evaluating monolayer lubricant films on a practical scale.

## 2. Modification and Smoothing of Glass Sliding Pins

Considering the millimeter-sized radius of curvature of the protruded head, we selected a BK7 planoconvex lens (Sigma Koki; SLB-05-10P) with a radius of curvature of 5.19 mm and a diameter of 5 mm. To modify the surface roughness of the lens, we applied GCIB processing to its surface. Because gas cluster ions are composed of thousands of gaseous atoms, the energy distributed to each atom remains within ultralow levels, even though the GCIB energy is high. This permits surface modifications such as etching, smoothing, and deposition to be performed without strongly damaging the surface. The smoothing effects obtained using GCIB

processing depend on parameters such as the type of atoms, electron bombardment energy, ion acceleration energy, and amount of dosed clusters [13]. Our aim is to optimize these parameters in order to smoothen the surface of the glass lens. Based on past research, the electron bombardment and the ion acceleration energies were fixed at 150 eV and 7 keV, respectively. Ar clusters were employed for the main processing and N<sub>2</sub> clusters for additional processing. Hereafter, Ar cluster irradiation is called one-step irradiation, and N<sub>2</sub> cluster irradiation, after Ar cluster irradiation, is called two-step irradiation. We also applied GCIB-assisted diamond-like-carbon (DLC) deposition (Nomura Plating; tough carbon) [14] to the Ar-GCIB-modified surface as successive processing from Ar irradiation by sublimating the C<sub>60</sub> fullerenes into the deposition chamber. The thickness of the tough carbon was fixed at 300 nm. Finally, N<sub>2</sub> clusters were applied to the top surface. All of the conditions for GCIB processing are listed in Table 1. Two glass pins were prepared for each condition.

After the GCIB operations, the surface roughnesses of the top surfaces were measured by atomic force microscopy (AFM) using Nanoinstrument IIIa. Typical surface profiles of the original surface and the surface fabricated by the GCIB irradiation on glass probe surfaces without the DLC film are shown in Figure 1. Table 1 shows the GCIB conditions and the average roughness obtained after 3 sets of measurements. Figure 1(a) shows the original glass surface for pin 1 in Table 1, Figure 1(b) shows that for pin 2, and Figure 1(c) shows that for pin 3. For reference, the AFM images are also shown in Figures 3(a) and 3(c) for the original surface and the smoothest surface, which correspond to Figures 1(a) and 1(c). Although Figures 1(a) and 1(c) show noise patterns in subnanometers, these noise patterns were generated by the external vibration and the measured roughness values were not affected considerably by the noise. The roughness of the glass probe surface was reduced by the two-step GCIB irradiation, although the asperity height of the probe surface was increased significantly by the one-step GCIB irradiation. The roughness profiles of the DLC surface on the probes irradiated by the GCIB are shown in Figure 2. Figure 2(a) shows pin 4, Figure 2(b) shows pin 5, and Figure 2(c) shows pin 6. For reference, the AFM images are also shown in Figures 3(d) to 3(f), which correspond to Figures 2(a) to 2(c). After GCIB irradiation to DLC film surface, there were more asperities on the surface than the original surface. Therefore, the one-step Ar GCIB irradiation increases the asperity height on both glass and DLC surface and the two-step Ar-N<sub>2</sub> GCIB irradiation reduced the surface roughness.

Using these figures, we could compare the changes in roughness produced by GCIB processing in terms of  $R_a$  units, which are defined as the centerline averaged roughness over a roughness curve,  $R_q$ , which is defined as the root mean square roughness, and  $R_{p,\text{ave}}$  which is defined as the maximum peak height averaged over the three highest points in a measured area of  $25 \times 25 \mu\text{m}^2$ . We chose the  $R_{p,\text{ave}}$  value as a representative value for determining the distance of separation between two solid surfaces in contact with one another. For Figure 2(a), the original glass surface, sharp peaks were sparsely distributed, which can be seen in

TABLE 1: Conditions for GCIB processing and surface roughness.

No.	Dose, ion/cm <sup>2</sup>		DLC	Roughness, nm		
	Ar × 10 <sup>16</sup>	N <sub>2</sub> × 10 <sup>16</sup>	nm	R <sub>a</sub>	R <sub>q</sub>	R <sub>p,ave</sub>
1	0	0	0	1.40	3.01	10.26
2	2	0	0	4.30	6.35	34.83
3	1	2	0	1.08	1.40	4.99
4	1	0	300	1.51	2.16	17.33
5	2	0	300	1.07	1.39	7.87
6	4	0	300	1.05	1.37	13.63

Figure 2(a) as white colored spots. R<sub>a</sub> was 1.40 nm, a value that indicated a well-finished surface for optical use, and R<sub>p,ave</sub> was 10.26 nm, which was seven times higher than R<sub>a</sub>. For Figure 2(b), one-step GCIB without DLC, the degree of roughness increased to more than that of the original surface, which indicated that the Ar clusters were considerably strong. In the case of Figure 2(c), two-step GCIB without DLC, the sparsely distributed peaks decreased to R<sub>p,ave</sub> of 4.99 nm, which indicated that N<sub>2</sub> GCIB was effective in smoothing and that R<sub>a</sub> improved to 1.08 nm. As a result, we obtained a wide variety of surface roughnesses ranging from 1.08 to 4.30 nm in R<sub>a</sub> units and from 4.99 to 34.83 nm in R<sub>p,ave</sub> units.

### 3. Friction Tests

Pin-on-disk-type friction tests were performed using GCIB-treated planoconvex lenses that were glued to a commercially available flying head slider and loaded by a slider suspension spring (with a spring constant of 19.0 N/m) onto a magnetic disk at a fixed load of 9.8 mN. Friction tests were performed five times for the same pin on the same sliding track, which was slightly shifted for each pin from the inside to the outside at intervals of 1 mm, with slightly varying disk rotation, to obtain a constant velocity of 2 mm/s. This rotational velocity was considerably slower than the actual HDI velocities. However, the friction forces measured by the pin-on-disk tester using the low rotational velocity were useful for comparing the basic tribological properties of lubricant films on magnetic disks because it was obvious that the friction forces played an important role in the interaction between the slider and the disk surface, as described in some references [15, 16]. The pin was cleaned with a solvent (DuPont; Vertrel XF) when the disk was changed, that is, before every first rotation for the different lubricant films.

The experimental disks were coated with a nitrogenated, 4 nm thick DLC film with an R<sub>a</sub> value of 0.2 nm. The experimental lubricants were PFPE Z-dol (with a molecular weight of 2000) with one hydroxyl group (–OH) at each end, Z-Tetraol (2400) with two –OHs at each end, and Z-Tetraol-multidentate (Z-TMD; 3000) with an additional four –OHs on the main Z-Tetraol chain [1, 2], as shown in Figure 4.

The film thicknesses, measured with an ellipsometer (MARY by Five Lab. Co.), were 1.1, 1.2, and 0.8 nm, and the bonding thickness were measured one day after the friction measurements to be 20%, 66%, and 80% for Z-dol, Z-Tetraol, and Z-TMD, respectively. Here, the bonding ratio is defined as the ratio of the coated lubricant thickness

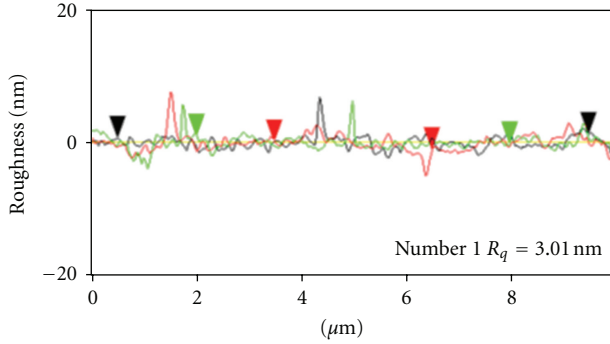
to the residual film thickness after rinsing the lubricant-coated surface with a solvent (Vertrel XF). The monolayer thickness of Z-dol2000 was approximately 1.4 nm, and that of Z-Tetraol was approximately 1.7 nm [17]. The monolayer thickness of Z-TMD was estimated to be of the same order as that of Z-dol2000 [18]. Note that the coated films in this study were either as thin as a monolayer or thinner. All experiments were performed in a clean booth in which the temperature ranged from 25° to 29° and the humidity from 55% to 65%.

### 4. Results and Discussions

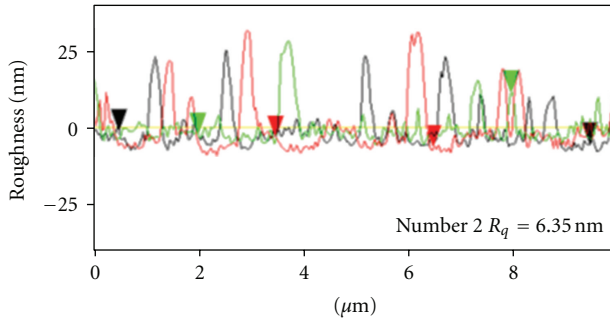
The experimental results are plotted in Figure 5, where Figure 5(a) shows the results for Z-dol, Figure 5(b) for Z-Tetraol, and Figure 5(c) for Z-TMD. The abscissa indicates the average peak height R<sub>p,ave</sub>, and the ordinate denotes the friction force F. In the figures, the symbols denote the BK7 original glass surface, the BK7 glass surface after Ar-GCIB processing, the BK7 glass surface after Ar/N<sub>2</sub>-GCIB processing, and the DLC surface after Ar-GCIB processing. The range of variation of the five experiments conducted under the same condition is marked by short bars sandwiching the symbols. These bars corresponded to the maximum and minimum values of the measured friction forces.

The data points were fairly scattered because of the local variations in the surface features, the film thicknesses, the roughness of the disk surfaces, and the sliding-induced vibration. In the case of the Z-dol film, the friction force remained nearly constant with varying roughness. This was attributed to the fact that the bonding ratio was as low as 20%, and, thus, the mobility of unbonded molecules was large and the movable molecules with low viscosity between the probe and the disk surface reduced the friction force in the same manner as hydrodynamic lubrication, as illustrated in Figure 6.

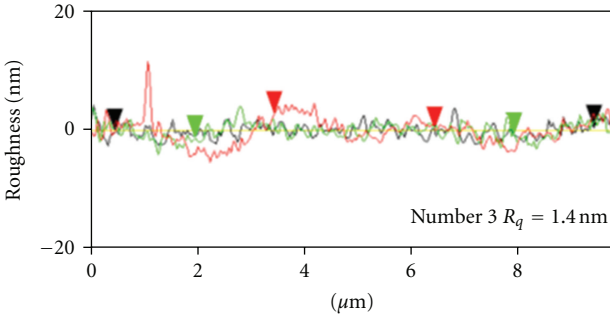
In the case of the Z-Tetraol film, the friction was almost unchanged for an R<sub>p,ave</sub> of more than 15 nm. However, when the roughness became smaller than 10 nm (at which point the R<sub>a</sub> value was roughly equivalent to the monolayer film thickness, as shown in Table 1), the scattering of the data points increased, but on average, the friction force tended to increase with decreasing roughness. Nevertheless, the bonding ratio was as high as 66%, and lubricant molecules could be removed for the relatively rough probes because of the high contact pressure; in the case of the relatively smooth probes, the contact pressure decreased because of



(a) BK7 glass lens original surface



(b) One-step GCIB irradiation without DLC

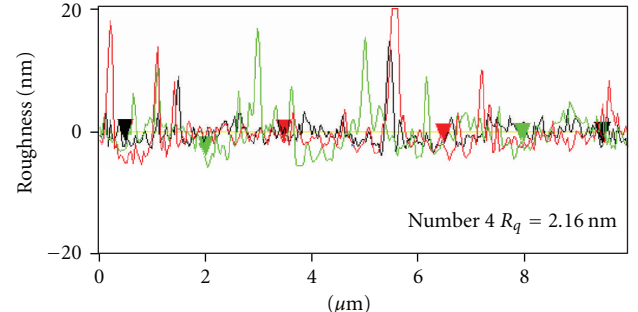


(c) Two-step CCIB irradiation without DLC

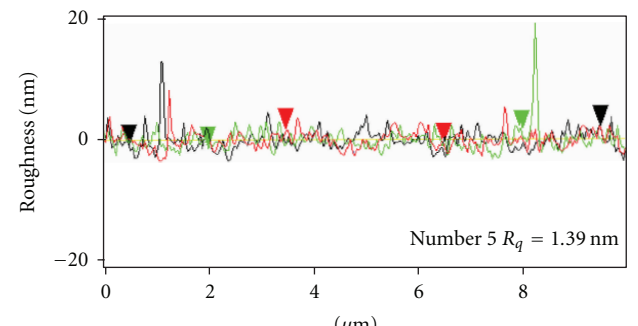
FIGURE 1: Changes in surface roughness profiles with GCIB irradiation without DLC. The abscissa indicates the scanning distance in micrometers, and the ordinate indicates the roughness amplitude in nanometers.

the increased contact area and many bonded molecules remained inside the contact area after being deformed, as illustrated in Figure 7, which was the confinement condition. Confined molecules exhibited a solid-like feature, and thus, the single-asperity condition became dominant [12]. This was considered a major reason for increased friction with decreasing roughness.

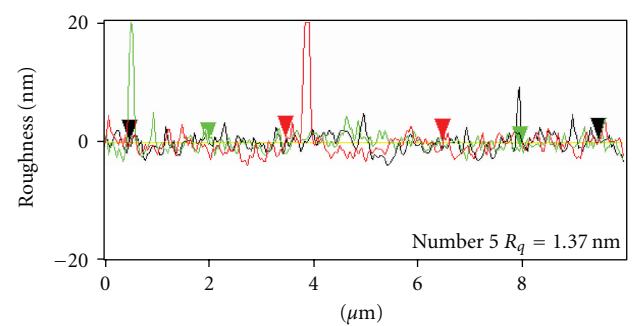
In the case of the Z-TMD film, the increase in friction with decreasing roughness became more pronounced. This was attributed to the bonding ratio that was as high as 80%, which was considerably higher than that in the case of Z-Tetraol, and, thus, a large majority of molecules remained inside the contact area. This strengthened the shift from the multiple- to single-asperity contact. Note that the friction forces were nearly equal for different lubricants for



(a) GCIB irradiation (Ar: 1e16) with DLC



(b) GCIB irradiation (Ar: 2e16) with DLC



(c) GCIB irradiation (Ar: 4e16) with DLC

FIGURE 2: Changes in surface roughness profiles with GCIB irradiation with DLC. The abscissa indicates the scanning distance in micrometers, and the ordinate indicates the roughness amplitude in nanometers.

a relatively large roughness range, which is a basic feature of Amonton's law followed from multiple-asperity contact. On the basis of these results, we concluded that the friction forces measured by the relatively smooth probes might depend on the dynamic viscosity of the lubricant materials, because the dynamic viscosity of Z-TMD, Z-Tetraol, and Z-dol2000 was 23 Pas, 3.5 Pas, and 0.153 Pas, respectively, [19, 20]. Further studies are required to clarify the differences in the friction property of these lubricants.

With respect to the effect of DLC coating, the effect reducing the friction forces was estimated to be small, because the trend of roughness dependence for the DLC-coated pin agreed with that for the glass pin without DLC in the case of Z-Tetraol and Z-TMD. The friction measurements did not show changes at small peak heights

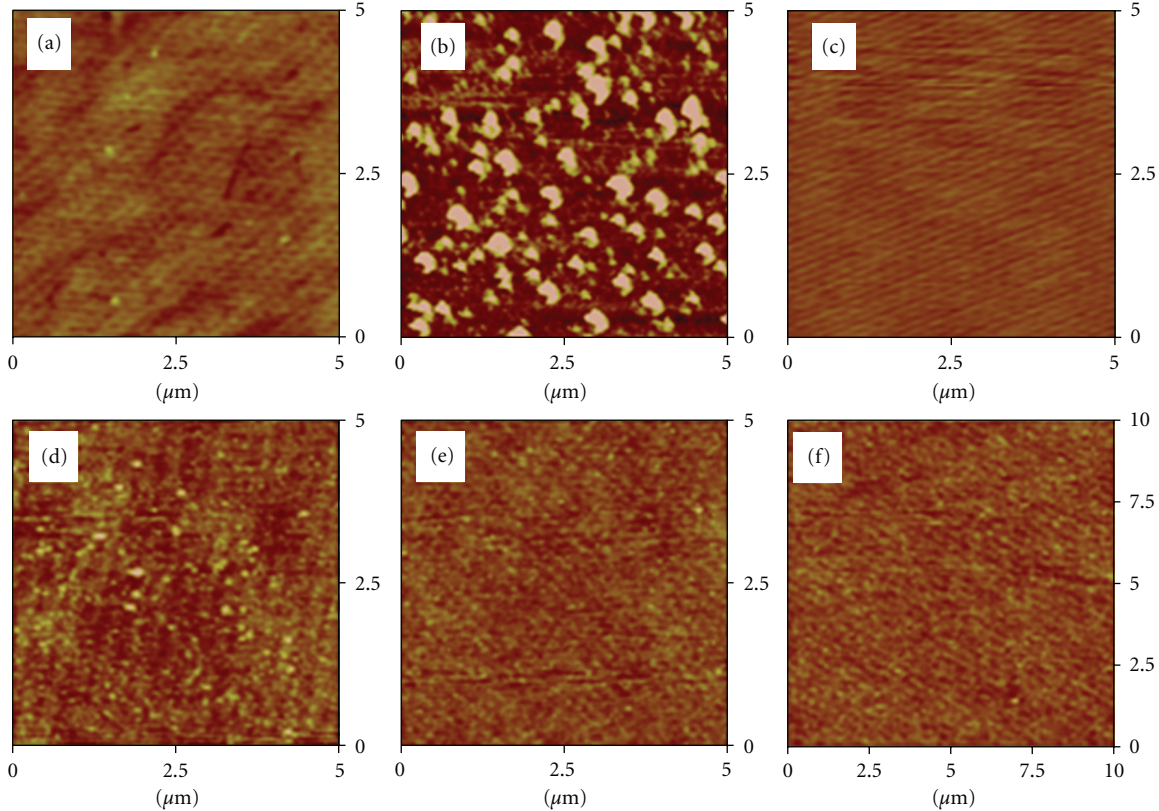


FIGURE 3: Comparison of tapping-mode AFM images of planoconvex lens before and after GCIB processing. (a) Original surface of glass lens, (b) one-step GCIB irradiation without DLC, (c) two-step GCIB irradiation without DLC, (e) one-step ( $\text{Ar}: 1 \times 10^{16} \text{ dose/cm}^2$ ) GCIB irradiation on DLC, (d) one-step ( $\text{Ar}: 2 \times 10^{16} \text{ dose/cm}^2$ ) GCIB irradiation on DLC, and (f) one-step ( $\text{Ar}: 4 \times 10^{16} \text{ dose/cm}^2$ ) GCIB irradiation on DLC.

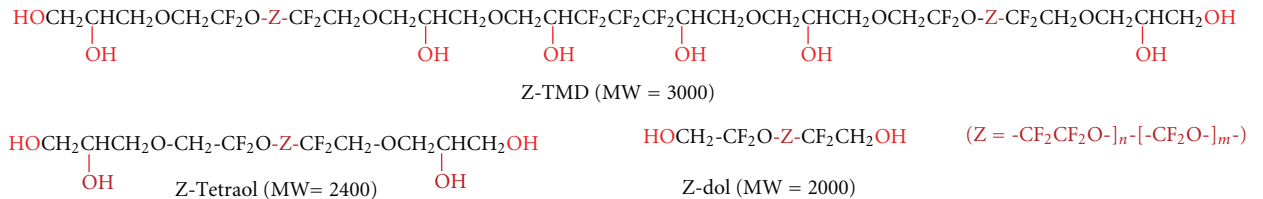


FIGURE 4: Chemical structures of PFPE lubricants used in this study.

for Z-dol-lubricated disks in contrast to the other lubricants evaluated.

On the basis of the previous experimental tests, we confirmed the usefulness of GCIB-fabricated probes with a wide variety of roughnesses for the evaluation of monolayer lubricant films. However, there is a possibility of a change in the chemical properties of the probe surface fabricated using the GCIB fabrication method, for example, the change in the lubricant affinity on the probe surface by argon and nitrogen implantation by GCIB irradiation [21] or DLC coating by the GCIB treatment [22]. Similarly, the DLC coating using the GCIB treatment might change the mechanical properties of the probe surface, for example, Young's modulus or hardness. The effects on these property changes brought about by

GCIB fabrication need to be studied further in order to understand them precisely.

## 5. Conclusions

We fabricated supersmooth probes for pin-on-disk sliding tests by applying gas cluster ion beam (GCIB) irradiation to glass convex lenses. Under varying GCIB processing conditions, we obtained a wide range of surface roughnesses of the probes, with values that ranged from 1.08 to 4.30 nm in  $R_a$  units. Using these probes, we compared PFPE monolayer lubricant films with different numbers of hydroxyl end groups (Z-dol, Z-Tetraol, and Z-TMD). In the case of Z-dol, the friction force remained nearly constant over the

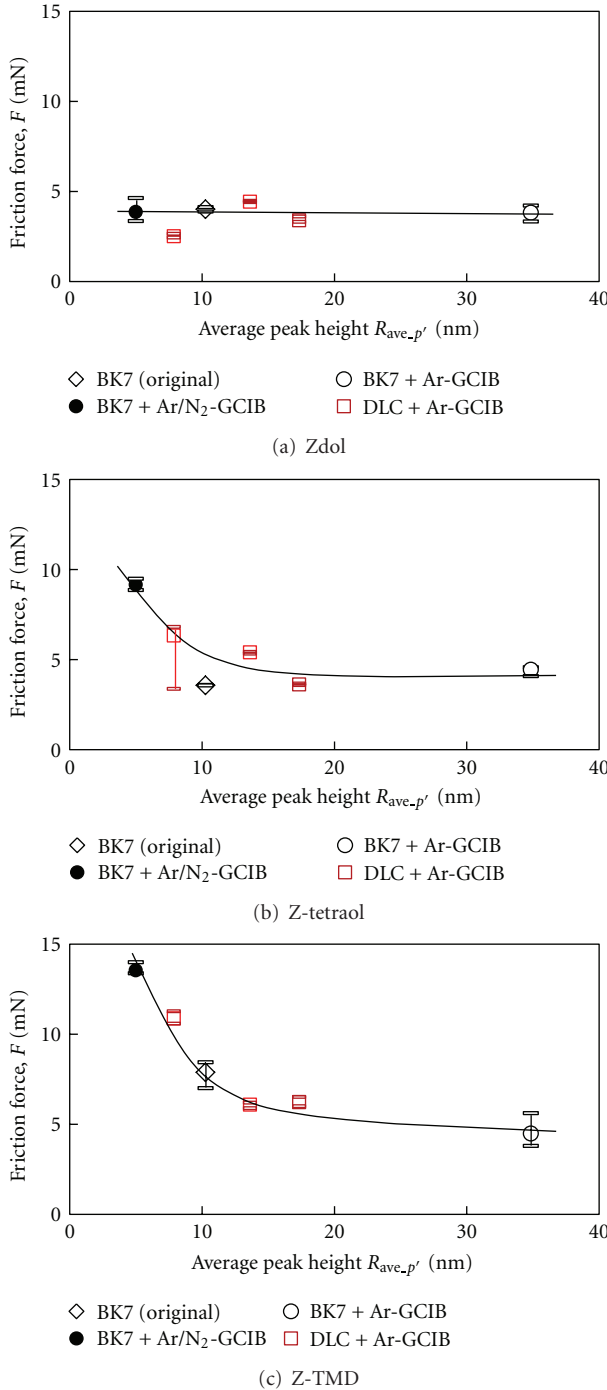


FIGURE 5: Comparison of friction forces among three types of lubricants with different numbers of hydroxyl end groups.

experimental roughness range. In the case of Z-Tetraol and Z-TMD, the friction force increased with decreasing roughness.

## Acknowledgments

This work was supported by a “Strategic Project to Support the Formation of Research Bases at Private Universities”: Matching Fund Subsidy, a Grant-in-Aid for Scientific

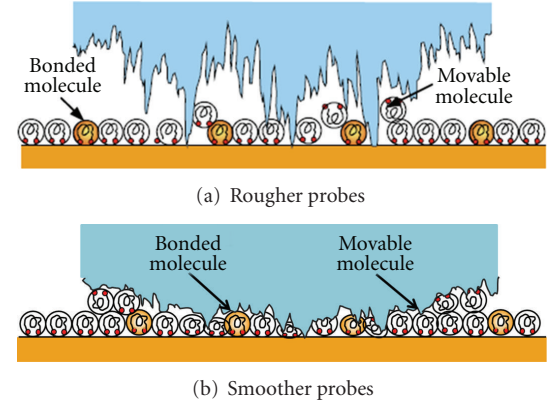


FIGURE 6: Multiple-asperity contact model that holds both for relatively rough and relatively smooth probes for a movable molecule dominant film.

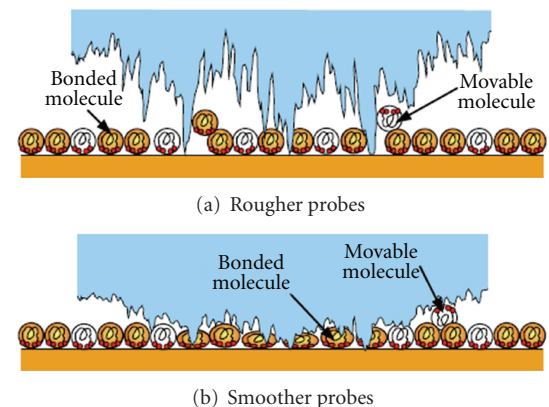


FIGURE 7: Transition model from multiple- to single-asperity contact that occurs with decreasing surface roughness for a bonded molecule dominant film.

Research (C; no. 225601530001) from the Ministry of Education, Culture, Sports, Science and Technology, and a grant from the Storage Research Consortium (SRC). The authors would like to express their gratitude to Dr. B. Marchon of HGST for his generous donation of the lubricants used in the experiments.

## References

- [1] B. Marchon, X. C. Guo, T. Karis et al., “Fomblin multidentate lubricants for ultra-low magnetic spacing,” *IEEE Transactions on Magnetics*, vol. 42, no. 10, pp. 2504–2506, 2006.
- [2] R. J. Waltman, H. Deng, G. J. Wang, H. Zhu, and G. W. Tyndall, “The effect of PFPE film thickness and molecular polarity on the pick-up of disk lubricant by a low-flying slider,” *Tribology Letters*, vol. 39, no. 2, pp. 211–219, 2010.
- [3] M. Kurita, T. Shiramatsu, K. Miyake et al., “Active flying-height control slider using MEMS thermal actuator,” *Microsystem Technologies*, vol. 12, no. 4, pp. 369–375, 2006.
- [4] Y. Shimizu, J. Xu, H. Kohira, K. Kuroki, and K. Ono, “Experimental study on slider dynamics during touchdown by using

- thermal flying-height control," *Microsystem Technologies*, vol. 17, no. 5–7, pp. 897–902, 2011.
- [5] K. Sonoda, D. Shirakawa, T. Yamamoto, and J. Itoh, "The tribological properties of the new structure lubricant at the head-disk interface," *IEEE Transactions on Magnetics*, vol. 43, no. 6, pp. 2250–2252, 2007.
- [6] J. N. Israelachvili, *Intermolecular & Surface Forces*, Academic Press, 2nd edition, 1992.
- [7] S. Itoh, K. Fukuzawa, Y. Hamamoto, H. Zhang, and Y. Mitsuya, "Fiber wobbling method for dynamic viscoelastic measurement of liquid lubricant confined in molecularly narrow gaps," *Tribology Letters*, vol. 30, no. 3, pp. 177–189, 2008.
- [8] S. Itoh, K. Fukuzawa, Y. Hamamoto, and H. Zhang, "Viscoelasticity of PFPE lubricant films on magnetic disk surface measured by optical-fiber-based nanorheometry," in *Proceedings of the Asia-Pacific Magnetic Recording Conference (APMRC'10)*, BA2, Singapore, November 2010.
- [9] P. M. McGuigan, J. Zhang, and S. M. Hsu, "Comparison of friction measurements using the atomic force microscope and the surface forces apparatus: the issue of scale," *Tribology Letters*, vol. 10, no. 4, pp. 217–223, 2001.
- [10] M. Ruths, "Boundary friction of aromatic self-assembled monolayers: comparison of systems with one or both sliding surfaces covered with a thiol monolayer," *Langmuir*, vol. 19, no. 17, pp. 6788–6795, 2003.
- [11] M. Ruths, "Friction of mixed and single-component aromatic monolayers in contacts of different adhesive strength," *Journal of Physical Chemistry B*, vol. 110, no. 5, pp. 2209–2218, 2006.
- [12] C. A. J. Putman, M. Igarashi, and R. Kaneko, "Singleasperity friction in friction force microscopy: the composite-tip model," *Applied Physics Letters*, vol. 66, pp. 3221–3223, 1995.
- [13] T. Hirota, N. Toyoda, A. Yamamoto, and I. Yamada, "Modification and smoothing of patterned surface by gas cluster ion beam irradiation," *Applied Surface Science*, vol. 256, no. 4, pp. 1110–1113, 2009.
- [14] T. Kitagawa, I. Yamada, N. Toyoda et al., "Hard DLC film formation by gas cluster ion beam assisted deposition," *Nuclear Instruments and Methods in Physics Research, Section B*, vol. 201, no. 2, pp. 405–412, 2003.
- [15] C.-D. Yeo, M. Sullivan, S. C. Lee, and A. A. Polycarpou, "Friction force measurements and modeling in hard disk drives," *IEEE Transactions on Magnetics*, vol. 44, no. 1, pp. 157–162, 2008.
- [16] A. I. Vakis, S.-C. Lee, and A. A. Polycarpou, "Dynamic head-disk interface instabilities with friction for light contact (surfing) recording," *IEEE Transactions on Magnetics*, vol. 45, no. 11, pp. 4966–4971, 2009.
- [17] H. Tani, T. Shimizu, N. Kobayashi, Y. Taniike, K. Mori, and N. Tagawa, "Study of molecular conformation of PFPE lubricants with multidentate functional groups on magnetic disk surface by experiments and molecular dynamics simulations," *IEEE Transactions on Magnetics*, vol. 46, no. 6, pp. 1420–1423, 2010.
- [18] H. Chen, Q. Guo, and M. S. Jhon, "Effects of molecular structure on the conformation and dynamics of perfluoropolyether nanofilms," *IEEE Transactions on Magnetics*, vol. 43, no. 6, pp. 2247–2249, 2007.
- [19] X. C. Guo, B. Knigge, B. Marchon, R. J. Waltman, M. Carter, and J. Burns, "Multidentate functionalized lubricant for ultralow head/disk spacing in a disk drive," *Journal of Applied Physics*, vol. 100, no. 4, Article ID 044306, 2006.
- [20] [http://bikvar.ru/Fombl/Magn\\_disk.pdf](http://bikvar.ru/Fombl/Magn_disk.pdf).
- [21] N. Toyoda, I. Yamada, H. Tani, and Y. Sakane, "Surface characterization and lubricant performance on amorphous carbon films irradiated with gas cluster ion beams," *IEEE Transactions on Magnetics*, vol. 46, no. 6, pp. 1464–1466, 2010.
- [22] H. Zhang, Y. Mitsuya, K. Namba, H. Sakakibara, K. Fukuzawa, and S. Ito, "Changes of surface roughness and surface energy of glass surfaces with gas cluster ion beam treatment," *JAST Tribologist*, vol. 57, no. 2, pp. 116–122, 2012 (Japanese).

## Research Article

# Flying Instability due to Organic Compounds in Hard Disk Drive

Koji Sonoda

Advanced Technology Development Department, Storage Products Design and Production Division,  
Toshiba Corporation, 2-5-1 Kasama, Sakae-ku, Yokohama 247-8585, Japan

Correspondence should be addressed to Koji Sonoda, koji4.sonoda@toshiba.co.jp

Received 27 July 2012; Accepted 2 December 2012

Academic Editor: Norio Tagawa

Copyright © 2012 Koji Sonoda. This is an open access article distributed under the Creative Commons Attribution License, which permits unrestricted use, distribution, and reproduction in any medium, provided the original work is properly cited.

The influence of organic compounds (OCs) on the head-disk interface (HDI) was investigated in hard disk drives. The drives were tested at high temperature to investigate the influence of gaseous OC and to confirm if the gaseous OC forms droplets on head or disk. In the experiment, errors occurred by readback signal jump and we observed the droplets on the disk after full stroke seek operation of the drive. Our results indicate that the gaseous OC condensed on the slider and caused flying instability resulting in drive failure due to slider contact with a droplet of liquid OC. Furthermore, this study shows that kinetic viscosity of OC is an important factor to cause drive failure using alkane reagents.

## 1. Introduction

To achieve 1 Tb/in<sup>2</sup> recording density, a head-disk clearance below 2 nm is required. At this small clearance flying instability, which results in a few nanometers of clearance variation, may cause read/write errors due to the high sensitivity of magnetic recording performance to clearance. In addition to direct contact between head and disk, collision between a lubricant droplet and head may cause vibrations and induce a read/write “signal jump” such as reported by Li et al. [1]. Fowler and Geiss [2] observed droplets of OC (alkane) on the head that can cause the stiction at the HDI with a visualization setup. With these references, we used model OC instead of using lubricant for accelerated testing to facilitate droplet observation as it is difficult to observe the lubricant droplet on the disk covered with the lubricant film. We found that OC, specifically hydrocarbons, can also make the flying head unstable by contact with a droplet of OC during the write operation, resulting in an unrecoverable read error. In this study, drive level test was carried out to investigate the influence of OC on reliability of head disk interface (HDI).

## 2. Experimental Details

To investigate the influence of OC, we applied 30 mg of hydrocarbon oil to the inside top cover of test drives.

The drives were placed with the top cover down to avoid dropping the hydrocarbon oil to disk. This hydrocarbon oil has a wide distribution of molecular weight from about 100 to 500 grams per mole. For the drive test, several 10000 rpm test drives were built. Tests were conducted at a controlled temperature of 55°C to volatilize components of the hydrocarbon oil. The test sequence is shown in Figure 1. First, full stroke seeks between maximum outer radius (OD) and minimum inner radius (ID) without write/read operation (no dynamic flying height control) were conducted for 10 hours. The flying height is about 10 nm during the full stroke seek. Next, a sequential write operation from OD to ID was conducted. Then, a sequential read operation similar to the sequential write was conducted. The flying height is 3.0 nm with dynamic flying height control in the sequential write and read operation. If a readback error occurred, Viterbi metric margin (VMM) measurement (read only) near the error position was performed to map the error location. VMM is a function conceived as a means of measuring signal quality during Viterbi decoding. The margin means the difference between the actually received data path (continuous 0/1 data) and ideal path. VMM correlates with sector error rate (SER). When the VMM is larger, SER is worse. The details of VMM measurement are shown in [3].

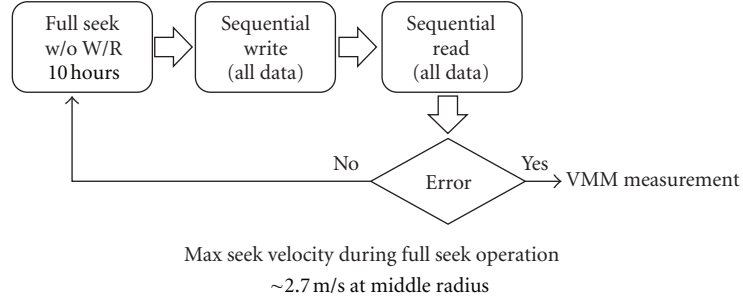


FIGURE 1: Sequence of drive test accelerated by OC. The fly condition is passive (no dynamic flying height control) during the full stroke seek operation without write/read operation.

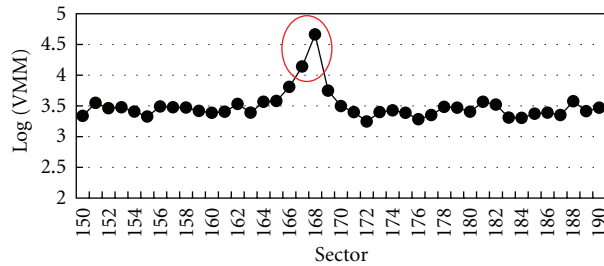


FIGURE 2: VMM changes near the error position.

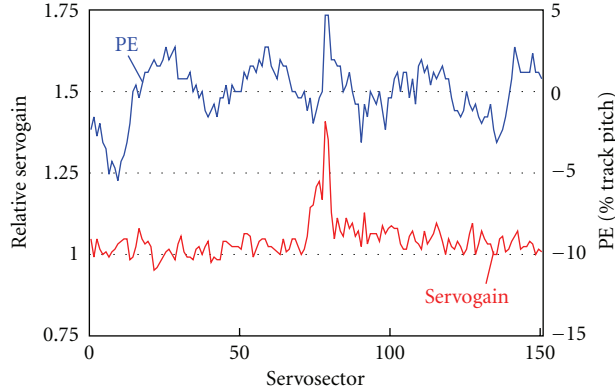


FIGURE 3: Relative servogain and position error (PE) changes when head may contact droplets.

We also tested drives where  $100 \mu\text{L}$  of alkane (paraffin or saturated hydrocarbon) solutions were injected into the inside of the drive enclosure on the base casting near the motor to understand what component of the OC causes the error. The test sequence is the same as the above test shown in Figure 1. Table 1 shows the alkanes we used for test and amount of volume/weight loaded into the drives. The weight of icosane, pentacosane, and triacontane excludes hexane's weight. In addition, test temperature was varied to investigate the influence of kinetic viscosity of alkanes.

### 3. Results and Discussion

#### 3.1. Signal Change Measurement Induced by Flying Instability.

Figure 2 shows an example of VMM changes near the error

position, indicated by red circle. Readback errors occurred at 2 sectors in a sequential read operation. No errors were detected in a sequential write operation. If the head cannot read the servodata and fails to set the positioning, the drive reports an error in a write operation. To determine if the errors were caused by a media magnetic defect or scratch the media was rewritten and VMM was remeasured. The VMM at the error positions recovered to normal value with rewriting, so it was concluded that there was no media magnetic defect or scratch present.

Figure 3 shows servogain and position error (PE) changes when abnormal servogain variation was detected in write operation. The large servogain means that the amplitude of the servo signal is small because automatic gain controller (AGC) adjusts the gain to maintain the signal level. When

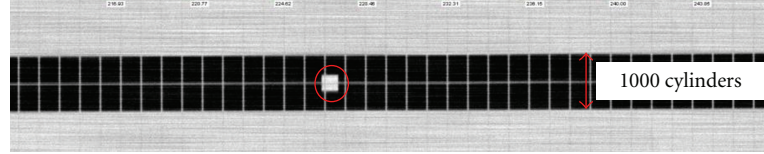


FIGURE 4: OSA image of media surface near the error location.

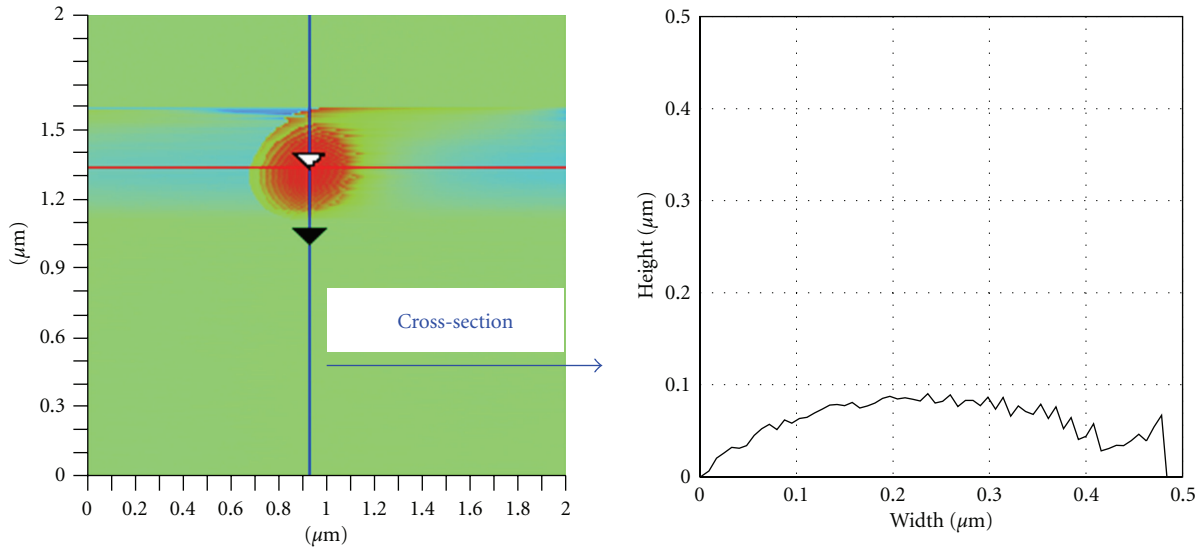


FIGURE 5: The droplet observation on the media by AFM.

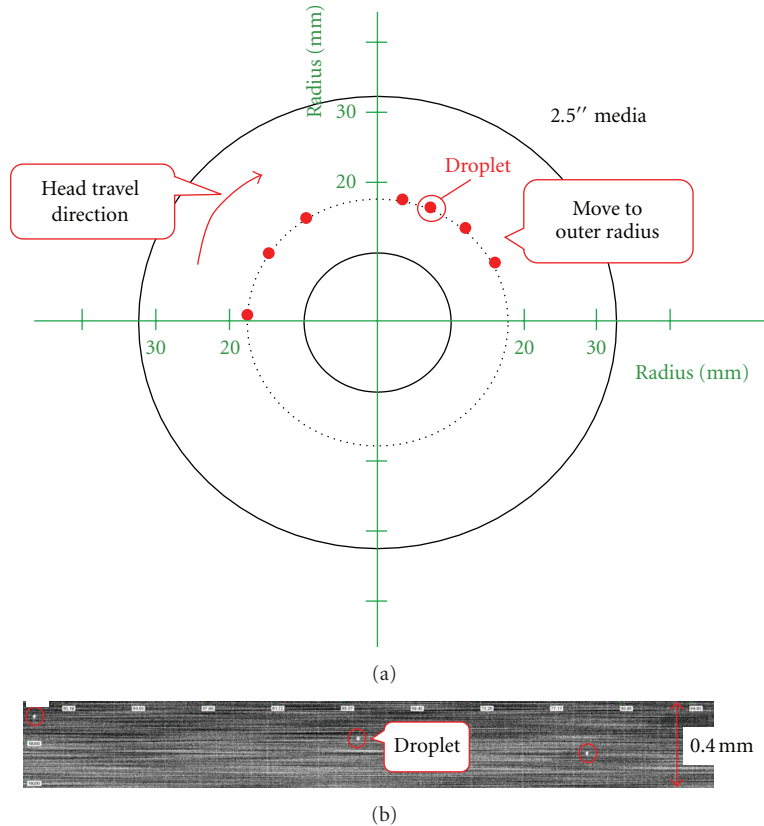


FIGURE 6: Droplet distribution map (a) and OSA image (b) on the media. The droplets in the down-track direction are located progressively further toward the disk outer radius, consistent with the head travel direction from inner to outer diameter.

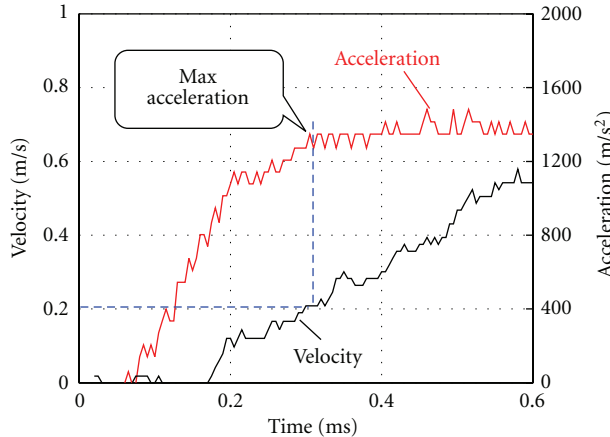


FIGURE 7: Radial velocity and acceleration of the head in full stroke seek operation.

the relative servogain changed from about 1.0 to 1.4 by flying instability, the flying height rise can be calculated to be around 7.5 nm using the Wallace spacing loss equation [4]. Although the 64 kHz sampling frequency in this study is not large enough to identify specific ABS vibration modes, such as pitch and roll mode, the vibration frequency can be estimated roughly to be 5 to 10 kHz which may correspond to that of suspension torsion mode.

On the other hand, PE was not seen to change significantly at the region where the servogain varied greatly. It indicates that the vibration does not move the cross-track direction, but vertical direction. The write operation was completed with no error being detected even though data could not be recorded correctly.

**3.2. Droplet Observation.** To further investigate the cause of the errors, we performed a drive teardown analysis and inspected the media and head surfaces for evidence of OC which may have caused the error. Before the drive teardown, the media was DC-erased around the error position to facilitate identification of the error location by an optical surface analyzer (OSA). No droplet was observed at the error location on the media surface indicated by red circle in Figure 4. We speculate that the droplets were removed by contacts with head during write/read operations. To test this hypothesis, we measured the media surface from another drive after full stroke seek operation only. Based on full surface mapping of the media by OSA, several droplets were detected. Figure 5 shows one of the droplets measured by AFM. The shape of this droplet is dome-like. The height of this droplet is about 100 nm, tall enough to make contact between the head and the droplet on the media.

Although we attempted to analyze the droplet by Auger electron spectroscopy and Raman spectroscopy, we did not succeed because the droplet vanished during their electron or laser irradiation inherent in the Auger and Raman techniques. Furthermore, some droplets disappeared when simply storing the media for a week at room temperature.

TABLE 1: Alkanes used for tests.

	Formula	Volume ( $\mu\text{L}$ )	Density (g/mL) at 20°C	Weight (mg)	MP* (°C)
Hexane	$\text{C}_6\text{H}_{14}$		0.70	70	-95.0
Hexadecane	$\text{C}_{16}\text{H}_{34}$	100	0.77	77	18.0
Icosane	$\text{C}_{20}\text{H}_{42}$	100	0.76	76	36.7
Pentacosane	$\text{C}_{25}\text{H}_{52}$	(Hexane Solution)	0.80	80	53.0
Triacontane	$\text{C}_{30}\text{H}_{62}$		0.78	78	65.8

Density data from International Chemical Safety Cards (ICSCs) or Material Safety Data Sheet (MSDS).

\*MP: melting point.

These observations suggest that the droplets are volatile liquid.

Figure 6 shows the location of several droplets and the OSA image of representative droplets. The path of the droplets follows a spiral path toward the outer radius. A radial velocity of about 0.2 m/s is calculated from the path. This velocity value indicates that the droplets dropped from head to media at the maximum acceleration in the full stroke seek operation, as shown in Figure 7.

Figure 8 shows an optical microscopy image of the head surface after the test. Some droplets were observed at the slider trailing edge and deposited ends. To identify whether the droplets are hydrocarbon or not, we analyzed these droplets on the head surface by Raman spectroscopy. The droplet on head surface was identified as hydrocarbon since the Raman spectrum of the droplet matched that of the reference hydrocarbon oil shown in Figure 9.

**3.3. The Influence of Kinetic Viscosity of Organic Compound.** Figure 10 shows the result of the alkane injection test. In general, melting point of higher molecular weight OC is higher as shown in Table 1. Therefore, lower molecular weight and high temperature make the OC more volatile. However, this result shows that higher molecular weight is prone to induce the error in spite of the amount of evaporated OC. In addition, for pentacosane ( $\text{C}_{25}$ ) time to failure of the test at lower temperature (50°C) is shorter than the one at higher temperature (75°C). It indicates that there may be another factor, distinct from the amount of gaseous OC causing the error.

Figure 11 shows examples of VMM changes near the error position or the position where VMM exceeds 3.8. Larger and longer VMM change occurred in the test for  $\text{C}_{25}$  at 50°C compared to other two tests (for  $\text{C}_{25}$  at 75°C and for  $\text{C}_{16}$  at 66°C). That may be one of the reasons why the droplets at the test for  $\text{C}_{25}$  at 50°C have higher viscosity or larger size for. On the other hand, VMM changes also appeared in the other two tests in Figure 11 even if no error occurred. This implies the existence of the droplets at the three tests in Figure 11. From these results, we inferred that the higher kinetic viscosity associated with lower temperature and higher molecular weight or volume of alkane droplets are one of the significant factors which cause drive failure. To clarify the relationship between the kinetic

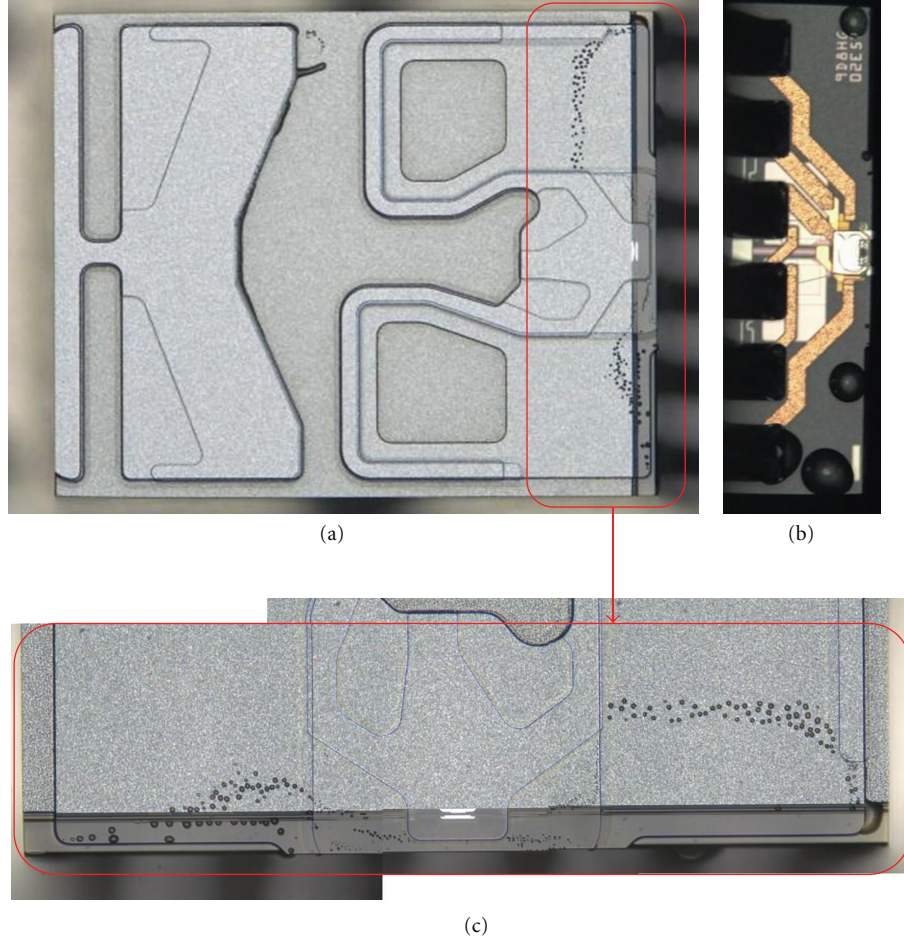


FIGURE 8: Optical microscope images (a) overall picture of ABS; (b) deposited ends of head; (c) enlarged picture of red square area in (a).

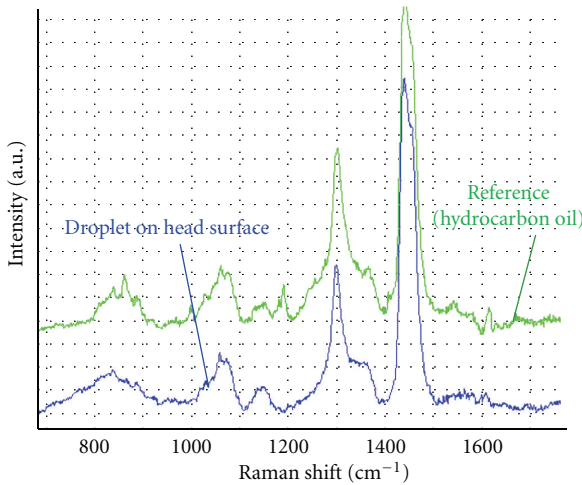


FIGURE 9: Droplet analysis by Raman spectroscopy.

viscosity of alkanes and occurrence of drive failure, plots of the test results were made as shown in Figure 12. We deduce from Figure 12 that there is a critical kinetic viscosity of OC for inducing drive failure, and the critical kinetic viscosity

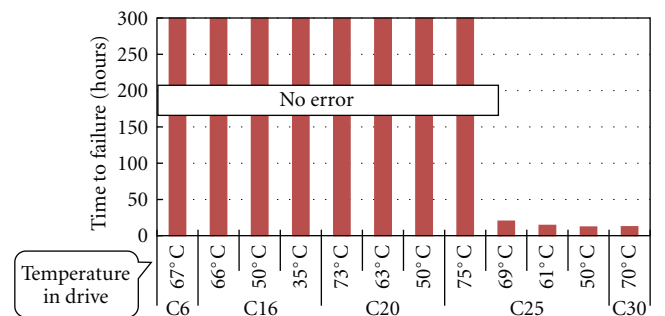


FIGURE 10: Alkane injection test result. The tests over 300 h were truncated.

is about 5 cSt in the test. However, we need further study to separate from the droplet size (or volume) influence on inducing drive failure.

#### 4. Conclusion

We studied the drive failure caused by the contact between the droplet of OC (hydrocarbon) and head. From our

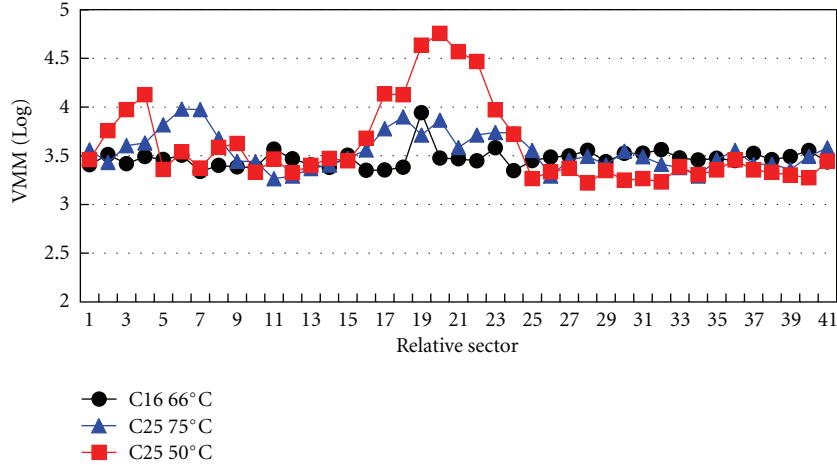


FIGURE 11: VMM change comparison near the error position (C25 50°C) or the position where VMM exceeds 3.8 (C16 66°C, C25 75°C) in the alkane injection tests.

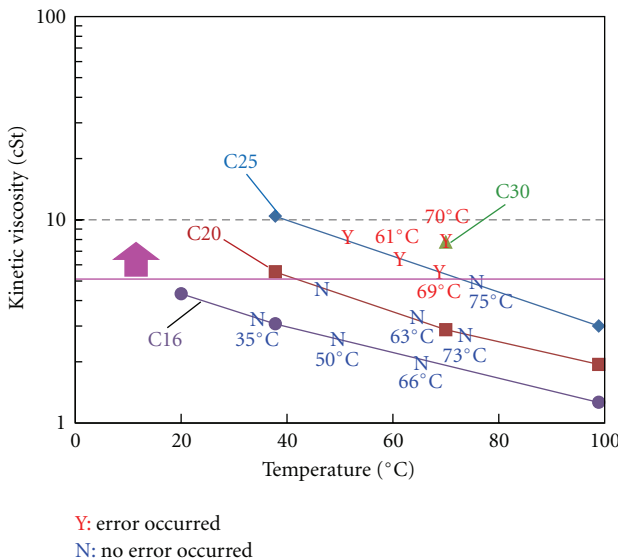


FIGURE 12: Correlation between kinetic viscosity of alkanes and the occurrence of drive errors.

investigations, we speculate the mechanism of the flying instability induced the OC as follows.

- (1) OC evaporated from inside top cover condenses into a droplet on the head due to the pressurization under ABS, or is adsorbed to disk surface. The OC adsorbed on the disk surface is picked up to the head surface then, the droplet is generated by accumulating the picked up OC.
- (2) Droplets on the head transfer to the media by inertia force as the head seeks over the media.
- (3) A large vibration occurs due to contact between the head and the droplet in the case of high kinetic viscosity components of OC or forming large droplet of OC.

## References

- [1] J. Li, J. Xu, and Y. Aoki, "Simulation on contact between the droplet and the slider at head-disk interface based on water-hammer pressure model," *Microsystem Technologies*, vol. 16, no. 1-2, pp. 57–65, 2010.
- [2] D. E. Fowler and R. H. Geiss, "Chemical contamination at the head-disk interface in a disk drive," *IEEE Transactions on Magnetics*, vol. 36, no. 1, pp. 133–139, 2000.
- [3] K. Aruga, "Probabilistic analysis of off-track capability assuming geometric track misregistration model for higher track density disk drives," *IEEE Transactions on Magnetics*, vol. 45, no. 11, pp. 5022–5025, 2009.
- [4] R. L. Wallace, "The reproduction of magnetically recorded signal," *Bell System Technical Journal*, vol. 30, pp. 1145–1173, 1951.

## Research Article

# Parametric Investigations at the Head-Disk Interface of Thermal Fly-Height Control Sliders in Contact

Sripathi V. Canchi,<sup>1</sup> David B. Bogy,<sup>1</sup> Run-Han Wang,<sup>2</sup> and Aravind N. Murthy<sup>2</sup>

<sup>1</sup>Computer Mechanics Laboratory, Mechanical Engineering, University of California, Berkeley, CA 94720, USA

<sup>2</sup>HGST, a Western Digital Company, San Jose, CA 95135, USA

Correspondence should be addressed to Sripathi V. Canchi, sripathi.canchi@cal.berkeley.edu

Received 3 August 2012; Accepted 12 November 2012

Academic Editor: Bo Liu

Copyright © 2012 Sripathi V. Canchi et al. This is an open access article distributed under the Creative Commons Attribution License, which permits unrestricted use, distribution, and reproduction in any medium, provided the original work is properly cited.

Accurate touchdown power detection is a prerequisite for read-write head-to-disk spacing calibration and control in current hard disk drives, which use the thermal fly-height control slider technology. The slider air bearing surface and head gimbal assembly design have a significant influence on the touchdown behavior, and this paper reports experimental findings to help understand the touchdown process. The dominant modes/frequencies of excitation at touchdown can be significantly different leading to very different touchdown signatures. The pressure under the slider at touchdown and hence the thermal fly-height control efficiency as well as the propensity for lubricant pickup show correlation with touchdown behavior which may be used as metrics for designing sliders with good touchdown behavior. Experiments are devised to measure friction at the head-disk interface of a thermal fly-height control slider actuated into contact. Parametric investigations on the effect of disk roughness, disk lubricant parameters, and air bearing surface design on the friction at the head-disk interface and slider burnishing/wear are conducted and reported.

## 1. Introduction

In order to realize higher magnetic storage densities in hard disk drives, it is necessary to reduce and control the read-write head-to-media spacing, or, equivalently, the physical spacing/clearance separating the head from the disk. Current hard disk drive (HDD) products operate with subnanometer clearances using the thermal fly-height control (TFC) technology, where the TFC heater locally deforms the region around the read-write head of the slider bringing it closer to the disk. The head-to-disk clearance can therefore be adjusted by changing the power supplied to the TFC heater.

A touchdown test is used to calibrate the TFC heater power to the clearance. The heater power required to make the head contact the disk lubricant surface, that is, the touchdown power (TDP), is first determined, and the heater power is then reduced to retract the head away from the disk in order to achieve a target clearance. Accurate TDP detection is therefore a key enabling step to using the TFC technology. Inaccurate TDP detection can severely compromise the drive

performance: if the actual clearance is too high, the recording performance suffers, and if the actual clearance is too low, it increases the probability for head-disk contact, which leads to unwanted head wear, thus compromising drive reliability.

Research studies on the slider-disk contact interactions and the resulting slider vibrations have been of interest to the HDD community for a long time. Research investigations on the traditional (non-TFC) slider dynamics were motivated by the need to design low flying sliders while mitigating the contact-induced slider vibrations and slider-lubricant interactions, and extensive literature exists on these topics [1–8]. After the introduction of TFC sliders, several researchers have tried to understand and explain the contact and touchdown behavior of TFC sliders owing to its importance in HDD spacing calibration. It has been shown through experiments and simulation that in addition to the slider air bearing surface (ABS) design the disk lubricant and suspension design play an important role in the slider touchdown process [9]. Numerical and analytical simulations accounting for the nonlinear forces at the head-disk interface (HDI) have also successfully explained the strong vibration dynamics of

the slider close to the TDP and the subsequent suppression of vibrations for powers higher than the TDP [10–12], and they qualitatively support the experimental results reported for certain ABS designs [12, 13]. A full understanding of the touchdown behavior of TFC sliders is still lacking, and it continues to be an active topic of research.

In this work, acoustic emission (AE) sensors and laser doppler vibrometers (LDVs) are used in spin stand experiments focused on touchdown detection and slider dynamics studies. The similarities and differences in the touchdown signature for different slider ABS designs are highlighted. Parametric investigations are conducted to explain the dependence of friction and head wear on disk roughness and lubrication condition. In conjunction with recent work on the interactions of TFC sliders with the disk lubricant during touchdown/contact [14, 15], these results help develop a better understanding of the touchdown process of TFC sliders and the complex interactions at the HDI.

## 2. Experiments

Experiments are conducted on a spin stand equipped with an AE sensor to detect contact and an LDV to detect vertical flexure motions of the head gimbal assembly. Three different ABS designs mounted on the same suspension are used in this study. The TDP (i.e., power required to achieve zero clearance or contact with the disk lubricant) is determined experimentally by supplying the TFC heater with a square pulse lasting 70 ms with increasing power. The AE signal standard deviation is monitored during each power pulse, and the power at which the AE signal standard deviation crosses a specified threshold (set to be 20% above baseline) is recorded as the TDP.

## 3. Results and Discussion

**3.1. Touchdown Behavior/Characteristics.** The touchdown plots for three different ABS designs are shown in Figure 1 where ABS-3 shows a favorable “sharp touchdown” while ABS-1 shows an unfavorable “gradual touchdown,” and has a slow rise in AE signal for increasing TFC power. ABS-2 has touchdown performance which falls between ABS-1 and ABS-3. A sharp touchdown behavior is preferred as it gives a well-defined estimate of the exact power at which contact with the disk lubricant is achieved.

The sharp touchdown for ABS-3 is characterized by strong individual spikes in the time history of the AE signal while the gradual touchdown for ABS-1 shows a uniformly increased AE signal during the TFC pulse as shown in Figure 2. (The AE signal on these plots have been shifted by 1 V to show them clearly).

In addition, tests in overpush (i.e., TFC power above the TDP) reveal that ABS-3 with “sharp touchdown” shows an “overshoot behavior” with very strong AE signal at powers slightly above the TDP and a subsequent suppression of AE signal when the power increases into overpush as seen in Figure 3. In contrast, ABS-1 with the “gradual touchdown” shows no “overshoot” behavior but a gradual increase in

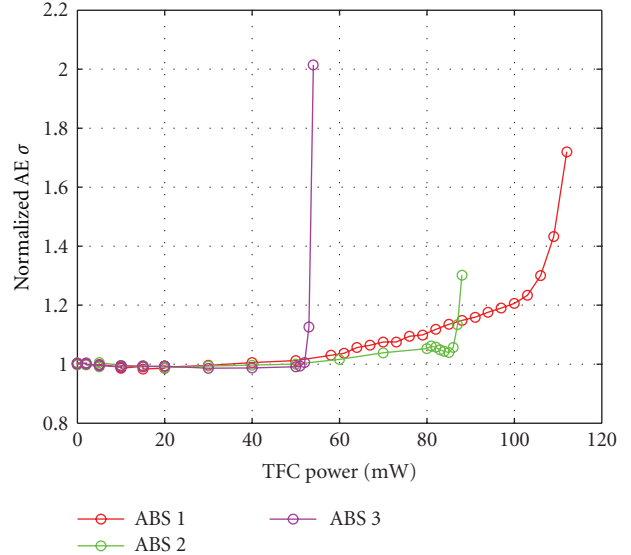


FIGURE 1: Touchdown plots for the three different ABS designs.

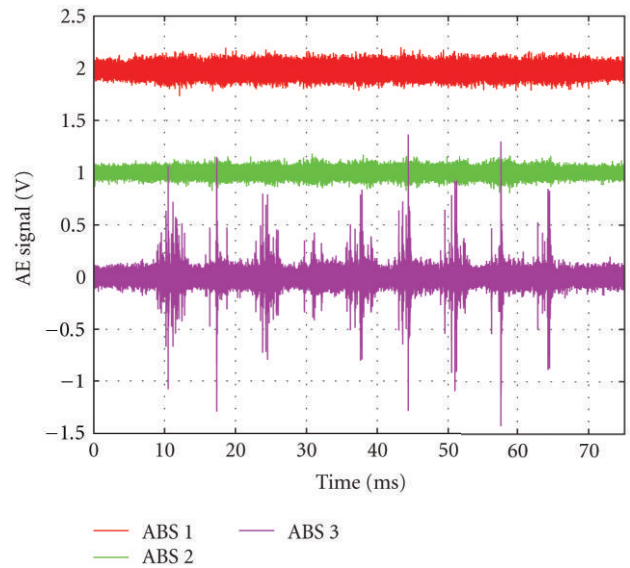


FIGURE 2: Touchdown signature for the three different ABS designs (plots offset by 1 V for clarity).

AE detected contact with overpush. ABS-2 has behavior in between those of ABS-3 and ABS-1.

Simulations for these three ABS designs show that the increasing sharpness of touchdown correlates with decreasing pressure under the TFC protrusion at touchdown, increased TFC efficiency, and lower TDP (Table 1). It is also observed that lubricant pickup is higher for ABS-3 compared to ABS-2 or ABS-1.

While an explanation of the physical mechanism behind the different ABS touchdown signatures requires a further comprehensive study, important correlations may be drawn from these results. The strong individual spikes for ABS-3 are evidence of a snap-in/snap-out behavior, which is an indication of the spontaneous instability of the slider

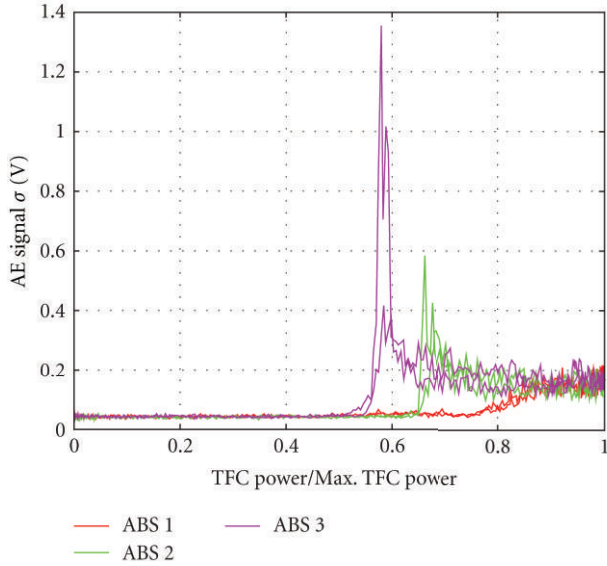


FIGURE 3: Contact behavior in overpush for the three different ABS designs.

TABLE 1: Simulated results for the three different ABS designs.

ABS design	Simulation TFC efficiency nm/mW	Touchdown power mW	Pressure at touchdown atm.
ABS-1	0.108	96	60
ABS-2	0.119	91	38
ABS-3	0.145	69	27

during touchdown. It is highlighted that the circumferential locations of the spikes do not remain fixed upon repetition of the touchdown test and hence are not caused by disk defects as such. The snap-in/snap-out process causes a higher level of head-disk lubricant interaction, which correlates well with the higher amount of lubricant pickup for ABS-3. It may also be reasoned that the lower pressure at the TFC bulge for ABS-3 makes it more susceptible for lubricant transfer from disk to the slider in comparison to ABS designs with higher pressure at the TFC bulge, such as ABS-1 and ABS-2.

**3.2. Analogous Experimental Results.** A separate set of experiments with ABS-2 reveals that the touchdown can be sharp or gradual depending on the disk RPM (or the linear velocity) as shown in Figure 4. Specifically, a lower disk RPM increases the touchdown sharpness and a higher disk RPM degrades the touchdown sharpness. It is also observed that the touchdown performance degrades for a burnished slider (as shown by the dashed lines in Figure 4), where the slider is burnished in a controlled fashion by increasing the TFC power above the TDP on a separate disk track. The results for the 7200 RPM case on Figure 4 highlight the possibility of false TDP detection; for the same 20% AE threshold, the unburnished case shows a gradual AE rise until about 95 mW, but the sharp AE rise at 102 mW is the actual TDP.

However, the burnished case reads a false TDP at 93 mW owing to the gradual rise in AE that occurs before the sharp AE rise marking touchdown. The time history of the AE signal is similar to that observed with the different ABS designs; namely, strong individual AE spikes appear for the 3600 RPM case with sharp touchdown, and a uniformly increased AE signal appears for the 7200 RPM case with gradual touchdown (Figure 5). These analogous results for ABS-2 provide a way to probe the same HDI under different disk RPM to understand the changes that occur in the AE and LDV signals for “sharp” and “gradual” touchdown signatures as well as in overpush.

**3.3. LDV Spectrum and AE Signal Content.** Experiments are conducted with ABS-2 to simultaneously capture the AE signal and the LDV signal in order to identify the frequencies that correspond to the flexure and slider vertical motions and to see how they appear in the AE signal. The tests are conducted with the power increased above the TDP (i.e., into overpush). For this ABS-2 design, the simulated air bearing frequencies at 5400 RPM and 1 nm minimum spacing are 142 kHz (roll), 167 kHz (pitch-1), and 324 kHz (pitch-2).

For each of the overpush tests conducted at different RPM, Figure 6 shows the profile of the applied TFC voltage and the time history of the LDV signal on one plot, and the corresponding joint time frequency spectrum of the LDV signal on a separate plot. As seen on the figures, the TFC voltage increases from zero to the target overpush value (between 50 ms to 100 ms), remains at this value (between 100 ms to 200 ms), and decreases back to zero (between 200 ms to 250 ms). During the overpush regime, the slider vibrations are excited due to contact, and the dominant excitation frequencies are identified on the plots showing the joint time frequency spectrum. It is observed that for 3600 RPM the lower frequencies (notably 139, 148, and 165 kHz which are close to simulated roll and pitch-1 air bearing frequencies) are dominant, while for the 7200 RPM the higher air bearing frequency 321 kHz (corresponding to pitch-2 air bearing frequency) is dominant. This result indicates that the mechanism/nature of touchdown and contact at the HDI is significantly altered by the disk RPM. Specifically in this case, the excited vibration modes at contact are shifted from the lower frequency pitch-1 and roll modes at lower disk RPM, to the higher frequency pitch-2 modes at higher disk RPM. The pitch-1 nodal line passes through the trailing end of the slider, and its excitation in general is associated with stronger motions of the entire slider body. Such excitation may, in fact, be responsible for the stronger “sharp touchdown” signature. In contrast, the pitch-2 nodal line lies closer to the leading end of the slider, and its excitation only causes the vertical bouncing motion of the trailing end, resulting only in localized contact at the TFC bulge location, and, therefore, leading to the weaker “gradual touchdown” signature. It is surmised that, in an analogous fashion, the touchdown process excites different vibrations modes for the three different ABS designs presented in Section 3.1, hence causing the very different sensitivities at touchdown.

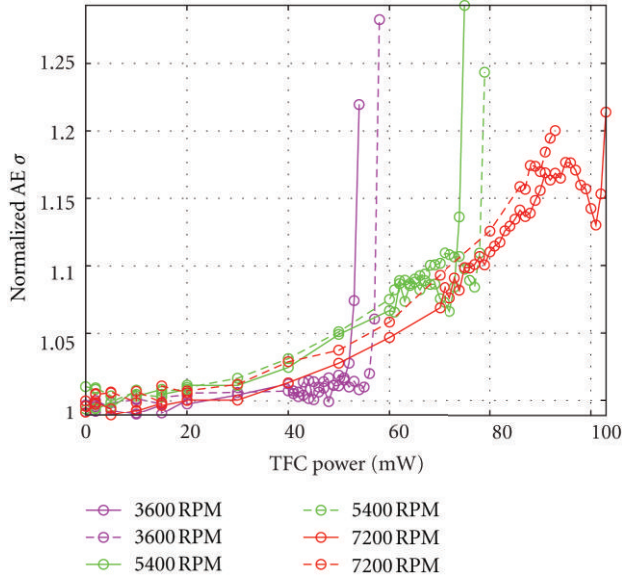


FIGURE 4: Touchdown plots for ABS-2 at different disk RPM (dashed lines for a burnished slider).

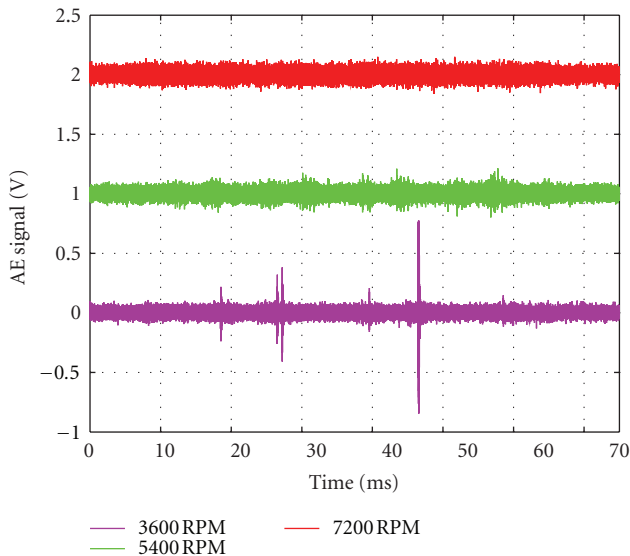


FIGURE 5: Touchdown signature for ABS-2 at different disk RPM (plots offset by 1 V for clarity).

The components of the AE signal at the different frequencies observed in the LDV signal are plotted in Figure 7 to observe how they change as a function of the TFC power. (The cumulative effect of adding all these components would result in the plot shown in Figure 4.) At 3600 RPM the touchdown is marked by the sharp rise in the 148 kHz component and there are no components that show gradual rise. At 5400 RPM, the 148 kHz component shows a gradual rise, but touchdown is marked by a sharp rise in the 321 kHz component. At 7200 RPM, there are no components with a sharp rise, and the 321 kHz component shows a gradual rise.

These results indicate that at 3600 RPM the contact is dominated by the slider's pitch-1 and roll motions (together with any suspension-related motions that give rise to frequency peaks in the 65–100 kHz region.) At 7200 RPM, contact is mainly dominated by the vibration of the slider at the pitch-2 frequency. At 5400 RPM, the interaction is a combination of the above two modes: as the TFC powers increase, a gradual rise in the 148 kHz component occurs first, but a strong vibration in the pitch-2 mode (321 kHz) eventually marks touchdown.

These results are in agreement with recent studies that show that at close spacing and at the onset of lubricant-contact, the in-plane shear forces and friction can destabilize the slider for certain ABS designs resulting in vibrations dominantly occurring at suspension and lower air bearing frequencies (60–200 kHz in our case), while stronger contact with the disk causes slider vibrations with higher frequency content (above 200 kHz) [9].

**3.4. Friction Measurements in Contact.** Friction forces at the HDI become important during contact conditions and may in fact play a dominant role in HDI performance and slider dynamics. Friction-induced slider wear, as well as disk lubricant redistribution and disk overcoat damage, needs to be examined carefully to explore future designs that can accommodate a certain level of head-disk contact.

Experiments are devised to measure the friction forces in the downtrack direction during contact and overpush conditions by instrumenting a strain gage on the fixture which holds the head gimbal assembly on the spin stand. The voltage signal from the strain gage may be converted into force measurement by determining the calibration constant for the strain gage. Such a calibration is performed using the usual technique: by noting the strain gage voltage signal corresponding to different standard forces, which are applied by suspending standard weights from the fixture, and subsequently fitting a linear curve.

Once the TDP is determined on the test track, the TFC is powered with a voltage profile having 100 ms dwell time at the maximum power. It is noted that strain gages have a low bandwidth, and several experiments reveal that a dwell time of at least 100 ms is necessary to allow the strain gage to respond to the friction force and give good, repeatable measurements. All experiments are conducted with ABS-2 on a reference “standard disk” unless specified otherwise.

**3.4.1. Friction, AE, and Slider Bouncing in Contact.** Figures 8(a) and 8(b) show the TFC voltage profile and the resulting slider bouncing (displacement and velocity), AE detected contact, and the friction force, for 10 mW and 20 mW overpush, respectively. It is evident that slider bouncing and AE signal remain high throughout the overpush region for 10 mW overpush case, and they get suppressed (after an initial overshoot region) for the 20 mW overpush case. The friction force measured by the strain gage, however, continues to increase with the amount of overpush indicating a higher level of interference and contact for larger overpush powers even though the AE detected contact and slider

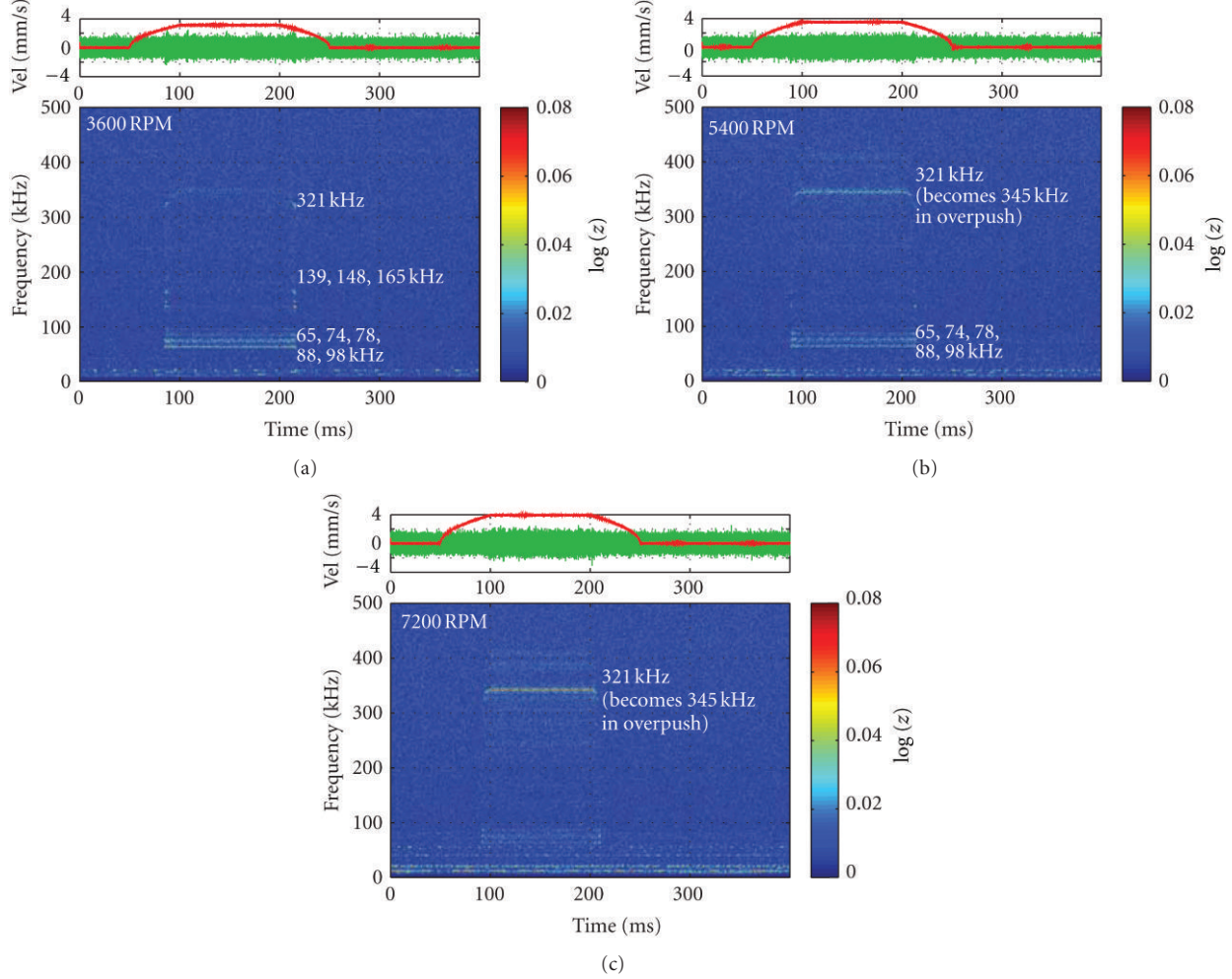


FIGURE 6: Applied TFC voltage profile, vertical velocity time history, and the joint time frequency spectrum of the vertical velocity for ABS-2 at different disk RPM.

dynamics get suppressed. (It is noted that the amplitude of the AE signal in the suppressed state is noticeably higher than the baseline AE signal with no TFC power, implying a certain amount of contact).

**3.4.2. Effect of Disk Roughness.** Disk roughness plays an important role in HDI performance. The combined slider and disk roughness affect the nominal physical spacing at the HDI, the magnitude of interaction forces (intermolecular/adhesive, etc.), and the actual area of contact, thereby influencing the magnitude of contact and friction forces. A parametric study is conducted with three disk types: disks A, B, and C with decreasing roughness, in that order, and with surface roughness parameters tabulated in Table 2, where  $R_q$  is the root mean square roughness,  $R_p$  is the maximum peak height, and  $R_v$  is the maximum valley depth. These disks are coated with ZTMD lubricant of nominal 12 Å thickness.

First, several tests are conducted using the same slider to determine the TDP on a standard disk and on each of the disks A, B, and C. Table 2 presents the change in

the TDP (i.e.,  $\delta$ TDP) on each of the disks A, B, and C compared to the TDP on a standard disk. The roughness of the standard disk is similar to that of disk A. This difference in TDP is converted into a clearance gain value (i.e. a gain in clearance from that on a standard disk) using a conversion factor of 0.119 nm/mW, which is the TFC efficiency estimated for ABS-2 from simulations. Figure 9 shows the same information in graphical form and highlights the linear relationship between the disk roughness ( $R_p$  or  $R_q$ ) and clearance gain. Since the thermal protrusion comes into contact with the peaks of the roughness, the relationship between the clearance gain and  $R_p$  (Figure 9(b)) is of importance, and it is seen that for every 1 nm decrease in  $R_p$  there is a 0.8 nm actual gain in clearance at the HDI for the range of surface roughness values considered in these experiments.

Next, the dependence of friction on the disk roughness is investigated by conducting a “friction test” on each of the three disk types. A new (unburnished) slider is flown on a fresh test track, the TDP is determined, and the TFC heater is then supplied with the power profile with a 100 ms

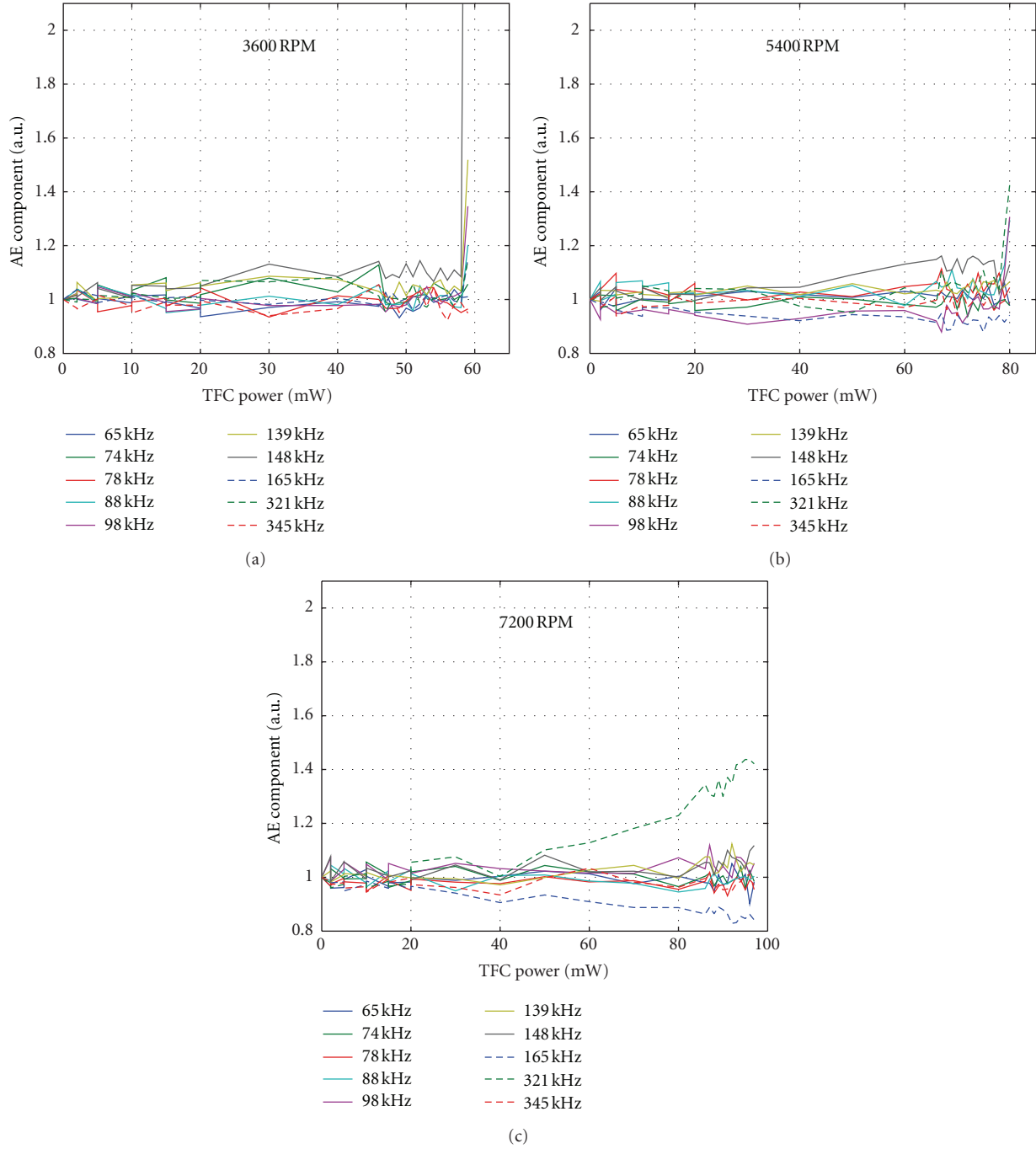


FIGURE 7: AE signal components in the touchdown plot for ABS-2 at different disk RPM.

dwell time (as shown in Figure 8). The peak TFC power is increased from TDP to a maximum of  $TDP + 50$  mW in 5 mW increments, and it is then similarly decreased back to TDP. The average friction measured by the strain gage at each power step is tabulated. All tests are conducted on the same disk track. The measured friction values are plotted as those for the “unburnished” case. The same slider, which is now deemed “burnished” because of the overpush testing, is flown on an adjacent track and the friction test is repeated to obtain friction values for the “burnished” case. Figure 10(a)

shows a representative plot for the strain gage measured friction values as a function of overpush power supplied to the TFC heater.

A quadratic curve passing through the origin is fit to the friction measurements for the “unburnished” and “burnished” cases, and the slope of this curve at the 10 mW overpush point is used to obtain the “friction ( $\mu N$ ) per milliwatt of overpush power” value. Figure 10(b) plots these friction values measured on the three disk types (A, B, and C) based on experiments conducted with three new sliders

TABLE 2: Disk roughness parameters and its effect on TDP/clearance gain.

Disk	$R_p$ nm	$R_q$ nm	$R_v$ nm	$\delta\text{TDP}$ mW	Clearance gain nm
A	2.02	0.49	1.87	0.08	0.01
B	1.89	0.36	1.47	0.97	0.12
C	1.00	0.24	1.11	6.71	0.84

on each disk type. While there is no particular trend relating the measured friction and surface roughness, the friction is higher for the burnished slider compared to the unburnished slider in all tests. Slider burnishing wears and smoothes the slider surface, increasing the actual contact area between the thermal protrusion and the disk, thereby resulting in the slightly higher friction force.

In order to directly compare the friction values between the three disk types, another set of experiments is conducted by flying the same “burnished” slider on the three disk types in succession. The slider is burnished in a controlled fashion separately before use in this test. The friction against the overpush power is plotted in Figure 10(c) using data from two “burnished” heads. It is concluded based on these results that within the range of disk roughness considered in this work there is no significant effect of the disk surface roughness on the measured friction.

**3.4.3. Effect of Lubricant Parameters.** Friction tests are conducted to determine the effect of lubricant type/bonding on the friction in contact. Disks with three different lubricant type/bonding ratios are used: Lube A (61% bonded ratio, 10.5 Å), Lube A (69% bonded, 10.5 Å), and Lube B (82% bonded, 12 Å). Figure 11(a) shows the friction measured for the three media for the “unburnished” and “burnished” slider cases (based on three experiments each). The friction values are comparable for the unburnished sliders on all three disks types. While the friction values for the burnished and unburnished sliders are comparable on the disks with Lube A 61% and 69% bonded ratio, the friction for the burnished slider on the disk with Lube B 82% bonded ratio is relatively higher than that for the unburnished slider. This result is consistent with results for the change in TDP occurring because of a friction test, where the TDP change after and before a friction test is a measure of slider burnishing. As shown in Figure 11(b), the highest burnishing (indicated by highest  $\delta\text{TDP}$ ) occurs to a new “unburnished” slider on the Lube B 82% bonded disk. As a result of greater slider burnishing on this disk, the friction is higher when a subsequent test is conducted with this burnished slider.

A direct comparison of friction values is reported in Figure 11(c) based on tests conducted in succession on the three different disks using two “burnished” sliders, and it shows marginally higher friction values on the disk with Lube B 82% bonded ratio.

Friction tests are conducted to understand the effect of the mobile part of the lubricant on friction and slider burnishing. The disk with Lube A 10.5 Å 61% bonded fraction is delubed by immersing it in a solution of Vertrel XF solution

TABLE 3: Effect of TFC efficiency (ABS/heater design) on friction.

ABS design	Simulation TFC efficiency nm/mW	Friction unburnished $\mu\text{N}/\text{mW}$	Friction burnished $\mu\text{N}/\text{mW}$
ABS-A (ABS-1)	0.108	9	17
ABS-B	0.111	24	31
ABS-C (ABS-2)	0.119	37	54
ABS-D (ABS-3)	0.145	56	67

to remove the mobile lubricant. The delubed disk has a lubricant thickness of 6 Å (bonded lubricant). Figure 12(a) shows the measured friction on the lubed and delubed disks for the unburnished and burnished slider cases. The friction values for the unburnished as well as burnished slider on the lubed disk are similar and comparable to the friction value measured for the unburnished slider on the delubed disk. However, the friction is substantially higher for the burnished slider on the delubed disk. Figure 12(b) shows that slider burnishing (indicated by  $\delta\text{TDP}$  after a friction test) is higher for tests conducted on the delubed disk implying that an unburnished slider is substantially burnished on this disk type, and the friction is higher for the subsequent test conducted with such a burnished slider. These results highlight the important role of the mobile part of the lubricant in reducing friction and slider burnishing, thereby increasing the reliability of an HDI with contact.

**3.4.4. Effect of TFC Efficiency.** The thermal protrusion size and shape make a significant difference in the slider’s touchdown and contact behavior. The friction during contact for different slider ABS/heater designs is plotted in Figure 13 for the unburnished and burnished cases, and the same data is tabulated in Table 3 together with each design’s TFC efficiency estimated from simulations. It is observed that the friction forces increase as the TFC efficiency increases and may be explained by the following argument. For the same amount of overpush power, a higher TFC efficiency slider will have greater level of interference (because of a larger protrusion). As a result, the effective contact area is larger for the higher TFC efficiency case, reflecting in a higher measured friction.

**3.4.5. Effect of Disk RPM.** The similarities between the touchdown plot and contact signature of ABS-2 at different disk RPMs to those of ABS designs with different TFC efficiencies are highlighted in Section 3.2. Particularly, it is shown that at a higher RPM ABS-2 behaves like a design with low TFC efficiency (showing a gradual touchdown plot), and at a lower RPM ABS-2 behaves like a design with high TFC efficiency (showing a sharp touchdown plot).

The friction results from tests with ABS-2 at different RPM are consistent with the above analogy and with the results presented in Section 3.4.4. Figure 14 shows that the friction increases as the disk RPM decreases; that is, when ABS-2 is made to behave like a slider with high TFC

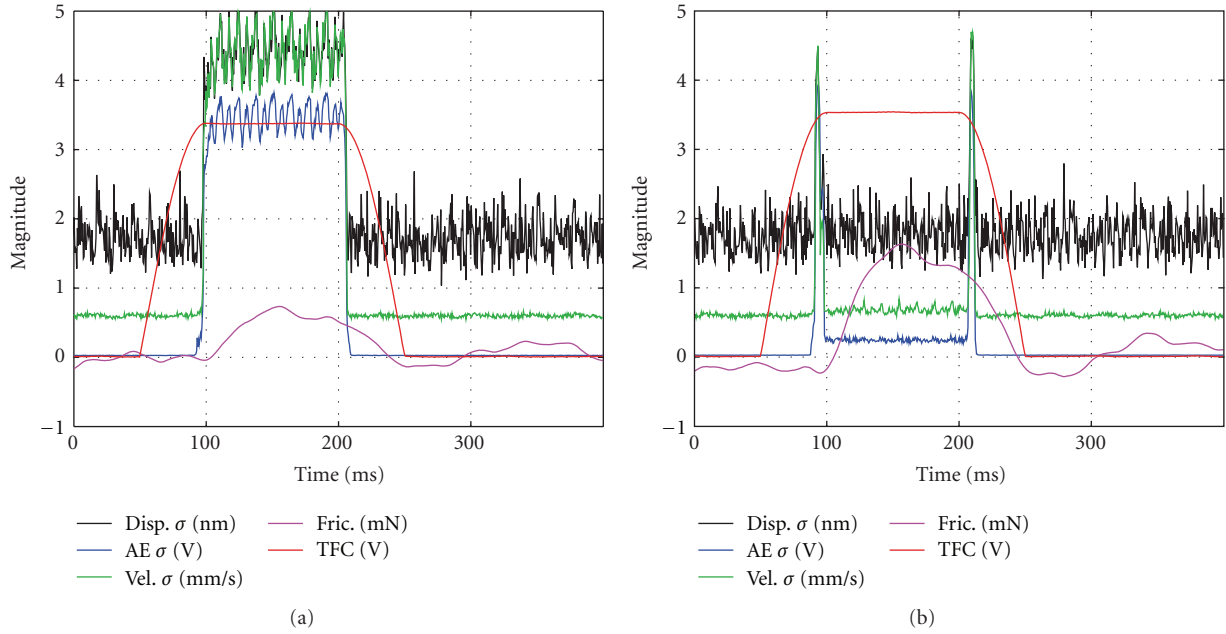


FIGURE 8: Time history of TFC power, vertical displacement, vertical velocity, AE signal, and friction. (a) 10 mW overpush, (b) 20 mW overpush.

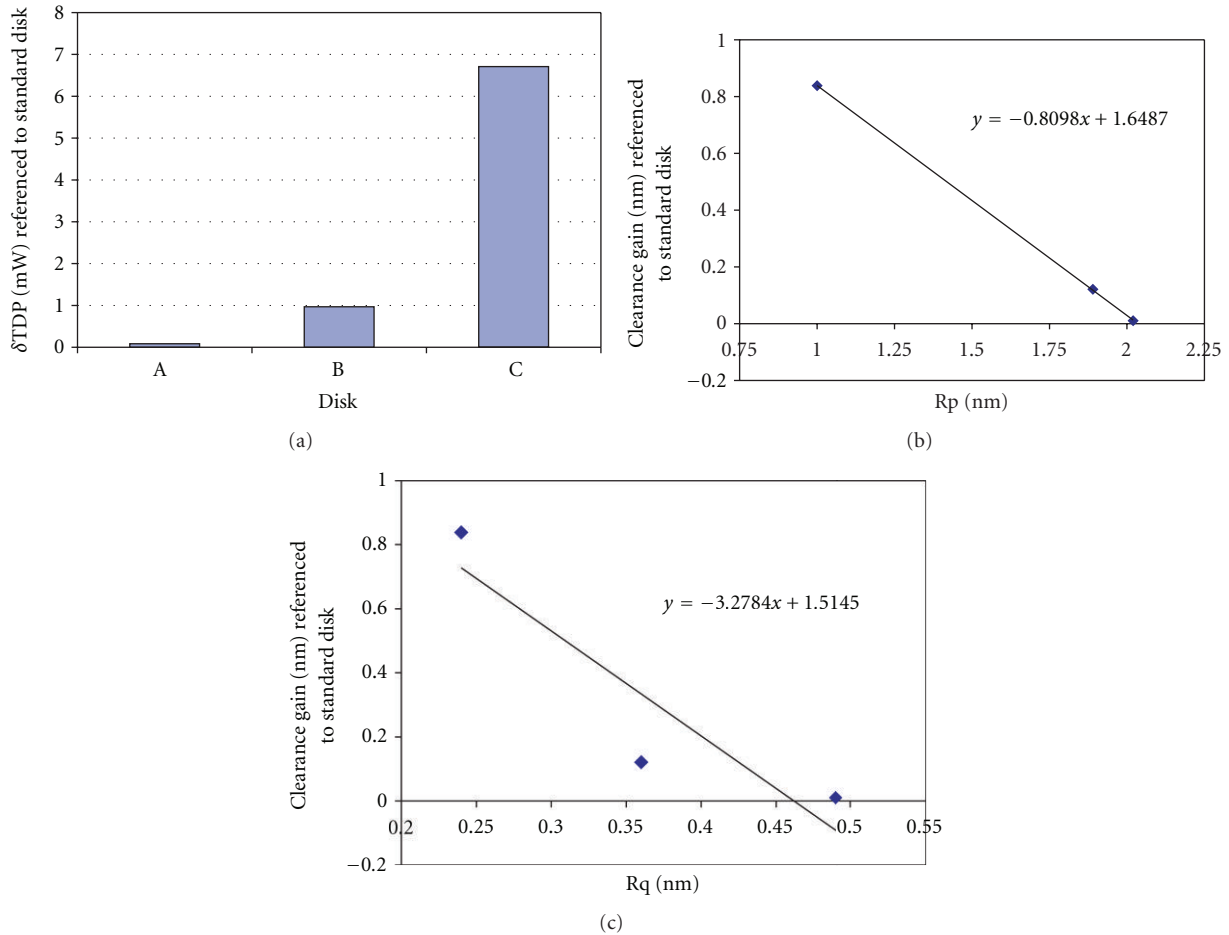
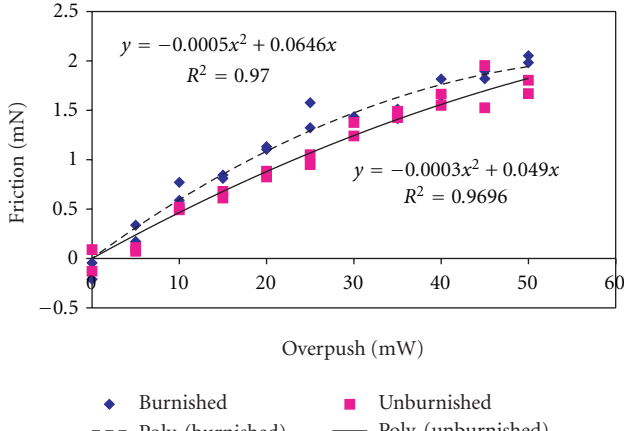
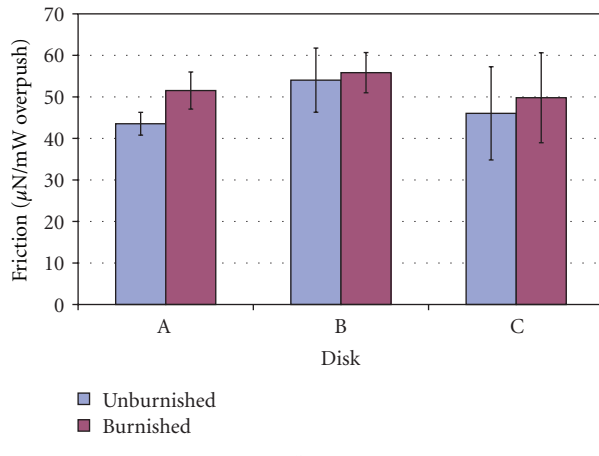


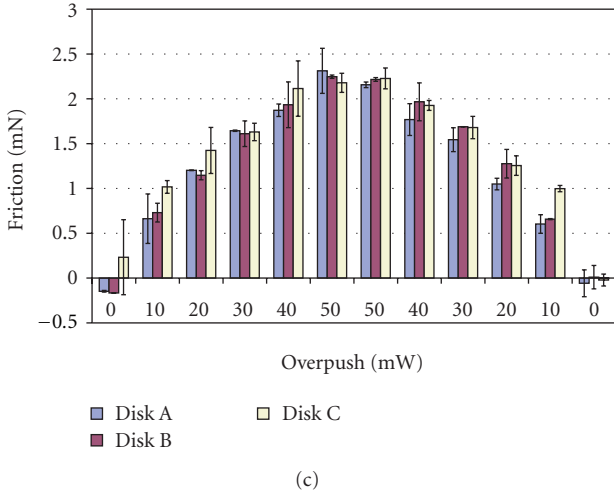
FIGURE 9: Effect of disk roughness on clearance.



(a)



(b)



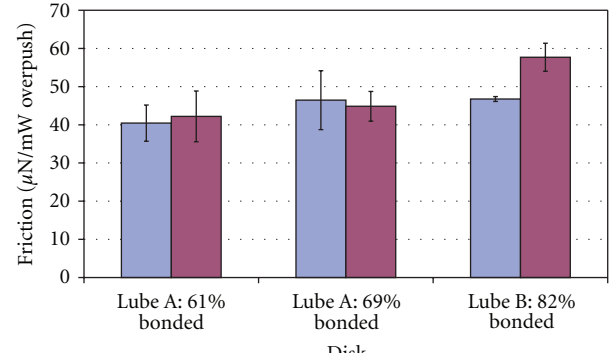
(c)

FIGURE 10: Effect of disk roughness on friction.

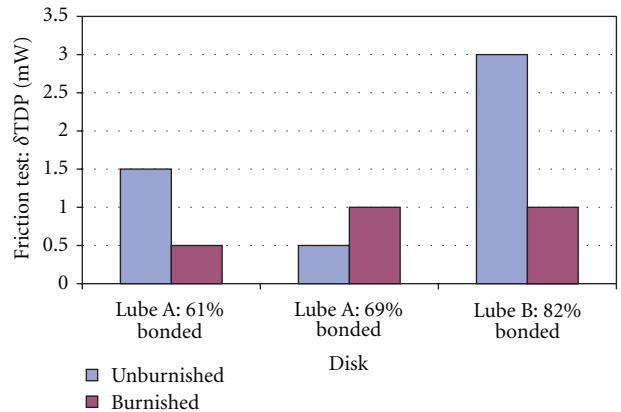
efficiency by decreasing RPM, it exhibits the characteristic sharp touchdown plot and higher friction.

#### 4. Conclusion

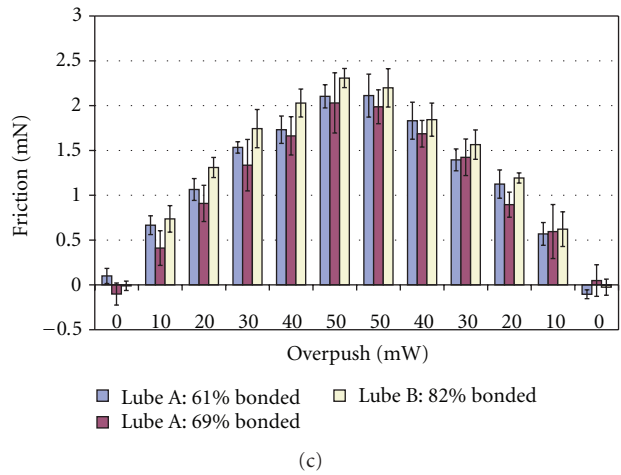
The touchdown behavior of TFC sliders is investigated through experiments. Certain sliders exhibit a sharp rise of



(a)



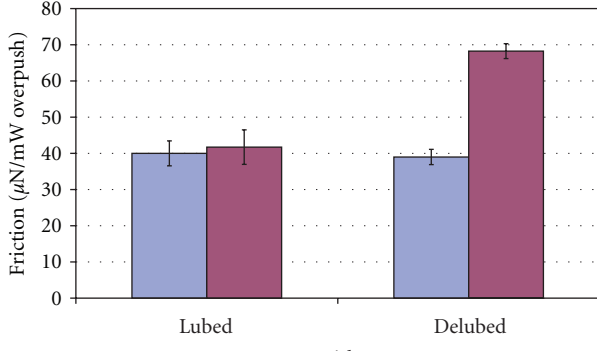
(b)



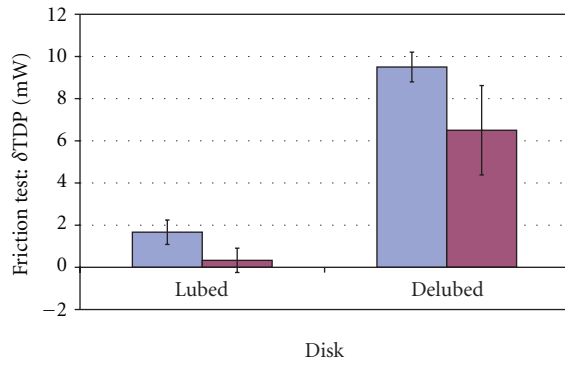
(c)

FIGURE 11: Effect of lubricant parameters on friction and slider burnishing.

AE signal at touchdown when the power is increased in milliwatt steps while others show a gradual rise making it difficult to exactly define the TDP to milliwatt resolution. An analogous behavior occurs when the disk RPM is changed for a particular slider ABS. It is found that the dominant modes/frequencies of excitation at touchdown are significantly different in these cases leading to the very different touchdown signatures. Particularly, the sharp touchdown



(a)



(b)

FIGURE 12: Effect of mobile lubricant on friction and slider burnishing.

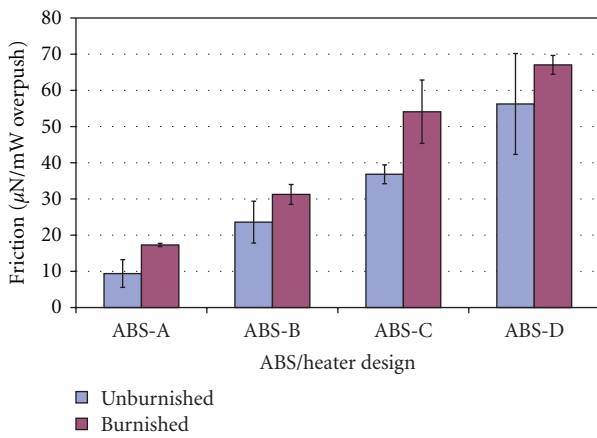


FIGURE 13: Effect of TFC efficiency (ABS/heater design) on friction.

case is characterized by strong individual contact events as observed in the AE signal, and the dominant excitation occurs at frequencies that correspond to the slider's first pitch and roll modes in addition to suspension related-frequencies. In contrast, the gradual touchdown case is characterized by a uniform rise in AE signal over the duration of the TFC

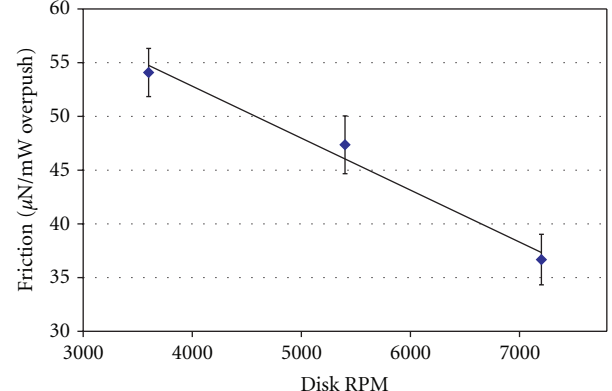


FIGURE 14: Effect of disk RPM on friction for ABS-2.

pulse, and the dominant excitation occurs at the slider's second pitch mode. The pressure under the TFC protrusion at touchdown, the TFC efficiency, and the propensity for lubricant pickup show correlation with touchdown behavior and may be used as metrics for designing sliders with good touchdown features. Experiments are devised to measure the friction at the HDI during TFC-induced contact, and several parametric investigations are carried out. In the range of parameter values considered, the disk surface roughness does not significantly affect the friction during contact. The mobile part of the lubricant plays an important role in reducing friction as well as slider burnishing. A burnished slider shows a higher friction value than an unburnished slider because of an increase in effective/actual contact area, and, for the same reason, sliders with higher TFC efficiency show higher friction compared to sliders with lower TFC efficiency.

## Acknowledgments

This work was supported by the Computer Mechanics Laboratory at the University of California at Berkeley and Hitachi Global Storage Technologies. The authors thank Q. Dai, L. Dorius, XC. Guo, B. Marchon, and R. Waltman for their support and helpful discussions during the course of this work.

## References

- [1] B. Knigge and F. E. Talke, "Dynamics of transient events at the head/disk interface," *Tribology International*, vol. 34, no. 7, pp. 453–460, 2001.
- [2] C. M. Mate, P. C. Arnett, P. Baumgart et al., "Dynamics of contacting head-disk interfaces," *IEEE Transactions on Magnetics*, vol. 40, no. 4, pp. 3156–3158, 2004.
- [3] J. Xu, H. Kohira, H. Tanaka, and S. Saegusa, "Partial-contact head-disk interface approach for high-density recording," *IEEE Transactions on Magnetics*, vol. 41, no. 10, pp. 3031–3033, 2005.
- [4] J. D. Kiely and Y. T. Hsia, "Slider dynamic motion during writer-induced head-disk contact," *Microsystem Technologies*, vol. 14, no. 3, pp. 403–409, 2008.
- [5] Q. Dai, B. E. Knigge, R. J. Waltman, and B. Marchon, "Time evolution of lubricant-slider dynamic interactions,"

- IEEE Transactions on Magnetics*, vol. 39, no. 5, pp. 2459–2461, 2003.
- [6] Q. Dai, F. Hendriks, and B. Marchon, “Washboard effect at head-disk interface,” *IEEE Transactions on Magnetics*, vol. 40, no. 4, pp. 3159–3161, 2004.
  - [7] B. Marchon, X. C. Guo, A. Moser, A. Spool, R. Kroeker, and F. Crimi, “Lubricant dynamics on a slider: ‘the waterfall effect’,” *Journal of Applied Physics*, vol. 105, no. 7, Article ID 074313, 2009.
  - [8] C. M. Mate, B. Marchon, A. N. Murthy, and S. H. Kim, “Lubricant-induced spacing increases at slider-disk interfaces in disk drives,” *Tribology Letters*, vol. 37, no. 3, pp. 581–590, 2010.
  - [9] Q. H. Zeng, C. H. Yang, S. Ka, and E. Cha, “An experimental and simulation study of touchdown dynamics,” *IEEE Transactions on Magnetics*, vol. 47, pp. 3433–3436, 2011.
  - [10] J. Zheng and D. B. Bogy, “Investigation of flying-height stability of thermal fly-height control sliders in lubricant or solid contact with roughness,” *Tribology Letters*, vol. 38, no. 3, pp. 283–289, 2010.
  - [11] J. Zheng and D. Bogy, “Dynamic instability of thermal-flying-height-control sliders at touchdown,” *Microsystem Technologies*, vol. 18, no. 9-10, pp. 1319–1322, 2012.
  - [12] S. Vangipuram Canchi and D. B. Bogy, “Thermal fly-height control slider instability and dynamics at touchdown: explanations using nonlinear systems theory,” *Journal of Tribology*, vol. 133, no. 2, Article ID 021902, 2011.
  - [13] S. Vangipuram Canchi and D. Bogy, “Slider dynamics in the lubricant-contact regime,” *IEEE Transactions on Magnetics*, vol. 46, pp. 764–769, 2010.
  - [14] S. Vangipuram Canchi and D. B. Bogy, “Slider-lubricant interactions and lubricant distribution for contact and near contact recording conditions,” *IEEE Transactions on Magnetics*, vol. 47, no. 7, pp. 1842–1848, 2011.
  - [15] S. Vangipuram Canchi and D. Bogy, “Experiments on slider lubricant interactions and lubricant transfer using TFC sliders,” *Microsystem Technologies*, vol. 18, pp. 1517–1523, 2012.

## Research Article

# Low Molecular Weight Z-Tetraol Boundary Lubricant Films in Hard Disk Drives

R. J. Waltman and H. Deng

Media Development, HGST Western Digital, 5601 Great Oaks Parkway, San Jose, CA 95119-1003, USA

Correspondence should be addressed to R. J. Waltman, robert.waltman@hitachigst.com

Received 16 August 2012; Accepted 5 November 2012

Academic Editor: Bruno Marchon

Copyright © 2012 R. J. Waltman and H. Deng. This is an open access article distributed under the Creative Commons Attribution License, which permits unrestricted use, distribution, and reproduction in any medium, provided the original work is properly cited.

Lower molecular weight Z-Tetraol films exhibit increased mechanical spacing in the slider-disk interface due to a lower z-profile. An increased resistance to lubricant disturbance on the disk surface (e.g., lube moguls) with decreasing film thickness is attributed to an increasing contribution from the polar component of the disjoining pressure. Evaporative loss at temperatures typically encountered in a hard-disk drive also increases with decreasing molecular weight but is strongly dependent on the initial bonded fraction.

## 1. Introduction

In order to keep pace with the higher areal storage density requirements of hard-disk drives (HDDs), the spacing between the read-write element of the slider and the surface of the rigid magnetic disk has been reduced to 1–2 nm. Perfluoropolyether (PFPE) boundary lubricant films having reduced dynamic expansion perpendicular to the disk surface (“low z-profile”) have allowed lower flying. Low z-profile PFPEs can be attained by reducing the film thickness, the main chain molecular weight, and its flexibility [1–3]. Based on these studies, a useful mnemonic relating slider-disk mechanical clearance,  $\Delta$ clearance, to these PFPE main chain properties is given in (1) as follows:

$$\Delta\text{clearance} \propto \frac{1}{(\text{MW}^{1/2})(h)(f)}. \quad (1)$$

MW is the molecular weight,  $h$  is the film thickness, and  $f$  represents the main chain flexibility.

In this report, we compare the boundary lubrication properties of lower MW Z-Tetraols for their potential use in HDDs. Thus the effect on mechanical clearance, surface energy, lubricant dewetting, and lubricant evaporation at drive temperatures is quantified.

## 2. Experimental

The substrates used in these studies were 65 mm diameter glass disks of nominally 2 Å RMS roughness as measured by a Dimension 5000 AFM using a standard AFM tip in the tapping mode. The typical scan size for these measurements was 1 μm × 1 μm with a scan rate of 0.5 Hz and 256 lines of resolution. Atop the substrates a cobalt-based magnetic recording layer (CoPtCr) was sputter deposited, followed by CVD deposition of 30 Å of an amorphous nitrogenated carbon film (called “CN<sub>x</sub>”) comprised of nominally 15 at % N. Z-Tetraol-GT of 1200 and 2200 dalton (MW) were purchased from Solvay-Solexis (Italy) and used directly (Figure 1). The NMR compositions of the samples are quantified in Table 1.

Specular reflection FTIR (Nicolet Magna Model 560, Thermo Fisher) was used to quantify the film thicknesses of the applied PFPEs. The main IR absorption band near 1280 cm<sup>-1</sup>, due to the combination of C–F and C–O stretching vibrations, was related to film thickness as determined by XPS (Physical Electronics Instruments) [4]. Thin films from 0.7 to 1.8 nm provided the film thickness calibration. A standard (XPS) takeoff angle (45 ± 15°) and an electron mean-free path of 2.5 nm were used to determine the PFPE film thicknesses.

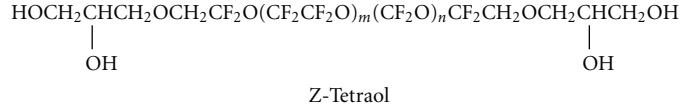


FIGURE 1: Chemical structure of Z-Tetraol.

TABLE 1: NMR data for the PFPE lubricants.

Lubricant	Mn	Tetraol	dol	bis
Z-Tetraol 1200	1200	0.98	0.02	0.00
Z-Tetraol 2200	2200	0.95	0.05	0.00

The mechanical clearance of the PFPE lubricants was quantified by measuring the acoustic emission (AE) generated at the head-disk interface as a function of slider-disk clearance. In these experiments, lubricated disks were placed on a spin stand and rotated at a constant 7200 RPM under ambient conditions. At the start of the experiments, the slider was allowed to fly over the rotating disk surface at a height of  $\sim 8$  nm, and the slider was heated to protrude the read-write element, that is, pole tip protrusion (PTP). During this procedure, the AE signal was continuously monitored, and the onset of an AE signal was interpreted as the occurrence of slider-disk interaction. The slider fly height versus (thermal fly height control) TFC power was used to calibrate the clearance based on the touchdown detection. The measurements were interleaved to minimize test variables. Each experiment was repeated 12–14 times, and the reproducibility of the data, despite the fairly large distribution, was taken as evidence that the slider flying characteristics were constant.

Lubricant moguls were induced on the disk surface by flying a slider on-track at a fly-height of 8 nm with no pole tip protrusion, under ambient conditions. A Vena VS-90 spin-stand tester was used. After 20 min of on-track flying, the disks were immediately interrogated by an optical surface analyzer (Q-phase image using a Candela Model 6120) and the lubricant mogul thicknesses were quantified.

### 3. Results

Representative data showing the AE signal as a function of the slider-disk clearance is shown in Figure 2(a) for Z-Tetraol 2200 and 1200 MW. A summary plot showing the average and distribution of all clearance data is shown in Figure 2(b) where the clearance values are plotted relative to 11.5 Å Z-Tetraol 2200. A positive clearance value therefore represents an increase or a gain in mechanical clearance. The lower MW Z-Tetraol shows approximately 0.8 nm improved clearance between the slider and disk surfaces, and this result is fully expected on the basis of (1); that is, a reduction in MW and a slightly thinner film (by 0.5 Å) allows lower flying before onset of slider-disk interference. The contribution to the clearance gain from the 0.5 Å film thickness difference is deconvolved from the inset figure ( $\sim 0.6$  nm/Å) to provide  $\sim 0.5$  nm clearance gain by the Z-Tetraol MW reduction from

2200 to 1200. The details are provided in the caption of Figure 2.

Figure 3 shows the lubricant disturbance on the disk surface as a function of MW and film thickness after head-flying. The lubricant disturbance leads to an accumulation of lubricant material in excess of the nominal film thickness that is shown as dark spots on the disk surface, and these are referred to as “lube moguls” [5]. The lighter spots in the images represent areas on the disk surface that has lost lubricant film thickness presumably to the moguls. It appears that the Z-Tetraol 1200 exhibits less lube moguls than the Z-Tetraol 2200 and may originate from the increased clearance (Figure 2). The reduction in lube moguls as a function of decreasing film thickness (Figure 3) has been attributed to increased adhesion with decreasing film thickness [6].

### 4. Discussion

According to (1), mechanical clearance from PFPE lubricants may be harvested by decreasing: (a) the film thickness, (b) the MW, and (c) the main chain flexibility. The extent to which each of these adjustments can be utilized is also limited because they can impact the HDD interface deleteriously. For example, reducing the film thickness to  $\leq \sim 8$  Å increases the surface energy significantly (Figure 4) thereby increasing the probability for contamination adsorption in the HDD. Since the focal point of this paper is the effect of MW reduction as a means to gain mechanical clearance, limitations attributable to decreasing the MW are now discussed.

Valuable information on PFPE MW effects is readily realized by measuring the surface energy as a function of film thickness and of MW. Information relevant to the adhesive strength, propensity for contamination adsorption, the lubricant monolayer thickness, and thus the critical dewetting thickness may be quickly assessed. Figure 4(a) shows the dispersive surface energy,  $\gamma_s^d$ , as a function of film thickness for Z-Tetraols on  $\text{CN}_x$ . The  $\gamma_s^d$  decreases monotonically with increasing film thickness in all cases, approaching what is expected to be the bulk dispersive surface energy near 14 mJ/m<sup>2</sup>. There does not appear to be a significant MW effect on  $\gamma_s^d$ . Quantitatively, the dependence of  $\gamma_s^d$  on the applied lubricant film thickness  $h$ , that is,  $\gamma_s^d(h)$ , can be described using  $\gamma_s^d(h) = \gamma_1^d + \Delta\gamma^d(h)$ , where

$$2\Delta\gamma^d(h) = \frac{1}{12\pi} \frac{A^*}{(d_o + h)^2}. \quad (2)$$

$d_o$  is a constant, and  $A^*$  is the “effective” Hamaker constant [7]. The  $d_o$  values used to fit the dispersive surface energy curves via (1),  $d_o = 2.5 \pm 0.5$  Å, is indicative that the interaction between the PFPE main chain and the underlying carbon film is relatively weak and hence cannot provide

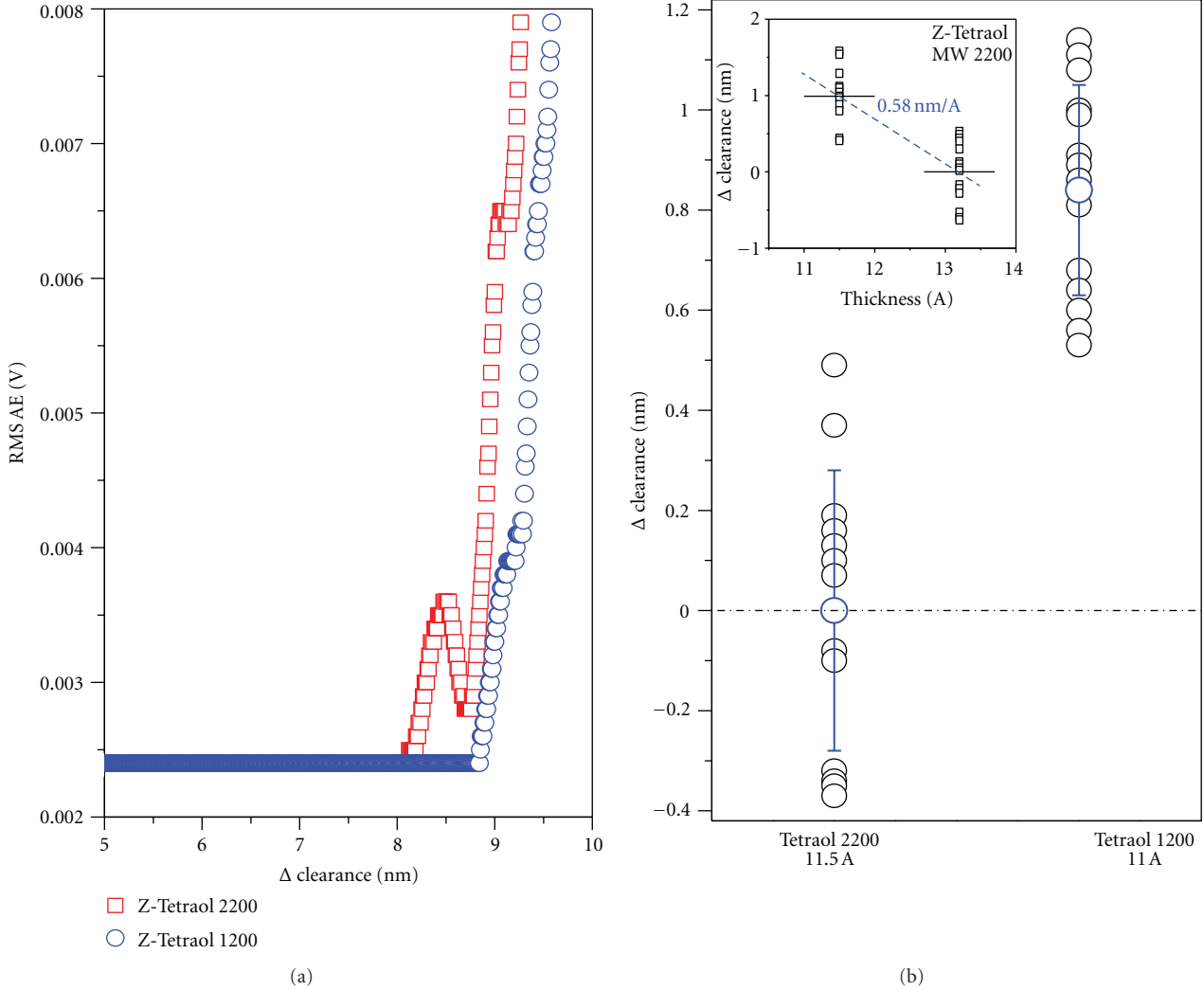


FIGURE 2: (a) Representative data plotting the rms acoustic emission (AE) as a function of slider-disk clearance for 11.5 Å Z-Tetraol 2200 and 11.0 Å Z-Tetraol 1200. The  $\Delta$ clearance is defined as the distance between the thermally protruding read-write element of the slider and the disk surface. (b) The slider-disk clearance data plotted relative to Z-Tetraol 2200. Open circles are the individual data points. Average data are represented by the blue points with 1 sigma standard deviation. The inset figure plots the  $\Delta$ clearance as a function of film thickness for Z-Tetraol 2200, providing a slope of 0.58 nm/Å. Thus, approximately 0.3 nm of the clearance difference between 11.5 Å Z-Tetraol 2200 and 11.0 Å Z-Tetraol 1200 can be attributed to the thickness difference.

significant adhesion. The corresponding  $A^*$  are equal to  $1.9 \times 10^{-19}$  J and  $2.1 \times 10^{-19}$  J for Z-Tetral 2200 and 1200 MW, respectively. The larger  $A^*$  for the lower MW Z-Tetraol is expected to provide a relatively better adhering film to the underlying carbon surface.

The corresponding polar surface energy,  $\gamma_s^P$ , as a function of film thickness is also shown in Figure 4(b). The distinct oscillations in  $\gamma_s^P$  as a function of film thickness are indicative of molecular layering in the PFPEs induced by the polar interactions with the underlying surface, much as observed previously for Zdols [8]. As shown in the figure, the structuring is propagated through several or more monolayers. The first minimum corresponds to the film thickness at which the surface becomes saturated with lubricant, that is, the monolayer film thickness, which is approximately 13 Å for 1200 MW and 20 Å for 2200 MW. Since HDDs today utilize

PFPE films near 10–12 Å, a reduction to a 1200 MW may not provide enough of a thickness margin to prevent moguls formation under HDD conditions unless thinner films are utilized.

While the identification of the monolayer film thickness is important for optimizing the boundary lubricant film properties, its resistance to the effects of the low-flying slider including air shear effects and chemical and physical forces [9] is another important aspect that can be addressed by the surface energy measurements. Surface energy-derived disjoining pressures [10], computed in Figure 5 as a function of the Z-Tetraol MW, provide a good comparison of anticipated lubricant reliability in the HDD interface. In the sub-monolayer film thickness regime, the total disjoining pressure gradient is larger for the lower MW Z-Tetraol due to the comparatively larger contribution from its polar component.

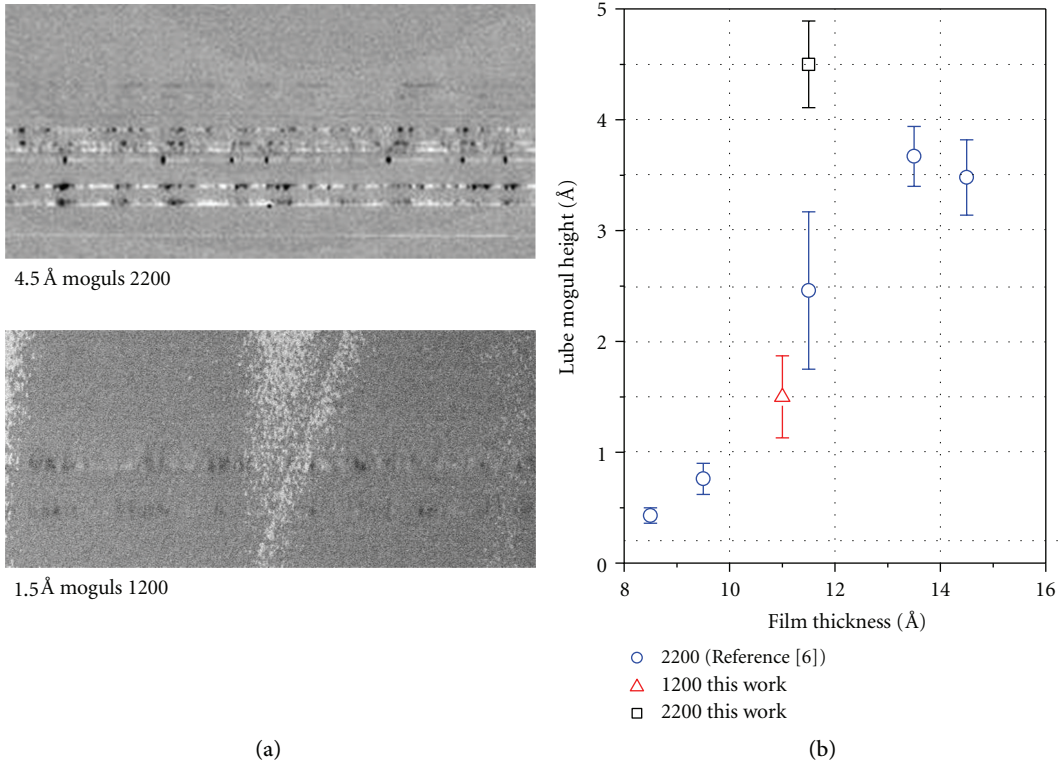


FIGURE 3: (a) Representative images of lube moguls after low flying on 11.5 Å Z-Tetraol 2200 (top) and 11.0 Å Z-Tetraol 1200 (bottom). These data were generated by flying the slider at 8 nm above the disk surface with no pole tip protrusion. (b) Summary plot showing the lube mogul height as a function of Z-Tetraol 2200 film thickness (blue circles are taken from [6]).

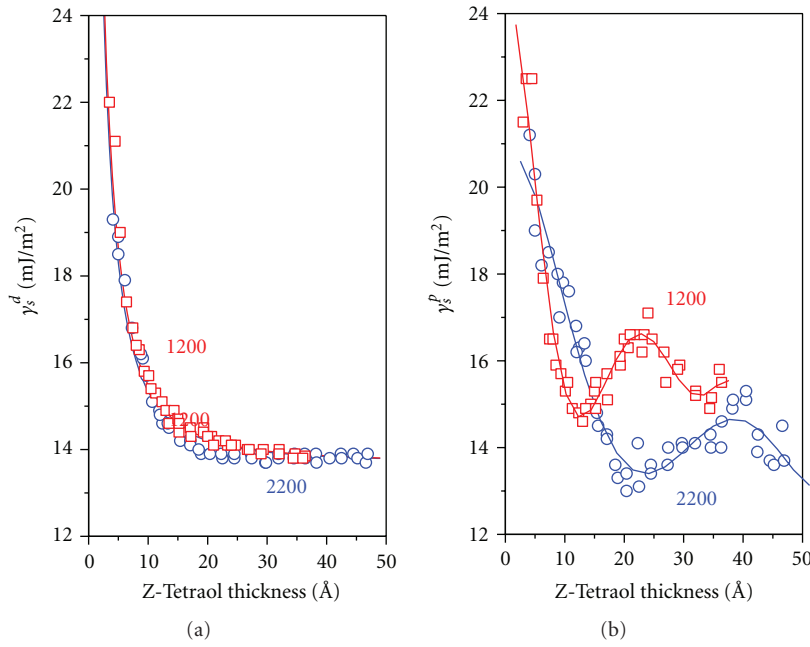
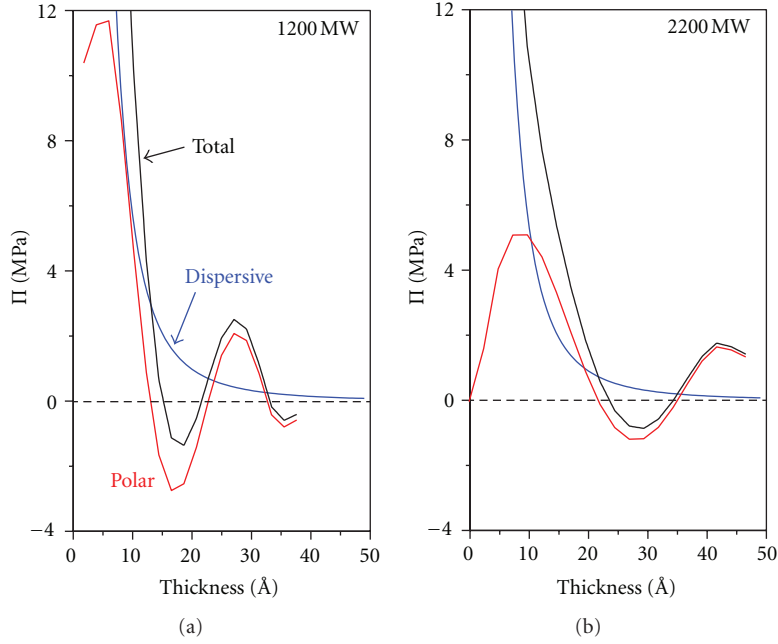
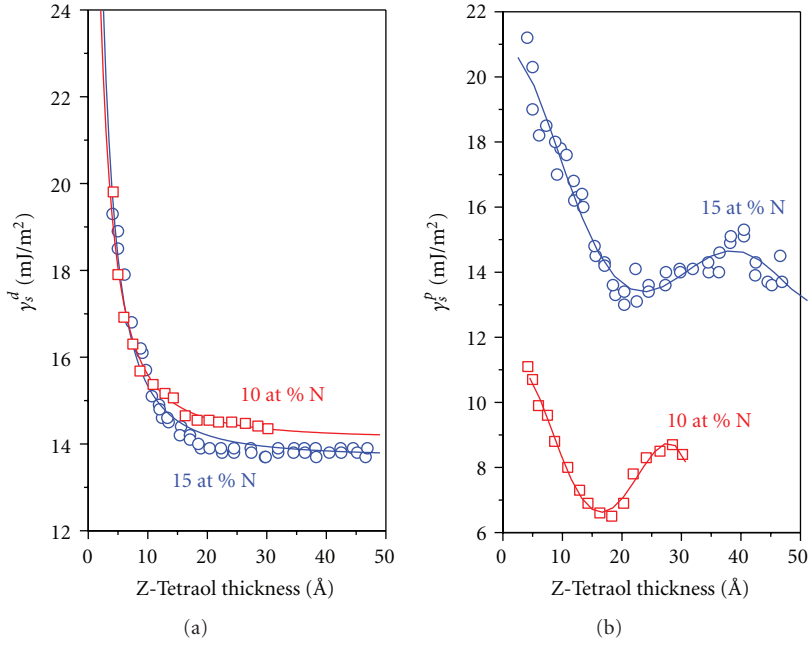


FIGURE 4: (a) Dispersive ( $\gamma_s^d$ ) and (right) polar ( $\gamma_s^p$ ) surface energy as a function of Z-Tetraol film thickness and MW.

FIGURE 5: Surface energy-derived disjoining pressure ( $\Pi$ ) as a function of Z-Tetraol film thickness.FIGURE 6: (a) Dispersive ( $\gamma_s^d$ ) and (b) polar ( $\gamma_s^P$ ) surface energy of Z-Tetraol 2200 as a function of film thickness and carbon film composition.

Therefore the lower MW film is expected to be more resistant to lubricant disturbance and moguls formation for thinner films ( $\leq \sim 10 \text{ \AA}$ ). However, since the monolayer thickness of lower MW Z-Tetraol is also thinner, the ability to resist film disturbance will decrease more rapidly than higher MW Z-Tetraol as the disjoining pressure converges towards zero. This would occur at approximately 14 and 22  $\text{\AA}$  for Z-Tetraol 1200 and 2200, respectively, (Figure 5). Thus the film thickness employed at the MW of choice is a significant

determinant. The monolayer thicknesses for Z-Tetraol 1200 and 2200, very useful quantities indeed, are summarized in Table 2.

A relevant observation regarding the quantification of the Z-Tetraol monolayer thickness by surface energy measurements is herewith disclosed. In particular, it has a pronounced dependence on the composition of the underlying carbon film. Figure 6 shows that the Z-Tetraol monolayer film thickness increases with increasing atomic % N, as

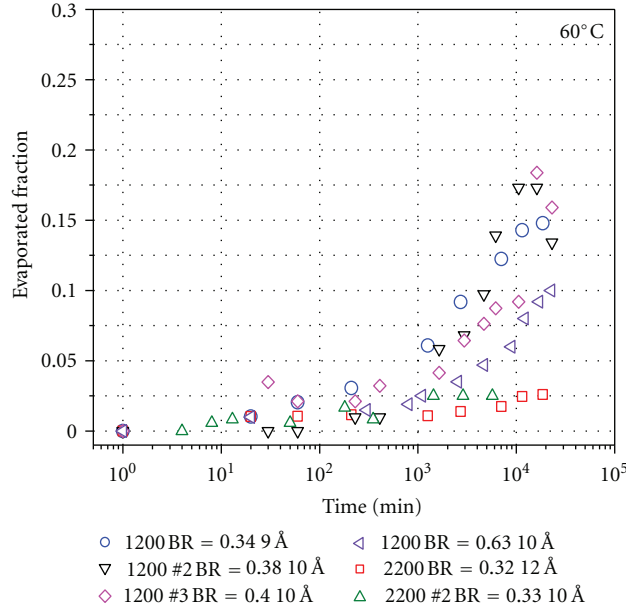


FIGURE 7: Evaporative loss of 9–12 Å Z-Tetraol films on CN<sub>x</sub> at 60°C. The experiments were repeated more than several times as a check of consistency. The inset legend specifies the MW (1200 or 2200), the bonded ratio (BR) when the experiment was begun, and the initial film thickness (9–12 Å). The bonded ratio was varied by disk aging under ambient conditions; that is, no annealing or UV treatment was applied to the disks.

TABLE 2: Monolayer thicknesses for Z-Tetraols on CN<sub>x</sub> (Å).

Z-Tetraol	$\gamma_s^p$ (Figure 4)	$\Pi = 0$ MPa (Figure 5)
1200	13	14
2200	20	23

previously observed for Zdol [11]. We therefore note that the film thickness of choice in HDDs can be influenced by factors other than the PFPE MW itself, and some compensation by the underlying film appears to be possible.

Another limitation of utilizing lower MW lubricants is the increased evaporative loss expected under HDD conditions. Figure 7 shows the film thickness loss as a function of time and of Z-Tetraol MW near the HDD temperature of 60°C. With decreasing MW, significant film thickness loss can occur leading to degraded performance in the HDD due to the lack of lubricant film coverage. Post-lubrication treatment such as annealing or UV curing may be employed to improve the bonded fraction and hence reduce evaporative loss of lower MW components in the lubricant film. Figure 7 shows decreased evaporation with increased initial bonded ratio (BR).

## 5. Conclusion

Lower MW Z-Tetraol films at the same total film thickness provide more mechanical clearance than higher MW Z-Tetraol due to its smaller z-profile. The increased resistance to lubricant disturbance on the disk surface (e.g., lube

moguls) is attributed to its increased molecular polarity; however, this behavior is strongly film thickness dependent and approaching the monolayer will quickly dissipate this advantage. The monolayer film thickness for the same Z-Tetraol MW may be manipulated by either increasing or decreasing the nitrogen content of the underlying carbon film.

## Acknowledgments

The authors thank J. Burns and D. Pocker of this laboratory for the NMR and ESCA data, respectively.

## References

- [1] A. Khurshudov and R. J. Waltman, “The contribution of thin PFPE lubricants to slider-disk spacing,” *Tribology Letters*, vol. 11, no. 3-4, pp. 143–149, 2001.
- [2] R. J. Waltman and A. G. Khurshudov, “The contribution of thin PFPE lubricants to slider-disk spacing. 2. Effect of film thickness and lubricant end groups,” *Tribology Letters*, vol. 13, no. 3, pp. 197–202, 2002.
- [3] R. J. Waltman, V. Raman, and J. Burns, “The contribution of thin PFPE lubricants to slider-disk spacing. 3. Effect of main chain flexibility,” *Tribology Letters*, vol. 17, no. 2, pp. 239–244, 2004.
- [4] M. F. Toney, C. M. Mate, and D. J. Pocker, “Calibrating ESCA and ellipsometry measurements of perfluoropolyether lubricant thickness,” *IEEE Transactions on Magnetics*, vol. 34, no. 4, pp. 1774–1776, 1998.
- [5] Q. Dai, C. Saint-Olive, R. Pit, and B. Marchon, “Genesis and evolution of lubricant moguls,” *IEEE Transactions on Magnetics*, vol. 38, no. 5 I, pp. 2111–2113, 2002.

- [6] R. J. Waltman, H. Deng, G. J. Wang, H. Zhu, and G. W. Tyndall, "The effect of PFPE film thickness and molecular polarity on the pick-up of disk lubricant by a low-flying slider," *Tribology Letters*, vol. 39, no. 2, pp. 211–219, 2010.
- [7] J. N. Israelachvili, *Intermolecular and Surface Forces with Applications to Colloidal and Biological Systems*, Academic Press, London, UK, 1985.
- [8] G. W. Tyndall, T. E. Karis, and M. S. Jhon, "Spreading profiles of molecularly thin perfluoropolyether films," *Tribology Transactions*, vol. 42, no. 3, pp. 463–470, 1999.
- [9] A. Y. Suh and A. A. Polycarpou, "Adhesive contact modeling for sub-5-nm ultralow flying magnetic storage head-disk interfaces including roughness effects," *Journal of Applied Physics*, vol. 97, no. 10, Article ID 104328, 11 pages, 2005.
- [10] C. M. Mate, "Taking a fresh look at disjoining pressure of lubricants at slider-disk interfaces," *IEEE Transactions on Magnetics*, vol. 47, no. 1, pp. 124–130, 2011.
- [11] R. J. Waltman and G. W. Tyndall, "Lubricant and overcoat systems for rigid magnetic recording media," *Journal of the Magnetics Society of Japan*, vol. 26, no. 3, pp. 97–108, 2002.

## Research Article

# Slider Posture Effects on Air Bearing in a Heat-Assisted Magnetic Recording System

Kyaw Sett Myo,<sup>1</sup> Weidong Zhou,<sup>1</sup> Xiaoyang Huang,<sup>2</sup> Shengkai Yu,<sup>1</sup> and Wei Hua<sup>1</sup>

<sup>1</sup> Data Storage Institute, Agency for Science, Technology and Research (A\*STAR), DSI Building,  
5 Engineering Drive 1, Singapore 117608

<sup>2</sup> School of Mechanical and Aerospace Engineering, Nanyang Technological University,  
50 Nanyang Avenue, Singapore 639798

Correspondence should be addressed to Kyaw Sett Myo, myo\_kyaw\_sett@dsi.a-star.edu.sg

Received 3 August 2012; Accepted 28 September 2012

Academic Editor: Jia-Yang Juang

Copyright © 2012 Kyaw Sett Myo et al. This is an open access article distributed under the Creative Commons Attribution License, which permits unrestricted use, distribution, and reproduction in any medium, provided the original work is properly cited.

This paper reports the effects of slider posture on the slider bearing in a heat-assisted magnetic recording (HAMR) system with the direct simulation Monte Carlo (DSMC) method. In this HAMR system, the heat issues on the slider bearings are assumed to be caused by a heated spot on the disk and/or slider body itself at various pitch angles. The simulation results show that with a heated spot on the disk, the air bearing pressure and air bearing force that acted on the slider surface will increase when the pitch angle becomes larger. It is also found that the bearing force increases with the heated spot size and the effects of a heated spot become more obvious at a larger pitch angle. On the other hand, the slider body temperature is observed to have a noticeable effect on air bearing pressure and force. The smaller pitch angle enlarges the tendency of bearing force variations with the slider temperature and makes the slider more sensitive to its temperature changes.

## 1. Introduction

With the increasing demands for large amount of storage nowadays, higher density recording technologies are required in hard disk drive industry. Heat assisted magnetic recording (HAMR) is one of the promising technologies to push the recording areal density of magnetic disk drives towards 10 Tb/in<sup>2</sup> and beyond. An HAMR system requires using a focused laser beam to heat up the media so as to reduce the media coercivity. It makes magnetic writing possible over high anisotropy magnetic media [1]. Performing the laser heating process requires the optimized slider designs integrating with the near field optical system inside for precise heating and recording. The integrated slider with an optical heating device normally requires flying at an extremely low head media spacing, which is only around few nanometers nowadays, to provide a high field at heated spot position for successful recording [2, 3]. With this spacing allowance, the Knudsen number, which represents the level of rarefaction effect in the flow, will be much larger than 1.0 and the flow in the head disk interface region can no

longer be assumed as a continuum one. Some modifications of continuum equations with appropriate slip boundary conditions are usually required.

However, it is very challenging to study the slider air bearing in a HAMR head disk interface with the current modified continuum equations due to the heat transfer issues involved in the HAMR system. Although some previous studies [4–6] proposed some heat transfer models for addressing such problems, these models cannot be used directly with the air bearing model to study heat effects on the slider air bearing. Therefore, we proposed to use direct Monte Carlo simulation (DSMC) method instead to solve the air bearing problems of HAMR application in our previous paper [7] because DSMC method has been used widely for modeling gaseous flows under rarefied conditions similar to the flow in the head disk interface. In that paper, the applicability of DSMC method in studying the air bearing effects of a HAMR slider was validated and the effects of heated spot size and slider body temperature to the slider air bearing were studied. Recently, Fukui et al. [8] studied the bearing pressure characteristics with a heated spot using both DSMC method

and the conventional molecular gas-film lubrication (MGL) equation with consideration of thermal creep flow. They observed that the results using both methods are agreeable [8].

In this paper, we will continue our works with the focus on the slider's posture effects on the air bearing in a HAMR system. We will investigate how the heat energy from a heated spot on the disk or high temperature slider body itself could contribute to the air bearing along with the slider posture changes.

## 2. DSMC Method and Code Verification

The DSMC method was introduced by Bird in the early 1970s [9] and it is a particle-based simulation method for rarefied gas flow problems. It uses a stochastic algorithm to calculate the molecule collision probabilities and scattering distributions conforming to kinetic theory. As for high-density recording, the head media spacing is reduced to few nanometers. Consequently, the flow in the head disk interface has the rarefaction effect. In the current head disk interface, the Knudsen number falls between 1 and 10. Therefore, the gas flow in the interface is considered as a transition flow or free-molecule flow and DSMC method offers a promising tool for numerical simulation of the interface gas flow.

Similar to what we have studied in our previous paper [7], the slider air bearing problem in DSMC simulations is simplified as a two-dimensional, microchannel flow with a stationary, slightly inclined surface (slider) above a horizontal plane (disk) moving in the  $x$ -direction with the tangential velocity  $U_b$ , as shown in Figure 1. The constant ambient temperature of  $T_0 = 273$  K and a pressure of  $P_0 = 1$  atm are maintained at inflow and outflow boundaries by adaptively adjusting the appropriate molecular velocity of particles at boundaries. Both slider and disk surfaces are assumed as fully accommodated ones and the collision model uses the variable hard sphere (VHS) particles. In order to facilitate the simple computation, argon gas is used in all simulation case studies in this paper because it is a simple monoatomic molecule gas with zero internal degrees of freedom. Besides, since the argon gas has similar mean free path and potential energy as those of the air, the bearing characteristics in argon gas should be close to that in air. Therefore, many previous air bearing studies [10, 11] regarded argon gas as a good candidate to replace air and used it in the DSMC simulations.

As for validating the DSMC simulation code, the results from Liu and Ng [10] were used to compare with the outcomes of our simulation tests. The channel length ( $L$ ) is set as  $5\ \mu\text{m}$  and the minimum channel height ( $H_o$ ) is  $50\ \text{nm}$  with disk moving velocity of  $U_b = 25\ \text{m/s}$ . In the validation tests, various pitch angles ( $\alpha$ ) from  $0.004$  to  $0.016\ \text{rad}$  are placed. The comparison of pressure distributions on the slider surface is shown in Figure 2 and it illustrates that they are in good agreement. Furthermore, the generalized lubrication equation solution of Fukui and Kaneko [12] using  $\alpha = 0.01\ \text{rad}$  is included for better evaluation and it also agrees with the DSMC result.

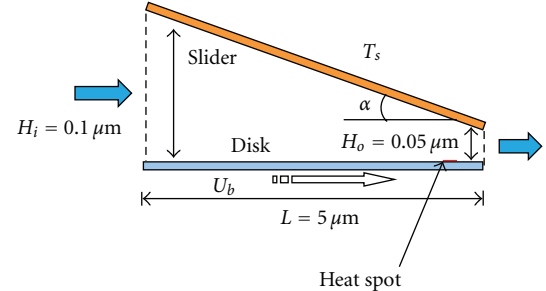


FIGURE 1: The slider and disk layout in the bearing interface.

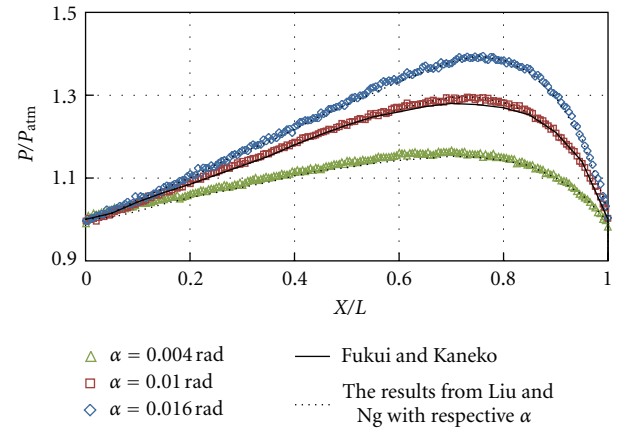


FIGURE 2: Comparison of pressure distributions on the slider surface from the present DSMC code, Liu and Ng [10] and the generalized lubrication equation solution of Fukui and Kaneko [12].

The streamwise locations of forces with three different pitch angles ( $\alpha$ ) are compared for validation purpose as shown in Figure 3 and they are also comparable. Here the stream-wise location of the bearing force acted on the slider surface is defined as

$$X_c = \frac{\sum_{i=1}^n (P_i - P_0) X_i}{\sum_{i=1}^n (P_i - P_0)}, \quad (1)$$

where  $n$  is the cell number along the  $x$ -direction,  $X_i$  is the individual cell position in  $x$ -direction,  $P_i$  is the localized pressure, and  $P_0$  is the atmospheric pressure.

From Figure 3, we can see that  $X_c$  is nearly fixed at a constant value when the pitch angle changes. Our DSMC results are also quite comparable with those of Liu and Ng [10].

After validating our DSMC code, we will use it to study the heat effects caused by a heated spot on the disk or, slider body itself at various pitch angles. The thermal distribution shape of a heated spot on the disk is assumed as a positive half-sine waveform with the peak temperature of  $500^\circ\text{C}$  ( $773\ \text{K}$ ) as shown in Figure 4. The slider body temperature ( $T_s$ ) is assumed to be uniform across the surface of air bearing slider.

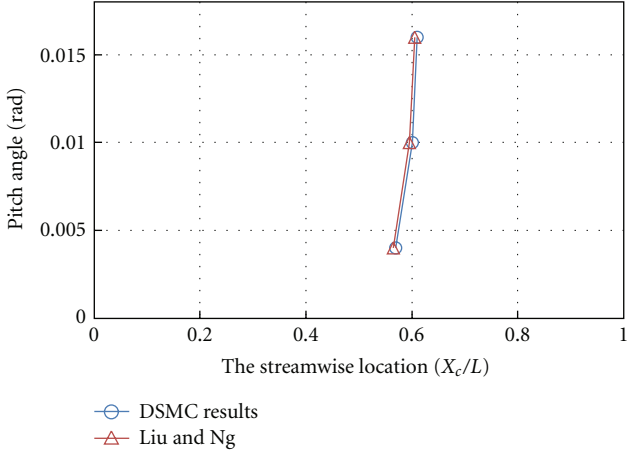


FIGURE 3: Comparison of streamwise locations of the slider bearing forces from the present DSMC code and those of Liu and Ng [10].

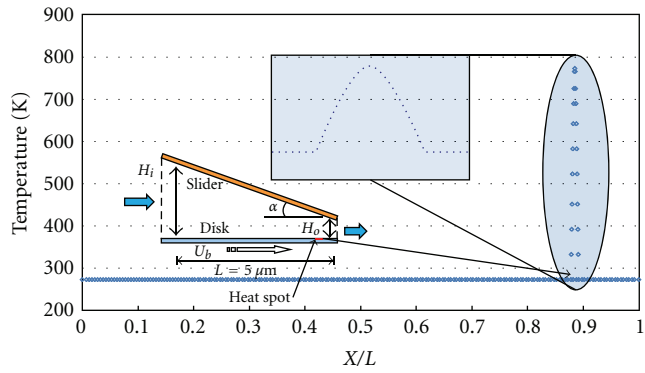


FIGURE 4: The temperature distribution profile with a heated spot on the disk.

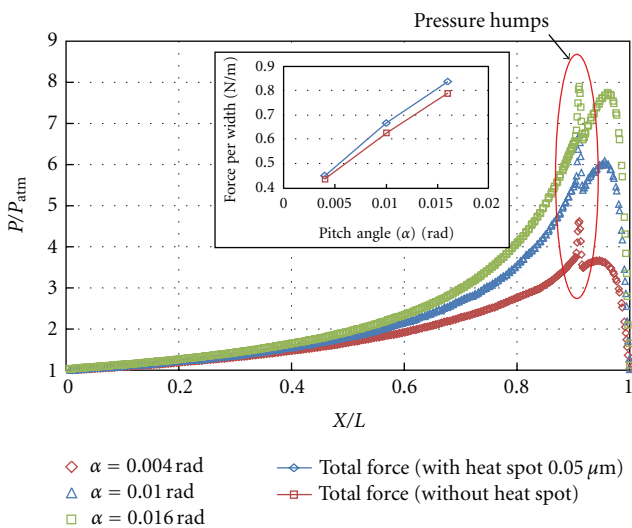


FIGURE 5: Comparison of air bearing pressure profiles on the slider surface with a  $0.05 \mu\text{m}$  heated spot on the disk for different pitching angles and (insert) the comparison of bearing forces at different pitch angles with a  $0.05 \mu\text{m}$  heated spot and without a heated spot.

### 3. Simulation Results and Discussions

In the simulation tests, the minimum channel height ( $H_o$ ) is fixed at 5 nm instead of 50 nm as for reflecting extremely low head-disk spacing in today's hard disk drives. With the fixed  $H_o$ , the growing pitch angles allow more molecules to come into the interface region. As a result, more molecule collisions happen and the velocities of molecules increase to build up higher pressures acted on the slider surface. The resulted pressure profiles increase with the slider pitch angles as shown in the main diagram of Figure 5.

From our previous study, it was observed that a heated spot on the disk causes the slider bearing pressure and force to increase with its size at the particular pitch angle. However, the heated spot size which is less than  $0.05 \mu\text{m}$  does not affect the air bearing substantially [7]. In this paper, the tests were conducted by varying pitch angle ( $\alpha$ ) from 0.04 to 0.16 rad with the  $0.05 \mu\text{m}$  heated spot located on the disk. The heated spot center is situated  $0.45 \mu\text{m}$  away from the flow exit in all tests. As in the main diagram of Figure 5, since the overall bearing pressure increases with the larger pitch angle, the amount of pressure hump due to a heated spot is elevated even with the fixed heated spot size. Hence, it assists increasing the bearing force acted on the slider surface.

It is also found that the base area of pressure hump around the heated spot location is wider in small pitch angle than that in the large one. This might be due to the narrower spacing between the slider and disk at a lower pitch, which causes the impact widely from the heated spot to its surrounding. In insert chart of Figure 5, it is observed that the increasing pitch angle enlarges the air bearing force almost in a linear way and the existence of a heated spot increases total bearing force at each posture position. Furthermore, the larger pitch angle causes the higher bearing force on the slider with the same size of a heated spot. Hence, the results suggested that the slider posture affects the air bearing performance with a heated spot which is  $0.05 \mu\text{m}$  or larger size in HAMR application.

Figure 6(a) shows the variation of the normalized total force acted on the slider with the heated spot size for different pitch angles. Here we define a normalized force value so that we could evaluate the effect of pitch angle on the total force more clearly. It is found that the variation of normalized bearing force with the heated spot size for a larger pitch angle is higher than that for a smaller one, which means that pitch angle effect becomes more and more important as its value increases. This is because the amount of pressure hump produced by a heated spot, as shown in Figure 5, increases with the pitch angle. Therefore, at a larger pitch angle, the slider bearing force will be more sensitive to the variation of heated spot size.

The stream-wise locations of bearing forces on the slider surface, as shown in Figure 6(b), move closer to the trailing edge as compared with those for larger  $H_o$  (50 nm) case. They will shift further towards the trailing edge of slider when a localized heated spot size, that is, larger than  $0.05 \mu\text{m}$ , is involved in the interface.

Next, as the head disk spacing could be reduced furthermore for higher density recording in HAMR application, it

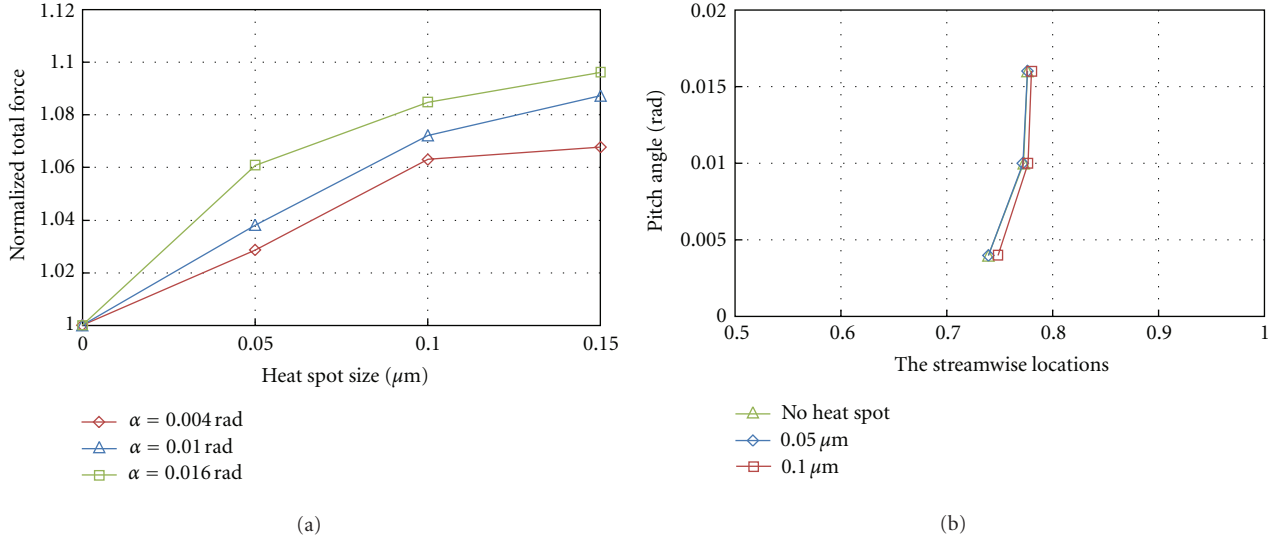


FIGURE 6: The variations of (a) total bearing force acted on the slider surface and (b) positions of resultant force with the heated spot size for different pitch angles. The normalized total force represents the respective total force with a heated spot divided by the total force without a heated spot.

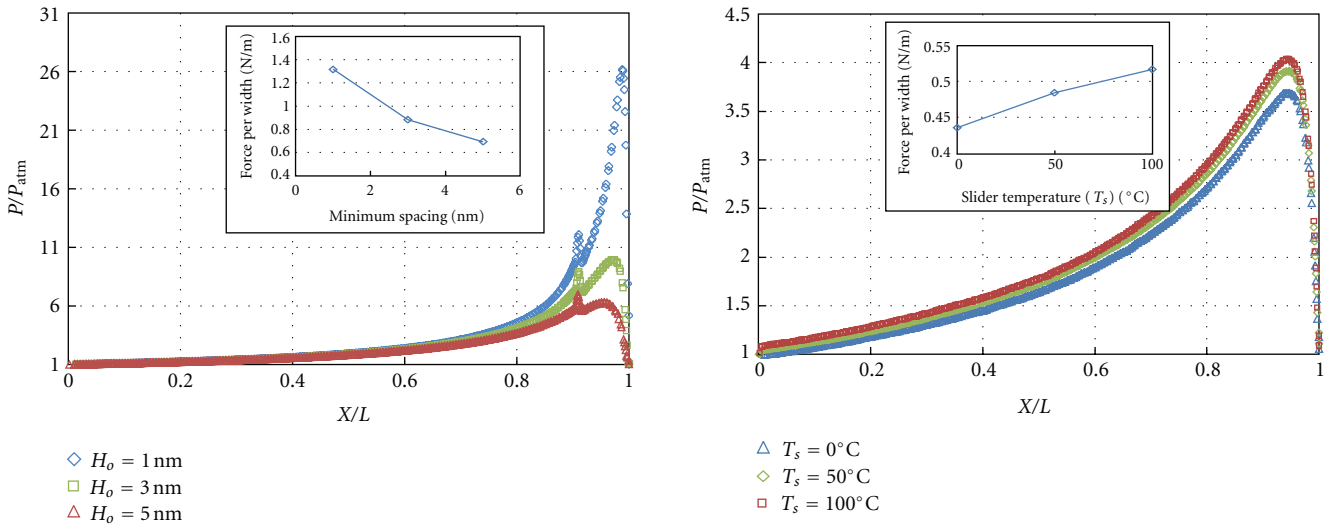


FIGURE 7: Comparison of air bearing pressure profiles on the slider surface with a  $0.05 \mu\text{m}$  heated spot on the disk for different minimum channel heights ( $H_o$ ) with a fixed pitch angle ( $\alpha$ ) of  $0.01 \text{ rad}$  and (insert) the comparison of bearing forces at different minimum channel heights with a  $0.05 \mu\text{m}$  heated spot.

is useful to study the effect of smaller gap spacing on the air bearing behavior. In order to study the gap effect, the minimum channel height ( $H_o$ ) is decreased from  $5 \text{ nm}$  to  $1 \text{ nm}$  with a fixed pitch angle at  $0.01 \text{ rad}$ . The results are shown in Figure 7. It is found that the bearing pressure increases significantly and its peak position moves away from the pressure bump caused by a heated spot when the minimum spacing  $H_o$  decreases. From the inset chart of

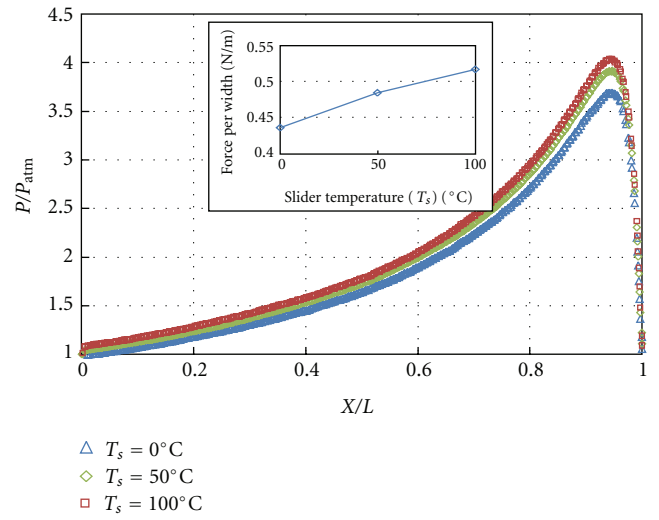


FIGURE 8: Comparison of air bearing pressure profiles on the slider surface with varied slider body temperatures for a fixed pitch angle ( $\alpha$ ) of  $0.004 \text{ rad}$ .

Figure 7, it is observed that the bearing force also increases proportionally as  $H_o$  decreases.

Finally, we study the effect of slider body temperature on the air bearing. We assume that the temperature on the slider surface is higher than the ambient one and it is uniform across the slider surface. Such high temperature on the slider body may be caused by the heat dissipation in the HAMR optical head, electrical heater, writer, or other components. Figure 8 shows that both bearing pressure and force increase gradually as slider body temperature ( $T_s$ ) changes from  $0^\circ\text{C}$  to  $100^\circ\text{C}$  at  $\alpha = 0.004 \text{ rad}$ . This is because the thermal energy

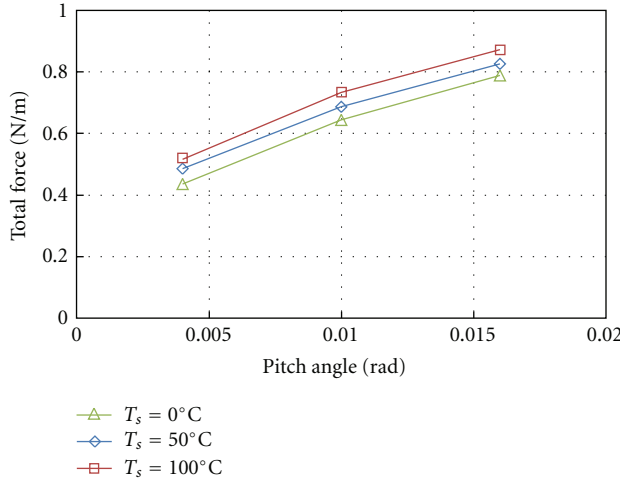
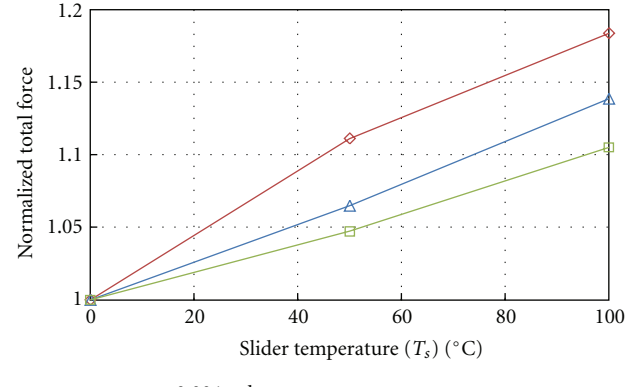


FIGURE 9: Comparison of total bearing forces acted on the slider surface with different slider temperatures and slider pitch angles.

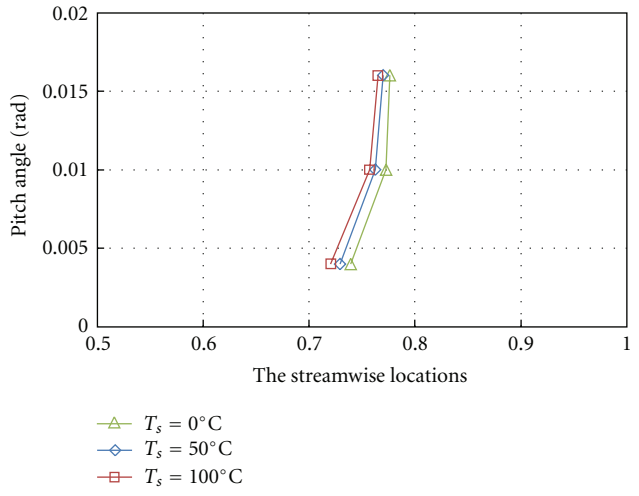
released from the slider body goes into the interface and affects the bearing pressure and force. In other words, the surrounding gas molecules in the interface gain more energy from the heat transfer of a heated spot or slider body and exert stronger pressure on the slider surface when the gas molecules strike on it. As a result, the bearing force, which is derived from the pressure distribution on the slider surface, will increase as the temperature of heated spot or slider body increases. Based on the simulation results with other pitch angles, it is also observed that the total bearing force increments due to slider temperature rises are quite uniform at any slider pitch angle as shown in Figure 9. This suggests that the heat energy from the slider has similar effects on the bearing pressure and force regardless of the pitch angle of the slider.

Figure 10(a) shows the variation of the normalized total force acted on the slider with the slider temperature for different pitch angles. Here we also define a normalized force value to evaluate pitch angle effect at various slider body temperatures. The results show that the normalized bearing force gradient increases with the falling pitch angle, which means that the pitch angle effect becomes less important at its higher values. This is because the total bearing force increment with the slider temperature is almost the same at each pitch angle, but the absolute total force value at  $T_s = 0^\circ\text{C}$  will increase with the pitch angle, as shown in Figure 9. Therefore, the normalized force value, which represents the relative change of bearing force at various slider temperatures, will become smaller as pitch angle increases; that is, the air bearing total force is insensitive to the variation of slider temperature at a higher pitch angle.

Figure 10(b) shows the relation of the pitch angle with the slider stream-wise location of force. It is found that the stream-wise location of bearing force shifts towards the leading edge with higher slider temperature. The effect of slider temperature on the location shift is found to be opposite to that of the heated spot.



(a)



(b)

FIGURE 10: The variations of (a) total bearing force acted on the slider surface and (b) positions of resultant force with varied slider temperatures for different pitch angles. The normalized total force represents the respective total force divided by the total force resulted from the test with  $T_s = 0^\circ\text{C}$ .

#### 4. Conclusions

From the simulation studies in this paper, it is concluded that the slider posture effects on the air bearing should be carefully considered in a HAMR system. The conclusions are drawn as follows.

- (1) Both air bearing pressure and total bearing force will increase with the slider pitch angle and the stream-wise location of bearing force shifts closer to the trailing edge with the growing pitch angle.
- (2) The pressure and force increment caused by a heated spot with a larger pitch angle is higher than that with a lower pitch angle. The slider bearing force will be more sensitive to the variation of heated spot size at a larger pitch angle.

- (3) With a low pitch angle, the effect of a heated spot is small on the air bearing but slider temperature effect will become larger. The slider bearing force will be more sensitive to the variation of slider temperature at a smaller pitch angle.
- (4) The stream-wise location of bearing force moves to the trailing edge with a larger heated spot while it goes to the opposite direction as the temperature on the slider body increases.

## References

- [1] J. J. M. Ruigrok, R. Coehoorn, S. R. Cumpson, and H. W. Kesteren, "Disk recording beyond 100 Gb/in.2: hybrid recording?" *Journal of Applied Physics*, vol. 87, no. 9, pp. 5398–5403, 2000.
- [2] M. H. Kryder, E. C. Gage, T. W. McDaniel et al., "Heat assisted magnetic recording," *Proceedings of the IEEE*, vol. 96, no. 11, pp. 1810–1835, 2008.
- [3] B. Liu, S. Yu, M. Zhang et al., "Air-bearing design towards highly stable head-disk interface at ultralow flying height," *IEEE Transactions on Magnetics*, vol. 43, no. 2, pp. 715–720, 2007.
- [4] W. D. Zhou, B. Liu, S. K. Yu, W. Hua, and C. H. Wong, "A generalized heat transfer model for thin film bearings at head-disk interface," *Applied Physics Letters*, vol. 92, no. 4, Article ID 043109, 3 pages, 2008.
- [5] D. Chen, N. Liu, and D. B. Bogy, "A phenomenological heat transfer model for the molecular gas lubrication system in hard disk drives," *Journal of Applied Physics*, vol. 105, no. 8, Article ID 084303, 8 pages, 2009.
- [6] W. D. Zhou, B. Liu, S. K. Yu, and W. Hua, "Rarefied-gas heat transfer in micro- and nanoscale Couette flows," *Physical Review E*, vol. 81, no. 1, Article ID 011204, 7 pages, 2010.
- [7] K. S. Myo, W. Zhou, S. Yu, and W. Hua, "Direct Monte Carlo simulation of air bearing effects in heat-assisted magnetic recording," *Microsystem Technologies*, vol. 17, no. 5–7, pp. 903–909, 2011.
- [8] S. Fukui, N. Kitagawa, R. Wakabayashi, K. Yamane, and H. Matsuoka, "Molecular gas-film lubrication analyses considering boundary temperature distributions," in *Proceedings of the Joint International Conference on Micromechantronics for Information and Precision Equipment (MIPE'12)*, pp. 194–196, Santa Clara, Calif, USA, 2012.
- [9] G. A. Bird, *Molecular Gas Dynamics and the Direct Simulation of Gas Flows*, Clarendon, Oxford, UK, 1994.
- [10] N. Liu and E. Y. K. Ng, "The posture effects of a slider air bearing on its performance with a direct simulation Monte Carlo method," *Journal of Micromechanics and Microengineering*, vol. 11, no. 5, pp. 463–473, 2001.
- [11] W. Huang and D. B. Bogy, "Three-dimensional direct simulation Monte Carlo method for slider air bearings," *Physics of Fluids*, vol. 9, no. 6, pp. 1764–1769, 1997.
- [12] S. Fukui and R. Kaneko, "Analysis of ultra-thin gas film lubrication based on linearized Boltzmann equation: first report—derivation of a generalized lubrication equation including thermal creep flow," *Journal of Tribology*, vol. 110, no. 2, pp. 253–262, 1988.